technische universität
dortmund

Fakultät Physik – Experimentelle Physik V

Physik E5

Messages from a Black Hole

A long-term analysis of the Active Galactic Nucleus Markarian 421 in the light of γ-rays measured by MAGIC-I

Dissertation

zur Erlangung des akademischen Grades eines

Doktors der Naturwissenschaften
(Dr. rer. nat.)

vorgelegt von

Dipl.-Phys. Ann-Kristin Overkemping

Februar 2015

Erstgutachter:	Prof. Dr. Dr. Wolfgang Rhode
Zweitgutachter:	Prof. Dr. Joachim Stolze
Abgabedatum:	26. Februar 2015

Contents

1 Introduction **1**

2 Astroparticle Physics **3**
2.1 Messenger particles . . . 3
2.2 Sources of radiation . . . 8
2.3 Active Galactic Nuclei . . . 9
2.4 Blazars - a special insight into AGNs . . . 10
2.5 The blazar Markarian 421 . . . 12

3 Ground-based detection of very high energy γ-rays **15**
3.1 Extensive Air Showers . . . 15
3.2 Detection technique . . . 17
3.3 Cherenkov telescopes at the present day . . . 19

4 Data analysis for the MAGIC-I telescope **25**
4.1 Monte Carlo simulations of γ-rays . . . 25
4.2 Signal extraction and calibration of raw data . . . 26
4.3 Image cleaning and parametrisation . . . 26
4.4 γ-Hadron-Separation, energy estimation and reconstruction of the source position . . . 28
4.5 Signal detection . . . 31
4.6 Sky map . . . 34
4.7 Energy spectrum and light curve . . . 34
4.8 Spectrum unfolding . . . 35

5 Mrk 421 data analysis **39**
5.1 Data overview and selection criteria . . . 39
5.2 Selected data samples for analysis . . . 42
5.3 Significance of Mrk 421 data . . . 45
5.4 Light curve determination . . . 46
5.5 Light curve in different energy ranges . . . 50
5.6 Flux variations on short time scales . . . 55
5.7 Spectrum . . . 61
5.8 Conclusions on the light curve and the spectrum of Mrk 421 measured by MAGIC-I . . . 67

6 Periodicity search in light curves **69**
6.1 Periodicity search with RobPer . . . 69
6.2 Mrk 421 light curve from 2007 to 2009 by MAGIC-I . . . 72
6.3 Mrk 421 light curve from 1992 to 2012 above 1 TeV . . . 75
6.4 Mrk 421 light curve from 2013 to 2015 by FACT . . . 80
6.5 Conclusions on the periodicity search . . . 83

7 Study of MWL correlations of Mrk 421 **85**
7.1 Considered instruments measuring in other wavebands . . . 85
7.2 Comparison of the light curves in other wavebands to γ-rays . . . 86
7.3 Variability . . . 89
7.4 Correlations . . . 92
7.5 Spectral energy distribution . . . 99
7.6 Conclusions on Mrk 421 in the MWL context . . . 104

8 Conclusions **107**

A Supplementary information: Mrk 421 analysis **109**
A.1 Overview of Mrk 421 data . . . 109
A.2 Overview of background data . . . 114
A.3 Overview of Crab Nebula data . . . 115
A.4 Significances of Crab Nebula and Mrk 421 data . . . 115
A.5 Cut values in *fluxlc* of Crab Nebula data . . . 116
A.6 Light curve results of Mrk 421 data . . . 116
A.7 Constant fit results for all light curves with daily bins . . . 119
A.8 Short-term light curves . . . 120
A.9 Spectrum results . . . 121

B Supplementary information: MWL correlations **123**
B.1 Light curves . . . 123
B.2 Results of variability studies . . . 126
B.3 Additional results for cross-correlation . . . 128
B.4 Spectral energy distribution . . . 129

C One-zone SSC model for the 2009 SED **131**

List of Figures **I**

List of Tables **III**

Bibliography **V**

List of Abbreviations **XVII**

Acknowledgement/Danksagung **XIX**

Chapter 1
Introduction

Once upon a time, more than 100 years ago, there was a physicist named Victor Hess, who went out in a hot-air balloon to explore the ionisation rate in the atmosphere. This led to the discovery of cosmic radiation...
In 1912 Hess discovered that the ionisation rate in the atmosphere increases with increasing height. So he concluded that charged radiation enters our atmosphere from space [Hes12]. He was awarded the Nobel Prize in Physics in 1936[1] for the discovery of cosmic radiation. This moment can be called the beginning of astroparticle physics. Since then the sources of cosmic rays (CR) and the propagation of CRs through the Universe have been studied, but they are not fully understood yet and therefore still a matter of recent research.

In order to get an insight into astrophysical sources, their emitted particles and radiation need to be considered. The cosmic rays arriving in the Earth's atmosphere are either charged particles, photons or neutrinos. Charged cosmic rays are not suitable for analyses of specified sources because they are deflected in intergalactic magnetic fields and cannot be traced back to their origin. This is different for neutrinos and photons. For both it is possible to reconstruct the originating position.
The low interaction cross-section of neutrinos is an advantage and a disadvantage at the same time. On the one hand they can stem from the innermost region of a source and thereby deliver information about ongoing processes, on the other hand it is hard to detect them. In contrast to that, photons are easier to detect. Different types of instruments have been developed to detect photons in all wavebands, from the low energetic radio waves to the high energetic γ-rays.
Sources in our Universe, which are capable of accelerating particles to high energies, are Active Galactic Nuclei. To reveal their structure and the particle composition inside them they are extensively observed over the whole electromagnetic spectrum. A subclass of the Active Galactic Nuclei are blazars, which are able to emit radiation up to the highest energies.
The closest and therefore best to be studied blazar is Markarian 421. With its brightness and its proximity it is one of the best candidates for studies on acceleration mechanisms in Active Galactic Nuclei. It is regularly observed by the MAGIC telescopes. Therefore, a more than two year long data set of Mrk 421 measured by MAGIC was selected for a study of long-term and short-term variabilities in the source's emission. Additionally, the dependence of the spectral shape on the emission strength is examined. To draw

[1] see `www.nobelprize.org/nobel_prizes/physics/laureates/1936/hess-facts.html`

conclusions on the acceleration mechanisms in the emission regions of blazars the overall picture of the emission over the whole electromagnetic spectrum needs to be considered. Therefore, the MAGIC results will be put in context with results of other telescopes. A better understanding of Mrk 421 might help to broaden the knowledge of Active Galactic Nuclei in general.
This thesis is structured as follows.

Chapter 2 provides a brief summary of astroparticle physics. It includes an overview of the different messenger particles, their production and acceleration processes as well as the interactions they undergo on their way through the Universe. The different types of galactic and extragalactic sources will be introduced. Particular attention will be given to the source class of Active Galactic Nuclei, whereby the subclass of blazars will be emphasised. Lastly, the blazar Mrk 421 is introduced because it is the source to be studied.

The detection of high energetic γ-rays is explained in chapter 3. Here, the formation of air showers in the atmosphere and their detection with Cherenkov telescopes are discussed. The MAGIC telescopes, which recorded the data analysed in this thesis, are introduced as well as the FACT telescope. The analysis procedure for MAGIC data is illustrated in chapter 4.

In chapter 5 the analysis of the Mrk 421 data is explained. An overview of the 2.3 year long data sample will be given. The results of the long-term and short-term study of the light curve as well the resulting spectrum will be discussed.

In chapter 6 a method for finding periodicities in light curves is outlined. This method is applied to the resulting MAGIC light curve of Mrk 421 from this thesis, to a merged TeV light curve of further Cherenkov telescopes spanning over 20 years, and to a light curve from the new Cherenkov telescope FACT.

The results of the MAGIC data analysis are put in context with data from other instruments in chapter 7. The γ-ray light curve of Mrk 421 will be compared to light curves of other wavebands. A variability study as well as a correlation study on these light curves are carried out. In addition some concluding remarks about emission models in Mrk 421 will be given.

All results will be summarised in chapter 8. Motivations for further research on this source will be discussed as well.

Chapter 2
Astroparticle Physics

This chapter gives a brief overview of the necessary and relevant basics of astroparticle physics for the understanding of the blazar Mrk 421. First of all, the emitted messenger particles from astrophysical sources will be introduced. Then their acceleration and interaction processes will be discussed as well as the astrophysical sources of cosmic rays. Then a deeper insight will be provided into the source class of Active Galactic Nuclei with special attention given to the subclass of blazars. Lastly, Mrk 421, the source of interest in this thesis, will be introduced.

2.1 Messenger particles

The only possibility to observe astrophysical sources is given by their emitted particles and radiation, the messenger particles. These include photons, neutrinos, and charged particles like protons, heavier nuclei, or electrons. In Figure 2.1 an illustration of the propagation of the messenger particles from their production site to the Earth and the subsequent detection possibilities are shown.

2.1.1 Charged cosmic rays

The charged component of the cosmic rays consists of protons, helium nuclei, other heavier ionised nuclei, and electrons, whereas protons make up the largest fraction (85%) [Gru05]. Due to their charge they are deflected in randomly distributed intergalactic magnetic fields. Therefore, their arrival directions at the Earth are isotropically distributed and it is not possible to reconstruct their source position.
The energy spectrum of the ionised atomic nuclei spans from the MeV range to at least 10^{20} eV. It follows a power law $dN/dE \propto E^{\alpha}$, which can be explained by the acceleration of charged particles in shock fronts. In the spectrum two spectral breaks are observed. The first kink in the spectrum is observed at about 10^{15} eV. For energies below this so-called knee, the spectral index is $\alpha = -2.7$. Above the knee the spectrum steepens with a slope of $\alpha = -3.1$. At about $10^{18.5}$ eV, the so-called ankle, the spectrum flattens again. The particle rate decreases rapidly with increasing energy. This means that e.g. at GeV energies about 1000 particles arrive per second and square metre, whereas this number is less than one particle per century and km^2 for energies of 10^{20} eV. [Blu09]
One explanation of the knee and the ankle could be that different sources accelerate particles up to different energies. In this scenario the upper acceleration limit of galactic

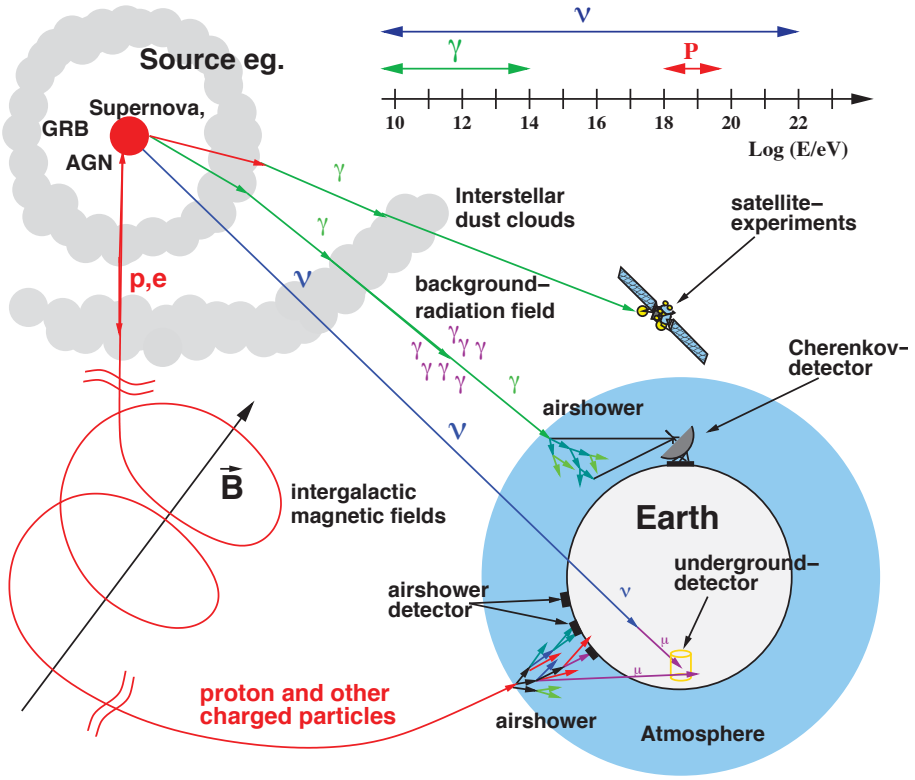

Figure 2.1: Overview of the propagation of the messenger particles from their sources on their paths towards the Earth. The different detection possibilities are indicated. The image is taken from [Dre09], after [Wag04].

supernovae (SN) would cause the steepening at the knee. Due to the dependence of the particle's energy gain on its charge number the particle rate smoothly decreases above the knee. The flattening at the ankle would be caused by an additional incoming component from extragalactic sources. In a different scenario the steepening of the spectrum at the knee is explained by the leakage of charged particles from our galaxy with higher energies. These particles are able to leave the Milky Way when their Larmor radius in the magnetic field of the galaxy is larger than the thickness of the galactic disk. [Blu09]
The maximum energy a particle can reach in acceleration processes depends on the size of the acceleration region R and its magnetic field B and it is given by

$$E_{\max} \propto \beta_s Z R B \,, \tag{2.1}$$

where β_s is the velocity of the shock front and Z is the charge number of the particle [Blu09]. In Figure 2.2 the relation of the size L and the magnetic field B of different sources is shown in the so-called Hillas plot. The sources with the potential to accelerate particles up to the highest energies are Active Galactic Nuclei (AGN), gamma-ray bursts (GRB), and jets of radio galaxies. These sources as well as further sources from this plot will be explained in section 2.2.

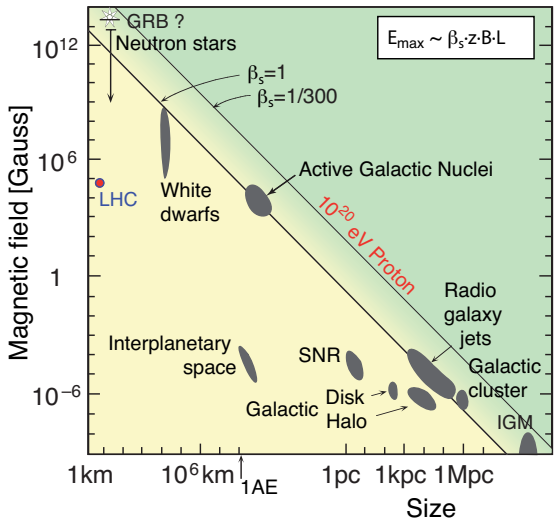

Figure 2.2: Hillas plot of different astrophysical sources. Typical magnetic fields B and sizes L of each source type are shown. The dashed and solid lines represent the necessary magnetic field and size to accelerate a proton to 10^{20} eV for two given shock velocities β_s. These two lines show that the larger β_s becomes the smaller B and/or L can become to reach the same maximum energy. The image is taken from [Blu09].

For energies above $6 \cdot 10^{19}$ eV the charged particles interact with photons of the cosmic microwave background (CMB). For protons p interacting with the CMB photons, a delta resonance Δ^+ is formed which subsequently decays as follows:

$$p + \gamma_{\mathrm{CMB}} \rightarrow \Delta^+ \rightarrow \begin{cases} p + \pi^0 \\ n + \pi^+. \end{cases} \tag{2.2}$$

This results in the Greisen-Zatsepin-Kuzmin (GZK) cut-off of the spectrum at this energy, which is named after Greisen [Gre66], Zatsepin and Kuzmin [Zat66] who predicted it. [Gru05]
The cut-off is confirmed by measurements of e.g. the Pierre Auger Observatory [Abr08].

Particle acceleration
A charged particle can collide with interstellar clouds which contain turbulent magnetic fields. When a particle enters the cloud it elastically interacts with the magnetic field. When the particle leaves the cloud it has gained an amount of energy which is proportional to the square of the relative cloud velocity $\beta_{\mathrm{cl}} = v_{\mathrm{cl}}/c$. As this process is quadratic in its velocity and was proposed by Fermi [Fer49], it is referred to as second-order Fermi acceleration. [Sta10]
The first-order acceleration of charged particles in astrophysical shocks is even more promising for the acceleration of particles to high energies. A shock is formed e.g. when a supernova remnant (SNR) expands into the interstellar medium (ISM) with a velocity larger than the sound velocity in the ISM. A particle ahead of the shock can cross the

shock front. It can then be reflected back in magnetic inhomogeneities around the shock front and cross it again. This process goes on until the particle can leave the environment of the shock front. In this scenario the energy gain is linear in the relative velocity of the shock front $\beta_s = v_s/c$. As the velocities of shock fronts are higher than those of magnetic clouds and the energy gain is proportional to β_s instead of β_{cl}^2, the first-order acceleration is more efficient than the second-order acceleration. [Sta10]

2.1.2 Neutrinos

Neutrinos are produced in astrophysical sources because the accelerated protons in the source interact with matter or radiation to produce pions, whereby charged pions subsequently decay into neutrinos. In the interaction of a proton with matter π^+, π^- and π^0 are produced. In the interaction of protons with ambient photons a Δ^+ resonance is formed. A π^0 and a proton or a π^+ and a neutron are the decay results, as was shown in Equation 2.2. [Kat12]
When the neutron decays neutrinos are produced: $n \to pe^-\bar{\nu}_e$. [Gru05]
Whereas a neutral π^0 further decays into two photons

$$\pi^0 \to \gamma\gamma\,, \tag{2.3}$$

neutrinos are produced in the decay of charged pions as follows:

$$\pi^+ \to \mu^+\nu_\mu \qquad \text{and} \qquad \pi^- \to \mu^-\bar{\nu}_\mu\,. \tag{2.4}$$

The decay of these muons produces even more neutrinos:

$$\mu^+ \to e^+\bar{\nu}_\mu\nu_e \qquad \text{and} \qquad \mu^- \to e^-\nu_\mu\bar{\nu}_e\,. \tag{2.5}$$

Due to their electrical neutrality and their low interaction cross-section with matter, neutrinos can propagate through the Universe without being absorbed or deflected. Therefore, their point of origin can be reconstructed. However, the low interaction cross-section makes it hard to detect them at all. [Kat12]
For this reason large underground detectors such as the IceCube detector at the South Pole are built. Just recently IceCube has detected 28 high-energetic neutrino events. There were no significant groups of neutrinos found to be coincident in time and space. The detection of neutrinos from a specific source type would give an insight into the acceleration mechanisms and the composition of particles inside the source. [Aar13]

2.1.3 Photons

Like the neutrinos the photons possess no charge. Hence, they are not deflected in intergalactic magnetic fields and they point back to their origin. In contrast to neutrinos they can be detected more easily. The exploration of the Universe began with observations in the optical waveband. One known production of photons is the thermal radiation following a black-body spectrum from e.g. stars like our Sun. After the invention of telescopes sensitive to other wavebands other than the optical waveband it became clear that other processes also produce radiation which is not necessarily visible to the naked eye. These processes are called non-thermal and they are capable of producing photons in

all wavebands ranging from radio photons to the highest energetic γ-rays. On Earth it is not possible to reproduce the environments given in astrophysical sources to produce these highest energies. The Large Hadron Collider (LHC) is added in the Hillas plot in Figure 2.2 in order to be able to compare it to the astrophysical sources. The study of astrophysical accelerators gives particle physicists the possibility to explore particle interactions in the most extreme environments. [Wee03]
This thesis mainly focusses on data of an astrophysical source recorded by a γ-ray telescope. Therefore, the production mechanisms of γ-rays and their possible interaction during the propagation through the Universe will be discussed in the following. The detection of high energetic γ-rays on Earth will be the topic of chapter 3.

Production of γ-rays

- **Synchrotron radiation:**
  When a charged particle moves through a magnetic field, it is deflected and will follow a spiral trajectory. The charged particle is being accelerated and therefore emits radiation. Cyclotron radiation is emitted for non-relativistic particles, synchrotron radiation for relativistic particles. The energy loss of the relativistic particle depends on its mass: $dE/dt \propto -m^{-4}$ [Pov09]. Therefore, electrons radiate the most efficiently. However, they need to be accelerated to very high energies for that, and this is again a problem because of the fast synchrotron cooling. Heavier particles like the protons can therefore be accelerated more easily than the light electrons, but they need to have very high energies to produce high energetic synchrotron radiation. [Boe12]

  Photons from the radio waveband up to the X-ray waveband are produced in this process [Wee03].

- **(Inverse) Compton scattering:**
  Compton scattering is known as the scattering of a photon on an unbound electron, whereby energy is transferred from the photon to the electron. In the case of a high energy electron scattering on a photon and transferring its energy to the photon, the process is called inverse Compton (IC) scattering. It is differentiated between two regimes dependent on the product of electron and photon energy. The electron energy E_e and the photon energy E_γ are given in units of $m_e c^2$. In the non-relativistic Thomson regime the following is valid: $E_e E_\gamma \ll 1$. The cross-section approaches the Thomson cross-section σ_T[1]. However, the transferred energy from the electron to the photon makes up only a small fraction of the electron energy. When $E_e E_\gamma \gg 1$ the cross-section is calculated in the relativistic Klein-Nishina regime. The cross-section decreases with increasing $E_e E_\gamma$, but the energy transfer from the electron to the photon becomes more efficient. A substantial fraction of the electron energy is transferred. The photons are boosted to very high energies during this process. [Aha04]

- **Bremsstrahlung:**
  The deflection of a charged particle as e.g. an electron in the field of an ion or an

[1] $\sigma_T = \frac{8}{3}\pi r_e^2$ [Beh12]

atomic nucleus is an acceleration for the electron. This causes the emission of a bremsstrahlung photon. [Wee03]

However, energy losses of the electrons are dominated by the IC and synchrotron losses for high energies. [Aha04]

- π^0 **decay:**
  As shown in Equation 2.3 two photons result as the decay products of a neutral pion π^0 with a probability of 99% [Fal12]. Pions are produced in interactions of protons or heavier nuclei with other protons or nuclei or with photons. This was already described in subsection 2.1.2.

Absorption of γ-rays
For optically thick sources the produced synchrotron radiation mentioned above can be reabsorbed by their former emitter particles. Therefore, low energetic photons might be unable to leave the source region. This process is known as synchrotron self-absorption. [Boe12]
After photons have left the emission region they can be absorbed in regions of gas or dust as is shown in Figure 2.1. Additionally, the high energetic photons can interact with other photons and produce electron-positron pairs. The second photon can either be a high energetic photon like the first one, or it is a lower energetic photon e.g. from a surrounding photon field near the emission region. For AGNs these could be e.g. photons from the accretion disk. Photons travelling cosmological distances until they reach Earth are affected by the extragalactic background light (EBL). These mainly infrared and optical photons stem from dust, galaxies and stars and can be found everywhere in the Universe. The higher the energy of a photon and the longer the path it travels, the larger the probability becomes for it to interact with an EBL photon. Models as given in [Fra08] can be used to reconstruct the original photon spectrum. [Boe12]

2.2 Sources of radiation

Sources of high energy radiation or particles can be found inside as well as outside our own galaxy. Inside our galaxy, shock waves produced in **supernovae** are possible sources for high energetic radiation to energies up to at least 10^{15} eV. During this explosion of a star, the star is destroyed. Its core collapses and forms a neutron star (NS) or a black hole (BH), while the outer shell expands into the interstellar medium. The SN itself is only visible for a short duration, but its remains, the **supernova remnant**, can be observed for thousands of years after the explosion. Shock fronts caused by the expanding shell are capable of accelerating particles to high energies. When a pulsar, a rotating neutron star, remains after the star's collapse, the SNR is called pulsar wind nebula. The Crab Nebula is an example of such a source. It is the remnant of a supernova that occurred in the year 1054. [Fal12, Wee03]
Binary systems of a star and either a neutron star or a black hole can be sources of high energetic radiation as well. The NS or BH accretes matter from the accompanying star, which can result in the formation of a jet with relativistic particle outflow. These systems are called **micro-quasars** and energies up to TeV have been observed from them. Another possible source of γ-rays might be regions hosting dark matter (DM). γ-rays might

be produced in DM decay or annihilation processes. A region with a possibly high density of DM is e.g. the centre of our own galaxy, the **Galactic Centre**. [Fal12]
Gamma-ray bursts are very short and very bright explosions. Although they are sources of high energetic radiation, it is not possible to do long-term studies in γ-rays with these sources because they are one-time events and their duration is very short. While there is a longer afterglow in X-ray and optical wavelengths, the outburst in γ-rays only lasts from below a second to a few minutes [Boe12]. Additionally, their position and time of occurrence are unknown. GRBs are believed to develop when two neutron stars merge and form a black hole, when a hypernova takes place - which is a collapse of a star with a mass of more than $10 M_\odot$[2] - or when a NS collapses into a BH, which was formerly developed in a SN. The emission of up to TeV energies is explained by relativistic shocks in these environments. Due to their isotropic distribution, GRBs are of extragalactic origin. [Fal12, Wee03]
Other extragalactic objects, which emit radiation, are galaxies. Normal galaxies without an active centre are generally not relevant for observations in γ-rays. However, **starburst galaxies** have been shown to emit γ-rays up to TeV energies. This is caused due to the high rate of star formations and SNs as well as the resulting stellar winds, which are a good candidate for particle acceleration. Another extragalactic source class is the class of **Active Galactic Nuclei**. In their centre a supermassive black hole (SMBH) is located, which accretes matter from the surrounding disk. It is the originating region for the relativistic ejection of plasma along its jets. With the acceleration of particles to the highest energies and resulting photons of up to TeV energies, they are interesting sources to be studied in all wavebands. [Fal12].
The class of AGNs will be discussed in more detail in the following section 2.3.

2.3 Active Galactic Nuclei

A galaxy with an active nucleus produces high luminosities in non-thermal processes. An AGN consists of a rotating SMBH with a mass between $10^6 - 10^9 M_\odot$ [Boe12] in the centre, which is surrounded by an accretion disk and a torus of dust. There are gas clouds rapidly moving in the potential of the SMBH, so that broad line radiation in the optical and UV wavebands is emitted. Clouds farther away from the SMBH emit further narrow emission lines. The SMBH pulls in matter of the accretion disk and makes it an active nucleus. It is possible that plasma is moving outwards at relativistic velocities in two jets, which are aligned with the rotational axis of the SMBH. The formation of these jets is not exactly known so far. Inside the jets, individual emission regions, which are called knots, are given [Boe12]. The jets can end in giant radio lobes. These AGNs are called radio-loud, while AGNs without these jets are called radio-quiet. [Urr95]
The jet itself is highly collimated due to strong magnetic fields. These follow helical paths around the jet possibly because of the rotation of the accreting and rotating central system. [Pud12]

[2] mass of the Sun $M_\odot = 1.99 \cdot 10^{30}$ kg [Beh12]

The expansion of the jets into the intergalactic medium can be up to the order of Mpc[3], which is by many orders of magnitude larger than the comparably small size of the BH of less than a parsec [Boe12]. Depending on the viewing angle of the observer onto the source, the AGN appears differently. Formerly, the different sources like radio galaxies, quasars, QSOs (quasi-stellar object), and blazars were believed to be different sources. Because the appearance depends on the viewing angle and not on different physical processes, all sources can be unified as one source type, the Active Galactic Nuclei. [Urr95]
A schematic view of an AGN as described by [Urr95] is shown in Figure 2.3.

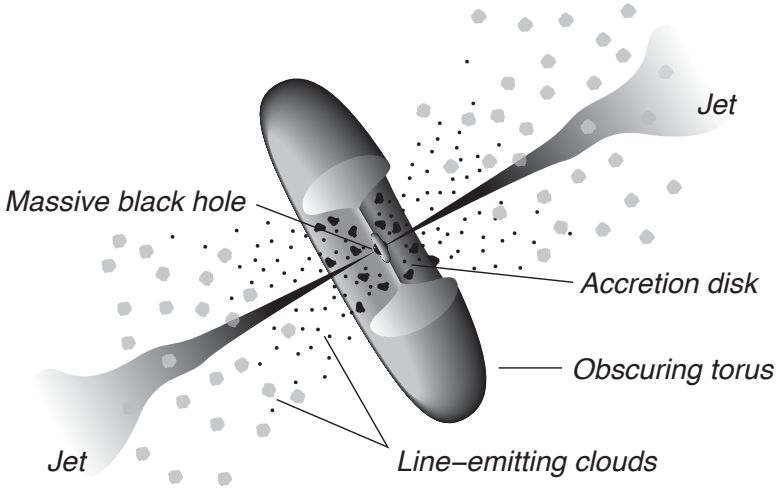

Figure 2.3: Schematic view of an AGN with its components. The dimensions are not to scale. The image is taken from [Tes10], after [Urr95].

When the orientation of the jets of the AGN is perpendicular to our line-of-sight the dust torus covers the emission of the core. The radio emission in the jets and the lobes dominate the appearance. If the viewing angle is reduced, the emission of the core in the radio and optical wavelengths becomes visible as well as the broad emission lines of the gas clouds close to the SMBH. The synchrotron emission in radio and X-ray wavelengths of the jet is then the dominant emission. If the observer's line-of-sight is aligned with the jet axis and the observer looks directly into the jet, the source is called blazar. [Wee03]

As this thesis focusses on the data of the blazar Mrk 421, this type of AGN will be explained in more detail in section 2.4.

2.4 Blazars - a special insight into AGNs

As mentioned above, blazars are AGNs with one of their jets pointing into our direction. They emit continuous radiation from radio to γ-ray wavelengths and feature fast variability in all wavebands. They are subdivided into two groups, namely the Flat Spectrum

[3] $1\,\mathrm{pc} = 3.09 \cdot 10^{16}\,\mathrm{m} = 3.26\,\mathrm{ly}$ [Beh12]

Radio Quasars (FSRQ), which feature optical emission lines, and BL Lacs, which lack these. BL Lacs are named after the first known source of this type, BL Lacertae [Oke74]. Additionally, they are classified by a characteristic in their spectral energy distribution (SED). An exemplary SED of Mrk 421 is shown in Figure 2.5. It shows the source's flux in dependence of the frequency and is usually given as νF_ν vs. ν, whereas F_ν is the flux for a given frequency interval. The typical two bump structure of blazars is recognisable. The low energy peak usually covers the radio to X-ray energies, whereas the high energy peak extends from X-rays to γ-rays. Depending on the position of the two peaks in the SED it is distinguished between FSRQ, low-frequency peaked BL Lac (LBL) and high-frequency peaked BL Lac (HBL), whereas $\nu_{peak,\mathrm{FSRQ}} \leq \nu_{peak,\mathrm{LBL}} \leq \nu_{peak,\mathrm{HBL}}$. [Boe12]
The shape of the SED can possibly be altered when other thermal components of the host galaxy are added. In order to explain and study the physical processes in AGN emission models, the shape of the SED is essential. [Wee03]
Different models based on leptonic or hadronic interactions will be explained after some more basic information on jet physics.

The plasma in the jet moves with relativistic velocities close to c, so that the emitted radiation in the jet is boosted. This can be explained by the Doppler factor δ, which is given by

$$\delta = \frac{1}{\Gamma(1 - \beta \cos\theta)} \,. \tag{2.6}$$

Here, Γ is the bulk Lorentz factor $\Gamma = \left(1 - \beta^2\right)^{-1/2}$ of the emission region and $\beta = v/c$ is the ratio of the region's velocity v compared to the speed of light c. The angle between the jet's direction of propagation and the line-of-sight of the observer is given by θ, which approaches zero for blazars. Due to the relativistic amplification of the flux emission by a factor of δ^3, the source appears so bright. In addition, the frequency ν is shifted towards higher energies by a factor of δ and time scales are shortened by δ^{-1}. [Boe12]
The relativistic beaming of photons is necessary for us to be able to see them. Otherwise the photons would interact with other photons and produce electron-positron pairs or be reabsorbed by synchrotron self-absorption. [Wee03]
The size of an emission region can be deduced from the minimum variability time scale t_{var} because these two values are connected via the speed of light. The characteristic size R of a source can be approximated by $R = c \cdot t_{\mathrm{var}}$. When the Doppler boosting and the redshift z are taken into account, the constraint on the emission region is modified as follows [Boe12, Gai96]:

$$R \leq \frac{c t_{\mathrm{var}} \delta}{1 + z} \,. \tag{2.7}$$

2.4.1 Blazar emission models

Emission models try to explain the two bump structure of the SEDs. Up to now it is believed that the low energy peak is caused by synchrotron emission of highly relativistic electrons [Boe12]. The high energy peak is explained by two fundamentally different models, namely the leptonic and hadronic model. These will be briefly introduced in the

following.

Leptonic models
In leptonic models the high energy peak is believed to be caused by the same electron population which causes the synchrotron radiation of the low energy peak. In this scenario photons gain energy when they interact with the electrons via inverse Compton scattering. In this Synchrotron Self-Compton (SSC) model the photons are the formerly produced synchrotron photons. Since both peaks are explained by the same population of electrons, simultaneous behaviour of both peaks is expected. In the External Compton (EC) model the photons are external photons. These can be e.g. optical, UV or X-ray photons from the accretion disk, from the emitting gas clouds or photons of the CMB. [Boe12]

Hadronic models
In hadronic models relativistic hadrons like protons or ions exist next to the electrons in the jet. These models explain the high energy bump either by synchrotron radiation of protons, by the interactions of protons with photons or protons, which would produce neutral pions that decay, or charged pions that emit synchrotron radiation themselves before they decay. Since the hadronic processes are not connected to the electron population, it is possible that the two peaks of the SED show different behaviour. Therefore, a hadronic based model could explain so-called orphan flares, which show outbursts only in the high energy peak, but not in the low energy one [Bla05]. Additionally, neutrinos are generated in hadronic models. A detection of neutrinos from AGNs would prove the existence of a hadronic component and would move the understanding of emission models forward. [Boe12, Wee03]

2.5 The blazar Markarian 421

The HBL Markarian 421 (Mrk 421) was detected as a γ-ray source in 1992 by the γ-ray telescope of the Whipple observatory. It is the first extragalactic object detected in TeV γ-rays. Only one source was detected in TeV energies before Mrk 421, namely the Crab Nebula. [Pun92]
Mrk 421 is located at RA $= 11^{\mathrm{h}}\,4^{\mathrm{m}}\,27.31^{\mathrm{s}}$, Dec $= 38^{\circ}\,12'\,31.8''$ [Abd11]. With a redshift of $z = 0.030$ ($\approx 136\,\mathrm{Mpc}$) [Pin99] it is the closest blazar [Sch08].

The source is named after Beniamin Markarian, who did a survey of galaxies which appear brighter in UV than regular galaxies. This survey started in 1965. [Mar72]
The optical observations of Mrk 421 date back to about 1900. In panel (a) of Figure 2.4 the optical image of Mrk 421 by the Nordic Optical Telescope (NOT) is shown. The elliptical shape of the host galaxy can be seen as well as an accompanying galaxy. [Nil99]
The BH mass is estimated at about $10^{8.23} M\odot$ [Wu 09].
In panel (b) of Figure 2.4 the image of Mrk 421 is shown as it is seen by MAGIC-I. It shows the relative flux of excess to background events as well as regions of different significances. In section 4.6 it is explained how such a so-called sky map is produced. The PSF (see section 5.1) in the bottom left corner in comparison to the relative flux map around the

source position of Mrk 421 shows that it appears as a point source in very high energy (VHE) γ-rays.

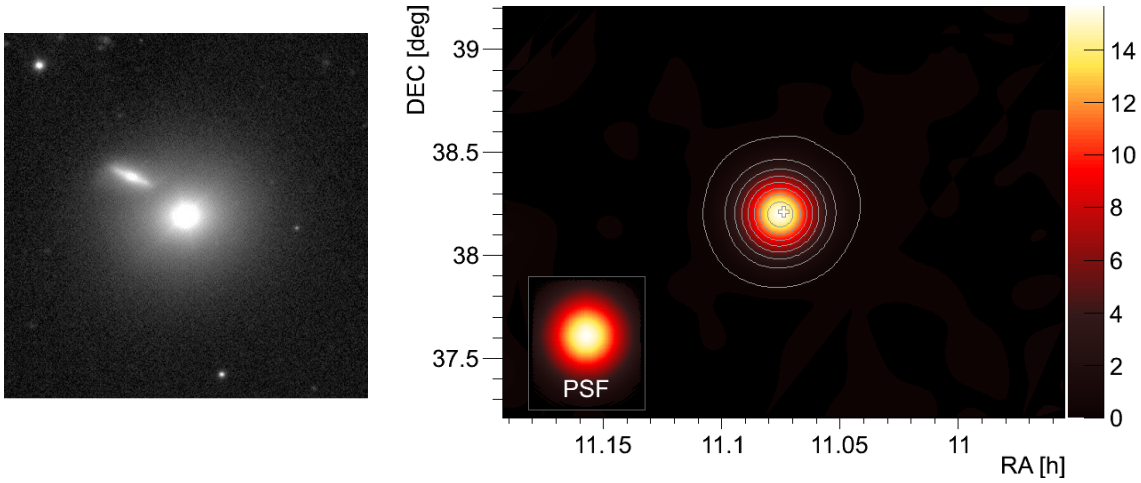

(a) Optical image of Mrk 421 by the NOT. On the top left of the elliptical host galaxy of Mrk 421 a companion galaxy is visible. The size of the image is 78" × 78". The image is taken from [Nil99].

(b) Sky map around the source position of Mrk 421, marked with a hollow cross, with MAGIC-I data from April 2007 until February 2009 for zenith angles below 30°. The relative flux of excess to background events is shown with the colour code indicated on the right. The white lines around the source position represent regions of different levels of significance.

Figure 2.4: Optical and γ-ray images of Mrk 421.

Mrk 421 has been regularly observed in VHE γ-rays by many Cherenkov telescopes. In [Tlu10] all observations from 1992 to 2008 are summarised. The data from this light curve are included in Figure 6.4. In section 6.3 the behaviour of Mrk 421 will be explained in more detail. So far it can be said that Mrk 421 exhibits different states of emission in γ-rays. The baseline of the Mrk 421 flux is overlaid by several time periods of higher activity, whereas these time periods can last up to several months. A correlation is found between the γ-ray data of this light curve to X-ray data. [Tlu10]
But variability is not only seen for long time scales. In e.g. [Gai96] and [Sch08] flux doubling times between 10 and 15 minutes are reported.

A SED of Mrk 421 is shown in Figure 2.5. It includes the averaged results from radio to TeV energies observed by many telescopes (each participating telescope's name can be found in the image) in the time range from 19th January to 1st June 2009, when a multi-wavelength (MWL) campaign was organised. The leptonic SSC model as well a hadronic model are both able to describe the shown SED well. [Abd11]
Between the end of 2000 and spring 2001 Mrk 421 was observed by Whipple. During that time period Mrk 421 was in a very active state. The light curve shows high fluxes and a high variability. It could be illustrated that the spectral shape of the TeV spectrum changes with the overall flux. This means that the spectrum is hardening with increasing flux. Additionally mentioned results in the X-ray range imply that the synchrotron peak moves to higher energies with increasing flux. [Kre02]

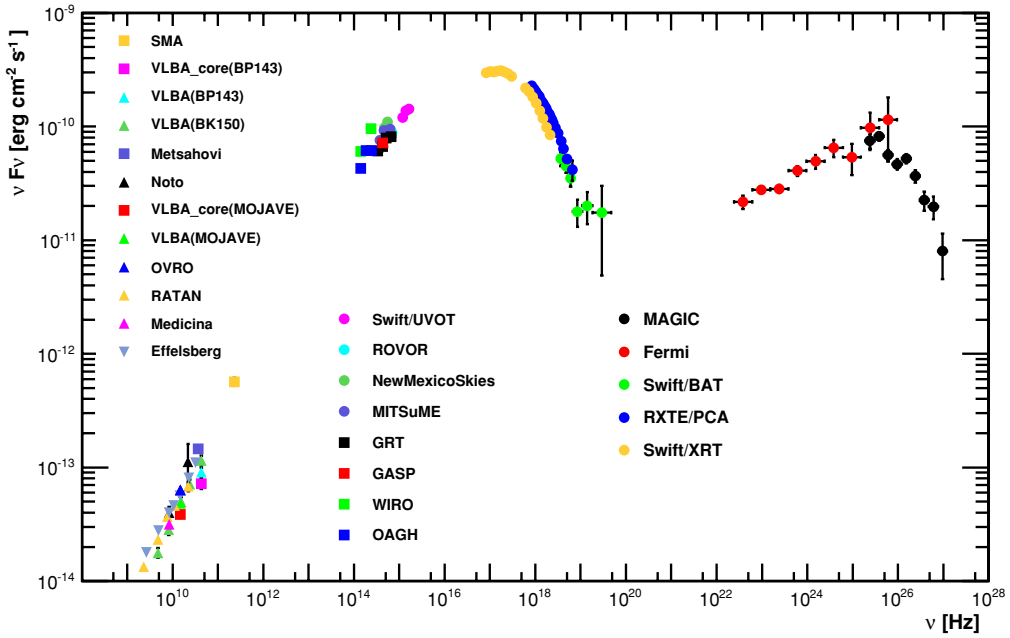

Figure 2.5: Average SED of Mrk 421 between 01/2009 and 06/2009 during a MWL campaign. The image is taken from [Abd11].

This dependence of the SED on the overall flux intensity makes it necessary to study the SED for different flux states. In this case the coverage of the whole SED by the different telescopes needs to be organised in MWL campaigns.

A large data set of Mrk 421 by MAGIC-I covering the time range from February 2007 to June 2009 is analysed in this thesis. In chapter 5 the analysis of the γ-ray data is explained and results of the long-term and short-term variability in the light curve will be discussed as well as the dependence of the spectral shape on the overall flux. In chapter 6 the Mrk 421 light curve will be examined for possible periodicities. A study of correlations of the MAGIC light curve to light curves of other wavebands will be illustrated in chapter 7, which might give hints towards a possible emission scenario.

Chapter 3
Ground-based detection of very high energy γ-rays

The electromagnetic radiation of two energy ranges is not absorbed in the atmosphere: namely radio and optical wavelengths. Photons from these wavebands reach the Earth's ground. In general, photons of other wavelengths are not able to reach the ground. Photons at the high energy end of the spectrum are called γ-rays. These interact with the Earth's atmosphere and consequently they cannot be detected directly by ground-based telescopes. For the direct detection of γ-rays, the detector needs to be placed above the atmosphere. This can either be realised with detectors on balloons, rockets or satellites. However, all of these experiments are limited in size and thus their detection area. Additionally, balloons and especially rockets are restricted in observation length. Therefore, these detectors are not suitable for the detection of VHE γ-rays. This is due to the fact that the photon flux decreases rapidly with increasing energy. For the detection of VHE γ-rays there is another possibility, namely the indirect detection of the sought-after γ-rays with ground-based telescopes. When γ-rays interact with molecules or atoms in the Earth's atmosphere, they induce an electromagnetic cascade of secondary particles. These secondary particles move with velocities faster than light in the atmosphere and hence produce Cherenkov radiation, which is subsequently detected by the ground-based Cherenkov telescopes. One challenge in the detection of γ-rays in the analysis is the suppression of the much more numerous background particles, mainly the charged component of cosmic radiation. [Wee03]
In the following, the cascades of secondary particles induced by γ-rays and hadrons will be introduced and their properties and differences will be referred to. Afterwards, the emission of Cherenkov radiation from these so-called Extensive Air Showers (EAS) will be briefly discussed. Then the principle of Imaging Atmospheric Cherenkov Telescopes (IACT) will be explained and the present telescopes will be introduced. As the Mrk 421 data analysed in this thesis was taken with MAGIC, subsection 3.3.1 is dedicated to this IACT. Then FACT is also mentioned as it is a new IACT which is monitoring Mrk 421.

3.1 Extensive Air Showers

The term "cosmic radiation" describes all incoming particles that hit the Earth's atmosphere permanently. This includes mainly a charged component consisting of protons, which make up the largest percentage with 85%, other atomic nuclei and electrons [Gru05]. The proton is taken as the representative for the charged, hadronic component of the cos-

mic radiation from here on. The electrically neutral component consists of γ-rays and neutrinos. As the latter have very low interaction cross sections in general [Kat12], they produce a negligible background compared with the other produced air showers and hence will not be discussed here.
At a height between 15 to 20 km [Gru05] the first interaction of a particle with a nucleus of the atmosphere takes place so that an EAS is initiated and develops in the atmosphere. When the primary particle is a γ-ray an electromagnetic cascade is induced, in the case of a proton it is a hadronic cascade with additional electromagnetic and muonic subcascades.

Electromagnetic showers
When very highly energetic γ-rays as well as electrons enter the atmosphere, they induce an electromagnetic shower. γ-rays can produce an electron-positron pair in the field of a nucleus. The generated electrons and positrons are emitted in a forward direction. When they are deflected in the electric field of further nuclei, they produce photons via Bremsstrahlung, which can again produce electron-positron pairs. The shower develops with a small lateral width along the trajectory of the primary particle. [Wee03]
These alternating processes continue until ionisation becomes the dominant interaction for electrons and positrons, and photons start to undergo Compton scattering or the photoelectric effect. At this point the shower maximum with the maximum number of particles is reached. This number is proportional to the energy of the primary photon and the position of the shower maximum is typically around a height of 10 km [Wee03]. From this point on the particle number decreases until the shower vanishes. [Gru05]

Hadronic showers
It is necessary to discuss the development of hadron-induced showers at this point because these particles occur about 1000 times more numerously for strong γ-ray sources and up to 10000 times more numerously in general [Wee03] as γ-rays. The shower properties need to be studied and known as well as the properties of electromagnetic showers in order to be able to separate the γ-rays from the hadronic background.
The hadrons, which enter the atmosphere, are mainly protons. They collide with atmospheric nuclei whereupon mostly charged and neutral pions are produced next to charged and neutral kaons as well as other nuclei in strong interactions. The hadrons and charged mesons further feed the hadronic part of the cascade. Additionally, neutral pions decay into two photons and thus initiate electromagnetic subcascades as described above. Besides strong interactions, the charged pions also decay into muons and neutrinos so that a muonic component of the shower exists. Muons can furthermore decay into electrons and neutrinos, but mostly they survive until they reach the ground. The pions and kaons in the centre of the shower are emitted at greater angles from the main trajectory because they undergo strong interactions. Therefore, the overall shape of the shower is more widely spread than an electromagnetic shower. [Gru05]

Cherenkov radiation
Instead of the direct detection of the secondary particles of an EAS, the produced Cherenkov radiation of these particles is detected. Every charged particle that travels through a dielectric medium, like air in our case, polarises the molecules along its path. When the charged particle has passed by, these molecules relax back to their normal state and elec-

tromagnetic radiation is emitted spherically along the particle's path. When the particle has a velocity lower than the speed of light in air, this light interferes destructively. In the case that the charged particle has a velocity greater than light in air, the emitted radiation interferes constructively in a forward direction. The emission angle of this Cherenkov radiation in the atmosphere is of the order of 1° and it increases with increasing refractive index n while the shower particles move deeper into the atmosphere. [Jel58], [Wee03]
This emission angle of 1° at the height of 10 km at the shower maximum leads to an illumination of an area with a radius of 120 m at an observation level of 2 km. This given fact needs to be regarded for stereoscopic observations of one shower. At detection level the spectrum of the Cherenkov light peaks at 300-350 nm, which is why it appears blueish. [Aha04]
Electromagnetic showers appear to have an elliptical shape in the camera [Aha04], whereas the Cherenkov light of hadronic showers is more scattered. This difference in their appearance can be seen exemplarily in real recorded camera images of MAGIC-I in Figure 3.1. Additionally, the spread of the arrival times of the Cherenkov photons is higher for hadronic showers in comparison to γ-ray induced showers. Parameters derived from these properties are used to distinguish between the two particle types in the analysis.

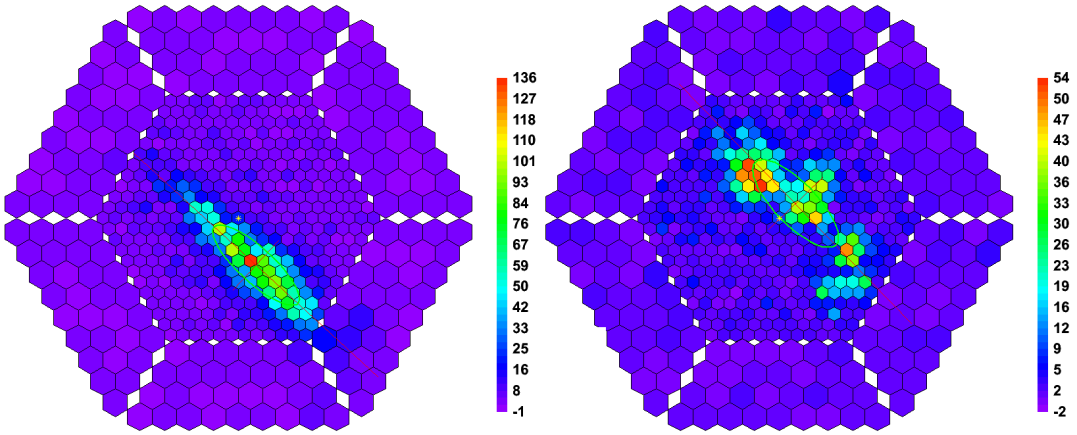

Figure 3.1: Real recorded MAGIC-I camera images of different events. The colour scale is related to the signal amplitude in each pixel. On the left the recorded image of a γ-ray candidate is shown. An elliptical shape is recognisable. The recorded camera image on the right shows a hadron induced air shower, which has a scattered light distribution where even subshower structures are visible.

3.2 Detection technique

For the detection of the Cherenkov light of EAS Imaging Atmospheric Cherenkov Telescopes are used. In Figure 3.2 the detection principle is illustrated schematically. A γ-ray induced air shower and its emitted Cherenkov light are shown. IACTs feature large mirror areas, consisting of many smaller single mirrors, to reflect the Cherenkov light onto a camera with a large number of photo sensors in the focal plane. An image of the Cherenkov light of the air shower is thus mapped in the focal plane. If a set trigger criterion is met,

all photo sensors are read out. For MAGIC this means e.g. that the amount of light in at least four neighbouring pixels has to be greater than the discriminator threshold (see subsection 3.3.1) in less than 4 ns [Pao07]. It is necessary that the photo sensors are suitable to detect UV to blue light. Additionally, fast readout electronics are required for the short duration of several ns of the air showers and to be able to capture its even faster temporal evolution. [Wee03], [Aha04]

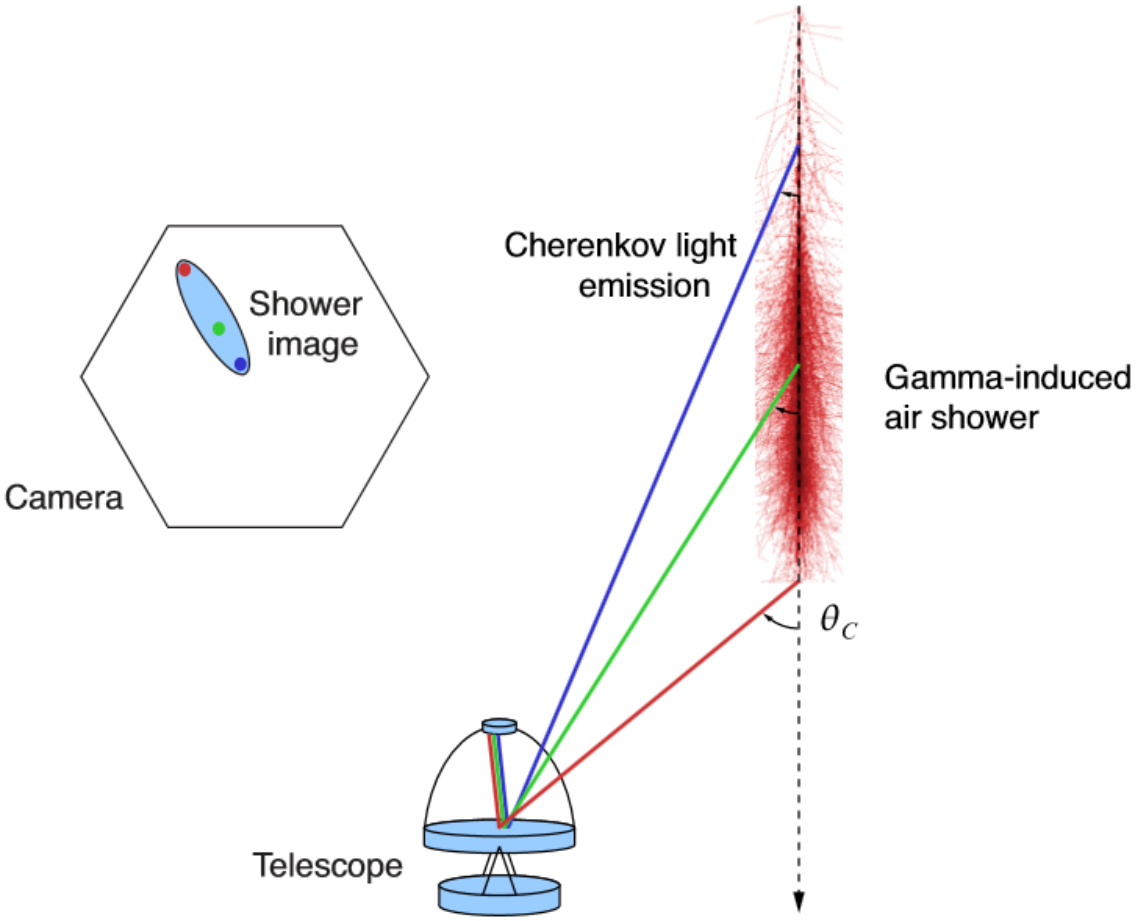

Figure 3.2: Illustration of the principle of the IACT technique. It is shown how the Cherenkov light is emitted from an EAS, in this case induced by a γ-ray. The Cherenkov light, which is emitted under the angle θ_C, is reflected on the mirrors onto the camera located in the focal plane. On the top left the recorded image of the shower in the camera can be seen. The image is taken from [Ste12].

The IACT technique was introduced to solve several tasks. Firstly, the particle type of the primary particle, which induced the EAS, shall be identified. Secondly, the position of its origin in the sky shall be reconstructed and thirdly, its energy shall be determined. After recording EAS, their images are analysed to solve these challenges. As was discussed in section 3.1 the shower development is different for primary γ-rays and protons. Hence, also the recorded image appears different and the image's characteristic and its temporal

evolution can be used to separate γ-rays from hadrons. To determine the source position in the camera the trajectory of the EAS is reconstructed. To obtain the primary particle's energy the amount of recorded Cherenkov light can be used. This is based on the correlation of the primary particle's energy and the number of secondary particles at the shower maximum and hence also the amount of produced Cherenkov photons. [Wee03]
When changing from single telescope operation to stereoscopic observations with two ore more telescopes, several advantages can be mentioned. If a shower is recorded from two or more sides the reconstruction of the shower's trajectory is improved and therefore also the angular resolution in the determination of the source position. It additionally improves the separation of γ-rays from hadrons. Furthermore, a coincidence trigger can be enabled to lower the overall energy threshold in comparison to a single telescope. It suppresses the muon background and a large amount of accidentally triggered background events like photons of the night sky background (NSB). [Wee03]

3.3 Cherenkov telescopes at the present day

Today three arrays of Cherenkov telescopes are operating with cameras made of Photomultiplier Tubes (PMT), namely MAGIC, H.E.S.S. [Gie13] and VERITAS [Raj14]. The first Cherenkov telescope with a new camera made of more robust Silicon Photomultipliers (SiPM), namely FACT [And13], started operations in 2011.
The Major Atmospheric Gamma-ray Imaging Cherenkov (MAGIC) telescopes are located on the Canary Island of La Palma at a height of 2.2 km above sea level. Observations were started in 2004 with one telescope with a reflector diameter of 17 m making it the biggest Cherenkov telescope for many years. A second telescope of the same size was added in 2009. [Ale14a]
MAGIC will be introduced in more detail in subsection 3.3.1.
The High Energy Stereoscopic System (H.E.S.S.) is in operation in Namibia at a height of 1.8 km. The array of four 13 m telescopes has been taking data since 2003. In 2012 a telescope, H.E.S.S. II, with a reflector of 28 m in diameter was added in the centre of the four other telescopes and is now the biggest Cherenkov telescope. [Gie13]
The third Cherenkov telescope observatory is the Very Energetic Radiation Imaging Telescope Array System (VERITAS), which has been operative with four 12 m telescopes since 2007. It was built in Arizona, USA, at a height of 1.3 km. [Raj14]
Since October 2011 a Cherenkov telescope with a new camera technique in Cherenkov astronomy has been actively monitoring γ-ray sources. It is named First G-APD Cherenkov Telescope (FACT) and was built to show the feasibility of these Geiger-mode Avalanche Photodiodes as photo sensors in Cherenkov astronomy and for long-term monitoring of bright TeV blazars. It has a diameter of about 3.5 m and is located at the MAGIC site on La Palma. [And13]
More details on FACT will be given in subsection 3.3.2.
All telescope sites were chosen to ensure the best observation conditions available. It is desirable to have mostly stable and good weather conditions and to have as little disturbances, either natural or man-made, for the observations as possible.

To extend the observable energy range of the present telescopes, the Cherenkov Telescope Array (CTA) is planned for the near future. To achieve this goal an array of tens of telescopes of three different sizes is planned and prototypes are already developed. [Act11]

3.3.1 The MAGIC telescopes

The MAGIC site is located at the Roque de los Muchachos Observatory (ORM) at 28.45° N, 17.54° W at an altitude of 2200 m above sea level [Alb08b] on the Canary Island of La Palma. In 2004 operations of MAGIC were started with a single telescope, namely MAGIC-I (M-I). A second telescope, MAGIC-II (M-II), was added just 85 m away from the first telescope, which started operations in 2009 [Ale12b]. Since then the two telescopes are usually operated in stereoscopic mode. The telescopes and their major hardware changes will be shortly introduced. A few words about the operations will be given as well.

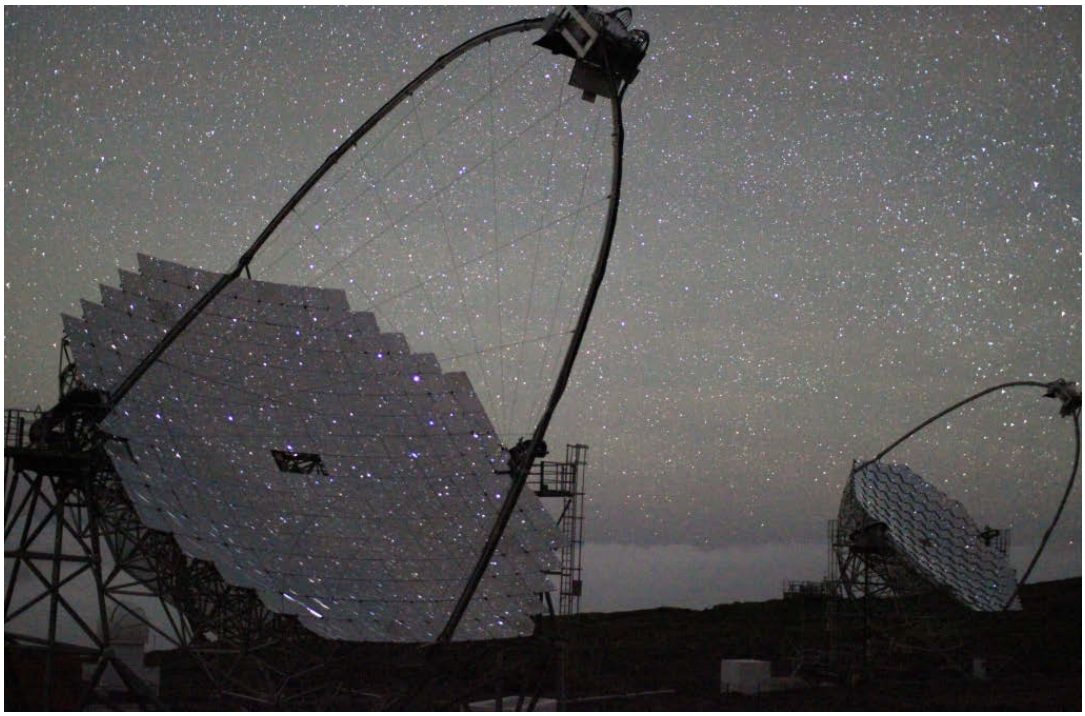

Figure 3.3: Photograph of the MAGIC telescopes at night during observations. In the foreground MAGIC-II can be seen, MAGIC-I is in the background.

The MAGIC telescopes (see Figure 3.3) are dedicated to the detection and observation of very high energy γ-rays of galactic and extragalactic sources in the energy range from as low as 50 GeV to about 50 TeV. These are namely SNRs, pulsars and the Galactic Centre as galactic sources and AGNs and GRBs as extragalactic sources. The light-weight carbon fibre structure of the telescopes makes it possible to move to any position in the sky within less than 25 s. This offers the possibility of the observation of short-lasting GRBs after receiving an alert from a satellite. [Ale14a]

Mirrors
The reflecting surfaces of the telescopes each have a diameter of 17 m and consist of hundreds of smaller mirrors. MAGIC-I has 964 square aluminium mirrors, each with a side length of 0.5 m. Four of these are each mounted on one panel. This number is reduced to three for some of the panels in the outermost ring. The overall reflective area sums up to 236 m^2. MAGIC-II has a total of 247 square mirrors with an area of 1 m^2, 143 being a large version of the aluminium mirrors of MAGIC-I and 104 glass mirrors, which are placed in the outer part of the reflective area. All mirror panels of M-I and the mirrors of M-II are equipped with an Active Mirror Control (AMC) to correct for the bending of the telescope structure at different zenith angles during the observations. [Dor08]

Cameras
The M-I camera was made of PMTs arranged in hexagonal shape from the beginning until an update in 2012. Its field of view (FOV) covered 3.5° of the sky. The camera consisted of hexagonal pixels of two different sizes, as can be seen in Figure 3.1. Each pixel was made of a hollow light concentrator, which reflected the incoming light onto a PMT. A plexiglass entrance window protected the sensitive area. In the inner area were 397 pixels with a size corresponding to 0.1°, the outer rings consisted of 180 larger pixels with a size of 0.2°. In contrary to this camera, the M-II camera is a homogeneous camera made of 1039 pixels of 0.1° in diameter, arranged in round shape. The FOV is also 3.5° for M-II. [Ale12b]
During the upgrade in 2012 the old M-I camera was replaced by a round and homogeneous camera with 1039 pixels following the design of the M-II camera. The new camera was one step towards a more homogeneous system. With the same camera design it was also possible to equalise the trigger areas. [Ale14a]

Readout and trigger system
The PMT signals are converted from electrical to optical and then transmitted to the readout electronics in the MAGIC counting house only a few meters away from the telescopes. The readout of M-I was based on Flash Analog to Digital Converters (FADC). In the first years the sampling rate was 300 MHz. After an upgrade in February 2007 the sampling rate was increased to 2 GHz. The M-II readout was based on the Domino Ring Sampler 2 (DRS2) chip and had the same sampling rate of 2 GHz. [Alb08b, Ale12b]
In 2012 both telescope readouts were upgraded to a DRS4 chip based readout, which was another step towards a more homogeneous telescope system. [Ale14a]
For an event to be recorded several levels in the standard trigger system have to be passed. The first level requires having a signal in a pixel that is greater than a certain threshold, the discriminator threshold (DT), which is adapted to the light conditions (see section 5.1). This threshold is set individually for each pixel according to its rate. This helps to discriminate accidental triggers due to moon light or from e.g. a bright star in the FOV. The next trigger level is a digital level. It requires that n next neighbours (NN) cross the threshold in a time window of about 4 ns, so that already accidental triggers due to the NSB are suppressed. In case of MAGIC-I mono observations the trigger configuration is set to 4NN which results in a rate between 200 and 250 Hz for galactic and extragalactic sources. [Pao07]

After the commissioning of MAGIC-II an additional trigger, the stereo trigger, was added. With this trigger more accidental triggers are rejected because only events hitting both telescopes in a certain time interval are recorded.
In addition to the standard digital trigger, an analogue trigger, called the Sum-Trigger is running in parallel in MAGIC-I [Ali08]. For the MAGIC telescopes a Sum-Trigger is also developed, implemented and already running in parallel to the standard trigger system. Its purpose is to further lower the energy threshold. [Gar13]

Telescope operation
Next to a technical team working at the telescope site mainly during daytime, a team of night shifters is responsible for the data-taking during the night. The shifters operate the telescopes, perform technical tests and observe scheduled sources. The taken data are directly analysed by an online analysis [Tes13] which provides preliminary analysis results. In case a source's flux is at a flaring level, other telescopes including H.E.S.S., VERITAS and FACT are informed to be able to observe the source in this interesting high state as well. The telescope operations are influenced by the strength of the moon light and weather conditions like clouds, rain and humidity.

Observation mode
Sources can either be observed in ON mode, where the telescopes directly point at the source, or in the so-called Wobble mode [Fom94], where the telescopes track a false source 0.4° away from the real source position. For the ON mode analysis it is required to additionally record OFF data for the estimation of the background rates. An OFF region is defined as a position in the sky without a known γ-ray source. As these OFF observations use up a lot of valuable observation time of real sources, the Wobble mode is a time saving alternative. In this case the source is not in the centre of the camera's FOV, but slightly shifted away from it. For MAGIC this distance is 0.4° for standard Wobble observations. The advantage of this observation mode is that the OFF observations are directly recorded along with the data. The position at the same distance to the centre of the camera opposite to the source position can be used as OFF region in the analysis. This number of OFF regions can also be increased in the analysis. Then these regions are evenly distributed over the camera, each with the same distance to its centre.

3.3.2 FACT

FACT (see Figure 3.4), the First G-APD Cherenkov Telescope, is the first IACT using Silicon Photomultipliers (SiPM), made of G-APDs, instead of PMTs as photo sensors. It is situated on the MAGIC site at the ORM. In October 2011 it started operations and was able to detect air showers already in the first night [CER11]. The usability of G-APDs in Cherenkov astronomy has already been shown in the past three years of operation. FACT mainly observes several γ-ray sources on a regular basis, called monitoring. Its camera could serve as a prototype camera for the planned CTA. [And13]
The advantages of G-APDs compared to PMTs is that they can be operated under brighter light conditions, are more robust and are operated at lower voltages in comparison to PMTs ($<$100 V instead of 1000 V). As they are more robust against damage through light during twilight and moon observations, the observation times can be enlarged. [And13]

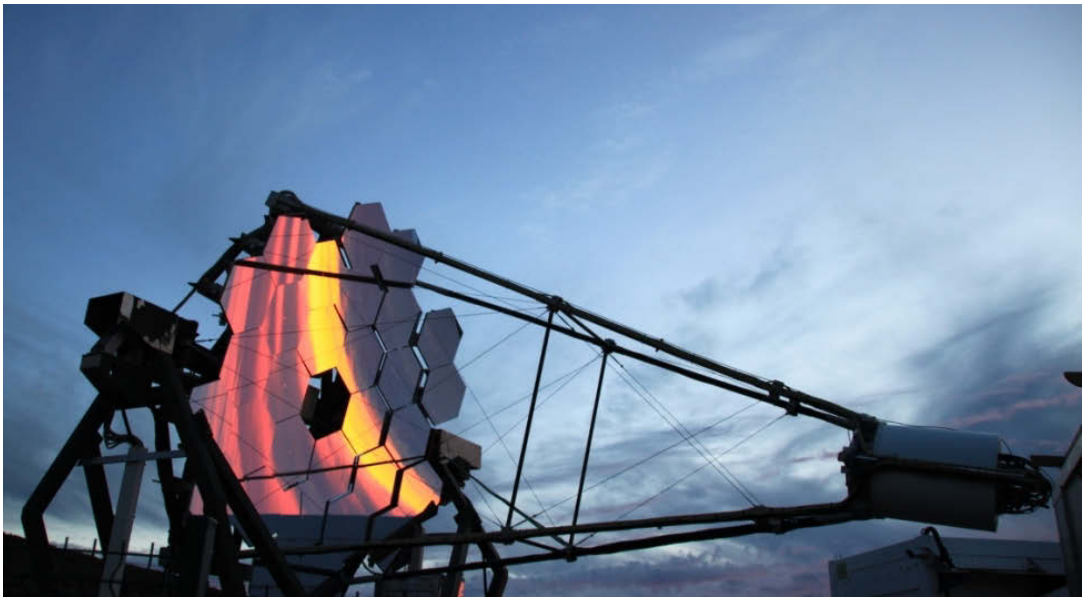

Figure 3.4: Photograph of the FACT telescope at sunset.

FACT's camera is a new technology in Cherenkov astronomy. The pixels are SiPMs, each consisting of 3600 G-APD cells, glued to a solid light cone. They are all glued to a plexiglass entrance window. The camera has a total of 1440 hexagonal pixels, each with a FOV of 0.11° so that the FOV of the whole camera adds up to 4.5°. The readout is based on the DRS4 chip. The mount of FACT is an old mount of the former HEGRA CT3 [Kon99] with an updated drive system. 30 hexagonal mirrors make up the reflective area, which is 9.5 m^2. The smaller area in comparison to e.g. MAGIC raises the lower energy threshold. Therefore, FACT is so far observing relatively strong γ-ray sources, like the Crab Nebula, Mrk 421 and Mrk 501 amongst others. [And13]
FACT is operated remotely, meaning that no one is at the telescope site to operate. It can be operated basically from anywhere with an available internet connection. A Quick Look Analysis (QLA) provides preliminary online analysis results in order to inform the Cherenkov telescope community directly in case of flaring activities of the observed sources. Results of this QLA will be shown in section 6.4.

Chapter 4
Data analysis for the MAGIC-I telescope

The analysis for data taken with the MAGIC telescopes is carried out by using mostly executable programs of the MARS package, the MAGIC Analysis and Reconstruction Software [Bre03], [Mor09]. In the following paragraphs the analysis chain for the single telescope operation will be explained because this thesis focusses on data taken in the years 2007 to 2009 when MAGIC operated only the MAGIC-I telescope. The basic goal of the analysis is the classification of the primary particles as either γ-ray or hadron, the determination of each particle's origin in the sky and the estimation of an energy for each γ-ray. With this information a γ-ray signal coming from a source can be detected, the γ-ray flux as a function of its energy, the so-called energy spectrum, can be calculated and the evolution of the source's integrated flux over time, the light curve, can be examined.
In addition to the recorded data of the source, Monte Carlo simulations are necessary for the data analysis. They are essential because without them the separation of signal and background events, as well as the estimation of the particle's energy, are impossible, amongst other things. Therefore, the production of these simulations will be illustrated first. Their application will be mentioned at every necessary step.
Afterwards, an explanation of the programs, which are used in the analysis of Mrk 421 data taken with the single telescope MAGIC-I, will be given.

4.1 Monte Carlo simulations of γ-rays

As mentioned above, simulated γ-rays with known initial properties are needed in the separation of the sought-after γ-rays in the overwhelming background of air showers induced by protons and other charged particles. Therefore, the observable features of the recorded showers, e.g. its appearance in the camera, of both γ-rays and hadronic background, are studied. Additionally, the simulations are needed in the estimation of the energy of the primary γ-rays. In this case the appearance of recorded images of solely γ-ray induced air showers is studied depending on the primary energy. For these reasons Monte Carlo (MC) simulations of γ-rays are produced. Using the air shower simulation program CORSIKA [Hec98], the evolution of γ-ray induced air showers of different primary energies is simulated. All particle interactions in the atmosphere of the γ-ray and the subsequent air shower particles are taken into account as well as the production of Cherenkov radiation.

With the program *reflector* the absorption of the Cherenkov light on its way from the production point to the telescope is simulated. The Cherenkov photons, which reach the telescope at the height of 2200 m, are then reflected on simulated mirrors. The subsequent program called *camera* simulates all functions of the readout electronics and the camera in order to get Monte Carlos that feature all the characteristics that are found in real raw telescope data. [Car08]

4.2 Signal extraction and calibration of raw data

The signal extraction and calibration of the data is the first step of the analysis. With the use of dedicated pedestal runs the so-called pedestal offset can be subtracted from the data. Then the digitised signal in each pixel is integrated with a cubic spline and the arrival time is specified. To calibrate the data, so-called calibration runs are needed. With them conversion factors can be determined in order to assign physical values, equivalents of photoelectrons (phe), to the FADC charge of the digitised signal. [Mor09]
Inside the MARS framework the program *callisto* is taking care of these steps. Afterwards, the information of other subsystems such as the starguider, the drive system, the trigger and the pyrometer are merged into the files [Gau08]. These features will be explained in more detail in section 5.1. The calibration does not have to be done personally because it is done automatically. However it is possible to do so under special data-taking circumstances. All data runs are available in calibrated format from the PIC (port d'informació cientifica) data centre where all MAGIC data is stored.

4.3 Image cleaning and parametrisation

In order to be able to parametrise the recorded shower images, the pixels belonging to the shower need to be found, and the pixels with signals induced by the NSB have to be removed. For this a cleaning of the image has to be performed. It is possible to choose between two different cleaning settings:

- **Absolute cleaning:** In this cleaning all pixels with a number of photoelectrons above a certain threshold and at least one neighbouring pixel fulfilling the same constraint are labelled as core pixels. In a second step all boundary pixels of a core pixel are checked for a minimum number of photoelectrons, which is lower than the first level. Typical numbers for this cleaning are 10 phe for core and 5 phe [Ali09] for boundary pixels.
  This cleaning was used before the hardware upgrade in February 2007 and was still used for data between February 2007 and the change to the stereoscopic system in summer 2009 in the case of observations under strong moon light.

- **Time cleaning:** Here the minimum number of photoelectrons for core and boundary pixel are lowered to 6 phe, resp. 3 phe [Ali09]. Additionally, there is a coincidence check of the arrival times of the signals. For all core pixels, which are above the 6 phe threshold, the arrival time is checked w.r.t. the mean arrival time of all. Any core pixel, which does not fulfil this criterion of at most 4.5 ns, is excluded from the group of core pixels. Then the absolute check for the boundary pixels starts, this time an

additional check is included if their arrival time difference to the neighbouring core pixel is less than 1.5 ns [Ali09]. The lower cleaning levels and the additional time information improve the sensitivity and lower the overall energy threshold of the analysis [Gau08].
This cleaning is the standard procedure for data taken for the stand-alone telescope MAGIC-I for the time range when the data of this analysis were taken, from February 2007 until June 2009.

All pixels surviving this cleaning are assigned to be part of the shower image. Then image parameters are calculated and assigned to characterise the cleaned shower image.
The basic parameters were introduced by Hillas [Hil85] and their number is increased by several more parameters inside the MAGIC analysis chain. The idea behind this is the description of the cleaned shower image with simplified parameters to determine its orientation and shape. With the help of the parameters one can distinguish between γ-rays and hadrons, which differ in their shower shape and hence as well in their parameter distributions. A selection of important parameters, which are used in this analysis, is listed below [Gau08].

- The **Size** is the sum of all photoelectrons belonging to the cleaned shower image. It is an important parameter because it is directly correlated to the initial energy of the primary particle.
- The first moment of the photoelectron distribution is described by the **COG**, the centre of gravity of the photon distribution.
- The second moment of the image along the major and the minor axis of the shower are quantified by **Length** and **Width**.
- The third moment along the major shower axis is saved in the parameter **M3Long**. It is needed for the determination of the direction of movement.
- **Dist** describes the distance between the calculated centre of gravity and the source position in the camera i.e. the pointing position of the telescope (which is the centre of the camera for ON-observation mode or 0.4° away from the centre for Wobble-observation mode).
- **Alpha** is defined as the angle between the major shower axis and the line connecting the COG and the source position. For particles coming from the direction of the source this value is small whereas background events are evenly distributed.
- The following two parameters deal with photon ratios of certain pixels. The ratio of the number of photoelectrons of typically the two brightest pixels to the size of the whole shower is called the concentration (**Conc**) of the shower. As γ-ray induced air showers are more compact than hadron induced showers, this is a parameter which can be used to distinguish between the two types of particles. The second parameter is the so-called **Leakage**. It gives the ratio between the photoelectrons of the shower which are contained in the outer pixel ring and the size. Therefore, it takes into account which fraction of the shower is outside of the camera's field of view. It is more important for bigger showers and therefore higher energies.

- The parameter **Number of Islands** indicates, as its name implies, the number of segments of the recorded shower in the camera. It is a useful indicator for the distinction between γ-rays and hadrons. γ-ray induced showers are in contrast to hadron induced showers compact and mainly only feature one island. Therefore, this parameter can again be used to distinguish between the two particle types.

For a better understanding these parameters are shown in Figure 4.1 with the camera image of a cleaned shower.

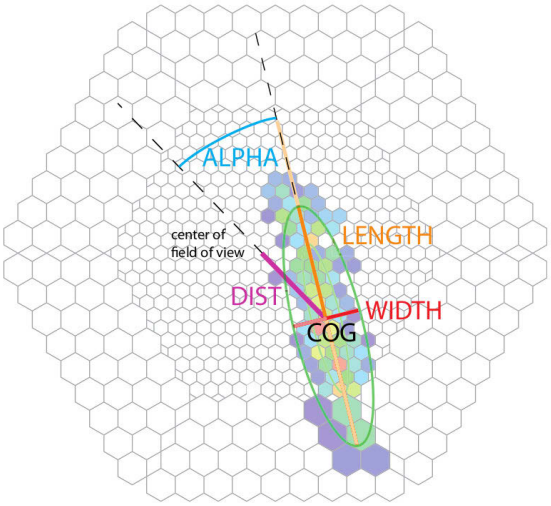

Figure 4.1: Some basic image parameters of a cleaned shower image. In this image the source position is located in the centre of the camera, i.e. the telescope observed in ON mode. The colour code of the pixels indicates the signal amplitude. The image is taken from [Sch13].

The image parameters can be classified as source-dependent and source-independent. For the source-dependent parameters it is mandatory to know the source position. **Dist** and **Alpha** are two of these source-dependent parameters. Most of the other parameters, e.g. **Size**, **Width** and **Conc**, can be calculated without the knowledge of the source position.
The data is automatically processed up to this level and can be found at the PIC data centre. The subsequent action to be taken by the analyst is the data selection. This has to be done in order to have an unbiased data sample in terms of technical problems or bad weather conditions. As this was a major part of the analysis, this part will be explained in detail in section 5.1.

4.4 γ-Hadron-Separation, energy estimation and reconstruction of the source position

The next step in the analysis is done by the program *osteria* in the case of mono analysis. With the multivariate method called Random Forest (RF) the γ-Hadron-Separation, the energy estimation as well as the source position estimation can be started. A RF is a

classification method based on decision trees which are trained with labelled data and are then able to classify unlabelled data [Alb08a].
The main principle of this method in the case of the γ-Hadron-Separation is to choose a sample of γ MCs and a sample of background data which represent the hadrons. With the parameters of the labelled events a selected number of forests is trained. The resulting models are applied to the real data using the program *melibea*. It is then possible to assign a probability to each event of the data sample to be a γ-ray or a hadron. An estimated energy as well as the estimated source position are assigned to each event using RFs trained on γ MC simulations.

Required data
For the training of the RFs, labelled samples of γ-rays and of hadrons are needed. For the γ sample, MC simulations, as introduced in section 4.1, are used. For the hadron sample, also named background, data taken of faint γ-ray sources are used. With a ratio of at least 1000 hadrons to one γ [Wee03] these data can serve as hadron sample. All sets of data have undergone the same steps of the analysis up to the *star* level.
It is crucial to select MCs as well as hadron data that cover the same zenith angle range as the data because the zenith angle has an influence on the shower appearance in the camera. For both samples it is important to have no gaps in their zenith distribution in order not to wrongly classify the data events only according to their zenith angle. Additionally, it is important that the light conditions, weather circumstances and imaging properties of the telescope should be equal to the ones which are chosen for the data to be analysed (see section 5.1). For the hadron sample any possible data from the observation period that matches the observation criteria of the data sample to be analysed should be chosen. *osteria* is picking events from the hadron sample according to the zenith angle and size distributions of the MCs.

- **γ-Hadron-Separation:**

  For the separation of the γ-ray induced showers from the more frequent hadron induced showers a Random Forest is built with *osteria*. In the case of the present analysis a number of 100 decision trees was chosen. They are trained with several of the image parameters, e.g. Size, Width, Length, Conc, and more (see section 4.3), either including the source-dependent image parameters or not, such that two different RFs are built. Timing parameters of the shower images are taken into account for the training as well because they help with the suppression of the background events [Gau08]. The zenith angle is also considered because the shape of the shower changes with changing angle. Therefore, the image parameters change as well. The input events are either labelled as "gammas" in the case of the Monte Carlo simulations or as "hadrons" in the case of the hadron data sample. The essential output parameter is the so-called **Hadronness** which ranges from 0 to 1 and indicates the probability for an event to be a hadron following the averaged decision of all trees of the RF. The result of the RF is directly checked on 5% of the input events which were set aside for this purpose and not used for the training. An example of such a test result can be seen in Figure 4.2. Here the distribution of the assigned Hadronness parameter is shown for the 5% test sample of the Monte Carlo simulations (Gammas) and the hadron sample (Hadrons). The desired values for the two samples are

accomplished, given that the γs have a tendency for low Hadronness values towards 0 whereas the hadrons have higher Hadronness values towards 1.

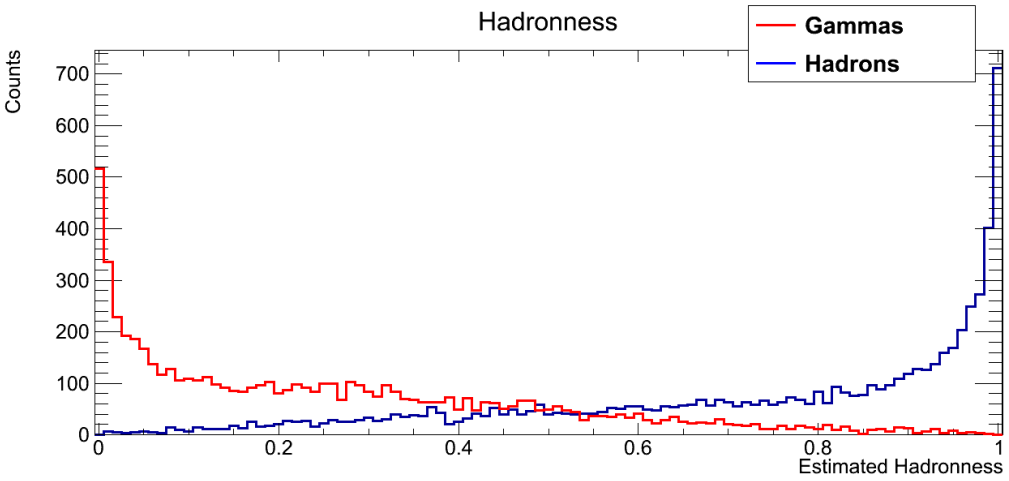

Figure 4.2: The distribution of the assigned Hadronness parameter for the 5% test sample can be seen above. The distribution of the γs (in red) is peaking at a Hadronness of 0. In contrast the Hadronness values for the hadrons is higher with the distribution's peak at 1.

In *melibea* the real data is imported and every event is classified by every single decision tree. Then the averaged Hadronness is assigned to each event, which defines the probability for it to be a γ or a hadron. A cut on this value determines how clean the data sample should be, i.e. how "γ-like" the events must be to be accepted as γ and to be further analysed.

- **Energy estimation:**

  For the energy estimation another RF is built with *osteria*, this time with 50 decision trees and only γ MCs as input. The trees are again trained on 95% of the input data using image parameters. Here again the source-dependent parameters can be included or not. It has to be considered that there are not two classes but a continuous variable in this case, the energy. That is why the MC simulations are separated into bins of energy to train a RF for each of these bins, so that each real data event receives the average resulting estimated energy of all trees [Sat10].

  The main principle behind the energy estimation is the dependency of the number of produced secondary particles on the primary particle's energy [Wee03]. This number is again correlated to the produced Cherenkov photons and hence the Size. Thus Size is amongst others a parameter used for the training. The Leakage is also taken into account, as it is mandatory to know what percentage of the shower is inside and outside of the camera. The most important input is the true energy of the simulated events. The performance of the RF is again tested on the remaining 5% of the input data.

- **Reconstruction of source position:**

  The source position in the camera can be determined by the **DISP** method [Dom05]. Provided that the source is located on the projected major axis of the shower image, the source position can be calculated with a DISP function including the image parameters Size, Width, Length and Leakage. As can be seen in Figure 4.3, DISP is the distance from the COG to the estimated source position. It has two possible solutions. Due to the asymmetrical light distribution along the major axis of the shower, the parameter M3Long decides where to find the source position. The distance between the real source position (pointing position) and the estimated source position is known as θ and is an important parameter for the next analysis steps, where e.g. a signal region around the source position is defined. As the real and estimated source position move closer together, θ decreases, which indicates that the particle is probably coming from the direction of the source.

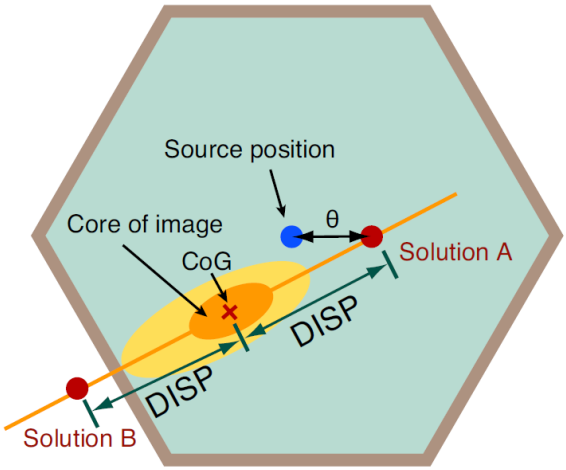

Figure 4.3: Illustration of the DISP and θ parameters in the camera. The two possible solutions for the reconstructed source position are shown in red. θ is the distance from the estimated source position (here Solution A) to the source position shown in blue. The image is taken from [Maz07].

A RF is used in *osteria* to improve the DISP method [Sai09]. Here again 50 decision trees are built. The image parameters are used to estimate DISP and the source position. In *melibea* the DISP parameter is assigned to every event and θ is calculated in the subsequent analysis steps using DISP.

4.5 Signal detection

The next step in the analysis is the detection of the γ-ray signal coming from the source. At first the hadronic background is reduced by applying a cut in Hadronness. Besides the sought-after γ-rays coming from the direction of the source, there is an additional and diffuse γ-ray flux evenly distributed over the sky, as well as remains of the uniformly distributed hadrons, which still passed the Hadronness cut. All these aspects have to be

taken into account when calculating the source's flux. The signal can be found either in the distribution of Alpha or θ^2. In this analysis θ^2 has been chosen. The program *odie* is used to detect the source's signal.
For the calculation of the γ-ray flux the fraction of randomly distributed background has to be determined. Therefore, one or several OFF regions are defined which are evenly distributed around the camera centre in the Wobble mode. In Figure 4.4 this principle is illustrated. As the estimated source position of the events is known, they can be assigned to the ON or OFF sample if their origin is in one of the regions.

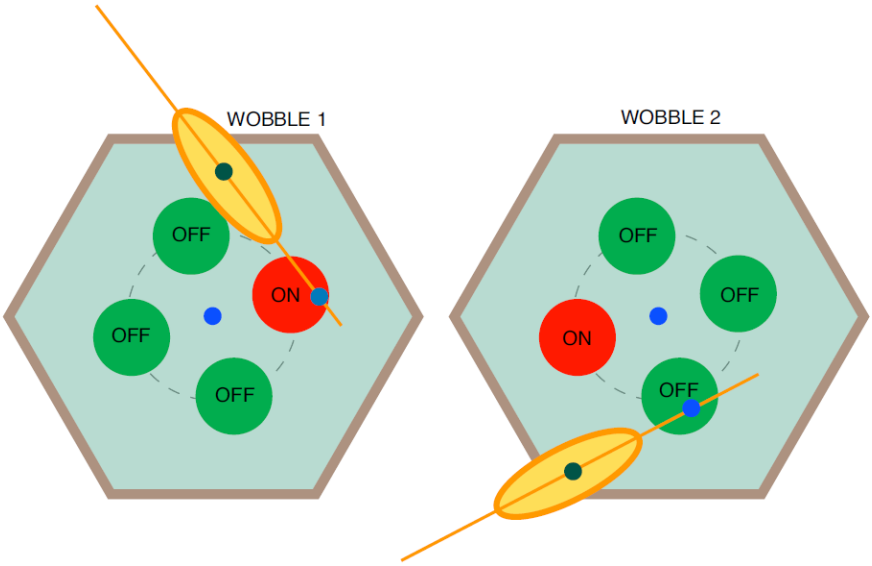

Figure 4.4: Illustration of ON and OFF regions in the camera for the signal detection. In both Wobble positions three OFF regions are defined for one ON region. On the left hand side an event with its estimated source position inside the ON region is shown. The event on the right hand side will be an event of the OFF sample, as its estimated source position is inside one of the OFF regions. The image is taken from [Maz07].

The number of OFF regions can be chosen, but they should be symmetrically distributed in the camera, in order not to be biased by e.g. inhomogeneities in the camera. In this analysis a number of three OFF regions has been chosen and kept for all further utilisations. After the application of a maximum cut in Hadronness and a minimum cut in Size, the number of events for the ON and OFF regions can be plotted as a function of θ^2.
In Figure 4.5 a signal plot from the Crab Nebula is shown as an example. The data sample consists of 5.69 h of data taken at zenith angles between 9° and 30° in the time range from 2007 to 2009. The black dots show the event distribution of the ON region, the black dots on top of the grey shaded area show the averaged event distribution of the OFF regions. Further a cut in θ^2 is done. It defines the signal region in the θ^2 distribution and it is possible to define a significance of the observation and the sensitivity of the instrument for this selected signal region. In this particular case a maximum cut in Hadronness of 0.06 and a minimum Size cut of 150 phe were chosen. The maximum cut in θ^2 was set

at $0.015°^2$ in order to reach a high significance in accordance with a low sensitivity value (explanation see below).

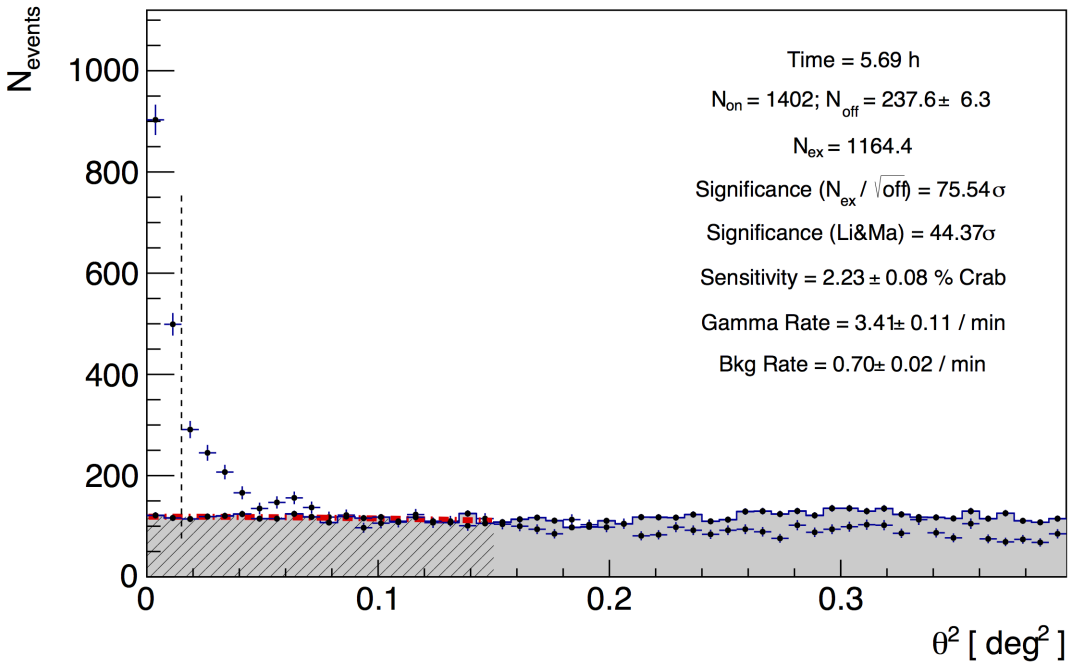

Figure 4.5: Signal plot of the Crab Nebula for a sample of 5.69 h in the time range from 2007 to 2009 for zenith angles below 30°. The number of events for the ON region (black dots) is plotted against θ^2. The event distribution of the OFF regions is scaled by a factor of three and is represented by the black striped region in the grey shaded area. The fit to this distribution is shown in red. The black dashed and vertical line is the cut applied in the parameter θ^2.

- **Excess events:**

  For the background distribution the events of the OFF region are averaged over all three OFF regions. A fit in the range from $0°^2$ to ten times the signal region, here $0.15°^2$, is applied to the events to determine a meaningful and averaged number of the OFF events N_{off}. In Figure 4.5 this fit is shown as a red dashed line.

  The number of ON events N_{on} simply comprises all events in the signal region of the ON sample. The difference of these two values is the number of so-called Excess events:

$$N_{\text{exc}} = N_{\text{on}} - \alpha N_{\text{off}} \,. \tag{4.1}$$

  Here α is the scaling factor to account for the higher number of OFF regions. In the case of three OFF regions $\alpha = \frac{1}{3}$.

- **Significance:**

  The significance of the detection can be calculated with Equation 4.2, which is taken from [Li 83].

$$S = \sqrt{2}\left(N_{\text{on}} \ln\left[\frac{1+\alpha}{\alpha}\left(\frac{N_{\text{on}}}{N_{\text{on}}+N_{\text{off}}}\right)\right] + N_{\text{off}} \ln\left[(1+\alpha)\left(\frac{N_{\text{off}}}{N_{\text{on}}+N_{\text{off}}}\right)\right]\right)^{\frac{1}{2}} \quad (4.2)$$

  Here α is the same scaling factor as above. The significance S is given in standard deviations. A source is classed as detected when it reaches a significance of $5\,\sigma$.

- **Sensitivity:**

  Another value, the sensitivity, is calculated by *odie*. In Figure 4.5 a sensitivity of $(2.23 \pm 0.08)\%$ Crab flux for the 5.69 h of observation time can be seen. This sensitivity is defined in terms of a flux in % of the Crab flux which can be significantly detected within 50 hours of observation. In this case a source with a flux of 2.23% of the Crab flux can be detected significantly by MAGIC-I in 50 hours of observation. Here the significance is not calculated as in Equation 4.2, but with $\frac{N_{\text{exc}}}{\sqrt{\alpha N_{\text{off}}}}$ [Alb08b, Li 83] and again has to be $5\,\sigma$.

4.6 Sky map

When plotting all γ-like events with their reconstructed arrival direction into a 2D histogram, a sky map of the source region is created in equatorial coordinates, i.e. right ascension and declination. Inside the MARS framework this is done by using the program *caspar*.
The excess events are selected with a minimum Size and a maximum Hadronness cut, as well as a cut in θ^2. The arrival direction of each photon is given by the DISP parameter. The background exposure map is modelled with the selected number of OFF regions. In this analysis three OFF regions are chosen. Additionally, a Gaussian smearing of the images is done so that the real smearing of the telescope imaging aperture, namely the point spread function (PSF), is represented.
One possibility of illustration of the sky map is a relative flux map. In this case the smoothed excess map is shown in relation to the smoothed background map. An example of a sky map was already shown in panel (b) of Figure 2.4. It shows the relative flux map around the position of Mrk 421 in the zenith angle range from 9° to 30° in the time range from April 2007 to February 2009. In addition, regions of different significances are included in the sky map.

4.7 Energy spectrum and light curve

At this stage of the analysis the most interesting physical results of a source can be obtained. In case of mono analysis the differential energy spectrum and the so-called light curve, which is showing the flux behaviour of the source with time, are calculated by the

program *fluxlc*. The output of *melibea* of the source's data as well as MC simulations are taken as input in *fluxlc*. The MCs are a different sample than the one used for the RF training. They are among other things needed for the calculation of the effective collection area which is necessary for the following computations.
To get a clean sample of signal events, cuts in Hadronness and θ^2 (or Alpha) have to be set. Either these cuts can be set individually for every single energy bin by the user or they can be determined by *fluxlc* with given cut efficiencies. In this case the user defines a value for the γ efficiency. This means that cuts in the parameters Hadronness and θ^2 are chosen on the basis of the distribution of the MC simulations. The cut in the two parameters is optimised by the program so that the desired percentage of γs will survive this cut. This is the so-called efficiency. In this analysis the cuts were determined using the cut efficiency approach.

In order to obtain the γ-ray flux of the source, it is mandatory to know the number of photons N_{exc} in the effective observation time t_{eff} as well as the effective collection area A_{eff}. A_{eff} includes the acceptance of the measurement given by the area in which the arriving photons can be seen and the detection efficiency of γ-rays, i.e. the ratio of simulated γ-rays and the ones surviving the analysis up to this stage. It can be computed with the help of the above mentioned MC simulations.
It is now possible to create the differential energy spectrum which shows the source's flux as a function of the energy. It is given by

$$\frac{dF}{dE}(E) = \frac{dN_{\text{exc}}}{dE\, dA_{\text{eff}}\, dt_{\text{eff}}}. \tag{4.3}$$

Additionally, the integral flux in a certain energy range or above an energy threshold can be computed. The temporal evolution of the integral flux of a source is called light curve. The time binning can be chosen individually. Either changes in the nightly flux can be investigated to study the long-term variabilities of the flux or short time bins of several minutes can be looked at to search for intra-night variabilities. In Figure 4.6 the light curve of the Crab Nebula can be seen for four selected nights in the time range from 2007 to 2009. The flux values for each night (red dots) as well as the constant fit (pol0, red line) are close to the comparison value of "Crab (MAGIC-I)", a data sample from 2005 [Alb08b], and the flux values are compatible with a stable flux. The flux of the background (blue dots) is stable as well from which stable analysis conditions and a valid analysis can be assumed.

4.8 Spectrum unfolding

The differential energy spectrum produced by *fluxlc* is a function of the estimated energy, but the aim is to have it as a function of the true energy of the primary particle. To solve this problem the unfolding method is used here.
To obtain the distribution of the primary particles' true energy several influences have to be taken into account. First of all the detector has a finite resolution. This means that the assigned observables for each recorded particle shower are only precise to a certain degree. Part of this is the indirect measurement of the energy via the observables. Additionally,

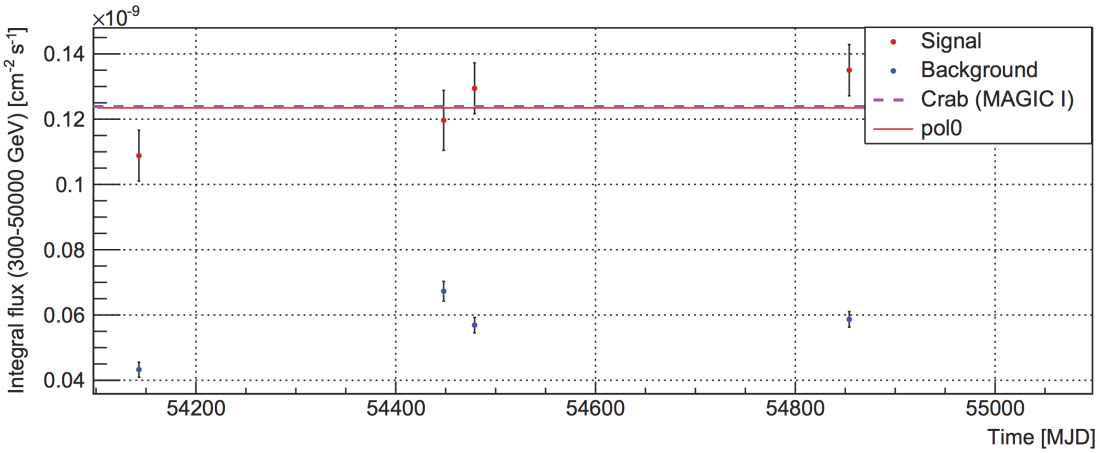

Figure 4.6: The light curve of the Crab Nebula shows the integral flux between 300 GeV and 50 TeV for a sample of 5.69 h in the time range from 2007 to 2009. The red dots show the nightly flux of the Crab Nebula. It is stable and around the reference line of Crab measured with MAGIC-I [Alb08b]. The constant fit to the flux points is represented by the red line. The stable flux of the background is shown in blue.

the acceptance of the detector is limited which means that not all particles which hit the atmosphere and start an air shower are detected by our telescope or survive the analysis chain. [Blo98]
The telescope is only able to measure a distribution $g(y)$ of the observables y instead of measuring directly the sought distribution $f(x)$ of the observable x, which is the true particle energy in this case. The dependency of these two distributions in the range $a \leq x \leq b$ is described by the Fredholm integral equation [Blo98]:

$$g(y) = \int_a^b M(y,x) f(x) dx. \tag{4.4}$$

The response function $M(y,x)$ gives the probability of obtaining a result y when a value x is given [Blo98] and is calculated with Monte Carlo simulations. Given that the data and their parameter distributions are existent in binned histograms, this equation can be discretised and then be written in matrix notation:

$$\vec{g} = \mathbf{M} \cdot \vec{f}. \tag{4.5}$$

The first obvious method of solving this equation would be the inversion of the response matrix $\mathbf{M}$. Due to the fact that the matrix is generally not quadratic inversion is not the solution. Alternatively the equation can be solved by minimising the least-squares expression [Alb07a]

$$\chi_0^2 = (\vec{g} - \mathbf{M} \cdot \vec{f})^{\mathbf{T}} \cdot \mathbf{V}_g \cdot (\vec{g} - \mathbf{M} \cdot \vec{f}), \tag{4.6}$$

with $\mathbf{V}_g$ as the covariance matrix of the measured distribution.

Solving an inverse problem often results in a solution for $\overrightarrow{f}$ containing strong fluctuations. These are caused by small entries in $\mathbf{M}$, which don't contribute significantly to the migration. To control these fluctuations a regularisation term $Reg(\overrightarrow{f})$ is introduced. [Doe13] It is added to the expression as follows:

$$\chi^2 = \frac{w}{2}\chi_0^2 + Reg(\overrightarrow{f}), \tag{4.7}$$

where w is a weight of the strength of the regularisation. There are several approaches for regularisation, e.g. by Tikhonov, Bertero and Schmelling. They shall not be explicitely discussed here, but further explanations can be found in [Alb07a] and the references therein. In the MAGIC standard analysis the standard unfolding procedure is implemented in *CombUnfold*. The distribution of the estimated energy is used for the unfolding. A choice can be made between the already mentioned regularisation methods of Tikhonov, Bertero and Schmelling. Additionally, forward folding can be applied where an assumed function is inserted for the sought-after distribution $\overrightarrow{f}$ to solve the matrix equation. It can be used as a check for the real unfolding results. [Alb07a]

Chapter 5
Mrk 421 data analysis

Since the beginning of MAGIC observations, Mrk 421 has been observed on a regular basis. Since 2009 MAGIC has been participating in multi-wavelength campaigns with many other telescopes, which observe the source in as many wavebands as possible at the same time. These campaigns are needed to understand the source's overall behaviour and thus to be able to conclude on the processes and the activity of the central engine of the AGN Mrk 421. This chapter concentrates on the data analysis and its results with the MAGIC-I telescope. These results will be put in the MWL context in chapter 7.
This chapter is structured as follows. At first the selection and data check of the single telescope data taken by MAGIC-I will be presented. This includes the data of Mrk 421 which are analysed, MC simulations of γ-rays and suitable background data for the training of the RFs, and Crab Nebula data for a reference analysis. Then the analysis and its results will be outlined with particular attention to the behaviour of the source in the examined time period. The light curve of a 2.3 year long data set is examined to describe this behaviour. Additionally, this is done in different energy ranges. Then it is investigated, if variability is present in the light curves on shorter time scales than days. Afterwards, the dependence of the spectral shape on the flux state is examined.

5.1 Data overview and selection criteria

Mrk 421 was first observed with MAGIC-I in April 2005. Since then it was and still is regularly observed between late November and the middle of June every year, when the source is observable. For this analysis data of the single telescope MAGIC-I were selected. The time span ranges from February 2007 to June 2009. The analysis of this large data set will help to understand the general view of the source especially over a long time span.
The first observations of this time span were taken on 11th February 2007 (MJD[1] 54142) with the convention in MAGIC that all data of one night is named after the day which starts at midnight UTC. The last observations of Mrk 421 with the single telescope MAGIC-I were taken on 15th June 2009 (MJD 54996.9). In this time span of 2.3 years Mrk 421 was observed on 149 nights in a total of 174 hours.
Not all data were taken under the same observation conditions. One of these conditions is the zenith angle of the observations which has an influence on the appearance of the shower in the camera and therefore e.g. the γ-Hadron-Separation and the energy estimation. The

[1] The Modified Julian Date is a commonly used date in astrophysics as well as in other fields because it counts all days consecutively. A new day starts at midnight in UTC.

second influencing factor is the point spread function (PSF) of the imaging system which alters again the appearance of the shower. The weather conditions also need to be taken into account as they have an effect on the data quality. The brightness of the moon has to be considered as well since it adds a non negligible fraction to the level of the NSB. These observation conditions are explained in more detail in the following.

- The data are separated for the analysis according to the **zenith angle** of the observation. The development of the showers and therefore their appearance in the camera depend on the zenith distance (Zd), especially for values greater than 30°. The distance the particle has to travel through the atmosphere changes with the zenith angle. This means that the greater the angle is, the thicker the atmosphere layer becomes through which the particle and its induced shower of secondary particles have to travel. The most obvious effect is that it gets harder to detect lower energetic particles. For this reason it is important to separate the data into low and high zenith distances and analyse the data sets individually. Monte Carlo simulations of γ-ray showers are produced for the different zenith angles so that the separation and energy estimation can be done in dependence on the zenith angle. The data I am using are separated into three parts: Zd smaller than 30°, Zd between 30° and 45° and Zd greater than 45°.

- An important value for the analysis is the telescope's **point spread function**. The PSF describes the widening of a point-like source in the optical system of the telescope. Using parameters of muon images the PSF of the telescope system can be calculated. This method was first introduced to MAGIC by [Mey05]. In Figure 5.1 the evolution of the PSF of MAGIC-I can be seen for the time range from February 2007 to June 2009. Comparing the nightly PSF values of the nights where Mrk 421 data were taken (black dots) to the available PSF value in the simulated γ Monte Carlos, which are represented by the red (10.6 mm), blue (13.0 mm) and orange (14.8 mm) line, the correspondent Monte Carlo set is chosen. Values when no Mrk 421 data were taken are symbolised with grey dots.

  As can be seen in the plot, the PSF changes over time. Therefore, the data is separated into two data sets according to their PSF. The division is applied between the 3rd and 25th of February 2009. Hence, the data from 11th February 2007 to 3rd February 2009 are analysed using γ Monte Carlos with a PSF of 13.0 mm and for the data from 25th February 2009 to 15th June 2009 simulations with a PSF of 14.8 mm are applied.

- To have a data sample with homogeneous observation conditions some restrictions on the **weather conditions** are made. Parameters which can help to evaluate the weather conditions are the so-called cloudiness, the number of stars and the trigger rate. The parameter cloudiness is measured with a pyrometer, which is attached to the MAGIC-I mirror mount pointing into the same direction as the telescope. It gives a percentage of what fraction of the sky is covered in the direction of the source.

  With a T-Point camera placed in the centre of the mirror dish the camera and the sky area next to it are recorded. It recognises stars in the sky region next to the camera.

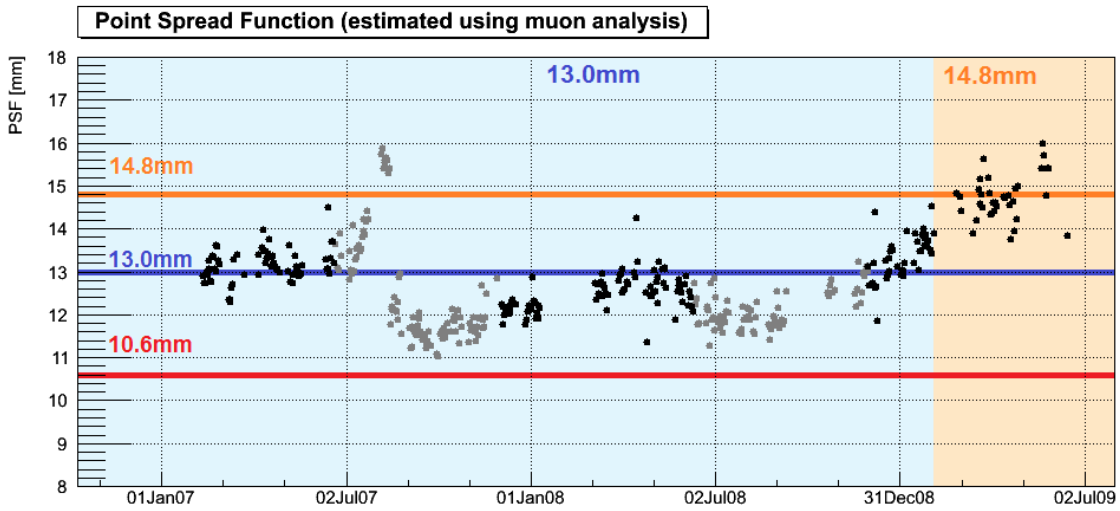

Figure 5.1: The PSF of MAGIC-I from February 2007 to June 2009. The values are calculated with muon images. The dots show the nightly value. In black the PSF is shown for the time range when Mrk 421 data were taken. The grey dots, when no Mrk 421 data were taken, are included due to completeness. The lines show the available simulated PSF in the Monte Carlo simulations and the blue and orange shaded areas show the chosen PSF for the time range, corresponding to a PSF of 13.0 mm and 14.8 mm.

If clouds and dust covered this area, a lower number of stars would be recognised. Setting a minimum cut value to the recognised number of stars, eliminates data taken with cloudy weather. Additionally, this camera is used to determine the accuracy of the telescope's pointing with the use of LEDs that are mounted around the camera. The cloudiness and number of stars are correlated values so that in case one of the instruments fails the other one can still be used to judge the weather conditions.

Another value to check for changes during the observations is the trigger rate. If it is not stable, clouds might have passed through the FOV. In some cases headlights of a car passing by the telescope can shine into the camera. Data subruns, which are affected by this, are filtered out through their trigger rate as well. A minimum value for the trigger rate is chosen as well to make sure that the air is clear and not affected by e.g. Calima. This dusty and sandy wind from the Sahara decreases the transparency of the air for the air showers when it is present. In addition outer influences, which cannot be seen by the analyser, are written down in a runbook by the shifters to help the analyser to judge the data quality and discard affected runs or even complete days.

In this analysis the following values for the above explained parameters are chosen.

- cloudiness: $< 40\%$
- number of stars: > 30

  - trigger rate: stable in a range of 100 Hz with a minimum of 200 Hz for dark nights and 175 Hz for data taken in twilight or moon conditions

- The reflected light of the **moon** alters the amount of night sky background especially in nights when it gets close to full moon. The moon conditions can be read from the automatically adapted discriminator threshold during the observation. This value corresponds to the trigger threshold in the first trigger level. The following values distinguish between data taken under dark or moon conditions. As there was a change in the definition of the DT, there are two values:
  - DT for data taken up to June 2008: 20 DAC units

    and
  - DT for data taken after November 2008: 42 DAC units.

Consequently, the analysis of the data is executed separately due to the zenith angle and the PSF. The data is selected or discarded according to the weather and moon conditions during the observations. Additionally, runs or subruns with a warning by shifters not to use this data are discarded as well. It also needs to be mentioned that only data taken in Wobble mode are analysed. Data taken in ON mode need to be considered separately and are not analysed in the scope of this thesis.

5.2 Selected data samples for analysis

Between 11th February 2007 and 15th June 2009 Mrk 421 was observed in 149 nights. All data were checked for the above mentioned quality criteria. For further analysis it is necessary to select MC simulations of γ-rays and a background data sample for the γ-Hadron-Separation in *osteria*. In addition, a sample of Crab Nebula data is picked to perform an unbiased analysis. The background data sample as well as the Crab Nebula data have undergone the same data check that was applied to the Mrk 421 data.

5.2.1 Mrk 421

A total of 173.9 h of Mrk 421 data was recorded in 149 nights. 97.5 h of the data, taken in 99 nights, survived the data check. In the following the different reasons for exclusion of data are listed.

Zd>45°:	6.6 h [2]
ON data:	3.9 h
runbook comments:	0.4 h, excluded because of car flashes
weather/light conditions:	60.3 h, bad weather or sky too bright
effective on time <10 minutes:	5.2 h

[2] Data with a Zd>45° would need a separate analysis. The excluded data would only have given data on four additional days. Most of the other data was part of observations that extend into the zenith range below 45° and would only have given more statistics for that night, but the major part of this data was short in effective observation time and would not have provided significant results. For other days the data would have been excluded anyway due to bad weather or light conditions.

The days where Mrk 421 data were taken, which at least partly survived the data check, can be found in Table 5.1. Due to the large amount of data only the date is listed in this table for convenience. For more detailed information on the daily data amount and zenith angle range, please see Table A.1 to Table A.4 in Appendix A.

Table 5.1: Mrk 421 data which (at least partly) survived the above mentioned quality criteria of the data check. The data for both PSF configurations and the whole zenith angle range from 9° to 45° are presented.

Year	**Month**	**Day**
2007	02	11, 15, 19, 27
	03	08, 12
	04	15, 22
	05	05, 13
	12	04, 05, 06, 07, 08, 09, 12, 14, 15, 16, 17
2008	01	01, 02, 04, 05, 06, 07, 08, 09, 10, 11, 12, 13, 14, 15, 16, 29
	02	02, 04, 05, 06, 08, 11
	03	01, 08, 11, 12, 31
	04	02, 04, 06, 12
	05	04, 05, 07, 10, 23, 25, 27, 28, 29
	06	03, 05, 06, 07, 08
	11	30
	12	02, 04, 05
2009	01	04, 22, 24, 26, 28, 30
	02	01, 03, 25
	03	01, 17, 19, 21, 23, 29, 31
	04	15, 16, 17, 19, 21, 22, 23, 24, 25
	05	21
	06	13, 14, 15

A list of all excluded days can be found in Table A.5. As the data analysis is separated into four parts due to the zenith angle and the PSF, the following four sets of data will be mentioned in the next sections:

PSF 13.0 mm and Zd<30°,
PSF 13.0 mm and Zd 30° - 45°,
PSF 14.8 mm and Zd<30°, and
PSF 14.8 mm and Zd 30° - 45°.

5.2.2 Monte Carlo simulations

MC simulations of γ-rays are produced for three different values of the PSF, namely 10.6 mm, 13.0 mm and 14.8 mm. As shown in section 5.1 two sets of MCs were chosen, namely one set with a PSF of 13.0 mm and one with 14.8 mm. Furthermore, they are

simulated for a wide range of zenith angles. They were selected to cover the whole zenith ranges of the two chosen separations, firstly, from 9° to 30° and secondly, from 30° to 45°. Additionally, they are simulated for Wobble and ON observation mode, so that the Wobble mode was chosen in this case.
Consequently, four sets of γ MCs were collected for the analysis, which can be categorised by their Zd range and PSF as the Mrk 421 data above.

5.2.3 Background data sample

To find a good sample of hadron data, real recorded data of faint γ-ray sources are used. With an impurity of a ratio of γs to hadrons of 1 to 10^3- 10^4 [Wee03], it is "clean" enough to serve as a hadron sample. The data have to undergo the same data check as the Mrk 421 data. The sample covers the same time range as the Mrk 421 data in order to have observation conditions as close as possible to the conditions of the data to be analysed and not to be biased by changes in the telescope performance. It is necessary to choose several different sources to ensure that the whole zenith range is covered. The following extragalactic sources are selected and checked to serve as hadron sample.

1ES1959+650	3C279	PKS1510-08
1ES2344+514	HB89-1553+11	PKS-1222+216
1H1722+119	MS1050.7+494	PKS-1717+177
2MASX0324+34	PKS1424+240	

A detailed overview of the selected days for each source is listed in Table A.6.

5.2.4 Crab Nebula

For the optimisation of cuts in the further analysis, a Crab Nebula data sample is used. To have the same observation conditions as during the data-taking of Mrk 421 preferably data of the same days or close to them are chosen. These data have to pass the same data check as the Mrk 421 data.
The selected days of Crab Nebula data are listed in Table 5.2. For more details on the durations of observation and the exact correspondence of the days to the four data sets of different PSF and Zd range, please see Table A.7.

Table 5.2: Crab Nebula data used for the reference analysis. The data for both PSF configurations and the whole zenith angle range from 9° to 45° are presented.

Year	**Month**	**Day**
2007	02	12
	12	14
2008	01	14, 23
2009	01	23
	03	01, 02, 14, 21, 22, 23

5.3 Significance of Mrk 421 data

The detection of Mrk 421 is not a particular goal of this thesis, as it was already significantly detected in 1992 with the Whipple telescope [Pun92]. For the sake of completeness, the significance of the data of this analysis is calculated nevertheless.
The significance of all observations is determined by the program *odie* as explained in section 4.5. A minimum Size cut and a maximum cut in Hadronness as well as in θ^2 are applied. For the background three OFF positions are selected. To find the optimal cut values for the signal detection, iterated cut values are applied to the Crab Nebula data samples. Then the significance and sensitivity are examined. The optimal cut values are determined when a good compromise of a high significance and a good sensitivity is found. These cut values for the four Crab Nebula data samples and the resulting significances and sensitivities can be found in Table A.8. These cuts are then applied to the Mrk 421 data. The results for the four different data sets are summarised in Table A.9.
The signal plot of the largest data set out of the four sets was chosen to serve as a representative plot for all signal plots. The chosen data set is covering the zenith angle from 9° to 30° in the time span from 15th April 2007 to 3rd February 2009. It is shown in Figure 5.2. In 50.35 hours of observation a total of about 14281 excess events were counted, which results in a significance of 171.31 σ with the given number of OFF events. A detailed explanation of a signal plot is given in section 4.5.

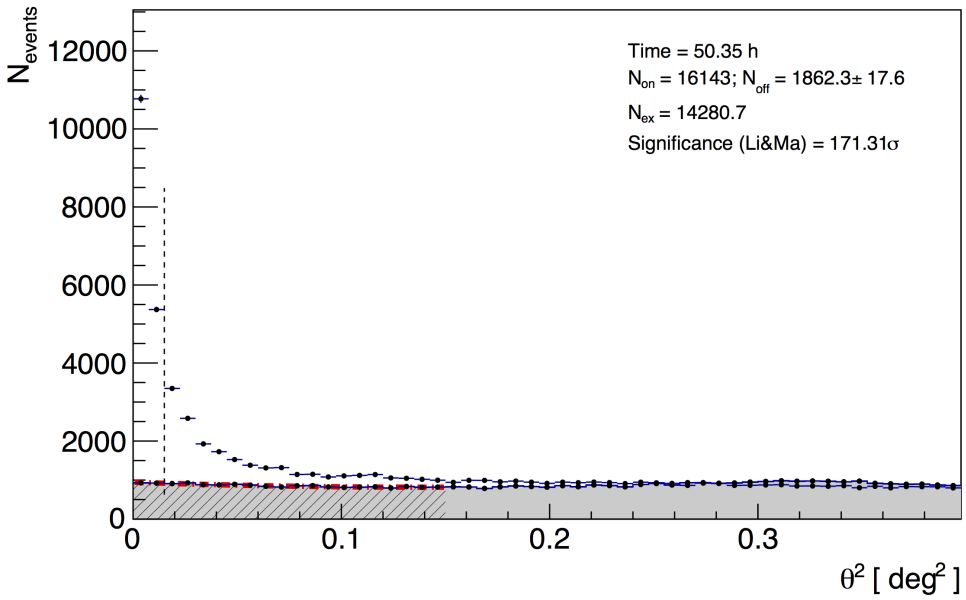

Figure 5.2: Signal plot of Mrk 421 from April 2007 until February 2009 for the zenith angle below 30°. The number of events for the ON region (black dots) is plotted against θ^2. The event distribution of the OFF regions is scaled by a factor of three and is represented by the black striped region in the grey shaded area. The fit to this distribution is shown in red. The black dashed and vertical line is the cut applied in the parameter θ^2.

All results reinforce the significant detection of the source. The significances were also calculated for the daily observations. These results are added in Table A.1 to Table A.4.

5.4 Light curve determination

The light curve is determined with *fluxlc*. The events are selected according to cuts in the parameters Size, θ^2 and Hadronness. These are optimised on data of the Crab Nebula as explained in section 4.7. The cut values are summarised in Table A.10. These cuts are subsequently applied to the four sets of Mrk 421 data.
The light curves with zenith angles below and above 30° are combined, but only data points which have at least 10 excess events and a significance greater than $3\,\sigma$ are included. This results in the rejection of four data points in February 2007 (namely the 11th, 15th, 19th and 27th), but it ensures reliable results. The resulting light curve spans over a length of 830 days and includes 95 data points.
In the following, the abbreviation "CU" will be used. This Crab Unit refers to the average integral flux of the Crab Nebula for the given energy range. For the energy range from 400 GeV to 50 TeV it equals $8.084141 \cdot 10^{-11}\,\mathrm{cm}^{-2}\mathrm{s}^{-1}$ [Alb08b], which was determined for MAGIC-I in mono operation.
In Figure 5.3 the combined light curve from 8th March 2007 to 15th June 2009 is shown with a daily binning, i.e. each flux point represents the integral flux summed over the whole night. If in one night data were taken below and above 30°, these data were combined. All resulting flux values are noted down in Table A.11. This table shall be considered if the reader is interested in the exact flux value in the case that the flux is only given in CU.

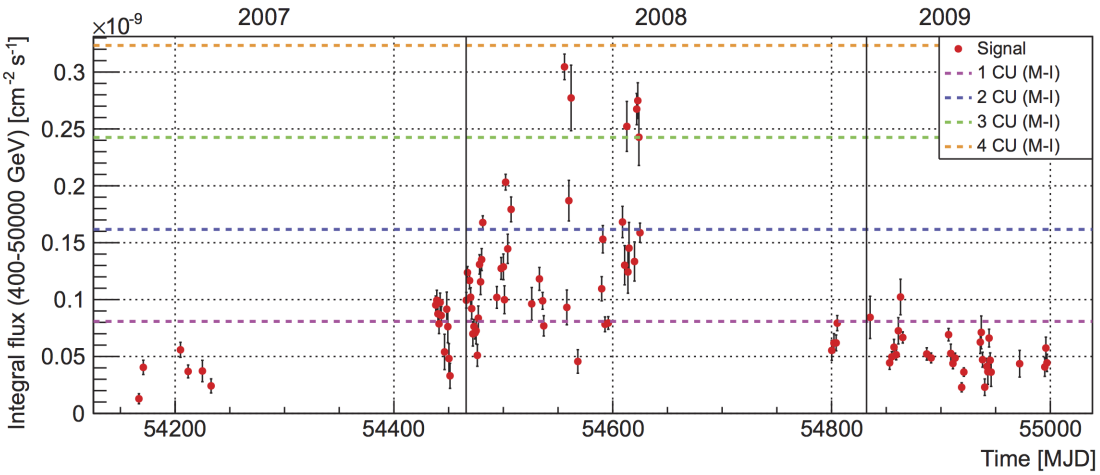

Figure 5.3: Light curve of Mrk 421 between 8th March 2007 (MJD 54166.9) and 15th June 2009 (MJD 54996.9) in the energy range from 400 GeV to 50 TeV. It shows the combined results of the separate light curves from 9° to 30° and from 30° to 45° for daily bins. For an estimation of the flux strength, the flux of the Crab Nebula and multiples of it are plotted as well. The black vertical lines represent the division from one year to the next.

The long-term light curve of Mrk 421 is naturally divided into three parts. Mrk 421 is only observable for about half of the year by Cherenkov telescopes due to astronomical circumstances, which explain the big observation gaps. The light curve exhibits different flux emission "states". Between March 2007 and May 2007 as well as between November 2008 and June 2009 it shows a low emission, whereas between December 2007 and June 2008 Mrk 421 shows a high and strongly variable flux.
The minimal flux value of Mrk 421 was recorded on 8th March 2007 (MJD 54166.9), in a quiet emission state. This flux value is $(1.29 \pm 0.44) \cdot 10^{-11}\,\mathrm{cm}^{-2}\mathrm{s}^{-1}$, which corresponds to 16% of the Crab Nebula. The highest flux is reached during the high emission state on 31st March 2008 (MJD 54555.9). During this night the flux reaches a value of $(3.05 \pm 0.11) \cdot 10^{-10}\,\mathrm{cm}^{-2}\mathrm{s}^{-1}$ corresponding to 3.77 times the flux of the Crab Nebula. This means that the highest flux value of Mrk 421 is about 23.7 times higher than the lowest recorded flux in the whole time range.
To determine an average flux value and to characterise the flux variability, a fit with a constant is done. The result of the constant equals about 0.88 CU. The probability for the fit with a constant flux is 0. This value emphasises the variability that could already be seen in Figure 5.3. The fit results are also noted down in Table A.12.
For further considerations, the three time ranges are examined separately. The constant fit results for these time ranges can be found in Table A.12 as well.

5.4.1 Light curve Mrk 421: March 2007 to May 2007

In Figure 5.4 the light curve between 8th March and 13th May 2007 is shown.

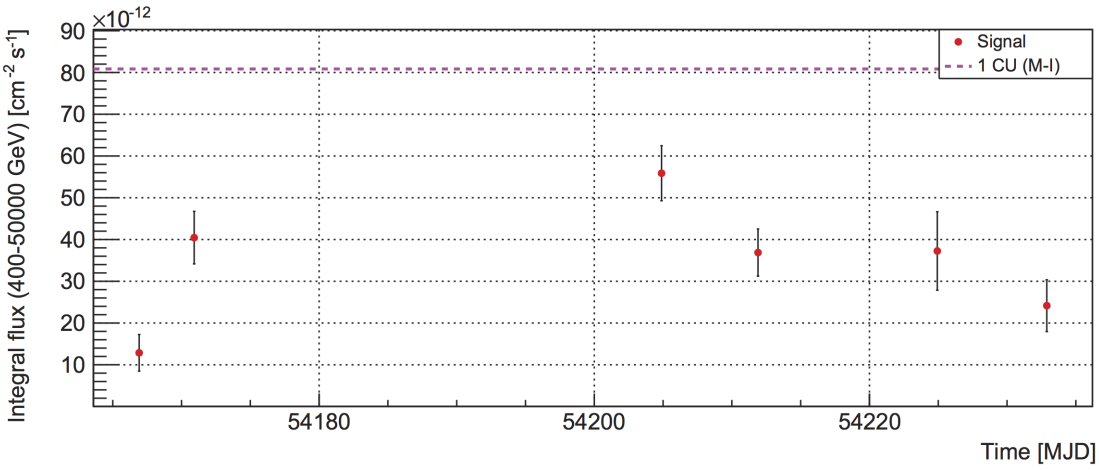

Figure 5.4: Light curve of Mrk 421 between 8th March (MJD 54166.9) and 13th May 2007 (MJD 54232.9) in the energy range from 400 GeV to 50 TeV with daily bins. For an estimation of the flux strength, the flux of the Crab Nebula is plotted as well.

A constant fit to the six flux values results in a flux of about 0.38 CU, which is a low flux value in comparison to the maximum flux value Mrk 421 reached in the whole time range. The constant flux fit results in $\chi^2/ndf = 36/5$ and the constancy hypothesis is

rejected. This can also be seen in the difference between the lowest and highest flux values in this time range. The lowest value is the overall lowest value from 8th March 2007 (MJD 54166.9), which is $(1.29 \pm 0.44) \cdot 10^{-11}\,\mathrm{cm}^{-2}\mathrm{s}^{-1}$. The highest flux in this time range is reached on 15th April 2007 (MJD 54204.9). Therefore, the flux ranges between 0.16 CU and 0.69 CU. This means that the flux is multiplied by a factor of 4.3 in 38 days. Then the flux drops again by a factor of 2.3 in 28 days to 0.30 CU on 13th May 2007 (MJD 54232.9).

5.4.2 Light curve Mrk 421: December 2007 to June 2008

The light curve of Mrk 421 from 4th December 2007 to 8th June 2008 is shown in Figure 5.5. It contains 56 flux points spread over 187 nights.

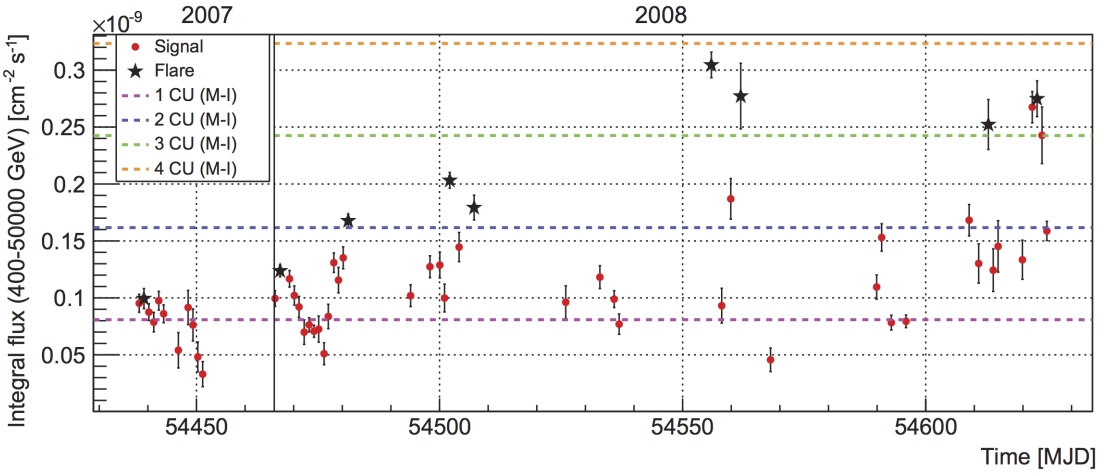

Figure 5.5: Light curve of Mrk 421 between 4th December 2007 (MJD 54438.2) and 8th June 2008 (MJD 54624.9) in the energy range from 400 GeV to 50 TeV with daily bins. For an estimation of the flux strength, the flux of the Crab Nebula and multiples of it are plotted as well. The black vertical line represents the division from year 2007 to 2008. The flares are symbolised by black stars.

In this time range Mrk 421 shows a high flux state with a high variability. A constant fit to the flux points results in an average flux equal to about 1.38 CU. With $\chi^2/ndf = 1485.72/55$ the probability for a constant flux is 0. The flux varies between $(3.30 \pm 1.10) \cdot 10^{-11}\,\mathrm{cm}^{-2}\mathrm{s}^{-1}$ (0.41 CU) on 17th December 2007 (MJD 54451.3) and the overall maximum value of $(3.05 \pm 0.11) \cdot 10^{-10}\,\mathrm{cm}^{-2}\mathrm{s}^{-1}$ (3.77 CU) on 31st March 2008 (MJD 54555.9). Between these values lies a factor of 9.2.
In this time period a total of nine flares takes place. In Figure 5.5 they are marked with black stars. Already in the beginning of the time span, the first flare appears. It takes place on 5th December 2007 (MJD 54439.2) where a flux equal to 1.23 CU is reached. Before the flare only one data point is available which has a slightly lower flux value. It cannot be said how the flux behaved before and if at this date a flare really took place. Afterwards, the flux drops so that with this information a flare is claimed for MJD 54439.2. In the following 12 days the flux drops by a factor of 3.0 to the lowest value in the whole

time period. As mentioned before this minimum is reached on 17th December 2007 (MJD 54451.3) and the flux equals 0.41 CU.
After a natural break because of the full moon, there is another flare with a subsequent drop of flux. On 2nd January 2008 (MJD 54467.2) the flux at the flare is 1.53 CU. It is reduced by a factor of 2.4 in 9 days, so that the flux is at a level of 0.63 CU on 11th January (MJD 54476.3). Directly after this the flux is rising by a factor of 3.3 in the short time interval of 5 days. This third flare on 16th January (MJD 54481.2) is, with a flux of 2.08 CU, the first flux above 2 CU.
After the next full moon break the flux is lower again in comparison to the previous flare. It is then rising again until the fourth flare on 6th February (MJD 54502.1), where a flux of 2.51 CU is given. Then a small drop occurs, but on 11th February (MJD 54507.1) another flare with a flux of 2.21 CU is given before the next full moon break.
The next four data points between MJD 54526.0 and 54536.9 are found at a comparably low and relatively stable level around 1 CU. After the next natural break due to the moon, the sixth flare takes place on 31st March 2008 (MJD 54555.9). As was already said above, this flare has the highest flux value of the whole data analysed and it equals 3.77 CU. Unfortunately, the number of observations is low and it cannot be said if the flux was already higher before or how fast it rose to this high value. Afterwards, the flux quickly drops by a factor of 3.3 to 1.15 CU in only two days. Right after that the flux rises again by a factor of 3.0 to 3.42 CU on 6th April (MJD 54562), which is the seventh flare. Only six days later, on 12th April (MJD 54568.1), the flux went down by a factor of 6.1 onto 0.56 CU. These days represent the highest flux values and also flux variabilities in the whole analysis.
The four data points between MJD 54589.9 and 54596.0 in between two full moons show again a lower flux ranging from about 1 to 2 CU. After the last full moon break, the flux is again more variable and it is never below the average of the whole time period. A flux of 3.12 CU is given on 27th May (MJD 54612.9), the eighth flare. This flux is by a factor 1.9 higher than two days before and a factor of 2.0 higher than one day later.
The ninth and last flare during this time period is observed on 6th June (MJD 54622.9). With a flux of 3.4 CU it lies in a plateau. The flux one day before and one day after are only 3%, resp. 13% lower. But three days before the flare the flux was at a level of 1.65 CU, i.e. it was lower by a factor of 2.0. On 8th June (MJD 54624.9), two days after the flare, the flux drops down by a factor of 1.7.
This time period is the most active of the three periods with the highest flux values and the highest variabilities.

5.4.3 Light curve Mrk 421: November 2008 to June 2009

The light curve between 30th November 2008 and 15th June 2009 can be seen in Figure 5.6. It contains 33 data points during an observation length of 197 nights.
In this time period Mrk 421 is back in a quiet emission state. A constant fit results in a flux of about 0.61 CU. There is again a probability of 0 for a constant flux with $\chi^2/ndf = 160/32$ for the fit. The flux values vary between a minimum of $(2.29 \pm 0.40) \cdot 10^{-11}\,\mathrm{cm}^{-2}\mathrm{s}^{-1}$ (0.28 CU) on 29th March 2009 (MJD 54919) and the 4.5 times larger maximum flux of $(1.02 \pm 0.16) \cdot 10^{-10}\,\mathrm{cm}^{-2}\mathrm{s}^{-1}$ (1.26 CU) on 1st February 2009 (MJD 54863.1).

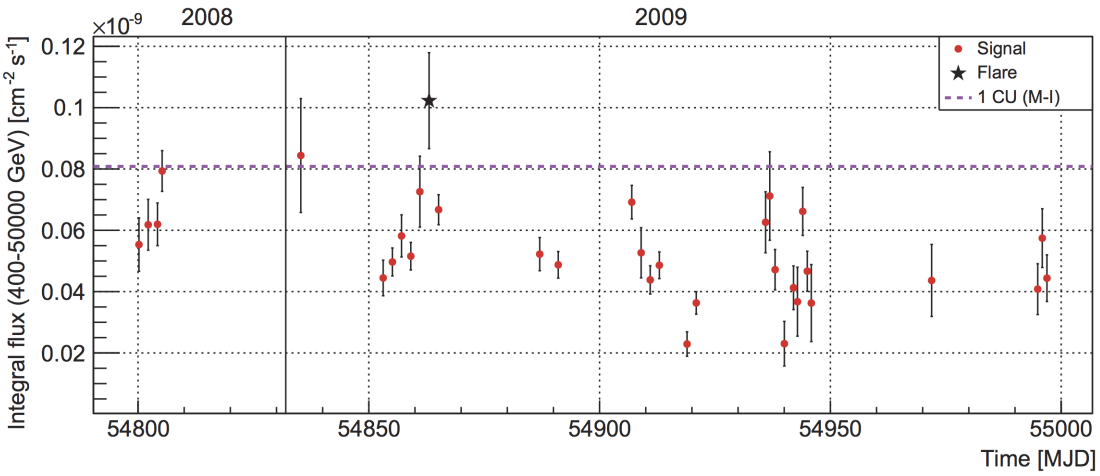

Figure 5.6: Light curve of Mrk 421 between 30th November 2008 (MJD 54800.2) and 15th June 2009 (MJD 54996.9) in the energy range from 400 GeV to 50 TeV with daily bins. For an estimation of the flux strength, the flux of the Crab Nebula is plotted as well. The black vertical line represents the division from year 2008 to 2009. The flare is symbolised by a black star.

Although this flux is small in comparison to the flares in the time period before, this maximum on MJD 54863.1 is claimed to be a flare. It is marked with a black star in Figure 5.6. With a flux of 1.26 CU, it is more than twice the average flux during this time period. In addition to that, the flux is rising from 22nd January (MJD 54853.1) from 0.55 CU by a factor of 2.3 in the 10 days until MJD 54863.1, the day of the flare. Two days after the flare the flux is again smaller by a factor of 1.5, now equal to a flux of 0.83 CU.

5.5 Light curve in different energy ranges

To investigate if the flux variations behave differently for different energies, the light curve is determined for three energy ranges in *fluxlc*. They are namely

- the low energy (le) range from 400 GeV to 600 GeV,
- the medium energy (me) range from 600 GeV to 1 TeV,
- and the high energy (he) range from 1 TeV to 50 TeV.

These names are arbitrarily given only in the context of this analysis. The term "whole energy range" stands for the energy range from 400 GeV to 50 TeV, for which the light curve from the previous section 5.4 was determined.
All of the following data points contain at least 10 excess events and have a significance larger than $3\,\sigma$. To directly compare all flux points of the different energy ranges, the flux is normalised to the flux of the Crab Nebula in the corresponding energy range. The resulting light curves for the low energy (red), the medium energy (green) and the high

energy (blue) are shown in Figure 5.7 to Figure 5.9. All results of a constant fit to the different light curves can be found in Table A.13.

Figure 5.7 shows the light curves from March to May 2007 for the three different energy ranges.

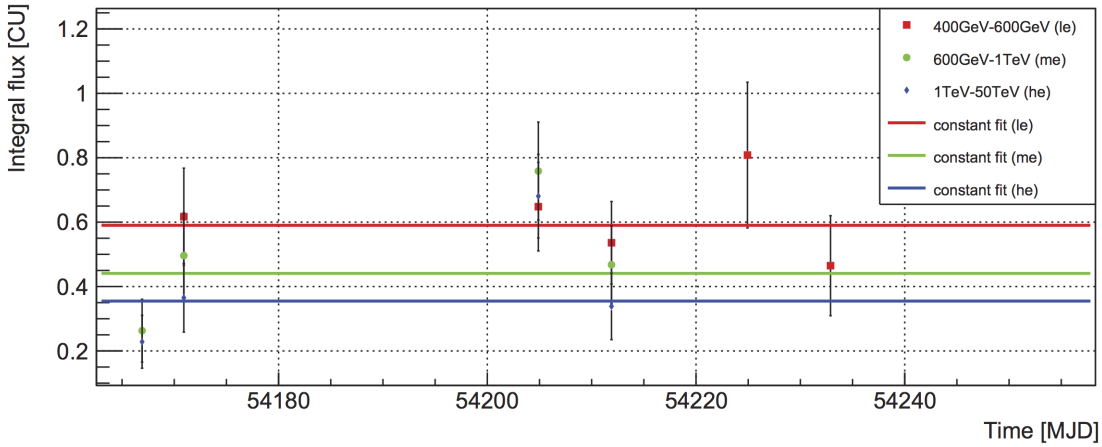

Figure 5.7: Light curve of Mrk 421 between 8th March (MJD 54166.9) and 13th May 2007 (MJD 54232.9) for the different energy ranges with daily bins. Each flux point is normalised to the Crab Nebula flux in its energy range.

This time period contains only 5 flux points for the low energy range and 4 for the medium and high energy range. Nevertheless, first cautious conclusions are drawn from the light curves. The flux is highest for the low energy range and it is compatible with being constant. The χ^2/ndf increases and the flux in CU decreases with increasing energy (see Table A.13). For the four flux points, where a comparison between the medium and high energy flux points is possible, the flux in the medium energy range is higher than in the high energy range. This gives the impression that the spectrum of Mrk 421 is steeper than the spectrum of the Crab Nebula.
For a comparison of the medium and high energy to the low energy, only three flux points are available. For two of these points, the low energy point has a greater flux than the other points. This supports the statement made before of the steeper spectrum of Mrk 421. But for the flux point with the highest flux in the light curve for the whole energy range, which is on 15th April 2007 (MJD 54204.9), the flux of the low energy range is a little bit lower than the other two points, but still within the error estimation.

The light curves for the three different energy ranges from December 2007 to June 2008 are shown in Figure 5.8.
The result of the constant fit to the low and medium energy range flux points are at about the same flux level. For the high energy range this value is again lower. All light curves are variable, but χ^2/ndf is, as before, increasing with increasing energy (see Table A.13). This means that the variations are larger for higher energies.

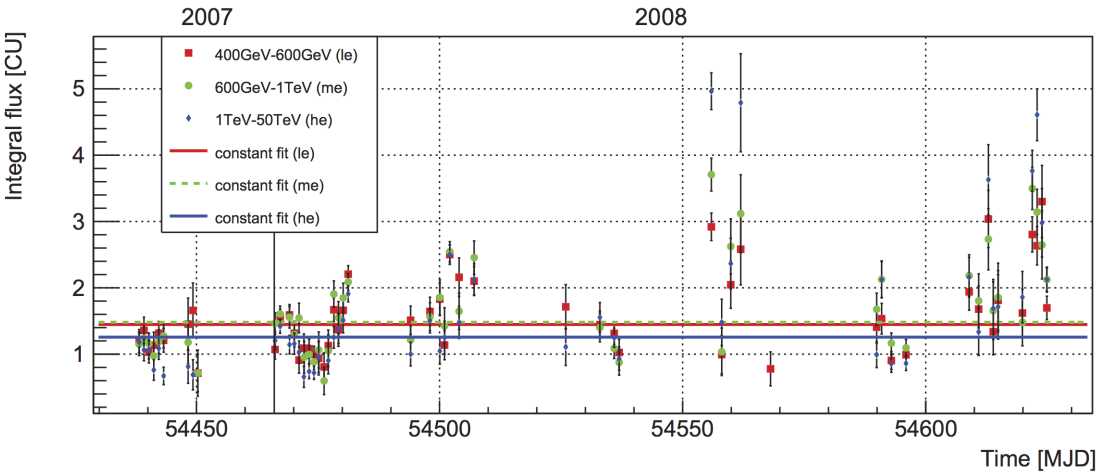

Figure 5.8: Light curve of Mrk 421 between 4th December 2007 (MJD 54438.2) and 8th June 2008 (MJD 54624.9) for the different energy ranges with daily bins. Each flux point is normalised to the Crab Nebula flux in its energy range. The black vertical line represents the division from year 2007 to 2008.

For most of the nights between 4th December 2007 (MJD 54438.2) and 12th March 2008 (MJD 54536.9), the flux in the high energy range is the lowest. The medium flux is higher and the low energy flux has the highest value. But it can be seen that mostly for the flare days another behaviour is present. As an example, on 4th December 2007 (MJD 54438.2), which is one day before the first flare, the fluxes of all three energy ranges are at the same level. This is also true for the flares on 2nd January 2008 (MJD 54467.2), 6th February (MJD 54502.1) and 11th February (MJD 54507.1).
The days including the overall highest flux and highest variability, which are the days from 31st March (MJD 54555.9) to 6th April (MJD 54562), shall be discussed now. For the two flares during this time, the high energy range has the highest flux with a value of almost 5 CU. The flux of the medium energy range lies below and the low energy flux is the lowest, which is approximately 2.5 CU and 3 CU on the two different flare days. On the two days between the flares, the differences between the fluxes of the three energy ranges are smaller. The flux of the low energy range remains the one with the smallest flux.
For the highly variable flux points between 4th May (MJD 54589.9) and 8th June (MJD 54624.9) it can be seen that for the nights with a lower flux in the whole energy range the high energy flux is below the value of the low energy range. On the flare days 27th May (MJD 54612.9) and 6th June (MJD 54622.9) however, the flux is again highest for the high energy range. It is lower for the medium energies and lowest for the low energy range, as it was observed before for the other flare days.

For the last time period from November 2008 to June 2009, the three light curves can be seen in Figure 5.9.
During this more quiet time period of the light curve, it is again given that the flux of the high energy range is the lowest of all. This time the medium energy range has a slightly

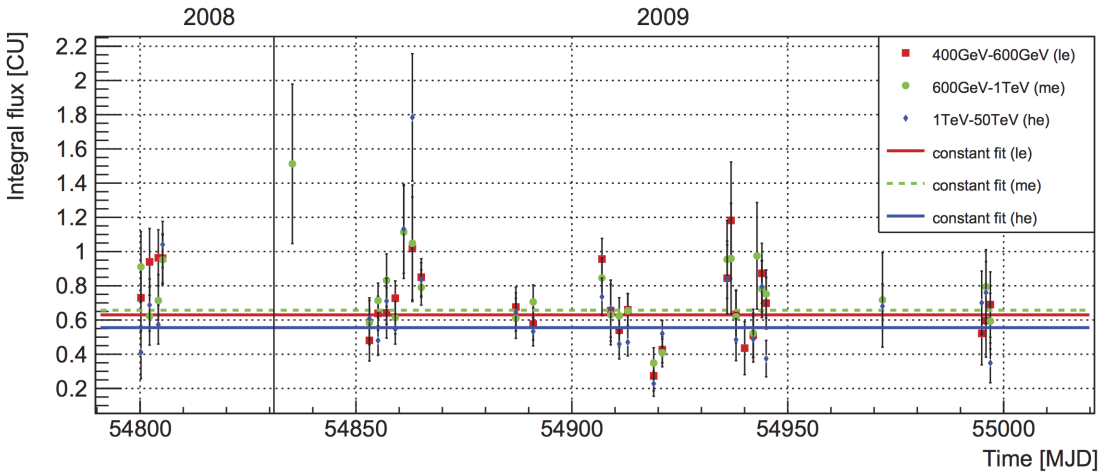

Figure 5.9: Light curve of Mrk 421 between 30th November 2008 (MJD 54800.2) and 15th June 2009 (MJD 54996.9) for the different energy ranges with daily bins. Each flux point is normalised to the Crab Nebula flux in its energy range. The black vertical line represents the division from year 2008 to 2009.

higher flux than the low energy range. The highest χ^2/ndf for a constant fit is again present for the high energy range, it is lowest for the light curve with the highest flux, the medium energy range light curve (see Table A.13).
It can be seen that the high energy flux mostly lies below the medium and low energy range fluxes. For the flare day 1st February 2009 (MJD 54863.1), the same behaviour as during the previous flares is seen. The flux is highest for the high energy range.

For the days when the high energy flux is the lowest flux and the low energy flux is the highest, the spectrum of Mrk 421 should be steeper than the spectrum of the Crab Nebula. For days when the fluxes are at the same level, both spectra should have the same slope. For the days when the high energy flux is the highest in comparison to the other two energy ranges, the spectrum of Mrk 421 should be flatter than the one of the Crab Nebula.
The relation between the steepness of the spectra and the height of the flux level will be discussed in section 5.7.

5.5.1 Flux ratios

To investigate if there exists a relation between the different energy ranges, their ratios $\frac{\text{flux}_{\text{he}}}{\text{flux}_{\text{me}}}$, $\frac{\text{flux}_{\text{he}}}{\text{flux}_{\text{le}}}$ and $\frac{\text{flux}_{\text{me}}}{\text{flux}_{\text{le}}}$ are calculated. The fluxes are not normalised by the flux of the Crab Nebula in this case. The ratios are only available when the fluxes in the given energy ranges are significant, i.e. a flux point needs more than 10 excess events and more than $3\,\sigma$ (see Figure 5.7 to Figure 5.9 for the significant days). The ratios are plotted versus the MJD. In the following Figure 5.10, the light curve in the whole energy range from 400 GeV to 50 TeV and all three ratio plots are shown. This light curve is given here to be able to have a direct comparison of the ratios to the overall flux level of that night.

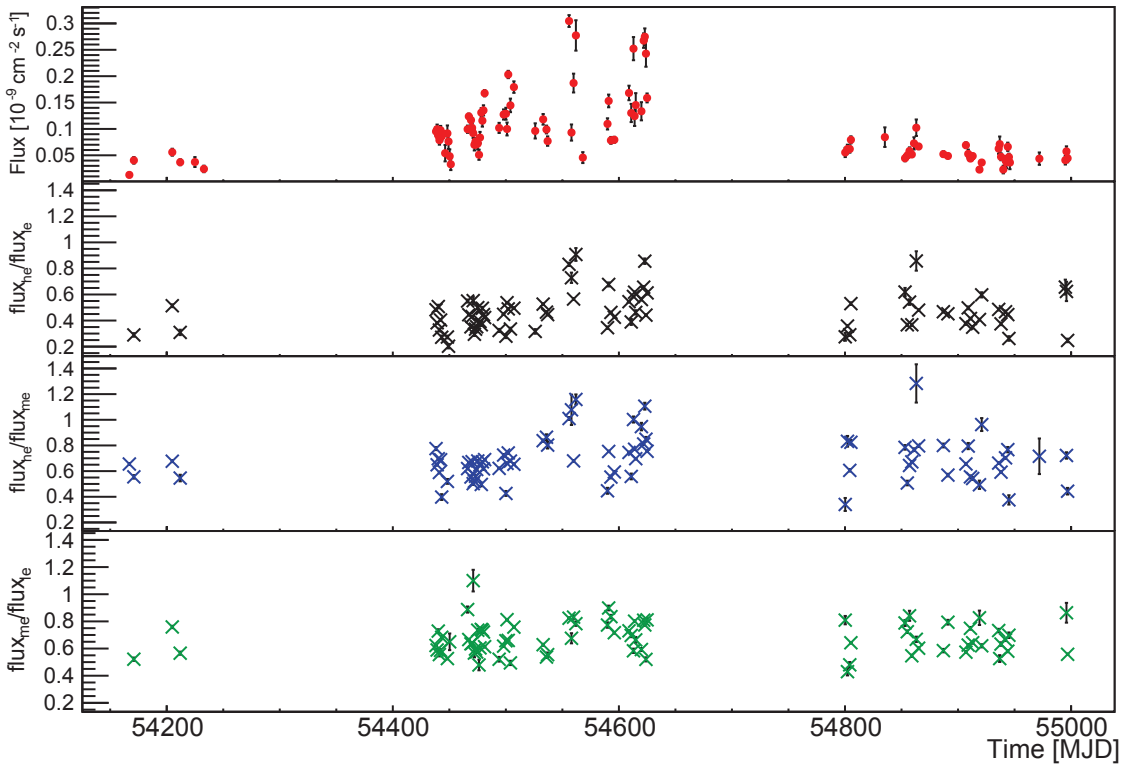

Figure 5.10: Ratios of the fluxes in the three different energy ranges from March 2007 to June 2009. In the uppermost plot the normal light curve from Figure 5.3 is shown so that the integral flux from 400 GeV to 50 TeV for every observation is on hand. In the second plot the ratios of the high energy range flux to the low energy range flux is shown. In the third plot the ratios of the high to the medium energy range flux can be seen. The ratios of the medium to the low energy range flux are shown in the plot at the bottom.

In the second plot from the top in Figure 5.10 the ratios of the significant flux points of the high energy range flux to the low energy range flux are shown as black crosses. For nights with a low overall flux in the whole energy range from 400 GeV to 50 TeV, the ratio is low. When the flux takes on a higher value, the ratio is rising. This can be seen in particular for e.g. the two flare nights on 31st March (MJD 54555.9) and 6th April 2008 (MJD 54562), the flare on 6th June 2008 (MJD 54622.9), and the last flare on 1st February 2009 (MJD 54863.1). There is a factor of about 4.5 between the highest and lowest ratio.
The ratios of the significant flux points of the high to the medium energy range flux points can be seen as blue crosses in the third plot of Figure 5.10. Here, the same behaviour as described above for the ratios of the high to the low energy range flux is present. In the case that the flux has a low value in the overall light curve, the ratio of the high to the medium energy range flux is low as well. The ratio is rising for higher overall fluxes. This means, that for the above mentioned flare days and an additional flare on 27th May (MJD 54612.9) the ratio takes on the highest values. Here, the factor between the highest and lowest ratio amounts to about 3.8.

For the ratios between the medium and low energy range flux, which can be seen in the fourth plot in Figure 5.10, the same behaviour is present, but it is not as pronounced as for the other two ratios. This can also be seen in the factor of about 2.6 between the highest and lowest ratio.
From all these statements, several conclusions are drawn. The ratios of the high to medium energy range fluxes changes the most with changing overall flux. The smaller the distances between the energy ranges, for which the ratios have been determined, the smaller this effect becomes with changing flux. This means that the high energy range flux is the most variable of the three energy ranges because it changes the most with changing overall flux. In addition, it can be concluded that spectra get harder when the source is brighter. This means that spectra on nights with a high flux are flatter, and consequently have proportionally more high energy photons, than spectra on low flux nights. This confirms the conclusions that have been drawn before when the light curves in the three different energy ranges were discussed.

5.6 Flux variations on short time scales

Besides the examination of flux variations on a nightly basis, this study can be extended to the search for variations on shorter time scales. Results from this study can be useful to quantify the short-term variability time scale of a light curve and subsequently draw conclusions about the emission region, see Equation 2.7. Therefore, the nightly light curves are examined for variability and flare models are fitted to candidate flare nights.
In earlier studies doubling or halving times for the flux have been found in the order of 15 [Gai96] or even as low as 10 minutes [Sch08, Bol13] for Mrk 421. To be able to resolve flux changes on these short time scales the time bin width has to be smaller than 10 minutes. In order to ensure flux points with enough excess events and a high significance, the time bin width is set to 5 minutes.

Variability
Candidate nights for the short-term study have to fulfil several criteria. First of all, a constant is fitted to the signal as well as the background data points of each daily light curve to quantify their variability. It is then necessary that the probability for a constant fit is smaller for the signal than for the background data points to be a candidate night. A high variability in the background could indicate changes in the observation conditions. Additionally, it is decided that a candidate for short-term variability is given when the fit probability for a constant flux is smaller than 25%. Lastly, a night should at least contain 5 data points to be considered.
All nights fulfilling these criteria are listed in Table 5.3. The other nights are expected to have a stable flux for the duration of the observation.
The table contains the χ^2/ndf and the probability for a constant fit for each selected night. From these values it can be concluded that the flux during the selected nights is not stable. The last column of the table gives the factor between the highest flux value flux_{max} and the lowest flux value flux_{min} during one night. This factor lies between 1.7 and 3.8. This change in flux happens within 30 minutes or less for the given light curves. In Figure 5.11 the short-term light curve of 31st March 2008 is shown. It is the night with

Table 5.3: Observation length and constant fit results of the short-term light curves of Mrk 421 for the selected nights. The factor between the lowest and highest flux is given as well.

Date	**MJD**	**Obs. length [h]**	χ^2/ndf	**Probability**	$\frac{\textbf{flux}_{\textbf{max}}}{\textbf{flux}_{\textbf{min}}}$
2008-02-02	54498.0	0.65	15.10/7	0.0348	2.6
2008-02-04	54500.1	0.59	10.18/6	0.1173	2.4
2008-02-05	54501.0	0.65	9.19/7	0.2392	2.4
2008-02-08	54504.0	0.39	14.41/4	0.0061	2.9
2008-02-11	54507.1	0.83	30.50/9	0.0004	3.4
2008-03-12	54536.9	1.03	15.29/11	0.1695	3.8
2008-03-31	54555.9	1.99	31.87/23	0.1028	1.7
2008-04-04	54559.9	0.59	16.23/6	0.0126	2.3
2008-05-04	54589.9	0.61	12.14/6	0.0588	2.5
2008-05-05	54590.9	1.04	14.96/12	0.2435	2.3
2009-01-30	54861.1	0.39	6.08/4	0.1936	3.5

the highest overall flux. The light curve spans over 2 hours of observations. Obviously, the flux is not stable during this night. In the beginning there is a small rise of flux. Then there is a second rise with a subsequent fall. Afterwards, the flux fluctuates around the constant fit.

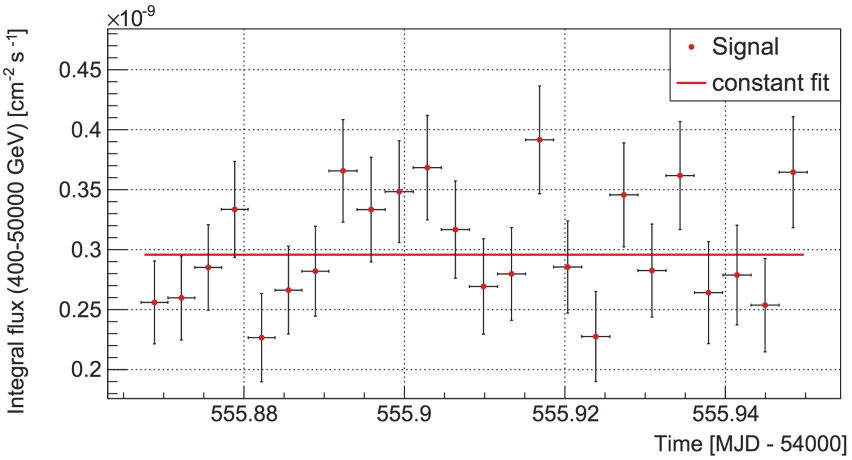

Figure 5.11: Short-term light curve with 5 minute bins of 31st March 2008 (MJD 54555.9) with a constant fit to the data points.

As further examples of light curves, three light curves with a constant fit are added in section A.8. The exemplary nights are namely 2nd February 2008 (see Figure A.1), 12th March 2008 (see Figure A.2), and 5th May 2008 (see Figure A.3). All three light curves show the variability of the flux.

On 2nd February the flux slowly drops by a factor of 2.6 to the minimum in 30 minutes, whereby one fluctuation is included in this drop. After the minimum the flux rises again by a factor of 2.0 in 10 minutes. The flux of the first 15 minutes on 12th March is at one level. The flux is at the half of the former flux level for the following 15 minutes. Then the flux rises to its maximum in about 10 minutes. Afterwards, it is back at a lower level and it is stable for the last 20 minutes. On 5th May the light curve has two breaks of about 75 and 45 minutes. In the middle part a large variation in flux is seen, whereas the flux during the last 40 minutes is relatively stable.
All selected 11 nights show a short-term variability of the flux. The largest factor between the highest and lowest flux during one night is 3.8.

Flare analysis
To quantify the time scale of the short-term variability t_{var} the characteristic rise and fall time of flares needs to be determined. It is defined as the time in which the flux changes by a factor of e [Alb07b]. As flare model an exponential rise and fall on top of a flux baseline is assumed. This exponential behaviour can be explained with the SSC emission scenario, in which the γ-rays are produced via IC scattering of electrons. Shock fronts inside the jet accelerate the electrons. Their energy gain increases exponentially after a shock front has built up. The exponential decrease after the flare describes that the electrons are not further accelerated. The cooling of the electrons via Synchrotron radiation or IC scattering starts to dominate. [Sch08]
The first model (model 1) that can be fitted to a flare was proposed in [Sch08] and is given by:

$$F(t) = b + \frac{a}{e^{-(t-t_0)/\tau_{\text{rise}}} + e^{(t-t_0)/\tau_{\text{fall}}}}\,, \tag{5.1}$$

whereas b is the baseline flux before the flare and a is the amplitude of the flare. The position of the peak is at t_0. The characteristic rise and fall time are given by τ_{rise} and τ_{fall}. Another possibility is to simply fit an exponential rise to the data before the flare and an exponential fall after it. The fit functions of this second model (model 2) are the following:

$$F_{\text{rise}}(t) = b_{\text{rise}} + a_{\text{rise}} \cdot e^{(t-t_0)/\tau_{\text{rise}}} \quad \text{(for a rising edge)} \tag{5.2}$$
$$F_{\text{fall}}(t) = b_{\text{fall}} + a_{\text{fall}} \cdot e^{-(t-t_0)/\tau_{\text{fall}}} \quad \text{(for a falling edge)} \tag{5.3}$$

As both fits describe the same flare the baseline b and the flare amplitude a are the same value for both fits.

Two of the above mentioned nights show a flare in their short-term light curve, namely 12th and 31st March 2008. Both flare models are fitted to the data points. The peak position is fixed to the position of the highest flux during the recognisable flare structure in each case.
The resulting flare fits are shown in Figure 5.12 for 12th March 2008 and in Figure 5.13 for 31st March 2008. The resulting rise and fall times of the flare fits with model 1 and 2 are summarised in Table 5.4.

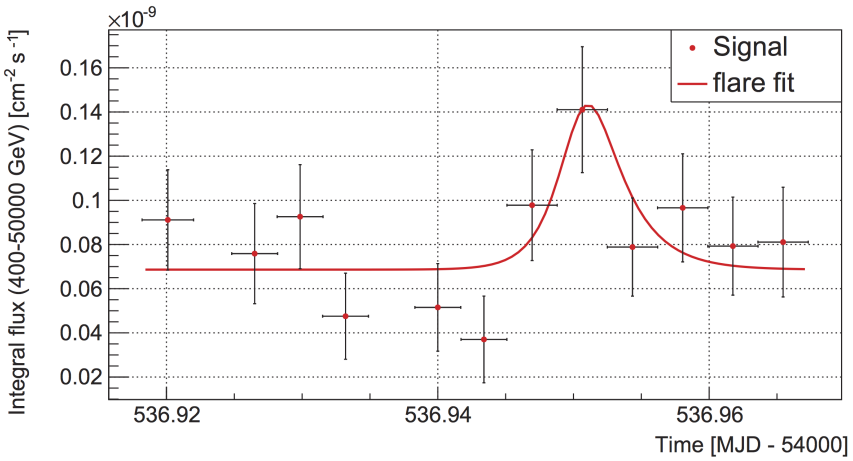

(a) Flare fitted with model 1.

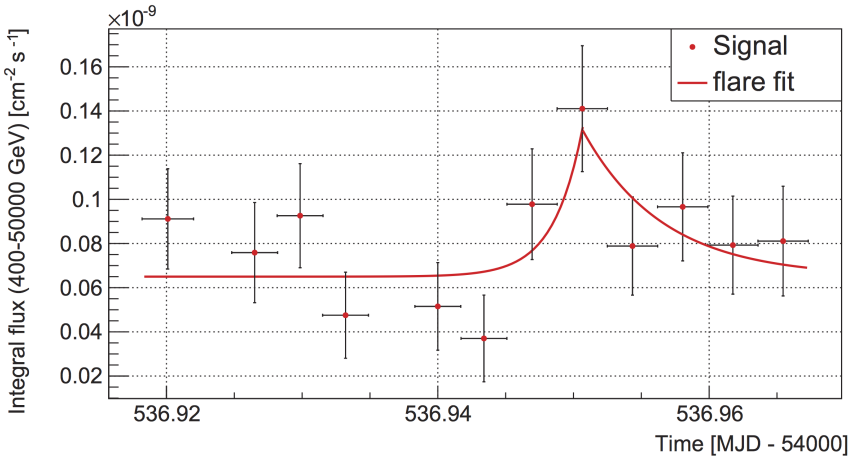

(b) Flare fitted with model 2.

Figure 5.12: Short-term light curve with 5 minute bins of 12th March 2008 (MJD 54536.9) with two different fits of flare models to the data points.

The short-term light curve of 12th March was fitted with a constant (see Figure A.2) and two flare models (see panel (a) and (b) of Figure 5.12). The constant fit results in a low fit probability of about 0.17.
The flare fit with model 1 describes the data points better than the constant fit because it has a fit probability of about 0.47. The first 30 minutes of the light curve describe the baseline. Then a short rise to the maximum takes place, which is then followed by a short fall back to the baseline. The resulting rise and flare time for this model are about 2.3 and 3.6 minutes.
Model 2 describes the rising and falling edge of the flare well. The rising edge has a fit probability of about 0.41 and the falling edge of about 0.73. They describe the data points better than a constant fit. The corresponding rise and fall times are 3.1 and 8.5 minutes,

respectively.

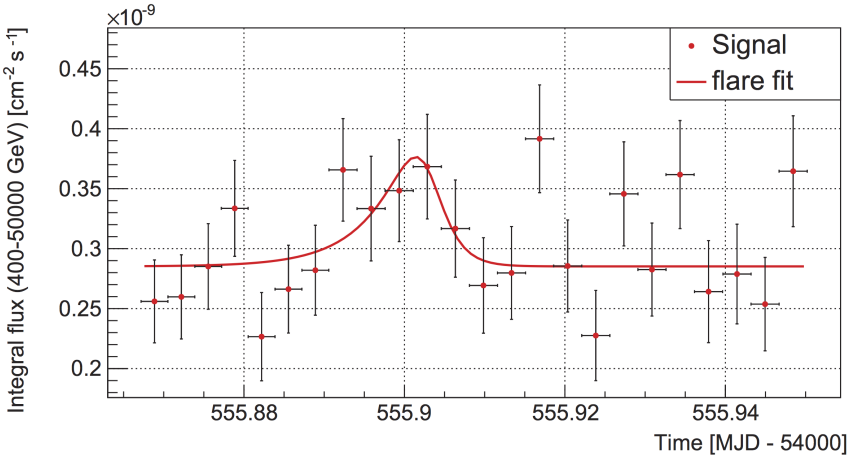

(a) Flare fitted with model 1.

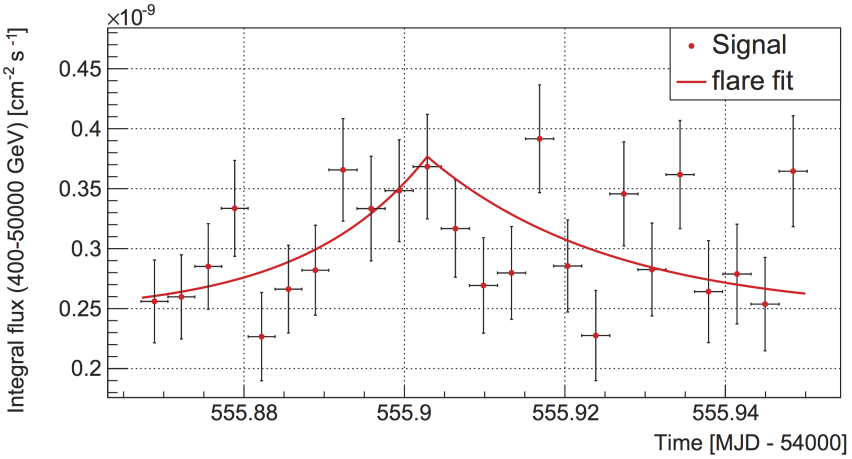

(b) Flare fitted with model 2.

Figure 5.13: Short-term light curve with 5 minute bins of 31st March 2008 (MJD 54555.9) with two different fits of flare models to the data points.

The constant fit to the short-term light curve of 31st March 2008 has a low fit probability of about 0.10 (see Figure 5.11). The flare fit model 1 describes the data points slightly better with a fit probability of about 0.20 (see panel (a) of Figure 5.13). The baseline before the flare is not a stable baseline, but it contains a second, small rising edge which cannot be described by the flare model. The flare itself is modelled well. However, the data points after the flare are fluctuating around the assumed baseline. With this model the characteristic rise and fall times are 7.7 and 2.9 minutes.
The flare fit with model 2 is able to describe the rising edge well with a fit probability of about 0.67 (see panel (b) of Figure 5.13). However, it can again be seen that the falling

edge cannot be modelled well. The fit probability is only 0.05. No model can explain the strongly fluctuating points after the flare. This model yields towards a rise time of 22 minutes. The resulting fall time is 33 minutes.

Table 5.4: Flare fit results for short-term light curves of Mrk 421 on 12th and 31st March 2008.

Date	**Flare fit**	χ^2/ndf	**Probability**	$\tau_{\mathbf{rise}}$ **[min]**	$\tau_{\mathbf{fall}}$ **[min]**
	model 1	8.70/9	0.4658	2.33 ± 1.28	3.62 ± 3.19
2008-03-12	model 2 (rise)	7.20/7	0.4085	3.09 ± 2.11	
	model 2 (fall)	1.30/3	0.7286		8.51 ± 7.04
	model 1	24.94/20	0.2038	7.69 ± 4.00	2.87 ± 2.69
2008-03-31	model 2 (rise)	6.72/9	0.6656	22.45 ± 9.08	
	model 2 (fall)	22.29/13	0.0510		33.00 ± 10.83

Results on short-term variability

The study on the variability in short-term light curves of Mrk 421 has shown that there are nights with a stable flux and nights with a variable flux. Flux doubling or halving has been seen on time scales smaller than 30 minutes for the days with variable flux.

For two days it was possible to fit two different models of an exponential rise and fall around a flare. The two models gave different results for the characteristic rise and fall times. They range between 2.3 and 33 minutes. These times correspond to doubling or halving times in the range from 1.6 to 22.9 minutes. Nonetheless, it could be shown that there exists variability on short time scales in the order of the characteristic time of 10 minutes, as discussed in [Sch08].

Taking Equation 2.7 into consideration an estimation of the size of the emission region can be given. In [Abd11] two different Doppler factors δ for the SSC emission model are given. They are 21 and 50, respectively, for two models with different characteristic time scales. For a first estimation of the size of the source region, the size is determined for both Doppler factors and the smallest and largest time scales t_{var} of 2.3 and 33 minutes. The resulting radius of the emission region ranges from $R \leq \frac{ct_{\mathrm{var}}\delta}{1+z} = 8.4 \cdot 10^{11}\,\mathrm{m}$ for $\delta = 21$ and t_{var}=2.3 minutes to $R \leq 2.88 \cdot 10^{13}\,\mathrm{m}$ for $\delta = 50$ and t_{var}=33 minutes.

In order to be able to compare this size to the size of the SMBH of Mrk 421, its Schwarzschild radius R_{Sch} [Beh12] is calculated. With a mass of $10^{8.23} M\odot$ [Wu 09] the radius of the BH is $R_{\mathrm{Sch}} \approx 5 \cdot 10^{11}\,\mathrm{m}$.

From this it might be concluded that the emission region inside the jet is larger than the BH. It needs to be mentioned that this result strongly depends on the minimum variability time scale t_{var} as well as the Doppler factor δ that are chosen. Here, two sets of possible values were used to get a first estimate. Additionally, it is possible that more than one emission region is responsible for variability on different time scales.

5.7 Spectrum

For the unfolding of the spectra produced in *fluxlc*, the standard unfolding tool in MAGIC mono analysis *CombUnfold* is used. It was introduced in section 4.8. The spectra from the different time periods, namely from March to May 2007, from December 2007 to June 2008, and from November 2008 to June 2009, are determined separately. This is because the spectrum is expected to appear differently in different flux states, as it was discussed in section 5.5. The spectrum results are combined results from the zenith ranges below and above 30°.
First of all, it needs to be mentioned that the unfolding was tested with all available regularisation methods available in *CombUnfold*. All of these show comparable results. In the following, the regularisation method of Tikhonov as explained in [Alb07a] is used, as it has delivered robust results with higher fit probabilities in comparison to the other methods in this analysis. Additionally, several functions are used for a correlated fit to the spectral points. Three of these will be explained in the following. Lastly, the effect of the EBL on the spectrum is corrected. The difference of an unfolded spectrum with and without correction will be shown afterwards.
After these explanations, the unfolding results for the three time periods will be presented. Because the relation of the overall flux state of the source to its spectrum is studied as well, the unfolding results of the daily spectra are discussed.

5.7.1 Tested functions for the fit

The fit functions, which are assumed for the sought-after resulting spectrum, are based on a power law (PL). A simple power law, a power law with a cut-off and a power law with variable slope are tested in this analysis. They are specified as follows:

PL:
$$\frac{dF}{dE} = f_0 \cdot \left(\frac{E}{r}\right)^{\alpha}$$

PL with a cut-off:
$$\frac{dF}{dE} = f_0 \cdot \left(\frac{E}{r}\right)^{\alpha} \cdot e^{-E/E_0}$$

PL with variable slope:
$$\frac{dF}{dE} = f_0 \cdot \left(\frac{E}{r}\right)^{\alpha + b \cdot \log_{10}(E/r)}$$

Here, r stands for the energy at which the flux normalisation f_0 is given and it is fixed to 0.4 TeV in this analysis. E_0 is the cut-off energy and b describes the strength of the curvature in the case of a variable slope.
For all three time periods, unfolding with Tikhonov regularisation is applied with the three functions above. The power law with variable slope describes all spectra best. This can be seen in Table 5.5, where the highest fit probability is given for this function for all three time periods. The complete listing of the results with all fit parameters can be found in Table A.15.

Table 5.5: χ^2/ndf and fit probability for the correlated fit of the unfolded spectra of the three time periods from March to May 2007, from December 2007 to June 2008, and from November 2008 to June 2009. For the resulting fit parameters, please see Table A.15.

Time period	Function	χ^2/ndf	Prob.
March to May 2007	PL	1.22/2	0.5445
	PL with cut-off	0.11/1	0.7451
	PL with variable slope	0.04/1	0.8470
December 2007 to June 2008	PL	1029.64/7	0.0000
	PL with cut-off	113.82/6	0.0000
	PL with variable slope	28.73/6	0.0001
November 2008 to June 2009	PL	53.64/5	0.0000
	PL with cut-off	11.54/4	0.0211
	PL with variable slope	3.31/4	0.5069

5.7.2 EBL correction

For the correction of the EBL influence on the spectral appearance, the model of Franceschini [Fra08] is applied. Because of the - in astronomical size scales - relatively small distance of Mrk 421 to the Earth, the effect of the EBL is moderate, but still visible. The effect is increasing both for higher energies and for sources farther away.
In Figure 5.14 the comparison of spectra, once with and once without EBL correction, is shown. In order to see the structures inside the spectra better, this spectrum and all of the following spectra are multiplied by E^2. To be able to assess the appearance of the spectrum of Mrk 421, the spectrum of the Crab Nebula [Alb08b] is plotted in addition.
Here, the unfolded spectrum of the Mrk 421 data, which were taken from November 2008 to June 2009, is shown. This time period is chosen because it features a relatively low and stable flux level over a long time period. Under the assumption that the flux level has an effect on the shape of the spectrum, this stable flux level assures a stable shape of the spectrum for the whole time period. The long observation time assures a large amount of data and a spectrum with significant data points over a wide energy range. For the unfolding the Tikhonov regularisation and for the fit function the power law with variable slope are chosen.
In blue the unfolded spectrum without EBL correction is shown. After applying the EBL correction, the red spectrum results. It can be seen, that the corrected spectrum lies higher than the spectrum without correction. The flux normalisation f_0 at 0.4 TeV is rising from $f_0 = (2.12 \pm 0.06) \cdot 10^{-10}\text{cm}^{-2}\text{s}^{-1}\text{TeV}^{-1}$ for the not corrected spectrum to $f_0 = (2.37 \pm 0.06) \cdot 10^{-10}\text{cm}^{-2}\text{s}^{-1}\text{TeV}^{-1}$ when it is corrected for the EBL influence. As was explained before, the influence of the EBL is higher for higher energies. This can be seen in the slope α of the fit results before and after the correction. Without correction the absolute value of the slope is $\alpha = -2.27 \pm 0.06$. After the correction it is $\alpha = -2.09 \pm 0.06$, which describes a flatter spectrum than without correction. The curvature stays within the error estimation.

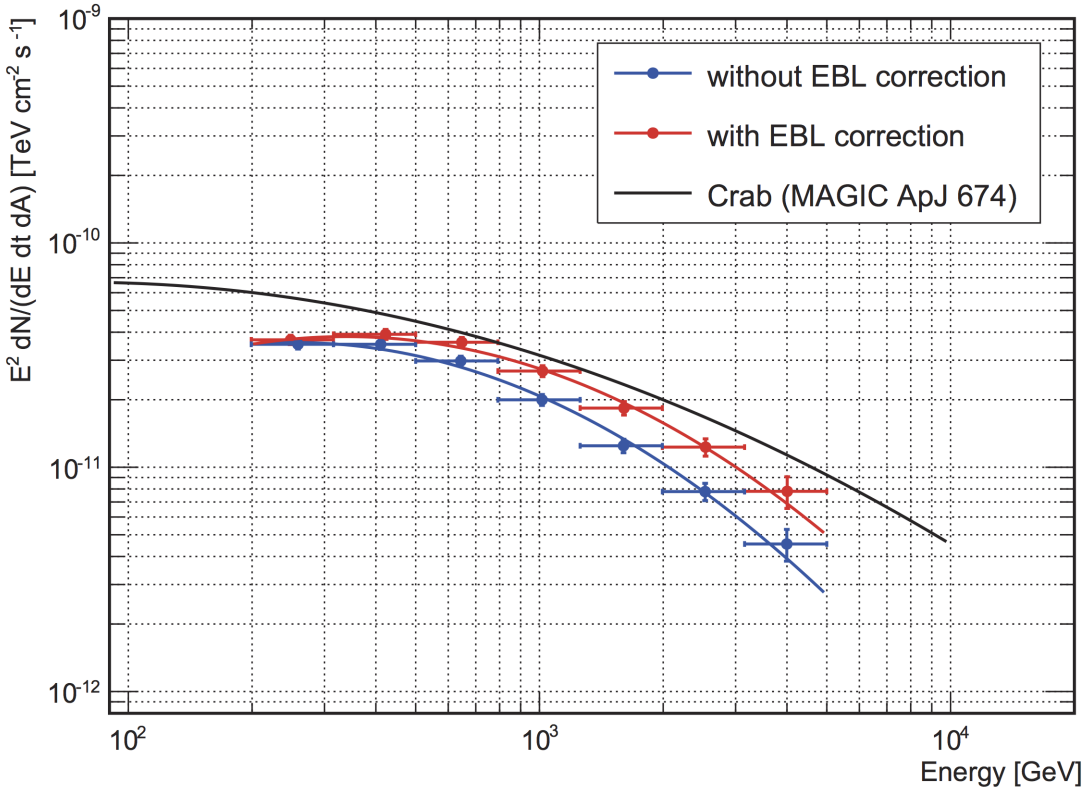

Figure 5.14: Effect of the EBL correction on the unfolded spectrum. In blue the unfolded spectrum without EBL correction is shown. The EBL corrected spectrum is given in red. The black solid line represents the spectrum of the Crab Nebula.

All following spectra are corrected for the influence of the EBL.

5.7.3 Results of unfolded spectra

The unfolding is applied for the three different time periods, which have already been introduced. This separation is carried out to study the possible influence of the flux state on the spectral shape. The first time period from March to May 2007 has an average flux of about 0.4 CU. The second time period spans from December 2007 to June 2008, when the average flux was high with a value of about 1.4 CU. The third time period is the one with the low flux level of about 0.6 CU from November 2008 to June 2009. The results of the correlated fit to the unfolded spectral points are summarised in Table 5.6.
The resulting spectra are plotted in Figure 5.15. The spectrum corresponding to the data from March to May 2007 is shown in blue. It is the data set with the lowest flux and the shortest observation time, which is why it is spread over the shortest energy range. The spectrum lies well below the spectrum of the Crab Nebula. Of the three spectra of Mrk 421, this spectrum is the lowest, which is also reflected in the lowest value of f_0. The slope α has the largest absolute value. It is therefore the steepest spectrum.

Table 5.6: Fit results of the correlated fit of the unfolded spectra for the three time periods from March to May 2007, from December 2007 to June 2008, and from November 2008 to June 2009. The power law with variable slope is used as the fit function. The flux normalisation f_0, the slope α, and the curvature strength b are noted down.

Time period	$f_0 \left[\frac{10^{-10}}{\mathrm{cm^2 sTeV}}\right]$	α	b
March to May 2007	1.39 ± 0.19	-2.47 ± 0.24	-0.91 ± 1.01
December 2007 to June 2008	5.29 ± 0.03	-1.97 ± 0.01	-0.63 ± 0.03
November 2008 to June 2009	2.37 ± 0.07	-2.09 ± 0.06	-0.65 ± 0.11

The spectrum shown in red contains all data from the time period from December 2007 to June 2008, which had the overall highest flux level. It is the spectrum with the highest flux normalisation f_0 of the three spectra and lies highest in the plot. The spectrum is the flattest, which can also be seen in the smallest absolute value of the slope α. This means that when the overall flux rises, the flux rises more strongly with higher energies.
The spectrum of the data from November 2008 to June 2009 is shown in orange. The overall flux lies between the flux values of the other two time periods. It can be seen that the spectrum lies between the other two, which is also true for the flux normalisation f_0 of the other two spectra. The slope α shows that this spectrum is flatter than the lowest spectrum and steeper than the highest spectrum. This confirms the above described behaviour, namely that the flux is rising more strongly for higher energies than for lower energies when the overall flux is rising.
The curvature of all three spectra are compatible within the error estimation. Furthermore, the position of the peak energy, which is the position of the highest flux, is moving towards higher energies for an overall higher flux level. This can be seen for the red and orange spectrum.
When comparing the three spectra to the Crab Nebula spectrum, it can be seen that the spectra of Mrk 421 are curved more strongly. The spectrum of the Crab Nebula has a curvature strength of $b = -0.26 \pm 0.07$ [Alb08b], which is a smaller absolute value than for Mrk 421. This difference in the curvature makes it complicated to compare the overall slope by eye. Hence, this can be compared by the slope α. For the Crab Nebula this value is $\alpha = -2.31 \pm 0.06$ [Alb08b]. Consequently, the spectrum of Mrk 421 is steeper when the flux is as low as 0.4 CU. When the flux is high as it is e.g. during the second time period, the spectrum is flatter. This confirms the conclusions that have been made in section 5.5, when the light curves in different energy ranges were discussed.
It could be shown that the spectral slope of the correlated fit changes with changing flux level. The higher the flux state, the flatter the spectrum becomes. As these overall spectra show the average over long time periods, they only represent the average behaviour. For the first and third time period, when the flux was always stable at a low level, this average is representative for all of the nights. But for the active time period from December 2007 to June 2008, when the flux takes different values every other night, this average spectrum

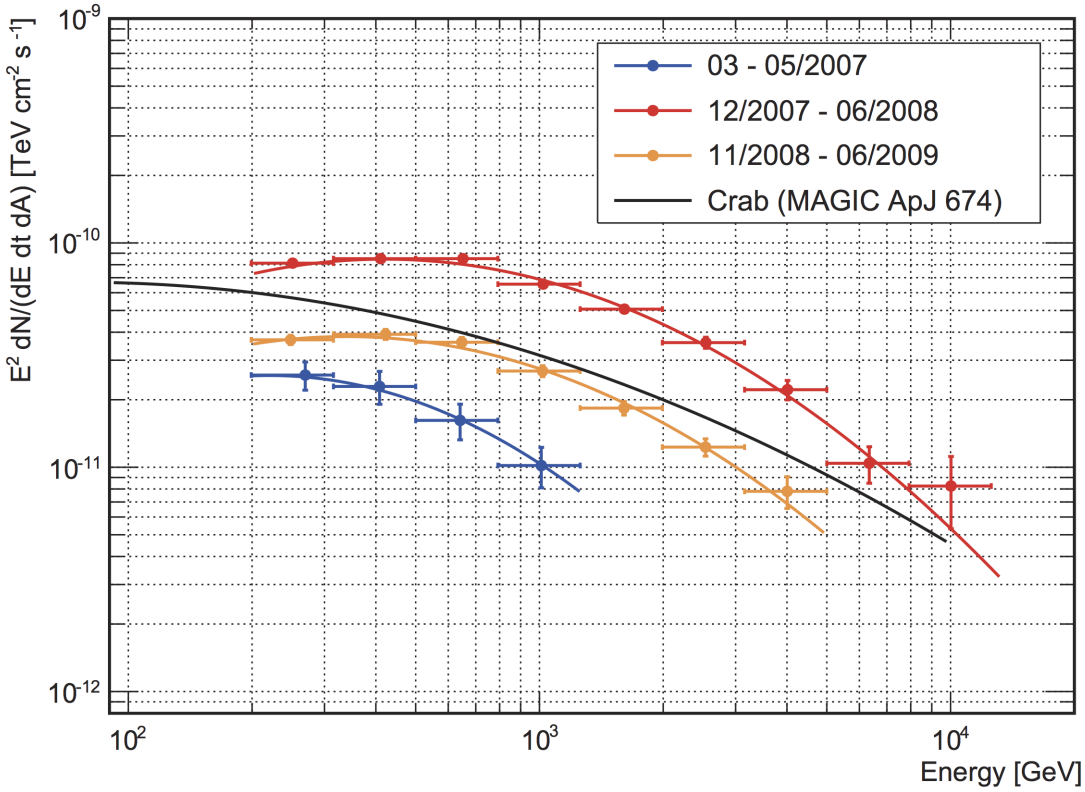

Figure 5.15: EBL corrected, unfolded spectra of the three time periods. In blue the spectrum from March to May 2007 is shown. The red spectrum contains all data from December 2007 to June 2008, the orange spectrum all data from November 2008 to June 2009. The black solid line represents the spectrum of the Crab Nebula.

is not representative for the spectra of every single night. In the next subsection this shall be studied in more detail.

5.7.4 Daily spectra

The unfolding is carried out for every night separately in order that the changes in the spectrum due to the changing flux level are seen. In the following, five nights from the time period from December 2007 to June 2008 are selected. They have relatively long observation times, so that the spectra are spread over a wide energy range. The selected nights represent different flux levels reaching from as low as about 0.88 CU on 9th January 2008 to about 3.77 CU on 31st March 2008, the night with the highest overall flux. The three other selected nights are 4th December 2007 with a flux of about 1.18 CU, 6th February 2008 with 2.51 CU and 6th June 2008 with 3.40 CU. The unfolded and EBL corrected spectra are shown in Figure 5.16. The average spectrum from the time period from December 2007 to June 2008 is plotted as well, so that the difference of the single days to the average can be seen. The fit results are summarised in Table A.14.

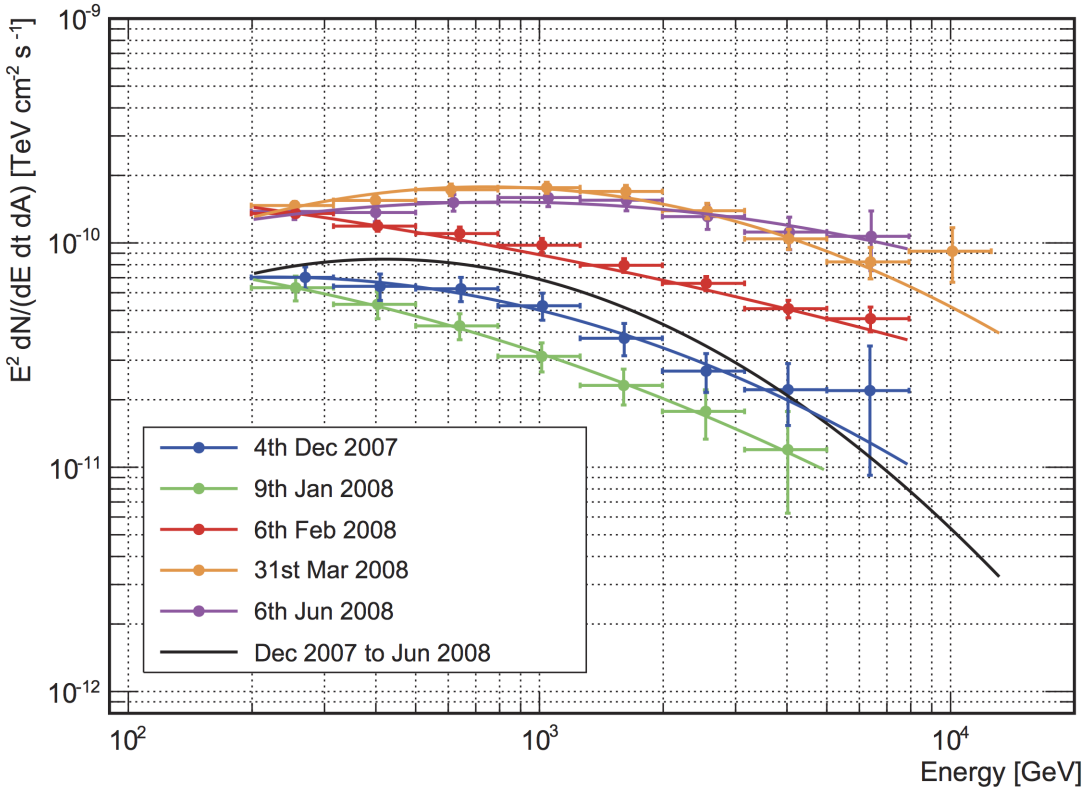

Figure 5.16: EBL corrected, unfolded spectra of several single nights. The spectra of the selected days are marked with different colours. The black solid line represents the average spectrum of the time period from December 2007 to June 2008.

The three nights with a flux above the average flux during the whole time period, which is about 1.4 CU, lie above the average spectrum. The two spectra from the nights with a lower flux, lie underneath. It is obvious that this behaviour can also be seen in the flux normalisation f_0. It is directly related to the overall flux during each night. f_0 rises with rising flux state. However, the absolute value of the slope α of the power law with variable slope is decreasing with increasing flux level. For all fit results, see Table A.14.
The curvature strength b is obviously larger for the average spectrum than for the single day spectra. This might be explained due to the fact, that most of the spectra with lower flux levels only have spectral points in the lower energy range. There are only few spectra with a high flux level that reach up to higher energies.
The position of the peak energy can be seen for 31st March and 6th June 2008, the two days with the highest flux level. The peak lies at a higher energy than for the average spectrum. For the spectra of the days with a lower flux, this peak position lies outside the shown energy range.
To have an overview of the slope of all data, α is plotted against the integral flux from 400 GeV to 50 TeV in Figure 5.17. The correlated fit with the power law with variable slope could be performed for 61 of the 95 nights. The main reason, that the fit could not

be performed for some of the days, is, that there were not enough spectral points for the fit. This mostly occurred for nights with short observations and low overall flux.

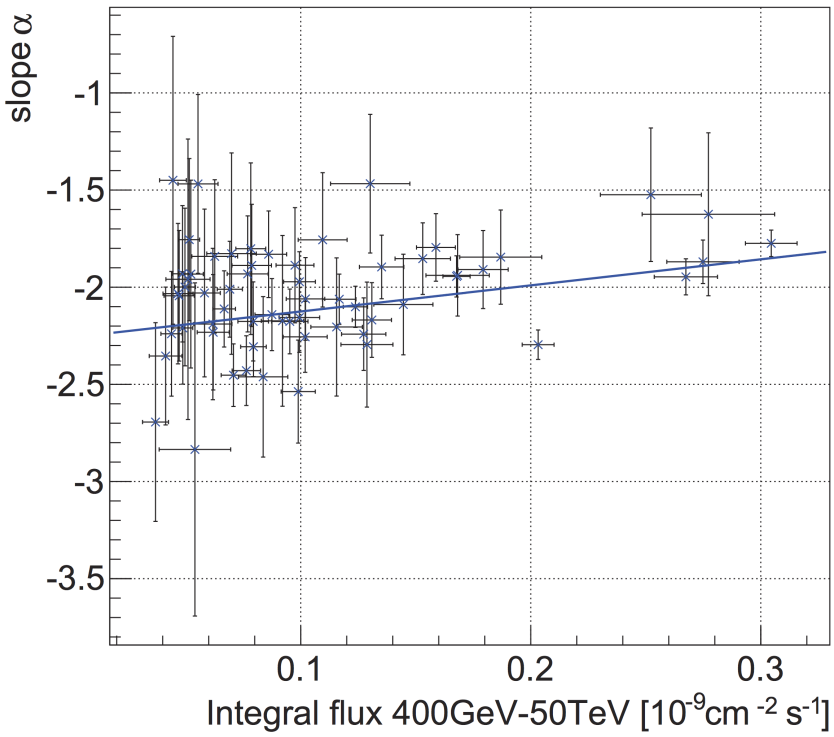

Figure 5.17: Spectral slope of the power law with variable slope as a function of the integral flux. The blue line represents a linear fit to the data points.

It can be seen that for the lowest integral flux values the slope α is spreading and has large errors. For the data with a flux above $10^{-10}\,\mathrm{cm}^{-2}\mathrm{s}^{-1}$, most of the slope values are rising with rising flux. Hence, a linear fit to all data points was applied. It results in $\chi^2/ndf = 56.57/59$ and a probability of 0.57. Therefore, the relation between α and the integral flux can be described by a linear correlation. For an increase of the integral flux of $10^{-10}\,\mathrm{cm}^{-2}\mathrm{s}^{-1}$, α is rising by 0.13 ± 0.03.

5.8 Conclusions on the light curve and the spectrum of Mrk 421 measured by MAGIC-I

The light curve of Mrk 421 analysed in the scope of this thesis exhibits different behaviour in different years. A variability in the light curve is present over the whole time range of 2.3 years. The flux is about 0.5 CU when the source is in the quiet state. When the source is flaring, higher fluxes can be reached. Here, a maximum of about 3.77 CU was observed.
In the beginning of 2007, Mrk 421 shows a low emission state and no flares. Between December 2007 and June 2008, Mrk 421 is in a very active emission state. A high average flux of about 1.4 CU is present for the dense sample of 56 data points in this time span

of 187 days. Additionally, the flux is very variable and a factor of 9 lies between the lowest and highest flux emission. During this period Mrk 421 flares nine times. These flares feature large differences in flux to their nearest data points. The greatest difference seen here is a drop of the nightly flux by a factor of 3.3 in two days, which happens from 31st March 2008 (MJD 54555.9) to 2nd April (MJD 54558.4), whereas on MJD 54555.9 the highest flux, equal to 3.77 CU, of the whole analysis is present. After the five month observation break from June to December 2008, the flux emission of Mrk 421 at the end of 2008 and in 2009 is down to about the same low level that it had in spring 2007. With the lower overall flux, a lower variability shows.
The examination of the light curve in three different energy ranges showed that the flux behaves differently in different energy ranges. It could be shown that the light curve is more variable the higher the energy range becomes. This means that the flux in the high energy range increases more than the two lower energy ranges when the overall flux increases. This was verified by a study of the dependence of the spectral shape on the overall flux state. This resulted in the conclusion that the spectra are harder the brighter the source is. This means that the spectrum becomes flatter and therefore contains proportionally more high energy photons when the emission of the source is increasing.
Additionally, the short-term light curves with 5 minute bins of each night were examined for variability. Many nights show a stable flux, but some nights show short-term variability. This means that their flux doubles or halves in time intervals shorter than 30 minutes. On two nights flare structures can be seen. For these nights a flare analysis was carried and the characteristic rise and fall times were determined. This resulted in short-term variability time scales t_{var} between 2.3 and 33 minutes, depending on the flare and the flare model. With these results the size of the emission region was estimated to be larger than the black hole.

Chapter 6
Periodicity search in light curves

Periodicities in light curves can occur, if the emitting source is part of a binary system. These binary systems can be systems on stellar or galactic scale. For example the light curve with periodic fluctuations of a binary stellar system was introduced in [Sar09]. In the class of AGNs, periodicities have been observed already for Mrk 501. Mrk 501 has a redshift of $z = 0.034$ and is the second closest blazar after Mrk 421. In its measured light curves in the TeV and X-ray energy range, periodicities of a length of about 24 days have been found. [Nis99]
In [Rie00] it has been discussed that a binary black hole system, which can develop during the merging process of two galaxies, can cause these periodicities.
For Mrk 421 no periodicities have been found so far. For the γ-ray energy range this was studied by [Acc14] with data measured by the Whipple telescope over a time span of 14 years from 1995 to 2009. Because Mrk 421 is an elliptical galaxy like Mrk 501 [Nil99], it is possible that it has a binary black hole system in its centre, too, and its light curve could therefore show periodic behaviour.
To search for periodicities, the function **RobPer** inside the R framework is used. It was written to detect periodicities in light curves and was especially designed to handle also irregularly sampled light curves, which are present in astroparticle physics. [Thi13b]
In this chapter it will be explained how **RobPer** searches for periodicities. Then the results of the periodicity search in several light curves of Mrk 421 will be presented. This includes the MAGIC-I light curve from 2007 to 2009 from this analysis, a light curve by several Cherenkov telescopes from 1992 to 2012, and an excess rate curve measured by FACT from 2013 to the beginning of 2015.

6.1 Periodicity search with RobPer

To find periodicities in a light curve, the function **RobPer** is used. It was written by [Thi14] and was already used for the periodicity search in light curves.
The light curve is given as a set of observation times t_i with corresponding flux value y_i and measurement error s_i. A selected periodic function g with period p is fitted to the light curve points with a chosen regression method for several periods. Then a periodogram bar $\mathrm{Per}(p)$ is calculated for each selected trial period p. This $\mathrm{Per}(p)$ corresponds to the goodness of the fit. To check if a trial period is outstanding, a beta distribution is robustly fitted to the distribution of periodogram bars. Then it is tested to see if one of

them exceeds a critical value, making it a detected period. [Thi14]

All of the upcoming information about the fit functions, the regression techniques, the weighted regression, the coefficient of determination, and the explanation about how to find an outstanding period, is summarised information from [Thi13a], [Thi13b] and [Thi14].

Fit functions
In **RobPer** several fit functions can be chosen for g. In the scope of this thesis four functions are selected for the modelling, which are shortly introduced in the following. For more details, see [Thi13b].

- The **step function** is made of 10 steps of equal width. It is usually not a continuous function.
- The **double step function** consists of two separate step functions, which are shifted relatively to each other so that the beginning of a step of the first function coincides with the middle of a step of the second function. Each step function is separately fitted to the light curve. The goodness of the fit is calculated by the mean of the goodness of the fit of both functions.
- The **sine function** is a continuous periodic function. For the periodic signal of a binary system, a sine shape might be assumed.
- Another continuous function is given by a **cubic spline** function, a polynomial of third degree.

Regression techniques
For the modelling of a periodic function to the light curve points, the measured flux values can be described as the vector $\vec{y}$ of measured flux values y_i. A flux value is assumed to consist of two parts and can be written as $y_i = y_{f,i} + y_{w,i}$. $y_{f,i}$ describes the assumed periodic fluctuation of the flux and $y_{w,i}$ stands for normally distributed white noise. This white noise describes fluctuations of the data points around the assumed periodic function.
The periodic fluctuation shall now be described by a periodic function from the above mentioned ones. Each flux point can be rewritten as $y_i = \vec{x}_i^{\mathsf{T}}(p)\vec{\beta}(p) + y_{w,i}$. $\vec{x}_i^{\mathsf{T}}(p)$ is a vector row of the design matrix $\mathbf{X}(p)$ representing the linear model of the periodic function g at the time t_i. $\vec{\beta}(p)$ is the parameter vector to be adapted. The error term $y_{w,i}$ will not be included in the modelling because firstly, it is unknown and secondly, the periodic behaviour is the desired behaviour that is to be modelled.
The modelling of a periodic function g to the given light curve points is done by minimising the following expression over $\vec{\beta}$

$$SE(p) = \zeta\left(\vec{y} - \mathbf{X}(p)\vec{\beta}(p)\right), \tag{6.1}$$

where $\vec{\beta}(p)$ is the fitted parameter vector for each period p. The function $\zeta(r)$, which is minimised over $\vec{\beta}$, depends on the regression technique. For a fitted model, the residuum $r_i(p) = y_i - \hat{y}_i(p)$ can be calculated at the time t_i for the trial period p, whereby $\hat{y}_i(p)$ is the modelled flux value. In the following, four of the available regression techniques in **RobPer** will be introduced.

A well-known regression technique is the least squares regression, abbreviated by L_2 in this work. The function to be minimised is defined as

$$\zeta_{L_2}(r) = \sum_{i=1}^{n} r_i^2. \tag{6.2}$$

The disadvantage about this regression technique is that it is not robust against outliers in the light curve.
The following three regression methods are robust against outliers. The L_1 regression is based on the absolute deviation of the residuals. Its definition is given by

$$\zeta_{L_1}(r) = \sum_{i=1}^{n} |r_i|. \tag{6.3}$$

Another type of robust regression technique is based on down-weighting the influence of the largest residuals. Here, the function to be minimised is based on

$$\zeta(r) = \sum_{i=1}^{n} \rho\left(\frac{r_i}{\hat{\sigma}}\right), \tag{6.4}$$

whereas $\hat{\sigma}$ is an estimator of the variation of the residuals r_i and acts as a scale estimate. It is introduced in this case so that the regression result is independent of the scale. This is necessary here because the following ρ functions are calculated differently depending on the value of the (scaled) residuum.
There are two different functions for ρ that are standard choices for this approach. One of them is called Huber regression. The corresponding ρ function is defined as

$$\rho_{\text{Huber}}(\nu) = \begin{cases} \nu^2 & \text{for } |\nu| \leq k, \\ 2k|\nu| - k^2 & \text{for } |\nu| > k. \end{cases} \tag{6.5}$$

The second function is called bisquare function and is given by

$$\rho_{\text{bisquare}}(\nu) = \begin{cases} 1 - \left(1 - \left(\frac{\nu}{k}\right)^2\right)^3 & \text{for } |\nu| \leq k, \\ 1 & \text{for } |\nu| > k. \end{cases} \tag{6.6}$$

The values of k were optimised to have an efficiency of 95% when applied to the normal distribution. In [Thi14] these values were determined to be $k = 1.345$ for Huber and $k = 4.68$ for bisquare regression.

Weighted regression
So far, only the case of unweighted regression was discussed. In **RobPer** it is possible to take measurement errors s_i into account, which makes the regression a weighted regression. This is done by normalising the entries of the vector and matrix with the measurement error. The normalised flux values are then given by $\frac{y_i}{s_i}$ and the normalised entries of the vector row $\vec{x}_i^{\intercal}$ of the design matrix by $\frac{1}{s_i}\vec{x}_i^{\intercal}$. In the following, the weighted regression is

applied.

Coefficient of determination
To determine how good the model fits the data points for a given trial period, the coefficient of determination is calculated. It is defined as

$$R^2 = 1 - \frac{SE(p)}{SY}. \tag{6.7}$$

$SE(p)$ is the deviation of the fitted model to the light curve points, which was introduced in Equation 6.1. SY is the result of the minimisation of the location model and is defined as

$$SY = \zeta\left(\vec{y} - \hat{\mu}\vec{\mathtt{i}}\right). \tag{6.8}$$

The location model assumes a constant μ instead of a periodic function. $\vec{\mathtt{i}}$ is a vector of ones in the case of unweighted regression and a vector of the inverse measurement errors in the case of weighted regression.
The coefficient of determination R^2 is called $\mathrm{Per}(p)$, the periodogram bar of the trial period p. For a real underlying period p, the periodogram bar is expected to be higher than for wrong trial periods. It should therefore be visible in the periodogram, where all resulting periodogram bars are plotted for all tried periods. An example of this can be seen in panel (b) of Figure 6.1.

Finding an outstanding period
It has been shown to be reasonable to approximate the distribution of periodogram bars by a beta distribution [Thi13a]. A valid period is recognised as an outlier of this distribution. The threshold, above which a period can be considered as detected, is calculated as the $\sqrt[q]{1-\alpha}$ quantile of the beta distribution $B\left(\frac{m-1}{2}, \frac{n-m}{2}\right)$, where n is the number of observations and m the dimension of $\vec{\beta}$. Here, q is the number of trial periods and $\alpha = 0.05$ the chosen maximum probability to wrongly detect a period under the null hypothesis of a constant flux. In panel (a) of Figure 6.1 the distribution of the periodogram bars is shown with the fitted beta distribution as a black curve and the resulting threshold as a black vertical line. This threshold can again be seen as a horizontal line in panel (b). As can be seen in this example, no periodogram bar crosses this line, so that no period is detected.

6.2 Mrk 421 light curve from 2007 to 2009 by MAGIC-I

The periodicity search is performed for the MAGIC-I light curve from March 2007 until June 2009, which was already shown before in Figure 5.3. In [Thi13b] it has been pointed out that the maximal trial period should be one tenth of the length of the examined light curve, following the advice of [Hal03]. The MAGIC-I light curve has a length of 830 days. Therefore, a maximum trial period of 83 days will be tested.
For the periodicity search all four previously introduced regression techniques and periodic functions are applied. For the bisquare regression and the sine function a period of 31 days is detected. This can be seen in panel (a) of Figure 6.2. The second highest peak,

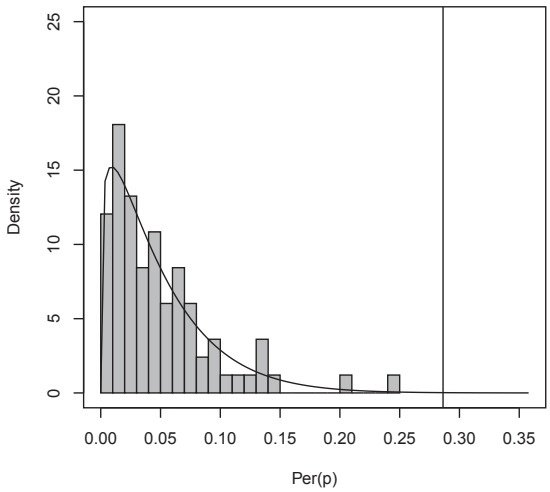

(a) Distribution of periodogram bars Per(p). The black solid curve shows the beta distribution, which is robustly fitted to the data distribution. The black vertical line is the threshold (for explanations, see the text).

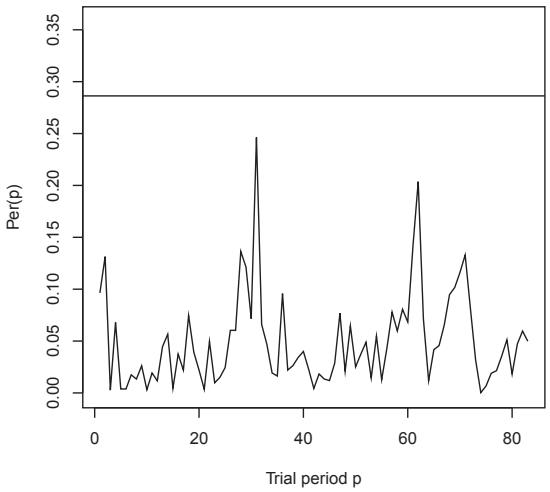

(b) Periodogram showing all periodogram bars Per(p) for each trial period from 1 to 83. The black horizontal line is the threshold from the distribution in (a). No period is detected here.

Figure 6.1: Principle of the determination of the threshold for detecting an outstanding trial period p. In (a) the distribution of the periodogram bars Per(p) and in (b) the periodogram, where the periodogram bars Per(p) are plotted for each trial period p, are shown. This is an exemplary result for the MAGIC-I light curve from 2007 to 2009 with the spline function and the Huber regression.

which is not above the threshold, is located at 29 days. This is mentioned here because 29 days is the duration between two full moons. Due to the observation break around the full moon, these periodic observation gaps can possibly be found as an underlying period for a modelled function.
Using the sine function with the other three regression methods still shows a high peak at 31 days and a second high peak at 29 days, but they don't cross the threshold. The results with Huber and L_1 regression are shown in panels (b) and (c) of Figure 6.2. For the L_2 regression, which is not a robust regression, the peak around 31 days is the least pronounced in comparison to the other regression techniques.
When the periodic function is replaced by the spline function, the highest peak is given for a period of 31 days, the second highest peak for 62 days, which is twice the period length of the first peak. None of the peaks crosses the threshold so that no period is detected with the spline function. In panel (d) of Figure 6.2, the result for the spline function and the bisquare regression can be seen. The result with the Huber regression was already shown as the example plot in Figure 6.1.
The results for the step function as periodic function show again a peak at 31 days, but it is not above the threshold and its height is comparable to other peaks. For the double step function, there is again a peak at 31 days, but also at 28 and 29 days as well as around 61 and 62 days. These results are not shown here.

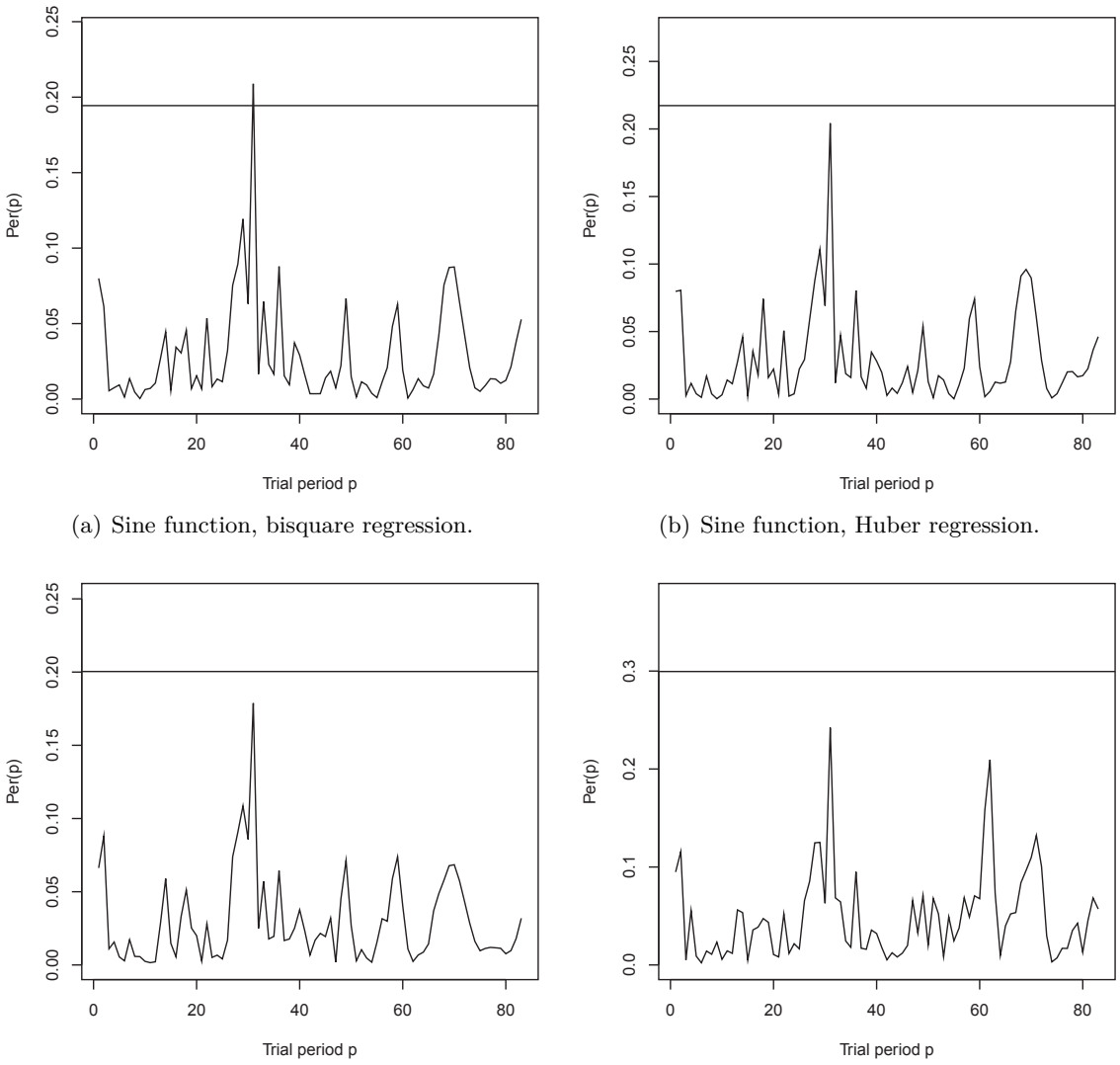

(a) Sine function, bisquare regression.

(b) Sine function, Huber regression.

(c) Sine function, L_1 regression.

(d) Spline function, bisquare regression.

Figure 6.2: Periodograms for the MAGIC-I light curve from 2007 to 2009. The chosen periodic function and regression technique are specified for each subfigure separately.

A period of around 31 days is not unreasonable. A closer look at the light curve reveals e.g. distances between two minima of 31 days (MJD 54536.9 to 54568.1) and of 61 days (MJD 54476.3 to 54536.9). Two of the highest flares between MJD 54555.9 and 54612.9 are 57 days apart and in the year 2009 there are three examples where high flux values are 28, 30 and 59 days apart. Therefore, it is understandable if periods around 30 days have a high coefficient of determination on the basis of this light curve. If the sampling were finer, the structure could be different. Unfortunately, the telescope observations are limited due to weather conditions and the moon phase, so that in this case the sampling

is just limited by this. The conclusion that can be drawn is that the results are dependent on the sampling and that a finer sampling would give clearer results. With the given data a period of around 30 days is explainable.
To test if the highest flares cause the period of 31 days to stand out, all nights with a flux above 1.5 CU are deleted. The modified light curve has 74 data points left. For the sine function and the bisquare regression the peak at 31 days is not detected any more as it was with all data. Now, the coefficient of determination is higher for all trial periods because now the highest outliers are gone. But this also causes the period of 31 days to be detected no longer. Nonetheless, it is still the highest peak. It might be that important points, which are essential to reflect the period of 31 days, were deleted by discarding all flux values above 1.5 CU. The resulting periodogram is shown in Figure 6.3.

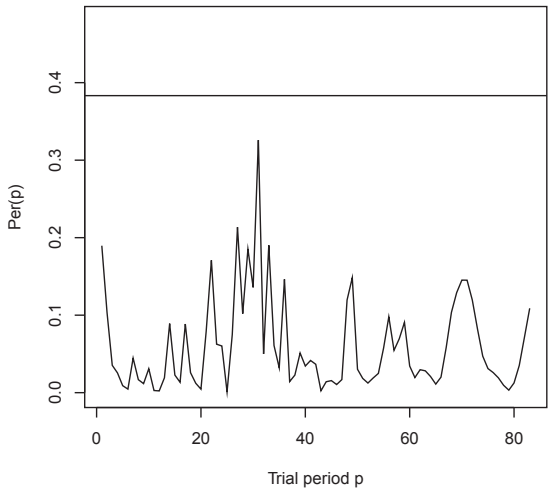

Figure 6.3: Periodogram for the modified MAGIC-I light curve from 2007 to 2009, which only includes flux values below 1.5 CU. Here, the sine function and the bisquare regression were applied. The period of 31 days is not detected in this case.

6.3 Mrk 421 light curve from 1992 to 2012 above 1 TeV

The light curve
In [Tlu10], light curves from Mrk 421 above 1 TeV from several Cherenkov telescopes from 1992 to 2009[1] were collected. The collected data were recorded by different Cherenkov telescopes and the results were published in different works. The telescopes, from which light curve data of Mrk 421 were publicly available, are namely the CAT (Cerenkov Array at Thémis), the HEGRA (High Energy Gamma-Ray Astronomy) CT1, the HEGRA telescope system, MAGIC, VERITAS and Whipple. The data shown here were first published in [Aha02], [Aha03], [Buc96], [Don09], [Ker95], [Kes03], [Kra01], [Reb06] and [Sch96] and collected and merged to one data set by [Tlu10].

[1] The data were downloaded from `astro.desy.de/gamma_astronomy/magic/projects/light_curve_archive/index_eng.html` on 27th August 2014.

Nine nights of recorded data by H.E.S.S. are discarded because it was reported that the observation threshold was above 1 TeV. Five nights of MAGIC data from the data set in [Tlu10] from MJD 54619.9 to 54624.9 are parallel to the data from the analysis of this thesis and are therefore not taken into account. Five nights of VERITAS data are discarded as well because their measurement error is given as 0. The weighted regression cannot handle this. As these five points only make up a small amount in the light curve, they are discarded in order to be able to use the weighting.
The light curve by MAGIC-I from 2007 to 2009 from this analysis was added, as well as the light curve from the MAGIC telescopes in 2012 published in [Fra15]. The resulting light curve above 1 TeV is shown in Figure 6.4.

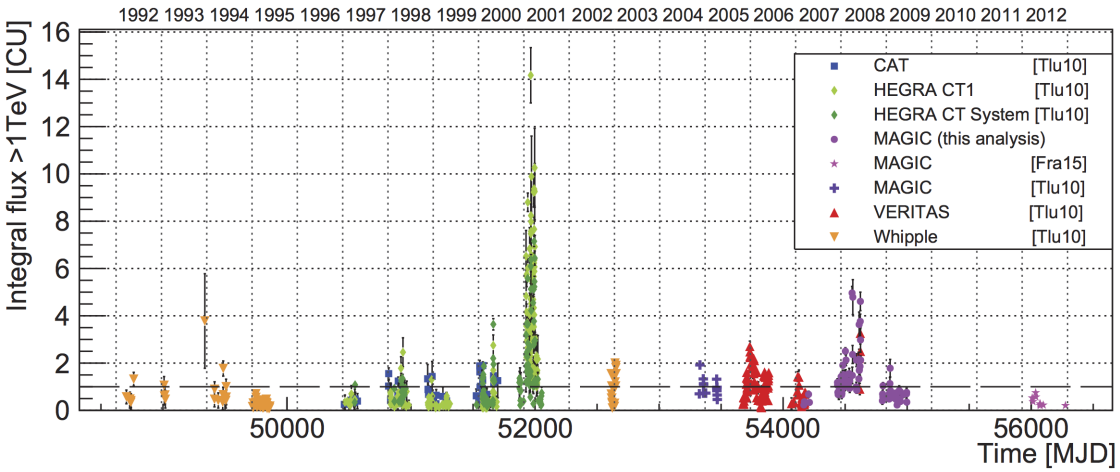

Figure 6.4: Light curve of Mrk 421 from 1992 to 2012 measured by several Cherenkov telescopes. The data are from [Tlu10], [Fra15] and from this analysis.

The flux measured by Whipple (orange triangles) from 1992 to 1997 is at a low level. It is mostly below 1 CU. A few points are above 1 CU, but below 2 CU. There is one exception with a higher flux, but with a large error. In the years 1997 to 2000, Mrk 421 was observed by CAT (blue squares), the HEGRA single telescope CT1 (light green diamonds) and the HEGRA telescope system (dark green diamonds). The flux is mostly below 2 CU. One exception in 1998 reaches a flux of about 2.5 CU and the highest of three exceptions in 2000 reaches 3.6 CU. Between November 2000 and May 2001 a very high activity was recorded by HEGRA. For a better view of this interesting time period, a zoomed version of the light curve from MJD 51873 to 52053 is shown in Figure 6.5.
At the end of the year 2000 Mrk 421 is in a quiet emission state with fluxes below 2 CU. The four months after the turn of the year show a very active time period, which only has very few data points with a flux below 1 CU. The flux reaches a maximum of more than 14 CU. In the last month of this observation period, Mrk 421 is quiet again with fluxes below 1 CU.
In winter 2002/2003 Whipple recorded a quiet flux of Mrk 421 with values below 2 CU. The same is true for the flux between the end of 2004 and the beginning of 2007 recorded by MAGIC-I (purple crosses), VERITAS (red triangles), and by MAGIC-I (purple circles), which was analysed in this work. Only four days in the winter 2005/2006 have a larger

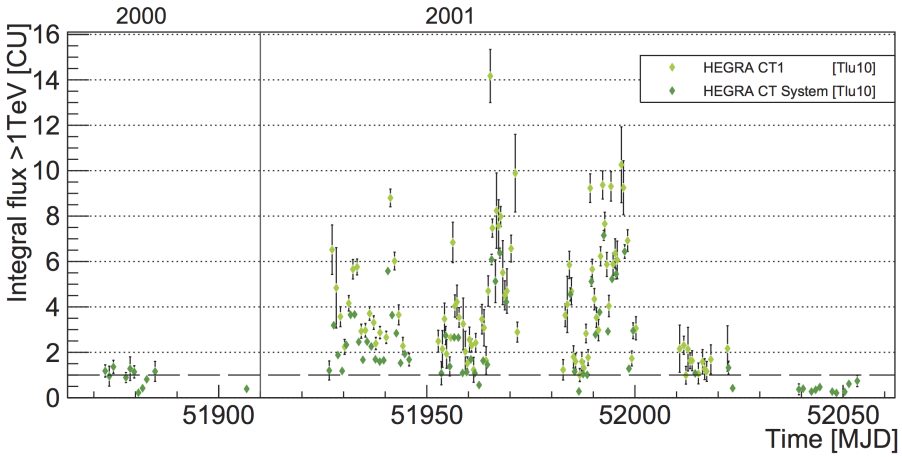

Figure 6.5: Light curve of Mrk 421 from the end of 2000 to the middle of 2001 measured by the HEGRA CT1 and telescope system. The vertical line represents the division from year 2000 to 2001. The data are from [Tlu10].

flux than 2 CU, whereas the maximum flux is at about 2.7 CU. From the end of 2007 to the middle of the year 2008, which includes the MAGIC-I data from this thesis and some data points from VERITAS, the flux is hardly ever below 1 CU. The maximum flux during this active period equals about 4.9 CU, as was discussed before in section 5.5. The subsequent data from the end of 2008 to the middle of 2009, which are also from this thesis, have again a low flux below 2 CU. The data in 2012 were recorded by the MAGIC telescopes (pink stars). Mrk 421 is in a quiet emission state with fluxes below 1 CU during that year.

Periodicity search

With a total length of the light curve of 8201 days, the maximum trial period would be limited to 820 days [Hal03]. However, the given light curve contains alternately phases of data and observation gaps. By this we mean the gaps which are caused by astronomical circumstances, so that Mrk 421 is only observable for about six months every year for Cherenkov telescopes. This results in data points only during about 180 days each year. That is why it makes no sense to search for periodicities at periods around 180 days or longer. Then only the scheme that data is available for 180 days and is not available for the next 180 days and so on would be modelled. This is the long-term synonym to the observation gaps due to the moon. Detected periods of 29 days have to be handled with care as well.

In order to give **RobPer** the chance to model at least about two periods during one observation period of 180 days, it has been decided to test periods up to 100 days. Additionally, the result plots are directly comparable to the results from the periodicity search in the MAGIC-I light curve shown above.

The periodicity search with a sine function results in a detected period of 29 and 31 days for the L_2 regression. The result is shown in panel (a) of Figure 6.6. For the Huber regression, the peak at the period length of 31 days is still the highest peak and the peak at 29 days the second highest, but they are both below the threshold. This can be seen in

panel (b) of Figure 6.6. For the other two regression methods the period of 31 days has the largest coefficient of determination, but it is always below the threshold and is thus not detected.

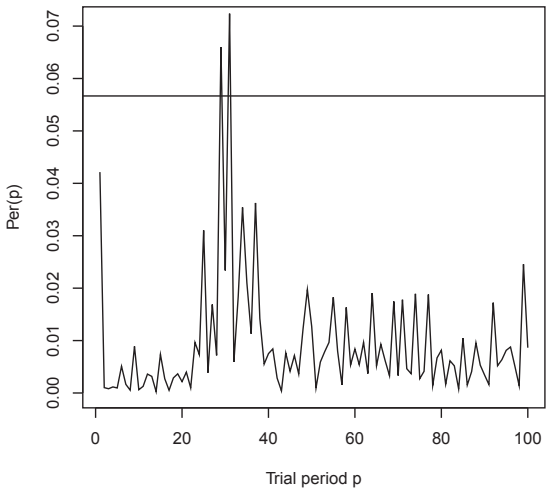

(a) Sine function, L_2 regression.

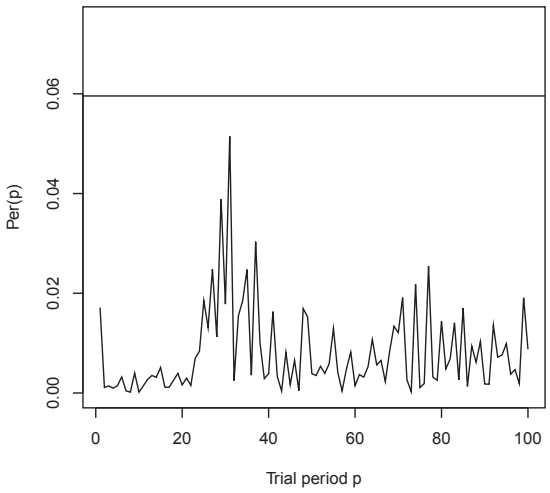

(b) Sine function, Huber regression.

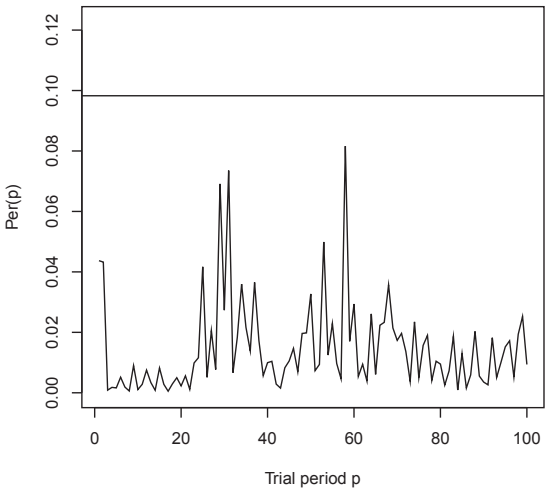

(c) Spline function, L_2 regression.

Figure 6.6: Periodograms for the Mrk 421 light curve from 1992 to 2012. The chosen periodic function and regression technique are specified for each subfigure separately.

The modelling with the double step function results in no detected period. There are peaks at 29, 31, 58 and 62 days, but they are not outstanding in comparison to other periods and don't cross the threshold. For the step function as periodic function, the peaks are even less pronounced. The results are not shown here. With the spline function, peaks are visible at the trial periods of 29, 31 and 58 days. They are best pronounced

with L_2 regression. This result is shown in panel (c) of Figure 6.6. Nevertheless, none of the periods is detected.
At this point it might be concluded that the detected period of 31 days only appears because the MAGIC-I light curve from 2007 to 2009 is included, for which a period of 31 days was detected before. Therefore, all data points from MJD 54438 to 54635 from the MAGIC-I light curve from this analysis are deleted. These are only the days from the active period from the end of 2007 to June 2008.
As can be seen in panel (a) of Figure 6.7, the periods of 29 and 31 days are still detected with the sine function and the L_2 regression, although the MAGIC-I data were deleted from the light curve. In the zoomed light curve of the data in 2001 in Figure 6.5, it can be seen that the difference between the highest and second highest peak is 30.5 days. Maybe this difference influences the results.
With the Huber regression, these two periods are again not detected, but they are clearly visible in the periodogram in panel (b) of Figure 6.7. The peak at 29 days is higher than the peak at 31 days.
The other three regression methods showed no detection, but peaks at 29 and 31 days, whereby the higher one is at 29 days.

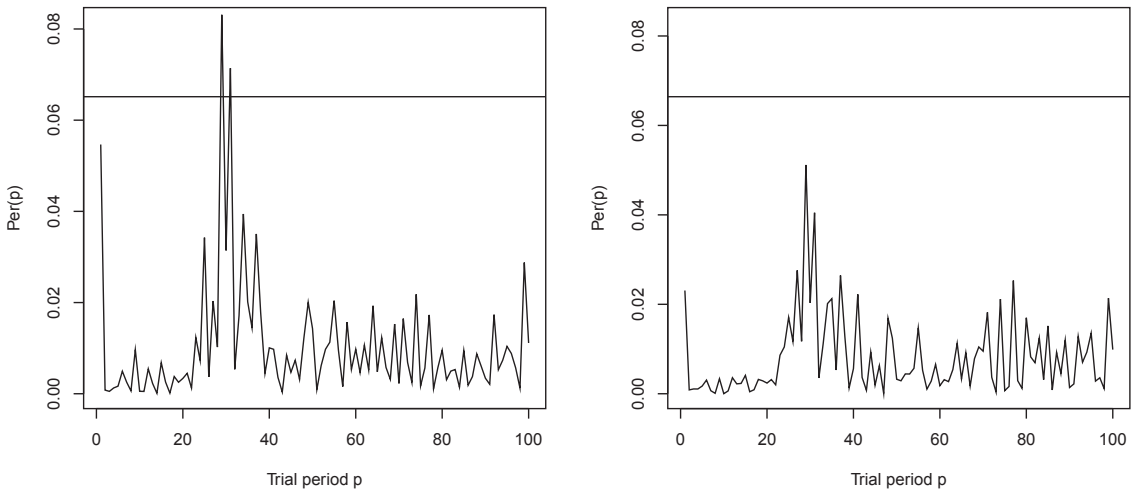

(a) Sine function, L_2 regression.

(b) Sine function, Huber regression.

Figure 6.7: Periodograms for the Mrk 421 light curve from 1992 to 2012 without the MAGIC-I data from 2007 to 2008. The chosen periodic function and regression technique are specified for each subfigure separately.

Another test was done to check the influence of the very high active region around 2001. Therefore, all flux points between MJD 51900 and 52000 were deleted. The MAGIC-I data were added again.
Without these data points no period is detected. The results for the sine function in combination with the L_2 regression and the Huber regression can be seen in Figure 6.8 in panels (a) and (b), respectively. None of the periodogram bars Per(p) crosses the threshold. The peak at 31 days is still visible, but it is low in comparison to neighbouring peaks. The highest peaks are in the region from 27 to 29 days in the case of L_2 regression.

For Huber, bisquare and L_1 regression, the highest peaks are between 26 and 28 days. Additionally, there are peaks at 35 and 37 days.

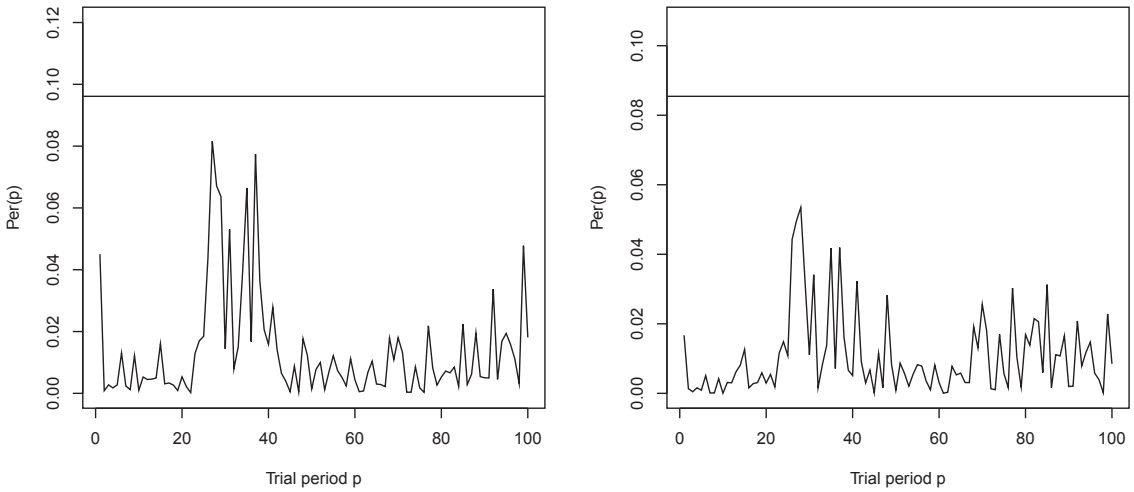

(a) Sine function, L_2 regression.

(b) Sine function, Huber regression.

Figure 6.8: Periodograms for the Mrk 421 light curve from 1992 to 2012 without the high flux HEGRA data in 2001. The chosen periodic function and regression technique are specified for each subfigure separately.

Earlier studies with these data

The light curve from [Tlu10] was already analysed in [Thi13a]. There, a period of 31 days was also detected. But if the data points around MJD 52000 were deleted from the light curve, the period of 31 days was no longer detected. However, it was still a high peak visible for 31 days. This result is in agreement with the results from the study in this thesis.

6.4 Mrk 421 light curve from 2013 to 2015 by FACT

The light curve

The recorded data from FACT are directly analysed by a Quick Look Analysis (QLA) and are available shortly after the observation online[2]. The shown results are excess rate curves, i.e. the number of excess events per hour is given. This QLA provides preliminary results and is not yet optimised for all zenith distances and sky brightness conditions. [And13]
For the excess rate curve shown in Figure 6.9, observations between 12th January (MJD 56304.2) and 3rd January 2015 (MJD 57025.3) are considered. The data shown here were taken at zenith distances below 35° and under dark sky conditions, which was defined here by a maximal value of the threshold of 350 DAC counts. This selection results in a light curve with 103 data points over a length of 720 days. This length defines a maximal trial period of 72 days in the periodicity search [Hal03].

[2] `www.fact-project.org/monitoring/`

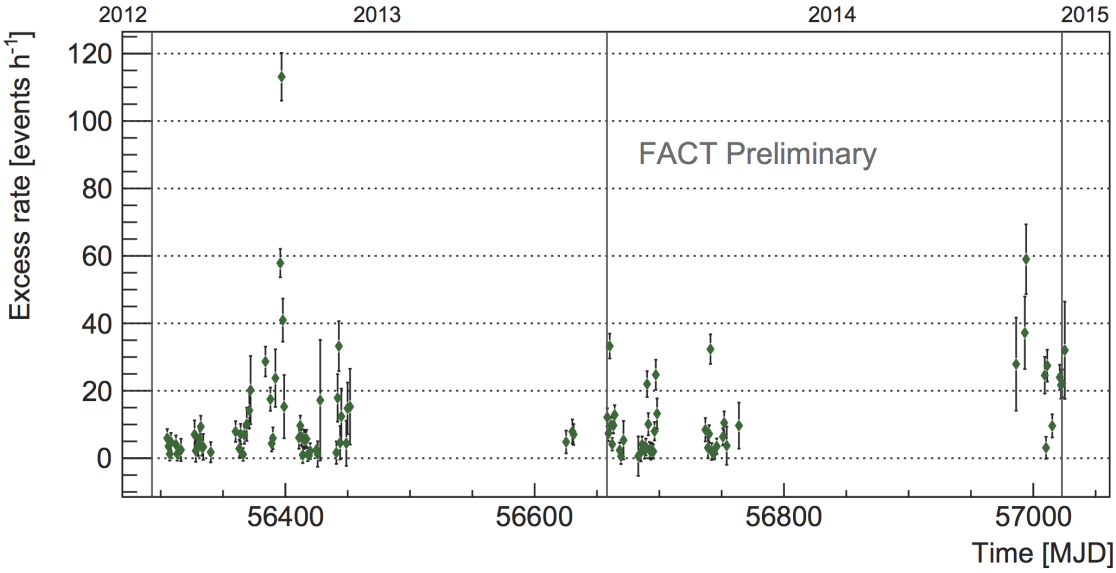

Figure 6.9: Excess rate curve of Mrk 421 measured by FACT between January 2013 and January 2015. The vertical lines represent the division from one year to the next.

The quiet baseline of the light curve lies at a rate of up to 10 excess events per hour. During the first two months of observation from MJD 56305 to 56340, the light curve is in such a quiet state. After that up to MJD 56452, the rate is higher and shows more variations. On MJD 56397 a maximum rate of 113 $\pm$ 7 excess events per hour is reached. This value almost doubled from the day before. It drops by a factor of 2.8 until the measurement of the day after. Around this time a flare was also observed by other telescopes, e.g. MAGIC and VERITAS in the TeV range [Cor13].
In the time range from MJD 56625 to 56764, the excess rate mostly stays below 15 excess events. On four nights the rate is higher with values between about 25 and 33. In the last time range, the rate is variable again with values between about 3 and 59 excess events. This means that the same behaviour is seen as it was measured with MAGIC-I. There are phases of low activity and phases of higher activity including flares.

Periodicity search
The periodicity search with the sine function gives no result for this light curve. The highest peak visible, which is below the threshold, is seen for a trial period of 52 days. The result for the sine function in combination with the bisquare regression is shown in panel (a) of Figure 6.10.
For the FACT light curve a period of 52 days is detected, if the step function is chosen as periodic function. The results with the L_1 and Huber regression, which detect this period, can be seen in panels (b) and (c) of Figure 6.10.
For the double step function no period could be detected. There is a peak at 52 days visible, but it does not reach beyond the threshold. For the spline function no period

could be detected either. There is again a peak at 52 days, which is not high enough to cross the threshold. The second highest peak lies at 62 days, as was already seen for the MAGIC-I light curve. These results are not shown here. Generally, it can be said that the peaks are least pronounced for the L_2 regression.
There are no distinct features with a time difference of 52 days in the light curve visible that would indicate a period of this length.

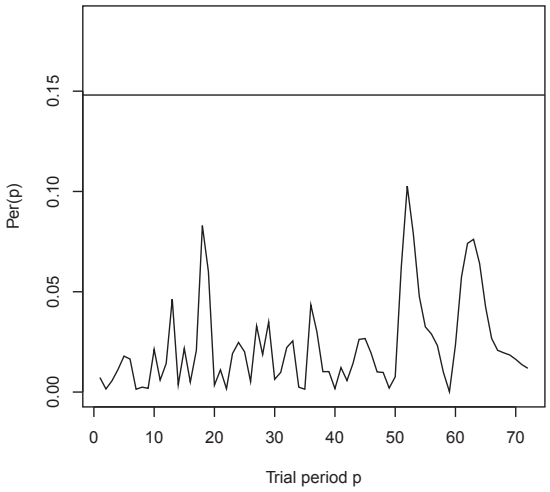

(a) Sine function, bisquare regression.

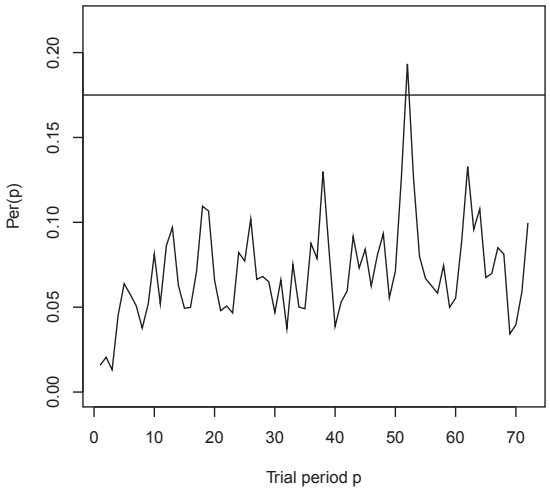

(b) Step function, L_1 regression.

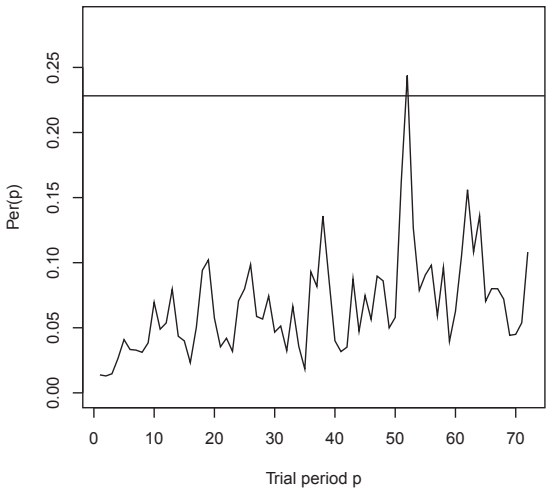

(c) Step function, Huber regression.

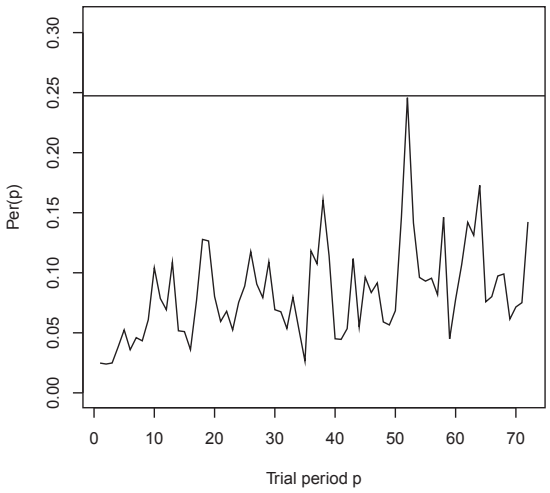

(d) Step function, Huber regression, without data from MJD 56392 to 56399.

Figure 6.10: Periodograms for the FACT light curve from 2013 to 2015. The chosen periodic function and regression technique are specified for each subfigure separately. The periodogram in (d) results from a modified light curve of FACT (see text).

To test if the flare at MJD 56397 has an influence on the results, the following four days around that date are deleted: MJD 56392, 56396, 56397 and 56399. The periodicity search with the Huber regression and the step function, which showed a detected period of 52 days for the whole light curve, does not detect this period any more. The result is shown in panel (d) of Figure 6.10. The peak at 52 days is the highest peak, but it does not cross the threshold.
A dedicated analysis for all the data taken by FACT would make the light curve more densely sampled because the data taken under bright sky conditions close to the full moon and data taken with higher zenith distances would be included. In the time range from above, data were taken on 196 nights. This would be an improvement for the periodicity search in the future.
So far, the data points of the light curves did not undergo a data quality check concerning weather conditions. This might have an additional influence on the result because days with bad weather - they could still be included in the above shown light curve - might have a different rate than shown. This could be corrected in a dedicated analysis and improve the results.

6.5 Conclusions on the periodicity search

Up to now, periodicities have not been found in the light curves of Mrk 421. Because periodicities have already been found for the AGN Mrk 501, it could be possible for Mrk 421 to have a binary black hole system in the centre as well. To check for possible periodicities, the search for these was performed with the function **RobPer**.
For the light curve of Mrk 421 measured by MAGIC-I from 2007 to 2009, a period of 31 days is detected with the sine function and the bisquare regression. However, for the other combinations of periodic function and regression method, this period is not detected, but still clearly visible as the highest peak.
For the light curve of Mrk 421 from 1992 to 2012 measured by several Cherenkov telescopes, again a period of 31 days is detected as well as an additional peak at 29 days. This time however, this result is achieved with the unrobust L_2 regression and not with a robust regression method. Again, it is detected with the sine function as periodic function.
The sine function seems to be the best model for an underlying periodic fluctuation in the light curves. The spline function also pronounces the peak at the period length of 31 days, but the peak is not high enough to be detected. With the step and double step function the feature at 31 days is still visible, but the peak is not much larger than other peaks.
Additional peaks next to the one at 31 days are found around 29 days and twice these values at 58 and 62 days. The period of 29 days could be modelled so well because of the periodic gaps in the light curves due to the full moon. This period would not be caused by a physical process in the source.
The influence of the flares was tested by deleting the highest flux points from the light curves. Then the period of 31 days is not detected any more. It is therefore concluded that the flares influence the detection of a period of 31 days. It is possible that this periodicity is only given, or at least clearer, during a high emission state.
For the FACT light curve of Mrk 421, the period of 31 days length does not show as a high peak. Here, the highest peak is found at 52 days. However, the sine function fails

for the FACT light curve and no period is detected. The detection occurs for the step function in this case. An additional peak is seen for a period of 62 days, which is double the period length which was found for the other light curves.

In [Thi14] it is stated that the applied method in **RobPer** is not fully theoretically substantiated. Therefore, the periods, which cross the threshold, are declared as detected and not as significant. The period of 31 days here detected will therefore not be claimed to be a real periodic fluctuation in the light curve. However, it can be taken as a hint of an underlying period of this length. Further tests with other methods to find periodicities should be carried out.
Another issue is the sampling of the light curves. The light curves measured by Cherenkov telescopes are often interrupted due to bad weather. Therefore, it might happen that important and essential features in the light curves are not observed. It is therefore important that all telescopes work together to get a sample as dense as possible. FACT is a telescope, which was built to serve exactly this purpose.
Although **RobPer** is supposed to be able to deal with outliers in the light curves, it was observed in this analysis that they still have an influence on the result. All three light curves were tested to see if the result changes when extreme outliers were deleted from the data sample. It could be seen in all three cases that the results changed, so that the periods detected before are not detected any more. This can be explained, if the extreme outliers are missing, all periods will model the data points better and the real period is not necessarily outstanding any more. Another reason for this could be that important points, which are needed to model the real underlying periodic function, are missing.

Conclusively, it can be said that **RobPer** is able to find periodicities in light curves. It could be shown that outliers influence the results. A period of 31 days was detected with the MAGIC-I light curve and the light curve of several Cherenkov telescopes covering a time range of 20 years. The sine function models the fluctuations best. However, the detection of the peak at 31 days only occurs when the time periods with a high emission state are included. When these high active time periods are excluded, the period of 31 days is not detected any more. Further investigations on this topic will be necessary to claim a periodic fluctuation in the light curve of Mrk 421.

Chapter 7
Study of MWL correlations of Mrk 421

In chapter 5 the behaviour of Mrk 421 in γ-rays was discussed. The light curve covering a time span of 2.3 years was examined for different emission and variability states. Additionally, the dependence of the spectral shape on the emission state could be shown.
In order to understand the behaviour of the source in all wavelengths better, these results are put into context with results of other instruments. These are two X-ray telescopes placed on satellites, namely the *Swift*/BAT and the *RXTE*/ASM, the optical telescope KVA, and the radio telescope OVRO. With these data it is possible to compare the source's behaviour in the different wavebands.
In order to be able to study the overall picture of Mrk 421 as well as other extragalactic and galactic sources, it is important that the whole astronomical community works together on these observations.
This chapter is structured as follows. At first the selected instruments for the MWL studies are introduced. Then the recorded light curves will be described and compared to the MAGIC light curve. Afterwards, the variability of each light curve is determined. Another topic is the examination of the light curves for correlations between them. Lastly, a SED of Mrk 421 will be shown. Results of different emission scenarios of former analyses will be discussed as well.
The results of the variability and correlation studies are going to be published in a paper in the name of the MAGIC Collaboration, which is led by the author of this thesis [Ahn15].

7.1 Considered instruments measuring in other wavebands

The light curves of Mrk 421 from telescopes measuring in other wavebands are essential in the understanding of the source. The data in the X-ray range used in this thesis are from the *Swift*/BAT and the *RXTE*/ASM. The optical light curves were observed by the KVA telescope. OVRO provides light curves in the radio energy range. These four instruments are introduced now.

***Swift*/BAT**
The Burst Alert Telescope (BAT) detects X-rays from 15 to 50 keV. It is placed on board the *Swift* satellite, which was launched in 2004. In addition to the purpose of monitoring

X-ray sources on a regular basis, it was built to detect GRBs. [Kri13]

***RXTE*/ASM**
The All-Sky Monitor (ASM) on board the *Rossi X-ray Timing Explorer* (*RXTE*) provides the data in the soft X-ray waveband from 2 to 10 keV for this analysis. The *RXTE* was operational from December 1995 to January 2012. The whole sky was scanned by the ASM several times a day and the data of these 90 second dwells can be used individually or as an averaged daily value. [Lev96]

KVA
The Kungliga Vetenskapsakademien (KVA) telescope is situated at the ORM on La Palma as the MAGIC telescopes. A 35 cm telescope takes photometric data. The light curve shown here was observed in the R-band [Bes05]. To determine the emission of the jet, the contribution from the host galaxy is subtracted. Since 2004 KVA has been monitoring the same blazars which MAGIC is observing, so that KVA has already been able to trigger MAGIC observations in the case of high flux in the optical band. [Tak08]

OVRO
For observations of Mrk 421 in the radio spectrum the Owens Valley Radio Observatory (OVRO), located in California, USA, is selected. It is monitoring more than 1500 γ-ray sources on a regular basis, including Mrk 421. It has a 40 m diameter dish and records radio photons with a frequency of 15 GHz. It started operations at the end of 2007. [Ric11]

7.2 Comparison of the light curves in other wavebands to γ-rays

In Figure 7.1 the light curves of Mrk 421 measured by MAGIC (purple), *Swift*/BAT (blue), *RXTE*/ASM (green), KVA (orange), and OVRO (red) are shown for the time range from February 2007 to June 2009. As the light curves cover a wide time range, zoomed versions of the plot are created. The light curves from February to August 2007 can be found in Figure B.1, from September 2007 to August 2008 in Figure B.2, and from September 2008 to June 2009 in Figure B.3. In these zoomed light curves all flares and minima, which will be discussed in the following, are marked. The MAGIC light curve was already shown in Figure 5.3 and its behaviour was discussed in section 5.4.
The data from the *Swift*/BAT are available online[1]. The light curve by the *RXTE*/ASM is available online as well[2]. For *Swift*/BAT and *RXTE*/ASM it needs to be said that only positive count rates are taken into consideration. The light curve from the KVA telescope was provided by E. Lindfors, Tuorla Observatory. OVRO makes its light curves available online as well[3].

[1] `swift.gsfc.nasa.gov/results/transients/weak/Mrk421.lc.txt`, downloaded on 15th April 2014. The "*Swift*/BAT transient monitor results" are "provided by the *Swift*/BAT team".
[2] `xte.mit.edu/asmlc/ASM.html`, downloaded on 22nd April 2014. The "results" are "provided by the ASM/RXTE teams at MIT and at the RXTE SOF and GOF at NASA's GSFC".
[3] `www.astro.caltech.edu/ovroblazars/data/data.php`, downloaded on 23rd May 2014. "The OVRO 40 m monitoring program is supported in part by NASA grants NNX08AW31G and NNX11A043G, and NFS grants AST-0808050 and AST-1109911".

The energy ranges, in which *Swift*/BAT and *RXTE*/ASM measure, are very close together. As can be seen in Figure 7.1, the light curves behave similarly. Therefore, the two light curves are discussed together. Some count rates in the *RXTE*/ASM light curve have large error bars. This is due to a low number of observation dwells, whereas a dwell is one observation unit of 90 seconds [Lev96].
Up to MJD 54400 the light curves in X-rays are rather quiet and show no flares. During the time period when MAGIC shows a high variable flux in γ-rays, this high variability is also present in X-rays. The flares on MJD 54439.2 and 54467.2 seen by MAGIC are also seen by *RXTE*/ASM on MJD 54439.5 and 54465.6 as well as by *Swift*/BAT on MJD 54442 and 54467. The double flare seen by MAGIC on MJD 54502.1 and 54507.1 is only seen partly in X-rays. The *Swift*/BAT light curve has a flare on 54503, *RXTE*/ASM has one on 54506.5, which is followed by a second flare on 54512.7. Due to the low temporal density of MAGIC flux points, it cannot be said if there was another flare in γ-rays as well. The second double flare on MJD 54555.9 and 54562, which is seen by MAGIC, is also seen by *RXTE*/ASM on MJD 54555.6 and 54562.6. *Swift*/BAT sees only the first flare on MJD 54555. *RXTE*/ASM sees a flare on MJD 54612.5. This matches the MAGIC flare on MJD 54612.9. The MAGIC flare on MJD 54622.9 is also seen by *Swift*/BAT on MJD 54622 and by *RXTE*/ASM on MJD 54622.6. Additionally, both see a second flare on MJD 54630 (*Swift*/BAT) and 54629.6 (*RXTE*/ASM). This flare cannot be compared to MAGIC because MAGIC did not observe around this date. The two X-ray light curves have two more matching flares on MJD 54649 and 54649.7 as well as on MJD 54697 and 54697.7. There are sometimes small shifts in the position of the flares, which might be caused by the different binning in time in the light curves. After MJD 54800, the two X-ray light curves are at a low emission state and the variability is lower than during the high activity period. This behaviour is comparable to the γ-ray light curve. The γ-ray flare on MJD 54863.1 is also seen by *RXTE*/ASM on MJD 54862.7.

In the Mrk 421 light curve of KVA a lot of structures are visible. Variability is present almost over the whole time range. Only between MJD 54800 and 54900 is a phase of low emission, where no variability is seen. When comparing the KVA light curve to the MAGIC light curve, it can be seen that they are not directly correlated. The flares visible in both light curves don't occur at the same time, but they are shifted relative to each other, whereby it seems that corresponding flares appear first in the optical light curve. As both light curves don't have a flux point every day due to limiting observation conditions, it might be that both did not directly catch the flare, but days before or after. Therefore, the comparison of the flare dates might not be exact on the scale of a few days.
A minimum in the MAGIC light curve on MJD 54476.3 might correspond to a minimum on MJD 54462.2 in the KVA light curve. Both light curves have a good sampling with data points almost every night for the falling and rising edge around this minimum. A flare on MJD 54475.3 for KVA might correspond to the MAGIC flare on 54481.2, however, this might not be the exact position of the flare. Unfortunately, there is no MAGIC data available after this day. The MAGIC flare on MJD 54555.9 could belong to the KVA flare on MJD 54536.1. Three more peaks are visible for KVA on MJD 54597.9, 54605.0, and 54611.9. In the MAGIC light curve two flares on MJD 54612.9 and 54622.9 are seen. For *RXTE*/ASM, three flares are seen around that time as well, namely on MJD 54612.5, 54622.9, and 54629.6. Therefore, it is deduced that the KVA flares on MJD 54597.9 and

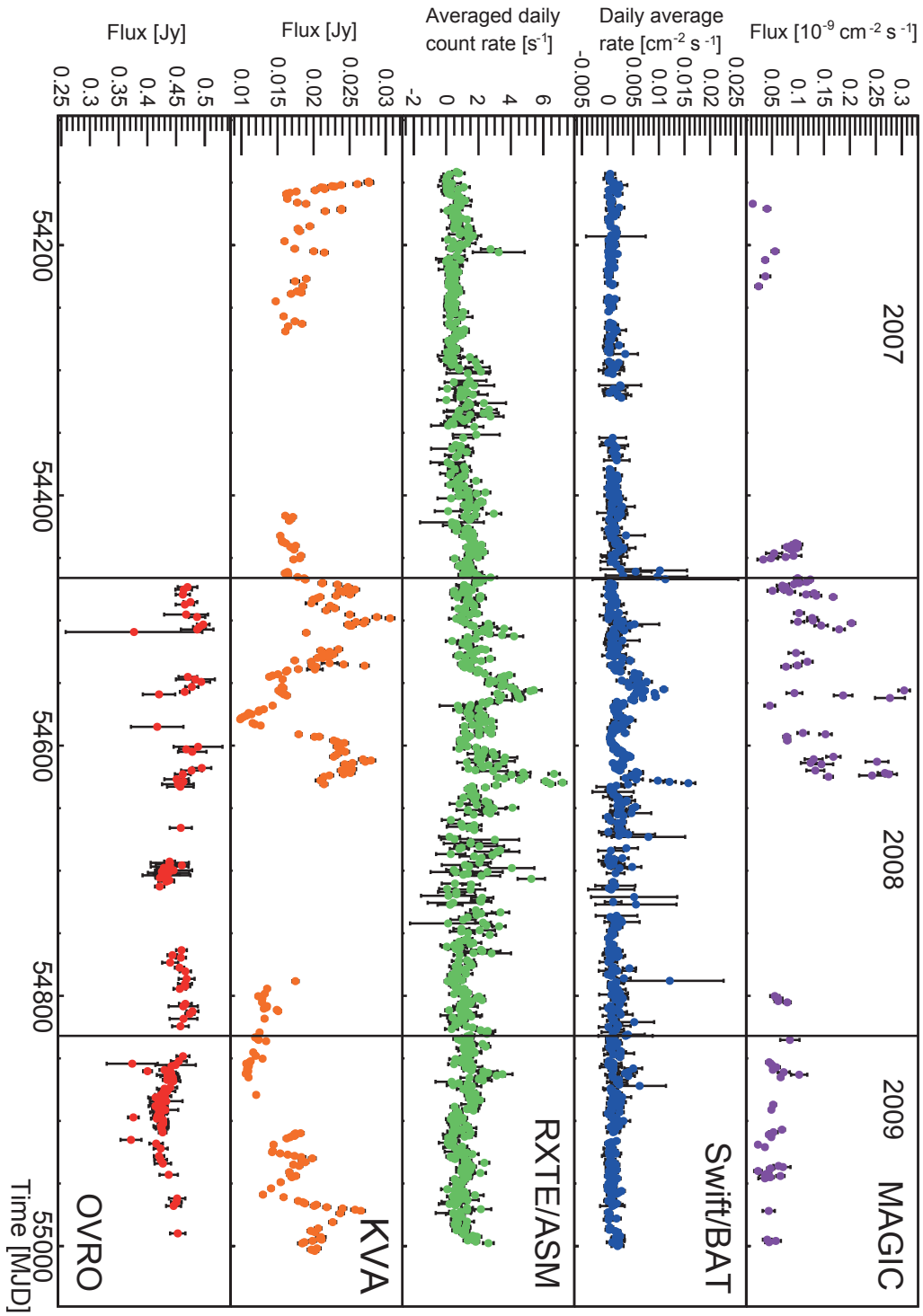

Figure 7.1: Mrk 421 light curves of MAGIC, *Swift*/BAT, *RXTE*/ASM, KVA, and OVRO from February 2007 to June 2009. The black vertical lines represent the division from one year to the next.

54605.0 belong to the MAGIC flares on MJD 54612.9 and 54622.9. The flares in the optical light curve occur between 15 to 20 days earlier than in the γ-ray light curve.

The OVRO light curve shows the first flux points in the beginning of 2008. The light curve doesn't show structures and flares as the other light curves. It seems that there is a behavioural pattern present on larger time scales. From MJD 54473 to 54666 the overall flux level is higher than from MJD 54692 to 54990.

7.3 Variability

To quantify the variability of a light curve, the approach of [Vau03] is used. The fractional variability F_{var} is given in equation 10 in [Vau03] and is calculated as follows:

$$F_{\mathrm{var}} = \sqrt{\frac{S^2 - \overline{\sigma_{err}^2}}{\overline{x}^2}}. \tag{7.1}$$

Here, the variance S^2 of the light curve points is corrected for the measurement errors σ_{err}. This excess variance is normalised by the mean of all N flux measurements $\overline{x}$.
As discussed in [Pou08] and [Ale15b], the error of F_{var} is given by equation 7 in [Pou08]:

$$\Delta F_{\mathrm{var}} = \sqrt{F_{\mathrm{var}}^2 + err\left(\sigma_{NXS}^2\right)} - F_{\mathrm{var}}, \tag{7.2}$$

where $err\left(\sigma_{NXS}\right)$ is given in equation 11 in [Vau03]:

$$err\left(\sigma_{NXS}^2\right) = \sqrt{\left(\sqrt{\frac{2}{N}} \cdot \frac{\overline{\sigma_{err}^2}}{\overline{x}^2}\right)^2 + \left(\sqrt{\frac{\overline{\sigma_{err}^2}}{N}} \cdot \frac{2F_{\mathrm{var}}}{\overline{x}}\right)^2}. \tag{7.3}$$

F_{var} is calculated for all five experiments. To be able to compare the results, it is necessary that the light curves have a comparable sampling in time because time scales are not taken into account in the calculation of F_{var}.
The MAGIC light curve used for the calculation contains nightly data points. This is also the case for the light curve of *Swift*/BAT. For *RXTE*/ASM, KVA and OVRO, the light curves sometimes contain more than one data point in one night. Therefore, data points from one night were merged in order to obtain comparable results. For KVA and OVRO data points of one night were weighted equally when averaging the flux values. For *RXTE*/ASM the information about the observation length was available so that the flux values were weighted according to their number of dwells.
Where F_{var} is negative either no variability is present or the telescope is not sensitive enough to detect it [Ale15b]. If this occurs, the value is set to 0.

7.3.1 Variability for the whole time range

The results for the whole observation period from February 2007 to June 2009 can be seen in Figure 7.2. All values are noted down in Table B.1.
F_{var} is shown for the frequency ranges of the instruments. These ranges are represented by the width of the data points in frequency.

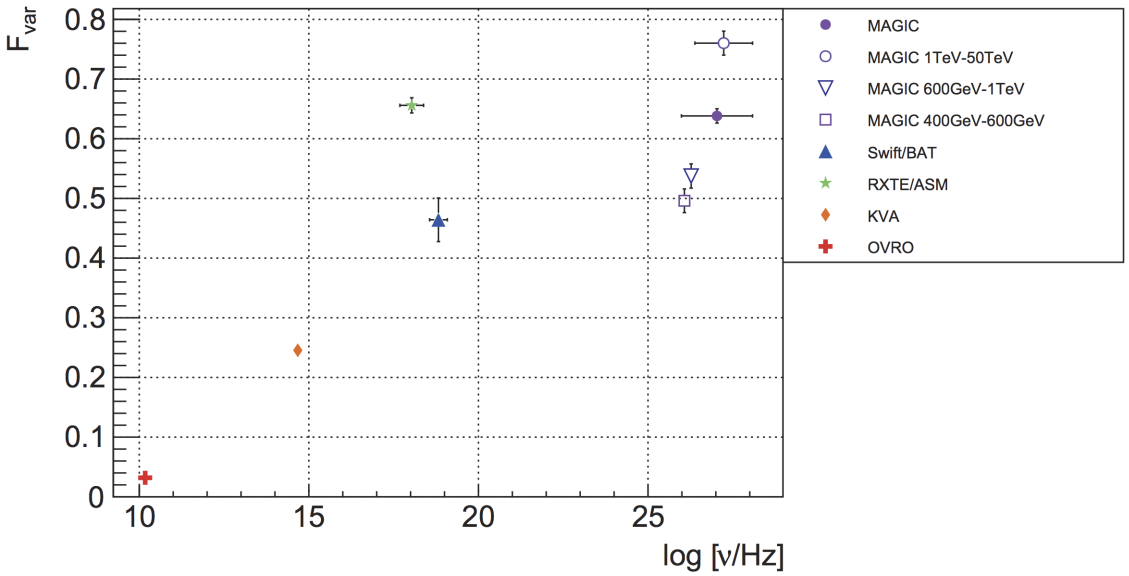

Figure 7.2: Variability for all five instruments for the whole time range. The width in the frequency ν represents the frequency range in which each instrument measures. The open markers for MAGIC show the results for the three different energy ranges.

In the radio range almost no variability ($F_{\text{var}} \approx 0.03$) is seen. In the optical light curve F_{var} is higher than in the radio light curve, but with $F_{\text{var}} \approx 0.25$ it is still lower than for the higher frequency ranges. *RXTE*/ASM shows a high variability of $F_{\text{var}} \approx 0.66$. For *Swift*/BAT it drops to about 0.46. For MAGIC it rises again to about 0.64. Additionally, the MAGIC light curve was separated into three different energy ranges, which was already shown in section 5.5. The three light curves range from 400 GeV to 600 GeV, from 600 GeV to 1 TeV and from 1 TeV to 50 TeV. F_{var} is determined separately for these three light curves. The results are added in Figure 7.2 with open markers. Here, the variability ranges from about 0.50 for the lowest energy range to about 0.76 for the highest energy range.
In general it can be said that the variability increases with increasing frequency. However, *RXTE*/ASM has the highest variability when only the MAGIC light curve in the whole energy range is considered.

7.3.2 Variability for the different observation periods

As discussed in section 5.4, the MAGIC light curve of Mrk 421 contains large gaps of several months every year from the end of June until the end of November when the source is not observable. Furthermore, the light curve has different flux levels and variability stages in the different observation periods. Therefore, F_{var} was determined again for all five telescopes for the three observation periods. The exact dates of the observation periods can be found in Table B.2. The results are shown in Figure 7.3 and noted down in Table B.2.

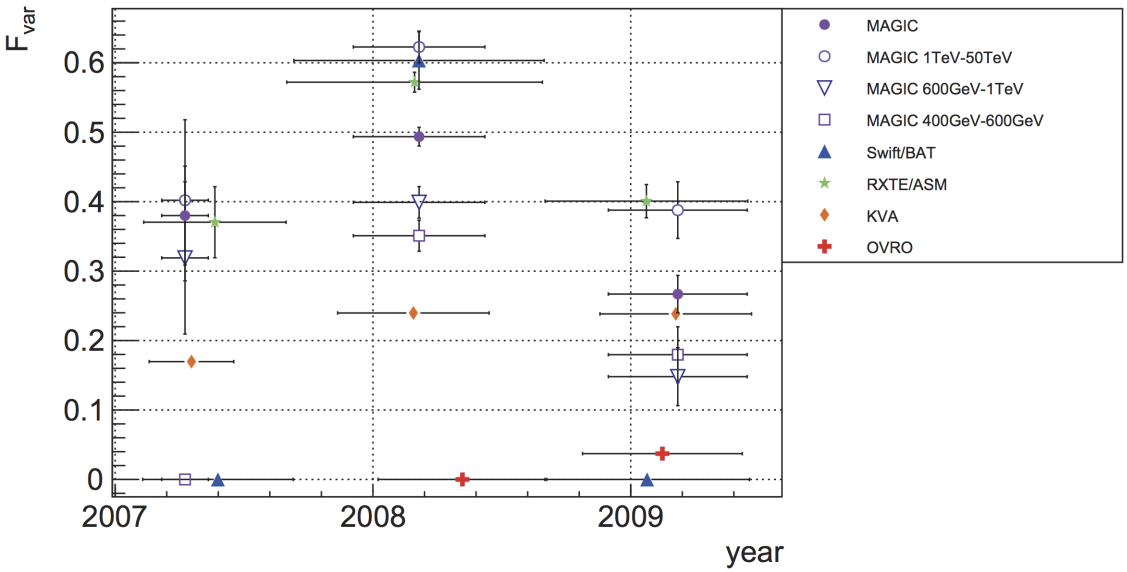

Figure 7.3: Variability for all five instruments for the three different observation periods. The width in time represents the time range of the observation period. The open markers for MAGIC show the results for the three different energy ranges.

In the radio frequency range, data recorded by OVRO is only available from January 2008 to June 2009. Therefore, the variability is only determined for two of the three periods. In 2008, no variability is detected. In 2009, with $F_{\text{var}} \approx 0.04$ almost no variability is present. The optical light curve from KVA shows almost the same variability in all three years. It ranges from about 0.17 to 0.24. However, for the higher energies more changes are visible.
For *RXTE*/ASM, *Swift*/BAT and MAGIC F_{var} is highest in 2008, which was already discussed in section 7.2. For *RXTE*/ASM this means that the variability is ranging from about 0.37 to 0.57. For *Swift*/BAT no variability is seen in 2007 or 2009. In 2008 it has a high value of $F_{\text{var}} \approx 0.60$. F_{var} for MAGIC varies from about 0.27 to 0.49.
When considering the three different energy ranges of the MAGIC light curve, it can again be seen that the variability is highest for the highest energy range. In the yearly comparison, F_{var} is again highest in 2008. There, the MAGIC light curve in the energy range from 1 TeV to 50 TeV reaches $F_{\text{var}} \approx 0.62$ as maximum value for the variability.

7.3.3 Conclusions on variability

Conclusively, it can be said that in general the variability increases with increasing energy. The results of this variability study clearly show that in the years 2007 and 2009 F_{var} is lower than in 2008. This confirms the assumptions that have been made in section 7.2. There, it was discussed that the γ-ray and X-ray light curves have a lower variability in 2007 and 2009 than in 2008. The KVA telescope shows a comparable variability in all three periods. The radio light curve by OVRO shows almost no variability.

For the three MAGIC light curves, which are separated into three different energy ranges, it can be seen that the light curve in the highest energy range from 1 TeV to 50 TeV has the highest variability. This is in agreement with the conclusions of section 5.5, where an increase of the variability was seen with increasing energy.

7.4 Correlations

To investigate if the emission in the different wavebands is directly correlated or shifted in time, the cross-correlations of sets of light curves can be determined. For this the method proposed by [Ede88] is applied, where the Discrete Correlation Function (DCF) is determined. The scripts used here were provided by N. Nowak.

7.4.1 Theoretical background

For two light curves a and b, the unbinned discrete correlation UDCF_{ij} is calculated for a pair (a_i, b_j) with a time lag $\Delta t_{ij} = t_j - t_i$. In [Ede88] it is defined as

$$\mathrm{UDCF}_{ij} = \frac{(a_i - \bar{a})\left(b_j - \bar{b}\right)}{\sigma_a \sigma_b} \,. \tag{7.4}$$

Here, $\bar{a}$ is the average flux of light curve a and σ_a its standard deviation. The equivalent is valid for light curve b. A positive result stands for a correlation, a negative for an anti-correlation of the data points. Then the average $\mathrm{DCF}(t)$ in a bin of width τ is calculated by the average of all n UDCF_{ij} in this bin. The corresponding pairs (a_i, b_j) for the bin at time t are assigned to it, if $t - \Delta\tau/2 \leq \Delta t_{ij} \leq t + \Delta\tau/2$. [Ede88]
The errors for the DCF given in [Ede88] are only suitable for light curves, which contain uncorrelated data points [Utt03]. They are therefore not included here. With the red noise data in our light curves, an approach based on MC simulations of light curves is used here to obtain confidence limits. [Ale15a]
For the determination of these confidence limits, 1000 light curves are simulated for each telescope. The exposure times and the sampling rates of each telescope are taken into consideration. Additionally, the simulated light curves follow a Power Spectral Density (PSD) as similarly as possible as the PSD of the original light curve. The PSD describes, like F_{var}, the variability of a light curve, but it corresponds to the variability of the light curve as a function of the time scale [Cha08]. For red noise data like the light curves given here, the PSD follows a power law. The light curves are simulated following a power law with the slope α from -1.0 to -2.9 in steps of 0.1. The set of simulated light curves with the PSD, which matches the PSD of the original light curve, is determined with the PSRESP method as described in [Cha08]. The DCF is then calculated for each of the 1000 simulated light curves with the matching PSD of one telescope and the original light curve of another telescope. From the distribution of these results, 95% and 99% confidence bands are determined. [Ale15a]
In the following plots these confidence bands of 95% and 99% for correlations and for anti-correlations are shown in blue and green, respectively. The median of all 1000 DCFs is shown in red. The resulting DCF values are shown as black dots. In the case that a

value lies above the confidence bands it is considered as a significant correlation. In the case it lies below the confidence bands it is a significant anti-correlation. Values, which lie between the confidence bands, are not significant.

7.4.2 Results

In section 7.2 it was discussed that the γ-ray light curve and the two X-ray light curves seem to be directly correlated. The peaks are sometimes shifted by up to 0.9 days. Sometimes this shift is even larger because data points are missing and others appear as a corresponding flare, but on a slightly shifted date. When the binning of two light curves is different by 0.5 days, the calculated DCF of this day would be assigned to a time lag of 1 day. To circumvent a possible bias due to unequal binning in the light curves, a bin width of $\tau = 2$ days is chosen.
When the light curve of the KVA telescope was compared to the MAGIC light curve, it could be seen that the flares happened about 15 to 20 days earlier in the optical than in the γ-ray waveband. Therefore, a time lag of -50 to +50 days will be examined. This range of time lags guarantees that the possible seen time difference between the optical and γ-ray light curve will be included in the DCF study. It also gives room to the possibility of finding more correlations at even larger time lags, which might be interesting for cross-correlations with the radio light curve. When comparing it to the other light curves, correlations cannot be seen by the naked eye.
Δt_{ij} is calculated by subtracting t_j of the second light curve from t_i from the first light curve. The MAGIC light curve is always selected as the second light curve. This means when a correlation is found at e.g. +10 days flares appear 10 days later in the MAGIC light curve than in the first light curve. When a correlation is found at e.g. -10 days the flares in the MAGIC light curve appear 10 days earlier than in the first light curve.
The DCF was once calculated for the whole time period from February 2007 to June 2009. Additionally, it was determined for the other three time periods separately. The exact dates of the time ranges were already mentioned before and can be found in Table B.2. The light curve in the first time period for MAGIC from February to May 2007 contains only 6 data points. Therefore, the correlations are not calculated for this time period. The results would not be representative because the few data points might not reflect the real behaviour of the source.

Swift/BAT and MAGIC

The correlation results for the *Swift*/BAT and MAGIC light curves are shown on the left hand side of Figure 7.4. In panel (a) the correlations were calculated for the whole time period from February 2007 to June 2009, in panel (c) from September 2007 to August 2008, and in panel (e) from September 2008 to June 2009.
First of all, a DCF of about 0.72 at a time lag of 0 days can be seen, which shows that the light curves are directly correlated. This was already discussed in section 7.2, when the positions of the flares were seen at the same dates. At a time lag of -6 days a DCF of about 0.86 is seen. This might be caused by the double flare on MJD 54622 and 54630, while MAGIC only sees the one flare on MJD 54622.9. Between the time lags of -8 to +4 days the DCF values also lie above the confidence limit. These might appear because the flares are usually not just on one day, but on a wider time scale. Due to this the light

curves still seem correlated even if they are shifted by a small amount of days. There are also DCF values above the 99% confidence limit for larger time lags. However, their values are mostly below a DCF of 0.5. They lie above the confidence limit because of the high activity period in 2008. Therefore, it often happens that the two light curves both have a high flux above the average at the same time, also because many points in the time period of 2008 lie above the average at the same time in both light curves.
When comparing the results from the whole time period in panel (a) of Figure 7.4 to the results from the high active time period in panel (c), it can be seen that DCF values, which were above the confidence limit before, are now mostly below. The time lags from -8 to +2 days are still all above the confidence limit, again with the highest values at a time lag of 0 and -6.
When looking only at the quiet flux of the third time period, the direct correlation of the light curves is not found any more. A time lag of +18 days has a relatively low DCF value of about 0.44, which is above the confidence limit.

***RXTE*/ASM and MAGIC**

The correlation results of *RXTE*/ASM and MAGIC are similar to the results of *Swift*/BAT and MAGIC. They are shown on the right hand side of Figure 7.4. The results for the whole time range are again in the top panel (b), in panel (d) the results of the high activity period from September 2007 to August 2008 are shown and in panel (f) at the bottom the results for the quiet emission period from September 2008 to June 2009 are shown.
Again, the direct correlation of the two light curves can be seen in a DCF of about 0.85 at a time lag of 0 days. This can be explained by the many flares, which occurred on the same dates. At a time lag of -6 days there is again a second peak with about the same DCF value. This corresponds to the same double flare of *Swift*/BAT, which was discussed above. MAGIC has seen a flare on MJD 54622.9, which *RXTE*/ASM has seen as well on MJD 54622.6. Additionally, a flare was recorded by *RXTE*/ASM on MJD 54630.
On MJD 54502.1 and 54507.1 a double flare in γ-rays was recorded by MAGIC. *RXTE*/ASM has only seen a flare on MJD 54605.6, which corresponds to the second of the MAGIC flares. A second flare is seen by *RXTE*/ASM 6 days later on MJD 54512.7. This can explain the correlation of the light curves at a time lag of -6 days as well.
The time lags between -10 and +2 days all have a DCF value above 0.5. Again this shall be explained by the already high fluxes around the flare days.
Again the behavioural pattern can be seen that more time lags seem to be correlated because they lie above the confidence limit. However, their values are smaller than 0.5. They can be explained as above because of the high activity period in 2008, which makes the light curves correlated at several time lags. When only considering the high emission period, the time lags further out don't lie above the upper confidence limit any more.
The resulting DCF values for the quiet third time period are all below 0.5. The correlation at 0 as well as for -2 and +2 days is seen. The flare on MJD 54863 was seen in both light curves. The other correlations at -28, -26, +22, and +32 days might be caused by further small peaks in the *RXTE*/ASM light curve.

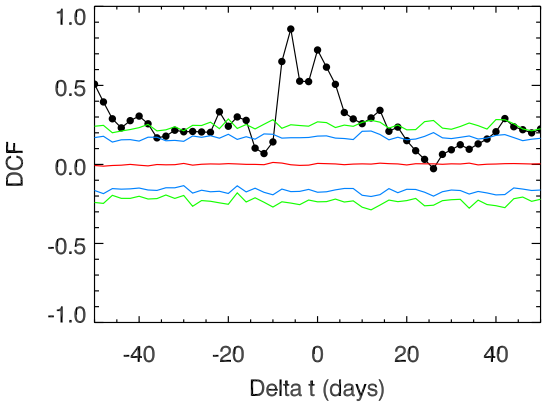

(a) *Swift*/BAT and MAGIC, 02/2007 to 06/2009.

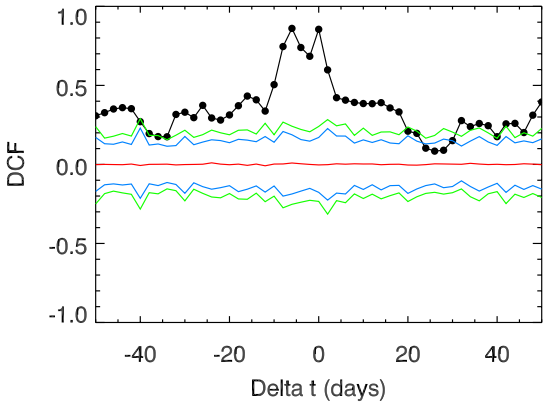

(b) *RXTE*/ASM and MAGIC, 02/2007 to 06/2009.

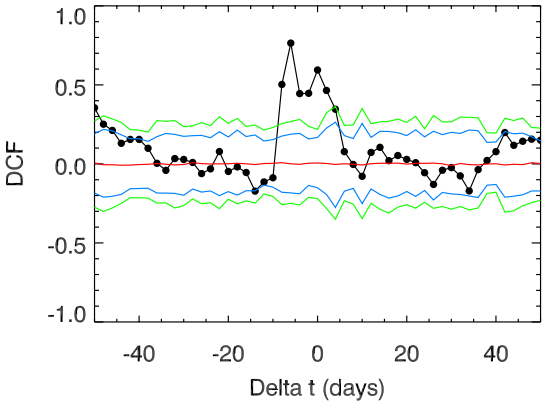

(c) *Swift*/BAT and MAGIC, 09/2007 to 08/2008.

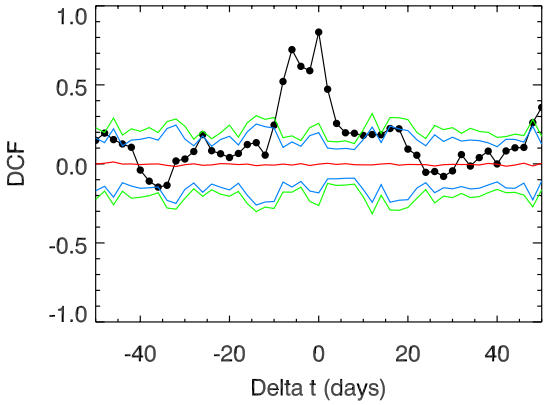

(d) *RXTE*/ASM and MAGIC, 09/2007 to 08/2008.

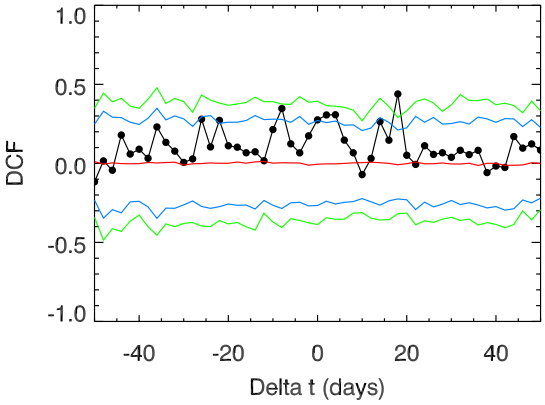

(e) *Swift*/BAT and MAGIC, 09/2008 to 06/2009.

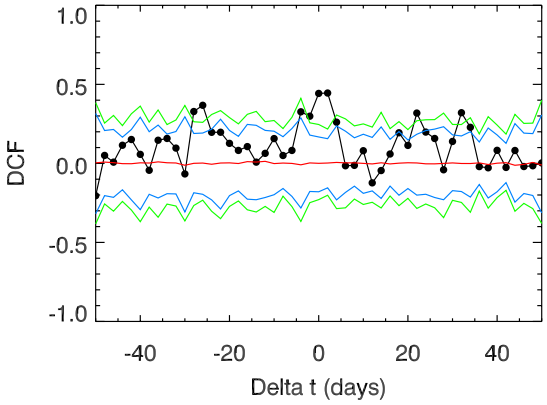

(f) *RXTE*/ASM and MAGIC, 09/2008 to 06/2009.

Figure 7.4: DCF results for *Swift*/BAT and MAGIC as well as for *RXTE*/ASM and MAGIC. On the left the DCF is shown for *Swift*/BAT and MAGIC, on the right for *RXTE*/ASM and MAGIC. The top row shows the results for the whole time period from February 2007 to June 2009, the middle row from September 2007 to August 2008, and the bottom row from September 2008 to June 2009. The red line is the median of all 1000 DCFs. The blue and green lines represent the 95% and 99% confidence limits.

KVA and MAGIC

On the left hand side of Figure 7.5 the DCF results of KVA and MAGIC can be seen. In panel (a) the results for the whole time period are shown. The first thing that can be seen is that there is no high peak at a time lag of 0 days. The DCF value of many time lags between -10 and +26 days lies above the confidence limits. Only four of them have a DCF value higher than 0.5, namely for +4, +8, +10, and +26 days. Thus, it is assumed that generally the structures appear earlier in the optical light curve than in the γ-ray light curve. There are some anti-correlations for a time lag of -26 days and time lags between 38 to 50 days.

The consideration of only the high activity period results in fewer time lags for which the light curves are correlated. This can be seen in panel (c) of Figure 7.5. These time lags are namely +4, +8 to +14, +20, +24, and +26 days. However, only the time lag of +10 days has a DCF value larger than 0.5. Already the second highest value for a time lag of +14 days lies at 0.47. There are again anti-correlations for time lags between -32 to -20 days, of -16 days, and between +40 and +50 days.

The light curves of KVA and MAGIC show no correlations for the quiescent third time period. The results are shown in panel (e) of Figure 7.5. Only some anti-correlations are seen.

OVRO and MAGIC

The results of the correlation study between the light curves of OVRO and MAGIC are shown on the right hand side of Figure 7.5. First of all, it can be seen that the two light curves are not directly correlated for a time lag of 0 days. The highest peak appears for a time lag of +4 days. Other DCF values above the confidence limit appear for several more days. The highest DCF values appear for time lags between +4 and +22 days. Therefore, these two light curves are rather correlated for positive time lags, which means that structures seem to appear first in the radio light curve.

The MAGIC and OVRO light curves were also tested for the correlations in the second and third time period. In panel (d) the results for the high activity period of MAGIC are shown. For time lags of +10 and +12 days correlations with DCF values of about 0.73 can be seen. Then, anti-correlations for time lags of -30, -28, -26, and +46 are observed.

The light curves in the third time period show a correlation at a time lag of +24 days with a DCF value of about 0.54. There is again anti-correlation seen for a time lag of -34 days.

Other cross-correlations

The cross-correlations of all other possible combinations of the other telescopes are determined as well. The resulting plots are shown for the time period from autumn 2007 to summer 2008 in Figure B.4.

At first a test is carried out in which the correlations of the MAGIC light curve with itself are determined. With the high DCF value at a time lag of 0 days, it is shown that the calculation of the DCF works. This is shown in panel (a) of Figure B.4. There it can be seen that there are additional correlations found for time lags of -60 and +60 days. This corresponds to about double the time which was found as a period length of 31 days in chapter 6, where the periodicity search in the light curve of Mrk 421 was discussed. Otherwise, this could be caused due to the observational gaps during full moon. There are two additional correlations found at -10 and +68 days.

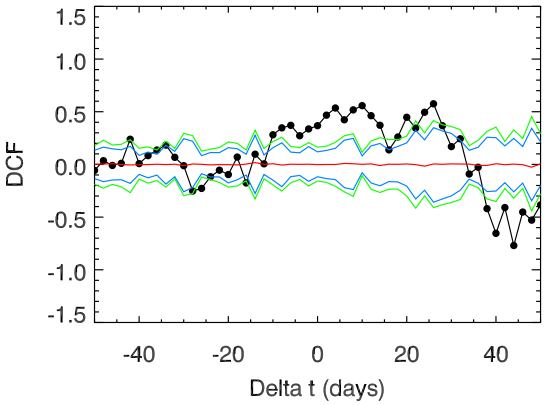

(a) KVA and MAGIC, 02/2007 to 06/2009.

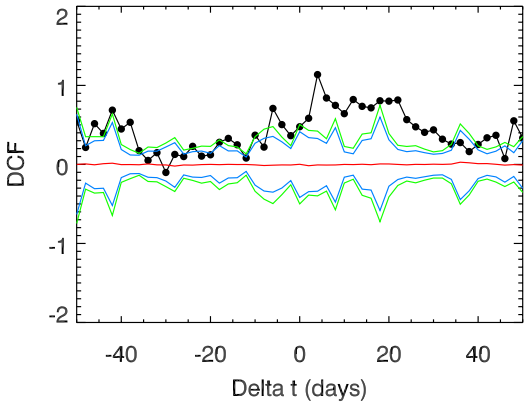

(b) OVRO and MAGIC, 02/2007 to 06/2009.

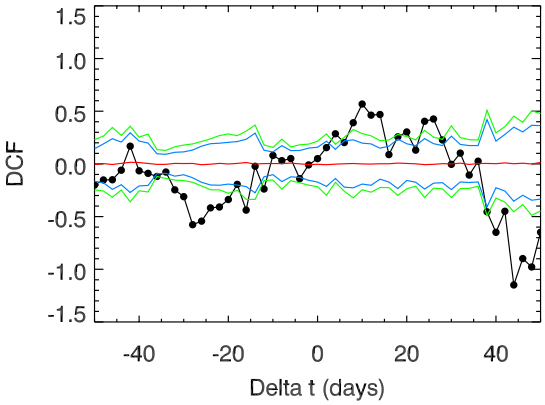

(c) KVA and MAGIC, 11/2007 to 06/2008.

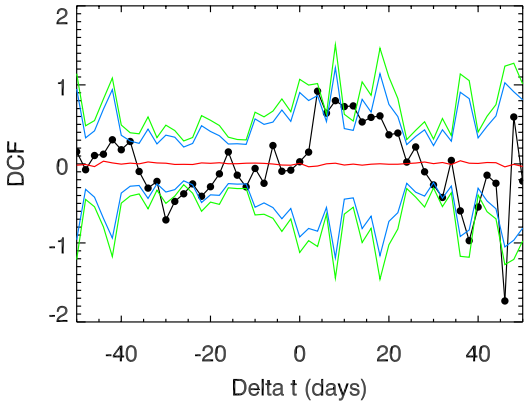

(d) OVRO and MAGIC, 12/2007 to 09/2008.

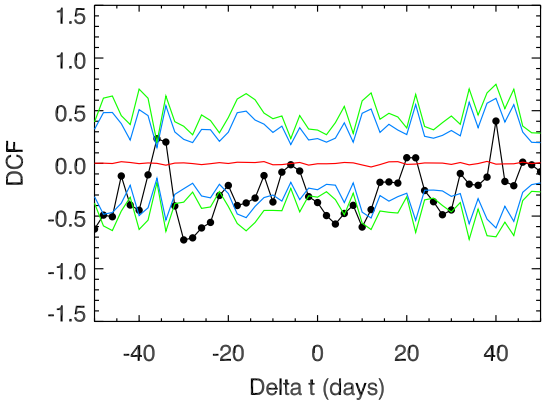

(e) KVA and MAGIC, 11/2008 to 06/2009.

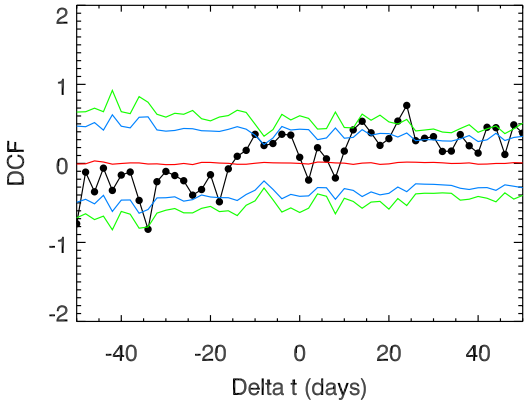

(f) OVRO and MAGIC, 10/2008 to 06/2009.

Figure 7.5: DCF results for KVA and MAGIC as well as for OVRO and MAGIC. On the left the DCF is shown for KVA and MAGIC, on the right for OVRO and MAGIC. The top row shows the results for the whole time period from February 2007 to June 2009, the middle row from autumn 2007 to summer 2008, and the bottom row from autumn 2008 to June 2009. For the exact dates, see the corresponding caption of each figure. The red line is the median of all 1000 DCFs. The green and blue lines represent the 95% and 99% confidence limits.

In panel (b) of Figure B.4 the correlations of the *Swift*/BAT and the *RXTE*/ASM light curves are shown. Their light curves are directly correlated with 0 days time lag.
The DCF results for *Swift*/BAT and KVA are shown in panel (c) and for *RXTE*/ASM and KVA in panel (d) of Figure B.4. Both plots show similar features. For *Swift*/BAT no correlations are found for the whole time period nor any of the three separate time periods. For *RXTE*/ASM the highest DCF value is given at a time lag of -10 days. This means that the flares occur about 10 days earlier in the optical light curve. During the quiescent first and third time periods, no correlations are found.
The DCF results of the correlations of OVRO with *Swift*/BAT and *RXTE*/ASM are shown in panel (e) and (f) of Figure B.4. They again have a similar shape. Both have a maximum DCF at a time lag of -10 days. This means that some structures might appear first in the radio light curve.
For the light curve of KVA and OVRO no conclusions are drawn here because the DCF results for the whole time period and the second and third time periods don't agree with each other. The resulting plots are not shown here.

7.4.3 Conclusions on cross-correlations

With the determination of the DCF the cross-correlations between the different light curves were investigated. It could be shown that both X-ray light curves are directly correlated to the MAGIC light curve, which can be explained by several matching flares in all three light curves. This correlation is smeared out because the flares have a rising and falling edge. A second peak at a time lag of -6 days can be explained by additional flares in both X-ray light curves following flares, which have a match in the MAGIC light curve. Correlations are found for the whole time period as well as for the high activity and quiet time periods.
It could be shown that the flares in the optical light curve appear +10 to +14 days earlier than in the γ-ray light curve. This behaviour was already described in section 7.2. The flares always appear first for the KVA light curve when comparing it to the MAGIC light curve. When the light curves of the whole time period were compared, it could only be stated that correlations are found for positive time lags, meaning that the optical light curve comes first. When comparing only the light curves during the high active period from November 2007 to June 2008, the DCF values for time lags between +10 and +14 days lie above the confidence limit. For the low activity period no correlation is found.
The same is true for the correlations between the X-ray light curve of the *RXTE*/ASM and KVA. For the high active second time period correlations are found, which confirm that flares occur first in the optical light curve. For the first and third time periods, which show a quiet emission of Mrk 421, no correlations are found.
For OVRO it could be shown that there might be a correlation with the γ-ray light curve at a positive time lag. For the whole time period several days are found above the confidence limit. When only the data from the end of 2007 to the middle of 2008 are considered, a correlation is found for a time lag between +10 to +12 days. For the low activity period from the end of 2008 to the middle of 2009, the light curves are not correlated at these time lags any more. Then a correlation appears for +22 days. Therefore, no general conclusion is drawn from the comparison of these two light curves. The features in the radio light curve also appear about 10 days earlier than in the X-ray light curves.

It can be concluded that the γ-ray light curve by MAGIC and the X-ray light curves by *Swift*/BAT and *RXTE*/ASM are directly correlated. The comparison of the MAGIC and *RXTE*/ASM light curves to the optical light curve by KVA shows that the flares always appear about 10 to 14 days earlier in the optical energy range than in the higher energy ranges. Additionally, it can be said that the results are dominated by flares in the high activity period in the light curves.

7.5 Spectral energy distribution

In order to produce a SED of Mrk 421 data from other telescopes are needed. For this purpose the Italian Space Agency (ASI) Data Center (ASDC)[4] can be considered. A large database with spectra from different instruments for many sources is available [Str11]. Mrk 421 data are available from the radio band to TeV γ-rays, whereby in the following only MAGIC data from this thesis are shown for the TeV energy range and none of the available MAGIC data from the ASDC. The shown data include data from OVRO in the radio band and from the KVA in the optical band. These points are retrieved from the light curves shown in Figure 7.1. All instruments used for the production of the SED are listed in Table 7.1 with the waveband they cover. For one part of the data the recording

Table 7.1: List of instruments for the SED of Mrk 421. The waveband of the instruments and, if known, the time range of the measurements are listed as well.

Abbreviation	Reference	Waveband	Time range [MJD]
NORTH	[Whi92]	radio	no info
DIXON	[Dix70]	radio	no info
JVASPOL	[Jac07]	radio	no info
OVRO	see section 7.2, [Ric11]	radio	54473 - 54990
2MASS	[Cut03]	infrared	no info
SDSS10	[Ahn14]	optical	no info
USNO	[Mon03]	optical	no info
KVA	see section 7.2, [Tak08]	optical	54149 - 55004
Catalina	[Dra09]	optical	54158 - 54975
2XMM	[Wat09]	soft X-ray	54229 - 54976
XMMSL1	[Sax08]	soft X-ray	54224
ARIEL	[War81]	soft X-ray	no info
BAT39	[Cus10a]	hard X-ray	53341 - 54526
BAT54	[Cus10b]	hard X-ray	53341 - 54983
IBISSG4	[Bir10]	hard X-ray	52672 - 54558
BAT58	[Bau10]	hard X-ray	53430 - 55256
BAT70	[Bau13]	hard X-ray	53341 - 55470
AGILE	[Pit09]	GeV γ-ray	54290 - 54648
Fermi	[Nol12]	GeV γ-ray	54683 - 55017
MAGIC	this work	GeV to TeV γ-ray	54167 - 54997

[4] `tools.asdc.asi.it/SED`, downloaded on 11th August 2014.

date or time range is available, whereas for the other part it is not. This is written down in the table as well. For a more detailed description of the instruments, the user is referred to Table B.3 and the references therein or in Table 7.1. The resulting SED of Mrk 421 is shown in Figure 7.6.

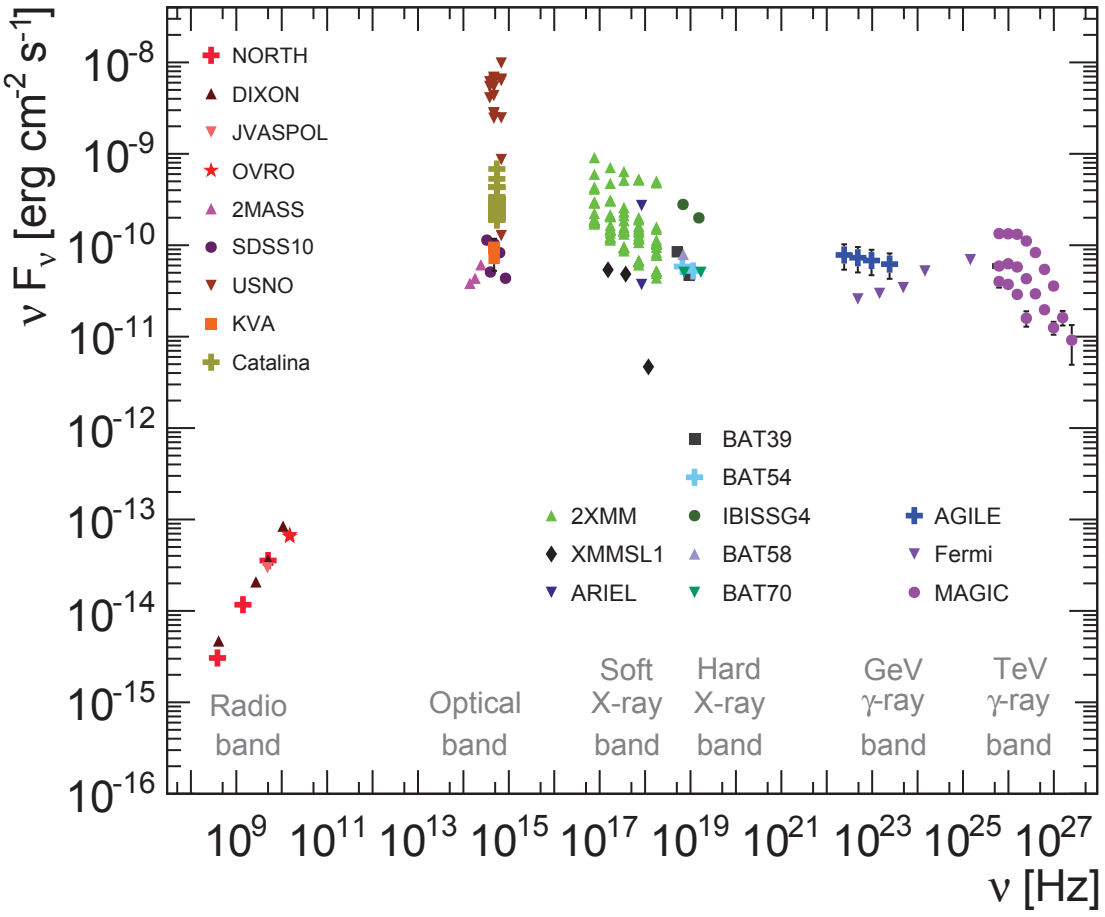

Figure 7.6: SED of Mrk 421 with data from this thesis and from the ASDC. The names of all instruments are given.

The overall two bump structure typical for blazars can be seen. The rising edge in the radio band is covered by four radio telescopes, namely NORTH, DIXON, JVASPOL, and OVRO. Except for OVRO no info about the recording time range of these data is given in the ASDC. The infrared and optical data were recorded by 2MASS, SDSS10, USNO, KVA, and Catalina, whereas only for the latter two instruments are the recording time ranges known. The data by the KVA are corrected for the contribution of the host galaxy. It can be seen that this is not the case for the data of USNO and Catalina. Therefore, an additional feature in the optical waveband is added to the two bump structure of the SED. The peak of the synchrotron peak lies between the optical and the X-ray data points. According to [Wu 09] the peak frequency is at $10^{16.4}$ Hz.

The data in the X-ray bands describe the falling edge of the first bump. The data shown here are from 2XMM, XMMSL1, ARIEL, IBISSG4 and the BAT on board the *Swift* satellite after summarising the results of different observation periods. This falling edge is spread over a wide range in νF_ν, e.g. about one order of magnitude for 2XMM at each frequency ν. This is caused by the different flux states during the large time period of more than two years.
The second bump of the SED is described by data from AGILE, *Fermi*, and MAGIC. A spread in height can again be seen, especially for the MAGIC data. This has already been discussed in section 5.7 and is caused by the different flux states.

In order to assign the different spectral points to the overall flux state, the SED is investigated in different time periods. The three time periods are again the time periods from before, namely from spring to summer 2007, from autumn 2007 to summer 2008, and from autumn 2008 to summer 2009. Mrk 421 has been in a quiescent emission state in the first and third time periods. In the second time period it was in an active emission state.
In section 5.7 it has been shown that the MAGIC spectrum of Mrk 421 changes when the overall flux level changes. In order to see if these changes are also visible in other energy ranges, the SED is produced for the three time periods. Therefore, all of the above shown data, which can exclusively be assigned to one of the three time periods, are included in Figure 7.7.
Data without time information are not taken into account. Spectral points, which are average results from a time span larger than one time period, are not considered. The shown spectral points from Catalina and 2XMM are averaged values over each time period. The MAGIC spectra were shown before in Figure 5.15.
All data from the first time period (2007) are shown in green, the data from the second time period (2007-2008) in red, and from the third time period (2008-2009) in blue. The exact dates or time ranges of all spectral points are listed in Table B.4.
The shown data include data from OVRO in the radio band and from the KVA in the optical band. Additional data in the optical band were recorded by Catalina. The data from these three instruments are comparable in the different time periods.
The spectral points of the falling edge of the synchrotron peak in the X-ray range are from 2XMM and XMMSL1. Here, a clear difference between the three time periods can be seen. The spectral points lie highest in the active second time period, when the flux state was highest in MAGIC. Additionally, the spectrum is flatter in the second time period than in the other two time periods. The overall flux state was lower in MAGIC in the third time period and it was the lowest in the first time period. The same behaviour is seen in X-rays. The spectral points from the third time period from 2XMM are below the ones from the second time period by about a factor of two. The spectral points from the third time period lie below the data from the other two time periods, whereby the flux points are lower than in the third time period by about a factor of two. The results from the slewing mode of XMM lie even below the ones from the pointing mode. The results from the slewing mode were recorded on one day, which might have been during a very low activity phase, whereas the 2XMM results are average results from several observations.
The second bump of the SED in 2007 only includes MAGIC data. It lies below the two other MAGIC spectra. In the second time period AGILE recorded data in the low energy γ-ray band. Its data points might seem like the prolongation of the falling edge of the

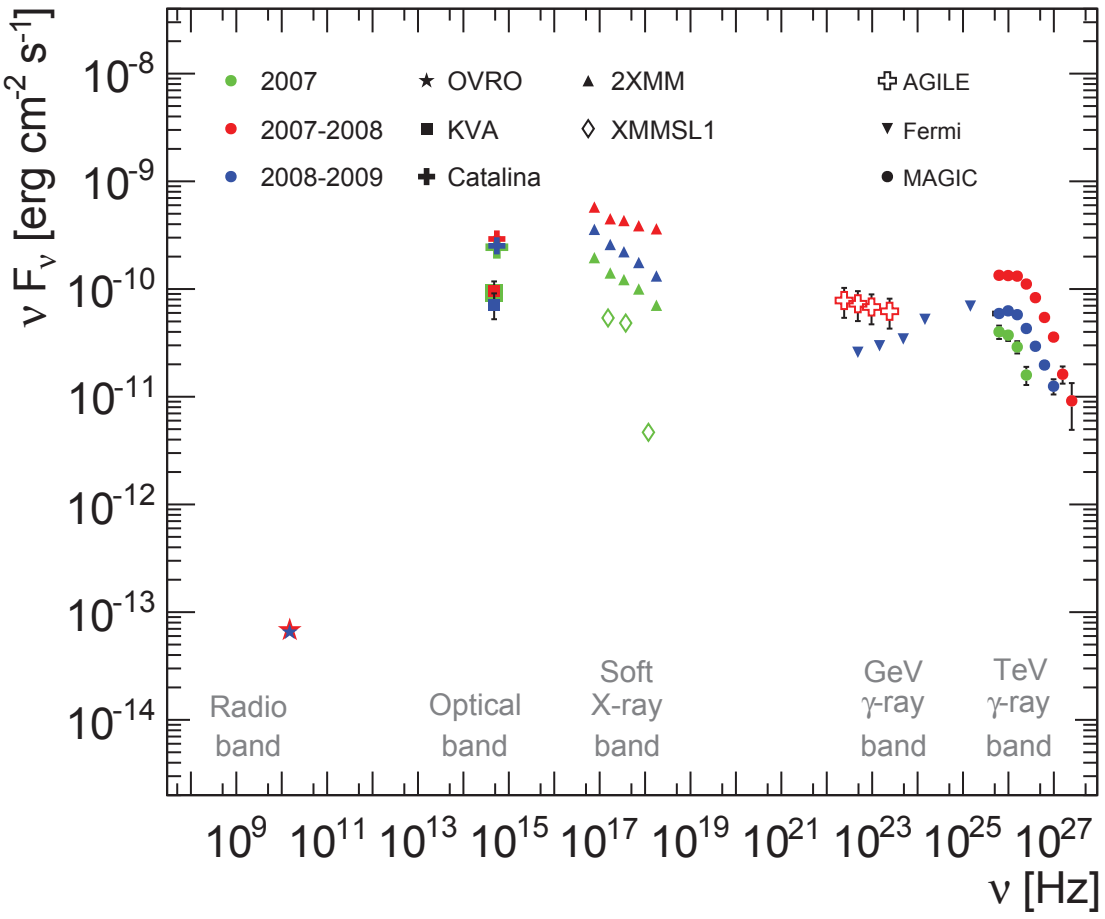

Figure 7.7: SED for the three different time periods (for the exact dates see explanation in the text). The colour code indicates the different time periods. Each instrument is represented by the markers given above.

synchrotron peak. The MAGIC spectrum lies highest in this time period. It is higher than in the third time period by about a factor of two and higher than in the first time period by a factor of four. In the third time period *Fermi* was able to cover the gap up to the MAGIC observations. Thanks to the launch of the *Fermi* satellite in August 2008 [Nol12], the second SED bump can be completely covered by it and Cherenkov telescopes like MAGIC. The *Fermi* and MAGIC data in the third time period completely describe this bump. Most importantly, a peak position of around 10^{25} Hz can be estimated for this time period. *Fermi* covers the rising edge of it and MAGIC the falling edge. The data points lie below the ones of the high active second time period.
This comparison of the spectral energy distributions in the three different time periods has shown that both peaks behave similarly. It can be said that the spectral points in the X-ray band are different by a factor of about four between the first and second time period. The same is true for the MAGIC data points. During the high activity time period the spectral points are higher than during the quiescent flux state in the first time period by

a factor of four. This synchronous behaviour of the two bumps favours the SSC emission model. Data from AGILE in the high active second time period might hint towards a shift of the dip between the two bumps towards higher frequencies when the overall flux state rises. Due to the limited amount of spectral points in this data set and the limited number of SEDs in a high state, no further conclusions are drawn here.

Former results from SED modelling

In former publications the application of different emission models to the SED of Mrk 421 was discussed. Some of these results are summarised in the following.
Fits of the SSC model have been successfully applied to SEDs of Mrk 421. This was e.g. discussed in [Acc11] and [Acc09], where this model was fitted to SEDs in the time range from 2006 to 2008. This result is supported by the modelling of the SED during the June 2008 flare as discussed in [Don09].
On eight days between January and April 2008 simultaneous data were available in the X-ray and γ-ray bands. For these eight selected days the SSC emission model was applied. It was again able to describe the SEDs well, but it needed large Doppler factors of $\delta > 40$. A model with multiple emission regions was proposed. These regions could be moving at different speeds and synchrotron photons from each region could be IC scattered in other emission regions. [Ale12a]
The one-zone SSC model was again the basic emission model for the average SED of Mrk 421 during the first half of 2009. This SED was already shown in Figure 2.5. It could explain the SED reasonably well. But it is stated that the one-zone model simplifies the problem and that there could be more than one emission region present. Additionally, a hadronic model was tested. It included e.g. the synchrotron emission of protons or muons as well as photons of decaying neutral pions. This model was able to describe the SED, too, but some of the model parameters seemed extreme. [Abd11]
In March 2010 Mrk 421 was again in a high active state. SEDs were produced for 13 days of this month. Each of them could well be modelled by a one-zone SSC model. However, some of the higher active days featured narrower peaks in the SED than other days. Therefore, a second emission zone of smaller size was added to the first zone in the SSC model. This second zone could be responsible for emission in the X-ray and γ-ray waveband and the change of the spectral shape in these wavebands. Additionally, it could explain the missing correlation between the optical and radio wavebands with the X-ray and γ-ray bands in 2010. [Ale14b]
However, for the time period from 2003 to 2004 the SED could not be modelled by the SSC emission scenario. During this time period some flares in the X-ray and in the γ-ray band showed short delays. It is hard to describe this given fact with a simple one-zone SSC emission scenario. After a second emission zone was added, a good fit model of the SED was found. Hybrid models of leptonic and hadronic models are proposed. [Bla05]
Conclusively, it can be said that no final statement about the one-and-only emission model can be made. Former applications of different emission models showed that all of them are able to describe the SED of Mrk 421 at different times. The simple one-zone SSC model showed good results as well as a model involving a second emission zone. But it is stated that even more emission regions might be responsible for the highly variable emission of Mrk 421. A hadronic model was tested as well and it was able to describe

the SED, too. Further investigations are needed to solve the mystery of the exact particle composition in the emission regions. The first peak is explained by synchrotron radiation of electrons in both leptonic and hadronic models. However, neither protons were proven to be responsible for photon emission in the jets, nor were hadronic emission models excluded. Thus, it is necessary to have a full coverage of the electromagnetic spectrum at the same time in order to have good sampled SEDs for the modelling. Due to the high variability of Mrk 421 the emission state and the shape of the SED can change on short time scales. Therefore, the coordination of observations in multi-wavelength campaigns is essential.

7.6 Conclusions on Mrk 421 in the MWL context

The comparison of the light curves of Mrk 421 in different wavelengths has shown that the X-ray light curves have a similar behaviour as the γ-ray light curve measured by MAGIC. Between the beginning of 2007 until the summer of 2007 all three light curves are in a low emission state. This changes for the time period from the autumn of 2007 to the summer of 2008. During this time the three light curves are all more variable than during the time period before. Flares in all three light curves appear at the same time, making the light curves directly correlated. This could be proven by the determination of the Discrete Correlation Function, with which the correlation between the light curves is quantified. The DCF also showed an additional correlation at a time lag of -6 days between the γ-ray and both X-ray light curves which could be explained by additional flares in the X-ray light curves 6 days after matching flares. The MAGIC light curve contains no data points after these specific matching flares, so that a shift in the light curves by 6 days results again in a positive correlation. The light curves of all three telescopes show a quiet emission state and lower variability in the time period from the autumn of 2008 to the summer of 2009. The observed difference in the variability in the three different time periods was verified by a quantification with the fractional variability F_{var}.
The optical light curve of the KVA telescope has a steady variability over the whole time period of 2.3 years. It could be shown that it is not directly correlated to the MAGIC light curve as well as to the two X-ray light curves. The flares seem to appear first in the optical light curve. This was confirmed by the DCF study for these light curves. It has shown that the optical light curve comes about 10 to 14 days before the γ-ray light curve of MAGIC and the X-ray light curve of the *RXTE*/ASM. It is important to mention that this could only be shown when high activity data were included. In the case of the quiet emission time periods no correlations were found.
The radio light curve by OVRO is different from all other four light curves. It lacks distinct flare features. Instead a long-term change of the flux can be seen. This means that it is a bit higher in 2008 than in 2009. The light curve has almost no variability and the DCF study could not give conclusive results. There could be a hint that the radio light curve comes several days before the light curves in γ-rays and X-rays, but anti-correlations are seen as well. The DCF study showed no conclusive results for the optical and radio light curve. An explanation for the lacking correlation might be that the radio emission is not produced in the same emission region as the photons of the other

wavebands [Ale12a, Acc11].

The overall variability study showed that the variability generally increases with increasing energy range of the instrument. It is low for the radio and optical wavebands. The light curves for the duration of more than two years have a high variability in the X-ray and γ-ray band. The light curve of *RXTE*/ASM does not follow the general increase of variability with increasing frequency. It has the highest variability of all instruments. However, when the MAGIC light curve is separated into three energy ranges, the variability of the MAGIC light curve in the highest energy range (above 1 TeV) exceeds the variability of *RXTE*/ASM. The same was seen when the light curves in the three different time periods were examined. During the high active second time period both X-ray light curves have a higher variability than the MAGIC light curve. When this light curve is separated into the three different energy ranges, the variability of the highest energy range exceeds the X-ray variability.

A SED of Mrk 421 was produced. It includes data of several telescopes recorded during different time ranges. It has the typical two bump structure of blazars with an additional host galaxy component in the optical waveband. Then three SEDs were produced for the three different time periods, namely the two quiet periods and the high active period determined before for the MAGIC light curves. This has shown that both peaks in the SED behave similarly in different emission states. The correlation of the light curves in γ-rays and in X-rays, the same behaviour of the peaks in the SED as well as the correlated variability hint towards the SSC emission scenario. The steady variability of the optical light curve differs from the changing variability in the different years in the X-ray and γ-ray light curves. From this it might be assumed that the one-zone SSC model cannot fully explain all mechanisms in the jet of Mrk 421. A second emission zone, which is only responsible for the production of X-rays and γ-rays, might explain the different behaviour in the variability. This second smaller emission zone has a higher magnetic field and a higher electron density in comparison to the first emission zone, and therefore, it is capable to add a variable amount of X-rays and γ-rays to the quiet SED [Ale14b]. This could explain that the variability in X-rays and γ-rays changes over time and that the variability stays at the same level in optical and radio wavebands. A correlation between the KVA light curve with the *RXTE*/ASM and MAGIC light curves was seen for a time lag of 10 days, i.e. features in the optical light curve appear before features in the two higher energetic light curves. This could hint to an additional emission region in the vicinity of the jet or somewhere in the host galaxy, where optical photons are emitted. These external photons could be seed photons in the External Compton model, where they are scattered to X-ray and γ-ray energies in the first emission zone.
In former publications it was shown that the SSC model can describe the SED of Mrk 421. But other models like the SSC model with two zones or a hadronic model were able to describe the given SEDs as well. No final conclusion on the emission scenario in Mrk 421 can be drawn at this point. Emission models of blazars are still of research interest. Therefore, extensive multi-wavelength campaigns of coordinated observations are necessary.

Chapter 8
Conclusions

In this thesis a more than two year long data set from 2007 to 2009 of the blazar Mrk 421 was analysed in order to get an insight into its behaviour and the underlying emission processes. We are able to detect high energetic γ-rays from Mrk 421 because it is the closest and brightest extragalactic emitter of TeV photons, which makes it a good candidate to be studied. Knowledge about it might help to understand Active Galactic Nuclei in general. After a brief introduction to astroparticle physics and the physics of AGNs was given, the detection of VHE γ-rays with Cherenkov telescopes was discussed. The analysis of the long-term data set of Mrk 421 recorded by MAGIC-I was the main part of this thesis. It was separated into three parts.

Firstly, the long-term and short-term behaviour of the 830 day long light curve and changes in the spectrum in γ-rays have been analysed because the knowledge about these facts is one piece of the puzzle in understanding the emission processes. It was possible to conclude that Mrk 421 has a variable flux over the whole time span, but that the variability is higher during the high emission state in 2008. The separation of the light curve into three different energy ranges showed that the flux is more variable the higher the energy range is. In the study of the dependence of the spectral shape on the overall flux state it could be shown that the brighter the source is, the flatter the spectrum becomes. The proportion of higher energetic γ-rays increases with a higher overall flux. Additionally, the light curves were examined for short-term variability. Some nights showed variability on time scales shorter than 30 minutes, which is consistent with former results. With the variability time scales found in this thesis the size of the emission region could be estimated.

In the second part of the analysis a search for periodicities in the light curve of Mrk 421 has been carried out in order to find out if the central engine is a binary black hole system. This idea is motivated by the fact that Mrk 421 has an elliptical host galaxy, which can develop through the merging of two galaxies. The method introduced for the periodicity search was applied to three different light curves of Mrk 421, namely the MAGIC-I light curve from this thesis, a 20 year long light curve including data of several Cherenkov telescopes, which was combined with the results from this thesis, and a light curve measured by the new Cherenkov telescope FACT. For the first two light curves a hint for a period length of 31 days was found. For the FACT light curve a hint for a period length of 52 days was found. All results seemed to be influenced by flares in the light curves. However, this could also mean that flares occur periodically. Additionally, period lengths of 29 and

58 days were found corresponding to (twice) the lunar cycle. Therefore, it is concluded that there are hints for periodicities, but no significant detection so far.

In the third analysis part of this thesis the MAGIC light curve was compared to light curves of four instruments measuring in other wavebands, namely the *Swift*/BAT and *RXTE*/ASM in the X-ray band, the KVA telescope in the optical band and OVRO in the radio band. A variability study showed a connected variability of γ-rays and X-rays. A cross-correlation study revealed that both wavebands are directly correlated. This is in agreement with the SSC emission scenario. The optical light curve had a lower variability and the flares in the optical waveband have been shown to appear about 10 to 14 days earlier than in the γ-ray as well as the X-ray light curves. This fact has already been used in the successful triggering of MAGIC observations by KVA observation results. The radio light curve had almost no variability and seemed not to be correlated to any of the other light curves. This hints towards a different emission region for radio photons than for photons of the other wavebands. The SED of Mrk 421 had the typical two bump structure of blazars. The produced SEDs of different activity phases revealed that the SED is shifted up- or downwards depending on the emission state. Due to the similar behaviour of the low energy and high energy peak in the SED and the direct correlation of X-ray and γ-ray light curves, the SSC emission scenario is favoured for the production of VHE γ-rays. The missing direct correlation of the radio and optical light curves with the X-ray and γ-ray light curves hint toward the expansion of the simple one-zone SSC model to a model including one ore more additional regions. Former studies have shown that the SSC scenario was mostly able to model the SED of Mrk 421 well, but SSC models with two zones and hadronic models were able to describe the SED as well.

Mrk 421 has an unpredictable high flux variability. Phases of high activity on top of the emission baseline can last up to several months. It cannot be foreseen when a high activity phase will start and for how long it will last. Significant periodicities have not been found so far in the light curves. In order to understand better the overall emission behaviour of the source and to possibly find periodicities in better sampled light curves in the future, a regular monitoring, as is carried out with FACT, is desirable. FACT could also help in filling the observational gaps due to the moon because its photo sensors are not damageable by the moon light.
Although Mrk 421 is one of the best studied γ-ray sources, there are still open questions. The cooperation of instruments measuring in all wavebands is essential to get a better understanding of the emission scenarios in sources in general. Therefore, it is important to continue with extensive MWL campaigns as they have been carried out e.g. for Mrk 421 since 2009. It is necessary for the observations to be coordinated in time because of the high variability of the source. Only combined results will help to reveal the questions about the emission processes. Additionally, the results obtained on Mrk 421 might broaden the knowledge on blazars in general.

Appendix A
Supplementary information: Mrk 421 analysis

A.1 Overview of Mrk 421 data

Table A.1: Daily results of *odie* of the Mrk 421 data with a PSF of 13.0 mm and a zenith range from 9° to 30°. The zenith range, the effective observation time, the number of excess events and the significance are shown for each night which survived the data check.

Date	MJD	Zd [°]	T_{eff} [h]	N_{exc}	Sign. (Li&Ma) [σ]
2007-04-15	54204.9	15-24	0.80	108.7	12.58
2007-04-22	54211.9	10-17	0.81	77.9	10.66
2007-05-05	54224.9	12-22	0.31	17.5	4.11
2007-05-13	54232.9	9-14	0.63	30.8	5.58
2007-12-04	54438.2	12-15, 28-30	0.40	97.7	13.57
2007-12-05	54439.2	23-30	0.55	161.7	17.69
2007-12-06	54440.2	13-30	0.66	174.9	17.94
2007-12-07	54441.2	18-30	0.93	190.5	16.41
2007-12-08	54442.2	10-11,19-27	0.88	189.9	17.32
2007-12-09	54443.2	9-11,21-27	0.92	242.1	21.20
2007-12-12	54446.3	9	0.16	24.6	6.50
2007-12-14	54448.3	9	0.26	38.5	7.85
2007-12-15	54449.3	9	0.27	46.7	8.95
2007-12-16	54450.3	9-10	0.27	36.4	7.48
2007-12-17	54451.3	9-10	0.28	31.3	6.83
2008-01-01	54466.2	9-30	0.93	255.0	21.74
2008-01-02	54467.2	9-30	3.53	1091.2	47.96
2008-01-04	54469.2	12-30	1.50	474.9	30.67
2008-01-05	54470.1	20-30	0.81	268.5	23.31
2008-01-07	54472.2	9-13	0.16	19.1	6.07
2008-01-08	54473.2	9-16	1.77	306.6	22.19
2008-01-09	54474.2	9-23	2.43	454.4	27.47
2008-01-10	54475.2	11-17,22-27,29-30	0.37	65.1	10.53

Date	**MJD**	**Zd** [°]	$\mathbf{T_{eff}}$ **[h]**	$\mathbf{N_{exc}}$	**Sign. (Li&Ma)** [σ]
2008-01-11	54476.3	10,14-19	0.46	57.2	8.36
2008-01-12	54477.1	9-21,23-29	0.46	113.6	13.29
2008-01-13	54478.3	10-17,26-29	1.03	318.2	26.09
2008-01-14	54479.2	9-13	0.57	149.8	17.99
2008-01-15	54480.3	19-29	0.94	397.0	29.68
2008-01-16	54481.2	9-19	2.63	1087.4	49.18
2008-01-29	54494.1	25-30	0.21	64.8	12.08
2008-02-04	54500.1	23-30	0.55	199.2	20.65
2008-02-05	54501	28-30	0.16	42.9	8.83
2008-02-06	54502.1	9-30	3.03	1515.1	62.44
2008-02-11	54507.1	12-20	0.79	321.2	27.80
2008-03-08	54533	18-24	0.60	196.0	20.86
2008-03-12	54537	19-30	0.50	128.8	16.35
2008-03-31	54555.9	14-30	1.37	1094.7	56.34
2008-04-02	54558	17-19	0.24	66.7	10.76
2008-04-04	54559.9	16-21	0.37	185.1	21.15
2008-04-06	54562	10-11	0.17	94.2	16.54
2008-05-04	54589.9	9-12,16-17	0.59	137.1	16.75
2008-05-05	54590.9	16-30	0.57	232.8	24.43
2008-05-07	54592.9	9,17-30	1.15	264.0	22.35
2008-05-10	54595.9	9-30	1.82	408.4	29.11
2008-05-23	54608.9	23-30	0.51	227.6	23.21
2008-05-25	54610.9	16-19	0.24	105.7	15.13
2008-05-27	54612.9	18-20	0.24	161.9	21.50
2008-05-28	54613.9	20-21	0.17	72.7	13.17
2008-05-29	54614.9	20-21	0.15	63.3	11.84
2008-06-03	54619.9	24-26	0.23	99.0	15.01
2008-06-05	54621.9	27-29	0.24	165.3	21.03
2008-06-06	54622.9	27-30	0.21	161.4	21.92
2008-12-04	54804.2	15-30	1.14	180.4	15.86
2008-12-05	54805.2	14-30	1.27	294.3	22.62
2009-01-04	54835.3	17-24	0.16	36.9	8.00
2009-01-22	54853.1	10-30	0.98	130.4	13.39
2009-01-24	54855.1	10-30	1.77	226.6	17.52
2009-01-26	54857.1	17-30	0.88	125.2	12.36
2009-01-28	54859.1	9-30	1.83	266.2	20.75
2009-01-30	54861.1	26-30	0.36	59.7	9.45
2009-02-01	54863.1	25-27	0.21	46.5	9.02
2009-02-03	54865	9-20	1.99	338.8	24.06

Table A.2: Daily results of *odie* of the Mrk 421 data with a PSF of 13.0 mm and a zenith range from 30° to 45°. The zenith range, the effective observation time, the number of excess events and the significance are shown for each night which survived the data check.

Date	**MJD**	**Zd** [°]	$\mathbf{T_{eff}}$ **[h]**	$\mathbf{N_{exc}}$	**Sign. (Li&Ma)** [σ]
2007-02-11	54142	38-41	0.24	7.4	2.13
2007-02-15	54146	37-45	0.54	17.3	3.35
2007-02-19	54150	37-45	0.50	25.5	4.85
2007-02-27	54158.2	30-45	0.47	19.5	3.53
2007-03-08	54166.9	34-45	0.82	31.0	4.69
2007-03-12	54170.9	32-40	0.63	77.7	11.21
2007-12-04	54438.2	30-45	1.17	295.7	23.98
2007-12-05	54439.2	30-39	0.82	215.4	20.29
2007-12-06	54440.2	30-44	1.20	312.8	24.75
2007-12-07	54441.2	30-33	0.29	61.8	10.89
2008-01-01	54466.1	30-44	1.26	348.5	27.89
2008-01-02	54467.1	30-33	0.30	109.2	16.31
2008-01-04	54469.1	30-40	0.73	222.9	21.51
2008-01-05	54470.1	30-39	0.77	225.4	20.85
2008-01-06	54471.1	33-36,38-40	0.52	157.1	17.70
2008-01-07	54472.1	34-39	0.50	103.4	12.93
2008-01-08	54473.1	31-40	0.74	149.2	15.51
2008-01-09	54474.1	34-39	0.55	108.1	13.61
2008-01-10	54475.1	30-33	0.34	69.8	12.18
2008-01-15	54480.1	33-39	0.48	167.9	19.28
2008-01-29	54494	30-40	0.83	220.6	22.53
2008-02-02	54498	32-40	0.63	283.5	24.26
2008-02-05	54501	30-36	0.47	125.7	15.97
2008-02-06	54502	30-35	0.53	244.5	25.06
2008-02-08	54504	30-36	0.38	145.7	20.01
2008-03-01	54526	33-35	0.21	63.1	11.94
2008-03-11	54535.9	32-45	0.88	267.1	24.28
2008-03-12	54536.9	30-45	0.55	112.5	15.12
2008-03-31	54555.9	30-40	0.54	387.9	33.65
2008-04-04	54559.9	31-33	0.17	78.5	13.93
2008-04-12	54568.1	36-39	0.23	24.1	5.99
2008-05-05	54591	30-35	0.43	153.4	19.58
2008-05-10	54596	30-42	0.90	201.7	20.35
2008-05-23	54608.9	30-34	0.26	96.6	16.18
2008-06-05	54621.9	32-41	0.79	585.5	42.17
2008-06-06	54622.9	30-37	0.63	434.2	36.02
2008-06-07	54623.9	30-31,44-45	0.15	77.2	14.50
2008-06-08	54624.9	30-32,35-45	0.88	385.4	31.47
2008-11-30	54800.2	32-38	0.42	72.7	12.07
2008-12-02	54802.2	30-36	0.53	102.0	14.55

Date	**MJD**	**Zd** [°]	$\mathbf{T_{eff}}$ **[h]**	$\mathbf{N_{exc}}$	**Sign. (Li&Ma)** [σ]
2008-12-04	54804.2	30-40	0.87	146.5	16.31
2008-12-05	54805.2	30-39	0.76	136.2	15.32

Table A.3: Daily results of *odie* of the Mrk 421 data with a PSF of 14.8 mm and a zenith range from 9° to 30°. The zenith range, the effective observation time, the number of excess events and the significance are shown for each night which survived the data check.

Date	**MJD**	**Zd** [°]	$\mathbf{T_{eff}}$ **[h]**	$\mathbf{N_{exc}}$	**Sign. (Li&Ma)** [σ]
2009-02-25	54887	10-30	1.13	148.1	14.37
2009-03-01	54891	9-23	1.78	261.9	19.49
2009-03-17	54907	10-15,18-29	1.35	239.8	20.40
2009-03-19	54909	10-14	0.54	74.6	10.83
2009-03-21	54911	10-26	1.49	189.3	14.95
2009-03-23	54913	10-30	1.85	263.5	18.12
2009-03-29	54919	10-22	1.28	68.8	7.32
2009-03-31	54921	9-30	2.10	235.5	15.99
2009-04-15	54936	16-30	0.45	95.3	11.68
2009-04-16	54937	24-26	0.21	33.8	6.46
2009-04-17	54938	16-30	0.98	145.0	13.08
2009-04-19	54940	22-30	0.55	51.5	6.41
2009-04-21	54942	16-30	0.83	119.7	11.88
2009-04-22	54943	20-22	0.17	24.0	4.95
2009-04-23	54944	16-30	0.83	205.8	17.72
2009-04-24	54945	16-30	1.03	162.8	14.03
2009-04-25	54946	16-18	0.19	28.9	5.27
2009-05-21	54972	27-30	0.29	27.3	5.26

Table A.4: Daily results of *odie* of the Mrk 421 data with a PSF of 14.8 mm and a zenith range from 30° to 45°. The zenith range, the effective observation time, the number of excess events and the significance are shown for each night which survived the data check..

Date	**MJD**	**Zd** [°]	$\mathbf{T_{eff}}$ **[h]**	$\mathbf{N_{exc}}$	**Sign. (Li&Ma)** [σ]
2009-04-15	54936	30-36	0.27	31.9	6.49
2009-04-17	54938	30-35	0.38	58.4	9.37
2009-04-19	54940	30-35	0.34	29.6	5.65
2009-04-21	54942	30-35	0.31	37.6	6.57
2009-04-23	54944	30-34	0.41	60.5	9.06
2009-04-24	54945	30-36	0.44	42.7	7.06
2009-05-21	54972	30-35	0.13	11.2	3.54
2009-06-13	54994.9	37-45	0.31	47.1	9.83
2009-06-14	54995.9	38-43	0.31	42.9	8.37
2009-06-15	54996.9	35-45	0.41	67.0	11.80

Table A.5: Excluded 50 nights of Mrk 421 data. The reasons for exclusion are more than 40% clouds, a number of recognised stars below 30, a trigger rate which is too low or too high (for exact limits see subsection 5.2.1), a too high discriminator threshold, if the length of the taken data is less than 10 minutes or reasons mentioned by the shifters in the runbook to exclude the data such as car flashes.

Year	**Month**	**Day**
2007	02	23
	03	16
	04	23
	06	04, 18, 20
	12	01, 02, 03, 10, 11, 13, 31
2008	01	03
	03	02, 03, 05, 10, 13, 14, 29, 30
	04	01, 03, 05
	05	03, 06, 11, 12
	06	01, 09, 10
	12	03, 06, 21, 29
2009	01	18
	03	15
	04	02, 04, 12, 13, 14, 26
	05	22, 23, 24, 25, 29
	06	10

A.2 Overview of background data

Table A.6: List of sources and dates for the selected hadron sample for the training of the Random Forest for the γ-Hadron-Separation.

PSF	Zd	Source	Year	Month	Day
13.0 mm	<30°	1ES2344+514	2007	12	28, 29, 30
		2MASX0324+34	2008	12	22, 29
		HB89-1553+11	2007	04	19
			2008	04	05
			2008	06	07
		PKS1424+240	2007	02	21, 22, 23
13.0 mm	30° - 45°	1ES1959+650	2007	04	22
			2008	05	30
			2008	06	03
		1ES2344+514	2007	12	28, 29, 30
		3C279	2009	01	22, 24
		HB89-1553+11	2008	06	07
		PKS1424+240	2007	02	21, 22
14.8 mm	<30°	1H1722+119	2009	03	31
		HB89-1553+11	2009	04	21
			2009	06	15
		MS1050.7+494	2009	03	17, 19, 23, 24
			2009	04	22
		PKS1424+240	2009	06	15
		PKS-1222+216	2009	04	18
		PKS-1717+177	2009	04	23
			2009	06	15
14.8 mm	30° - 45°	3C279	2009	04	16
		HB89-1553+11	2009	04	21
			2009	06	15
		MS1050.7+494	2009	03	19, 23, 24
			2009	04	22
		PKS1510-08	2009	03	19, 21, 23, 24, 30, 31

A.3 Overview of Crab Nebula data

Table A.7: Four data sample sets of Crab Nebula for the different PSFs and zenith ranges. In addition the amount of data in hours is listed as well.

PSF	Zd	Year	Month	Day	T_{eff} [h]
13.0 mm	<30°	2007 2007 2008	02 12 01	12 14 14, 23	5.69
13.0 mm	30° - 45°	2007 2008 2009	12 01 01	14 14 23	2.59
14.8 mm	<30°	2009	03	01, 14, 22, 23	2.61
14.8 mm	30° - 45°	2009	03	02, 21, 23	1.56

A.4 Significances of Crab Nebula and Mrk 421 data

Table A.8: Cut values for the significance calculations in *odie*, optimised on data of the Crab Nebula.

PSF	Zd	Size	Hadron-ness	θ^2	Sign. (Li&Ma) [σ]	T_{eff} [h]	Sensitivity [%Crab]
13.0 mm	<30°	150	0.06	0.015	44.37	5.69	2.23
13.0 mm	30° - 45°	200	0.06	0.015	32.24	2.59	1.97
14.8 mm	<30°	150	0.06	0.020	27.24	2.61	2.69
14.8 mm	30° - 45°	200	0.07	0.015	20.26	1.56	2.64

Table A.9: Cut values for the significance calculations in *odie*, applied to Mrk 421 data.

PSF	Zd	Size	Hadronness	θ^2	Sign. (Li&Ma) [σ]	T_{eff} [h]
13.0 mm	<30°	150	0.06	0.015	171.31	50.35
13.0 mm	30° - 45°	200	0.06	0.015	124.81	24.87
14.8 mm	<30°	150	0.06	0.020	55.12	17.04
14.8 mm	30° - 45°	200	0.07	0.015	25.19	3.31

A.5 Cut values in *fluxlc* of Crab Nebula data

Table A.10: Cut values for the calculation of the light curve and spectrum in *fluxlc*, optimised on data of the Crab Nebula. θ eff. and Had. eff. are the γ efficiencies after a cut in θ and in Hadronness, respectively.

PSF	Zd	Size	θ eff.	Had. eff.
13.0 mm	<30°	150	0.8	0.9
13.0 mm	30° - 45°	200	0.8	0.9
14.8 mm	<30°	200	0.8	0.9
14.8 mm	30° - 45°	200	0.8	0.9

A.6 Light curve results of Mrk 421 data

Table A.11: Light curve results of the Mrk 421 data determined with *fluxlc*. The integral flux is given in the energy range from 400 GeV to 50 TeV.

Date	MJD	Integral flux [$\mathrm{cm^{-2}s^{-1}}$]
2007-03-08	54166.9	$1.29 \cdot 10^{-11} \pm 4.39 \cdot 10^{-12}$
2007-03-12	54170.9	$4.05 \cdot 10^{-11} \pm 6.29 \cdot 10^{-12}$
2007-04-15	54204.9	$5.59 \cdot 10^{-11} \pm 6.59 \cdot 10^{-12}$
2007-04-22	54211.9	$3.69 \cdot 10^{-11} \pm 5.64 \cdot 10^{-12}$
2007-05-05	54224.9	$3.73 \cdot 10^{-11} \pm 9.40 \cdot 10^{-12}$
2007-05-13	54232.9	$2.42 \cdot 10^{-11} \pm 6.21 \cdot 10^{-12}$
2007-12-04	54438.2	$9.53 \cdot 10^{-11} \pm 7.91 \cdot 10^{-12}$
2007-12-05	54439.2	$9.94 \cdot 10^{-11} \pm 8.81 \cdot 10^{-12}$
2007-12-06	54440.2	$8.75 \cdot 10^{-11} \pm 7.36 \cdot 10^{-12}$
2007-12-07	54441.2	$7.87 \cdot 10^{-11} \pm 8.57 \cdot 10^{-12}$
2007-12-08	54442.3	$9.75 \cdot 10^{-11} \pm 8.23 \cdot 10^{-12}$
2007-12-09	54443.3	$8.60 \cdot 10^{-11} \pm 7.85 \cdot 10^{-12}$
2007-12-12	54446.3	$5.40 \cdot 10^{-11} \pm 1.55 \cdot 10^{-11}$
2007-12-14	54448.3	$9.16 \cdot 10^{-11} \pm 1.50 \cdot 10^{-11}$
2007-12-15	54449.3	$7.62 \cdot 10^{-11} \pm 1.41 \cdot 10^{-11}$
2007-12-16	54450.3	$4.82 \cdot 10^{-11} \pm 1.31 \cdot 10^{-11}$
2007-12-17	54451.3	$3.30 \cdot 10^{-11} \pm 1.10 \cdot 10^{-11}$
2008-01-01	54466.2	$9.95 \cdot 10^{-11} \pm 6.91 \cdot 10^{-12}$
2008-01-02	54467.2	$1.24 \cdot 10^{-10} \pm 5.28 \cdot 10^{-12}$
2008-01-04	54469.1	$1.17 \cdot 10^{-10} \pm 7.27 \cdot 10^{-12}$
2008-01-05	54470.1	$1.02 \cdot 10^{-10} \pm 8.38 \cdot 10^{-12}$
2008-01-06	54471.1	$9.21 \cdot 10^{-11} \pm 9.24 \cdot 10^{-12}$
2008-01-07	54472.2	$6.99 \cdot 10^{-11} \pm 1.08 \cdot 10^{-11}$
2008-01-08	54473.2	$7.64 \cdot 10^{-11} \pm 6.18 \cdot 10^{-12}$
2008-01-09	54474.2	$7.08 \cdot 10^{-11} \pm 5.35 \cdot 10^{-12}$

Date	**MJD**	**Integral flux [$\mathbf{cm^{-2}s^{-1}}$]**
2008-01-10	54475.1	$7.26 \cdot 10^{-11} \pm 1.15 \cdot 10^{-11}$
2008-01-11	54476.3	$5.10 \cdot 10^{-11} \pm 9.60 \cdot 10^{-12}$
2008-01-12	54477.1	$8.37 \cdot 10^{-11} \pm 1.07 \cdot 10^{-11}$
2008-01-13	54478.3	$1.31 \cdot 10^{-10} \pm 8.54 \cdot 10^{-12}$
2008-01-14	54479.2	$1.16 \cdot 10^{-10} \pm 1.12 \cdot 10^{-11}$
2008-01-15	54480.2	$1.35 \cdot 10^{-10} \pm 9.66 \cdot 10^{-12}$
2008-01-16	54481.2	$1.68 \cdot 10^{-10} \pm 5.92 \cdot 10^{-12}$
2008-01-29	54494.1	$1.02 \cdot 10^{-10} \pm 9.57 \cdot 10^{-12}$
2008-02-02	54498.0	$1.27 \cdot 10^{-10} \pm 9.63 \cdot 10^{-12}$
2008-02-04	54500.1	$1.29 \cdot 10^{-10} \pm 1.13 \cdot 10^{-11}$
2008-02-05	54501.0	$9.99 \cdot 10^{-11} \pm 1.22 \cdot 10^{-11}$
2008-02-06	54502.1	$2.03 \cdot 10^{-10} \pm 6.93 \cdot 10^{-12}$
2008-02-08	54504.0	$1.45 \cdot 10^{-10} \pm 1.28 \cdot 10^{-11}$
2008-02-11	54507.1	$1.79 \cdot 10^{-10} \pm 1.09 \cdot 10^{-11}$
2008-03-01	54526.0	$9.62 \cdot 10^{-11} \pm 1.44 \cdot 10^{-11}$
2008-03-08	54533.0	$1.18 \cdot 10^{-10} \pm 1.01 \cdot 10^{-11}$
2008-03-11	54535.9	$9.89 \cdot 10^{-11} \pm 7.42 \cdot 10^{-12}$
2008-03-12	54536.9	$7.69 \cdot 10^{-11} \pm 8.92 \cdot 10^{-12}$
2008-03-31	54555.9	$3.05 \cdot 10^{-10} \pm 1.12 \cdot 10^{-11}$
2008-04-02	54558.0	$9.32 \cdot 10^{-11} \pm 1.53 \cdot 10^{-11}$
2008-04-04	54559.9	$1.87 \cdot 10^{-10} \pm 1.78 \cdot 10^{-11}$
2008-04-06	54562.0	$2.77 \cdot 10^{-10} \pm 2.88 \cdot 10^{-11}$
2008-04-12	54568.1	$4.56 \cdot 10^{-11} \pm 1.03 \cdot 10^{-11}$
2008-05-04	54589.9	$1.10 \cdot 10^{-10} \pm 1.06 \cdot 10^{-11}$
2008-05-05	54590.9	$1.53 \cdot 10^{-10} \pm 1.20 \cdot 10^{-11}$
2008-05-07	54592.9	$7.83 \cdot 10^{-11} \pm 6.50 \cdot 10^{-12}$
2008-05-10	54596.0	$7.95 \cdot 10^{-11} \pm 5.56 \cdot 10^{-12}$
2008-05-23	54608.9	$1.68 \cdot 10^{-10} \pm 1.38 \cdot 10^{-11}$
2008-05-25	54610.9	$1.30 \cdot 10^{-10} \pm 1.72 \cdot 10^{-11}$
2008-05-27	54612.9	$2.52 \cdot 10^{-10} \pm 2.20 \cdot 10^{-11}$
2008-05-28	54613.9	$1.24 \cdot 10^{-10} \pm 1.87 \cdot 10^{-11}$
2008-05-29	54614.9	$1.45 \cdot 10^{-10} \pm 2.26 \cdot 10^{-11}$
2008-06-03	54619.9	$1.33 \cdot 10^{-10} \pm 1.72 \cdot 10^{-11}$
2008-06-05	54621.9	$2.67 \cdot 10^{-10} \pm 1.37 \cdot 10^{-11}$
2008-06-06	54622.9	$2.75 \cdot 10^{-10} \pm 1.57 \cdot 10^{-11}$
2008-06-07	54623.9	$2.43 \cdot 10^{-10} \pm 2.48 \cdot 10^{-11}$
2008-06-08	54624.9	$1.59 \cdot 10^{-10} \pm 8.45 \cdot 10^{-12}$
2008-11-30	54800.2	$5.53 \cdot 10^{-11} \pm 8.70 \cdot 10^{-12}$
2008-12-02	54802.2	$6.18 \cdot 10^{-11} \pm 8.29 \cdot 10^{-12}$
2008-12-04	54804.2	$6.20 \cdot 10^{-11} \pm 6.96 \cdot 10^{-12}$
2008-12-05	54805.2	$7.93 \cdot 10^{-11} \pm 6.65 \cdot 10^{-12}$
2009-01-04	54835.3	$8.44 \cdot 10^{-11} \pm 1.86 \cdot 10^{-11}$
2009-01-22	54853.1	$4.45 \cdot 10^{-11} \pm 5.80 \cdot 10^{-12}$
2009-01-24	54855.1	$4.97 \cdot 10^{-11} \pm 4.56 \cdot 10^{-12}$

Date	**MJD**	**Integral flux [$\mathbf{cm^{-2}s^{-1}}$]**
2009-01-26	54857.1	$5.82 \cdot 10^{-11} \pm 6.87 \cdot 10^{-12}$
2009-01-28	54859.1	$5.16 \cdot 10^{-11} \pm 4.49 \cdot 10^{-12}$
2009-01-30	54861.1	$7.26 \cdot 10^{-11} \pm 1.16 \cdot 10^{-11}$
2009-02-01	54863.1	$1.02 \cdot 10^{-10} \pm 1.56 \cdot 10^{-11}$
2009-02-03	54865.1	$6.67 \cdot 10^{-11} \pm 4.90 \cdot 10^{-12}$
2009-02-25	54887.0	$5.22 \cdot 10^{-11} \pm 5.42 \cdot 10^{-12}$
2009-03-01	54891.0	$4.87 \cdot 10^{-11} \pm 4.34 \cdot 10^{-12}$
2009-03-17	54907.0	$6.92 \cdot 10^{-11} \pm 5.47 \cdot 10^{-12}$
2009-03-19	54909.0	$5.27 \cdot 10^{-11} \pm 8.18 \cdot 10^{-12}$
2009-03-21	54911.0	$4.38 \cdot 10^{-11} \pm 4.61 \cdot 10^{-12}$
2009-03-23	54913.0	$4.86 \cdot 10^{-11} \pm 4.35 \cdot 10^{-12}$
2009-03-29	54919.0	$2.29 \cdot 10^{-11} \pm 3.99 \cdot 10^{-12}$
2009-03-31	54920.9	$3.63 \cdot 10^{-11} \pm 3.67 \cdot 10^{-12}$
2009-04-15	54936.0	$6.26 \cdot 10^{-11} \pm 9.96 \cdot 10^{-12}$
2009-04-16	54936.9	$7.12 \cdot 10^{-11} \pm 1.44 \cdot 10^{-11}$
2009-04-17	54938.0	$4.72 \cdot 10^{-11} \pm 6.58 \cdot 10^{-12}$
2009-04-19	54940.0	$2.30 \cdot 10^{-11} \pm 7.27 \cdot 10^{-12}$
2009-04-21	54942.0	$4.13 \cdot 10^{-11} \pm 7.12 \cdot 10^{-12}$
2009-04-22	54942.9	$3.67 \cdot 10^{-11} \pm 1.12 \cdot 10^{-11}$
2009-04-23	54944.0	$6.62 \cdot 10^{-11} \pm 7.83 \cdot 10^{-12}$
2009-04-24	54945.0	$4.67 \cdot 10^{-11} \pm 6.52 \cdot 10^{-12}$
2009-04-25	54945.9	$3.63 \cdot 10^{-11} \pm 1.26 \cdot 10^{-11}$
2009-05-21	54971.9	$4.36 \cdot 10^{-11} \pm 1.17 \cdot 10^{-11}$
2009-06-13	54994.9	$4.08 \cdot 10^{-11} \pm 8.29 \cdot 10^{-12}$
2009-06-14	54995.9	$5.74 \cdot 10^{-11} \pm 9.58 \cdot 10^{-12}$
2009-06-15	54996.9	$4.44 \cdot 10^{-11} \pm 7.60 \cdot 10^{-12}$

A.7 Constant fit results for all light curves with daily bins

In the following, the results of a constant fit to the light curves from section 5.4 and section 5.5 are summarised. The χ^2/ndf and the fit probability are given, as well as p_0 of the constant fit in $cm^{-2}s^{-1}$ and/or units of the Crab Nebula CU.

Whole energy range

Table A.12 summarises the constant fit results for the light curves from section 5.4 for the whole energy range from 400 GeV to 50 TeV.

Table A.12: Constant fit results of the light curves for the whole energy range from 400 GeV to 50 TeV. The results are given separately for the whole observation length and divided into the three different time periods.

Time period	χ^2/ndf	Probability	p_0 [$cm^{-2}s^{-1}$]	p_0 [CU]
03/2007 to 06/2009	3382/94	0	$7.14 \cdot 10^{-11} \pm 7.82 \cdot 10^{-13}$	0.88 ± 0.01
03/2007 to 05/2007	35.32/5	$8.2 \cdot 10^{-7}$	$3.07 \cdot 10^{-11} \pm 2.43 \cdot 10^{-12}$	0.38 ± 0.03
12/2007 to 06/2008	1486/55	0	$1.11 \cdot 10^{-10} \pm 1.25 \cdot 10^{-12}$	1.38 ± 0.02
11/2008 to 06/2009	160.3/32	$5.2 \cdot 10^{-19}$	$4.91 \cdot 10^{-11} \pm 1.10 \cdot 10^{-13}$	0.61 ± 0.01

Different energy ranges

Table A.13 contains all constant fit results for the light curves from section 5.5 for the three different energy ranges from 400 GeV to 600 GeV, from 600 GeV to 1 TeV and from 1 TeV to 50 TeV.

Table A.13: Constant fit results of the light curves for the three different energy ranges. The results are given separately for the whole observation length and divided into the three different time periods.

Time period	Energy range	χ^2/ndf	Probability	p_0 [CU]
03/2007 to 06/2009	400 GeV to 600 GeV	956.3/86	0	0.96 ± 0.02
	600 GeV to 1 TeV	1032/84	0	0.96 ± 0.02
	1 TeV to 50 TeV	1331/82	0	0.80 ± 0.02
03/2007 to 05/2007	400 GeV to 600 GeV	1.97/4	0.7417	0.59 ± 0.07
	600 GeV to 1 TeV	7.89/3	0.0483	0.44 ± 0.06
	1 TeV to 50 TeV	8.69/3	0.0337	0.35 ± 0.05
12/2007 to 06/2008	400 GeV to 600 GeV	361.9/53	0	1.45 ± 0.03
	600 GeV to 1 TeV	424.2/50	0	1.48 ± 0.03
	1 TeV to 50 TeV	702.5/50	0	1.26 ± 0.03
11/2008 to 06/2009	400 GeV to 600 GeV	61.37/27	0.0002	0.63 ± 0.02
	600 GeV to 1 TeV	47.88/29	0.0151	0.66 ± 0.02
	1 TeV to 50 TeV	80.64/27	$3.0 \cdot 10^{-7}$	0.56 ± 0.02

A.8 Short-term light curves

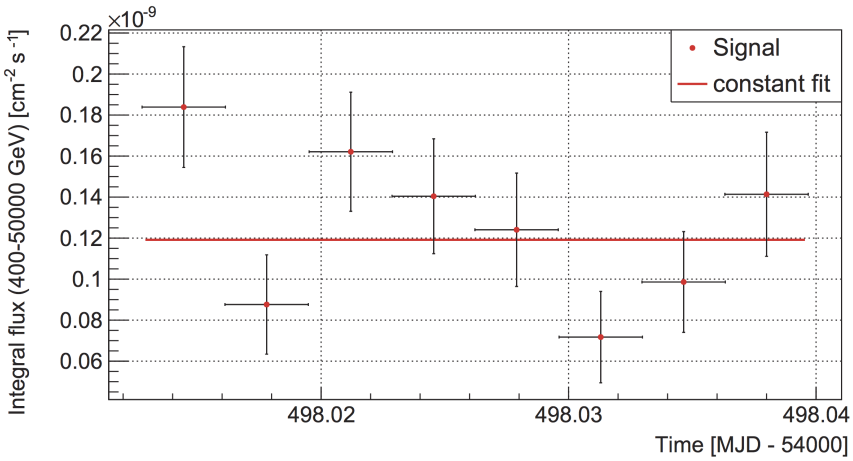

Figure A.1: Short-term light curve with 5 minute bins of 2nd February 2008 (MJD 54498.0) with a constant fit to the data points.

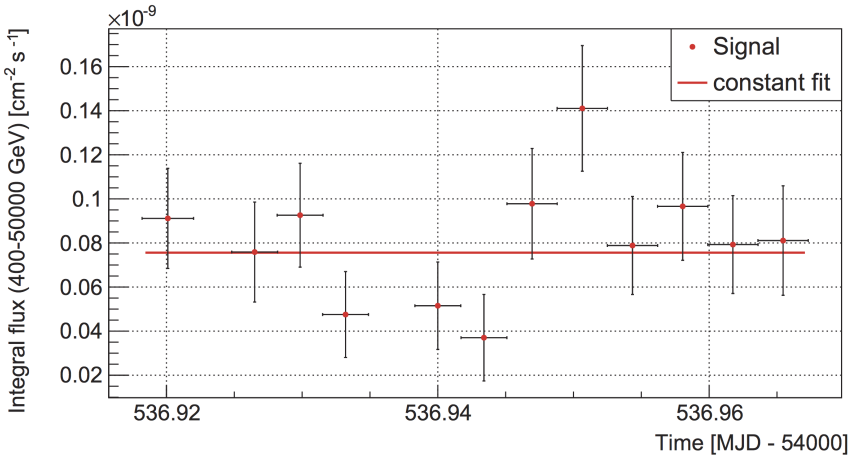

Figure A.2: Short-term light curve with 5 minute bins of 12th March 2008 (MJD 54536.9) with a constant fit to the data points.

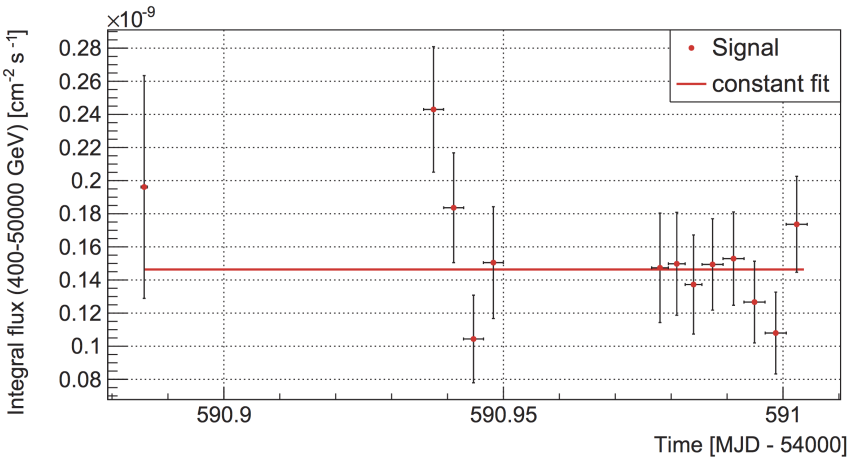

Figure A.3: Short-term light curve with 5 minute bins of 5th May 2008 (MJD 54590.9) with a constant fit to the data points.

A.9 Spectrum results

Table A.14: Fit results of the correlated fit of the unfolded spectra of several single nights. The Tikhonov regularisation is applied and the power law with variable slope is used as fit function. The flux normalisation f_0, the slope α, and the curvature strength b are noted down.

Date	$f_0 \left[\frac{10^{-10}}{\mathbf{cm^2 sTeV}}\right]$	α	b
2007-12-04	4.18 ± 0.29	-2.45 ± 0.16	-0.20 ± 0.30
2008-01-09	3.28 ± 0.28	-2.18 ± 0.17	-0.35 ± 0.26
2008-02-06	7.47 ± 0.35	-2.30 ± 0.08	-0.08 ± 0.10
2008-03-31	10.04 ± 0.32	-1.77 ± 0.07	-0.42 ± 0.09
2008-06-06	9.08 ± 0.39	-1.87 ± 0.11	-0.21 ± 0.14

Table A.15: All fit results of the correlated fit of the unfolded spectra for different fit functions in the three time periods from March to May 2007, from December 2007 to June 2008, and from November 2008 to June 2009. The flux normalisation f_0, the slope α, a possible cut-off energy E_0, and the possible curvature strength b are listed, as well as χ^2/ndf and the probability of the fit.

Time period	**Function**	$f_0 \left[\frac{10^{-10}}{\mathbf{cm^2 sTeV}}\right]$	α	E_0 **[TeV]**	b	χ^2/ndf	**Prob.**
03/2007 to 05/2007	PL	1.12 ± 0.09	-2.81 ± 0.17			1.22/2	0.5445
	PL with cut-off	2.40 ± 1.92	-1.93 ± 0.90	0.60 ± 0.63		0.11/1	0.7451
	PL with variable slope	1.26 ± 0.18	-2.62 ± 0.24		-1.03 ± 1.0	0.04/1	0.8470
12/2007 to 06/2008	PL	4.35 ± 0.02	-2.52 ± 0.01			1029.64/7	0.0000
	PL with cut-off	5.77 ± 0.10	-1.97 ± 0.03	1.73 ± 0.10		113.82/6	0.0000
	PL with variable slope	4.74 ± 0.03	-2.14 ± 0.01		-0.68 ± 0.03	28.73/6	0.0001
11/2008 to 06/2009	PL	1.93 ± 0.05	-2.65 ± 0.03			53.64/5	0.0000
	PL with cut-off	2.54 ± 0.15	-2.12 ± 0.10	1.78 ± 0.36		11.54/4	0.0211
	PL with variable slope	2.12 ± 0.06	-2.27 ± 0.07		-0.67 ± 0.11	3.31/4	0.5069

Appendix B
Supplementary information: MWL correlations

B.1 Light curves

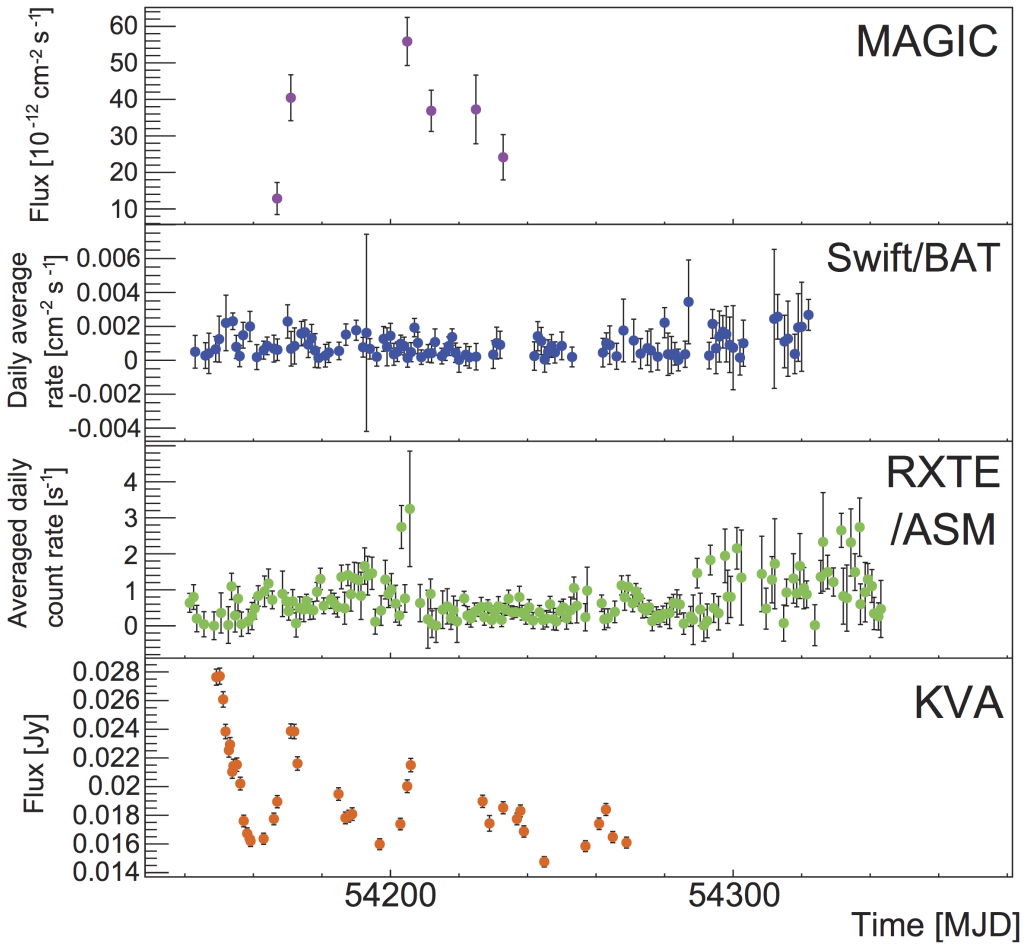

Figure B.1: Mrk 421 light curves of MAGIC, *Swift*/BAT, *RXTE*/ASM, and KVA from 02/2007 to 08/2007.

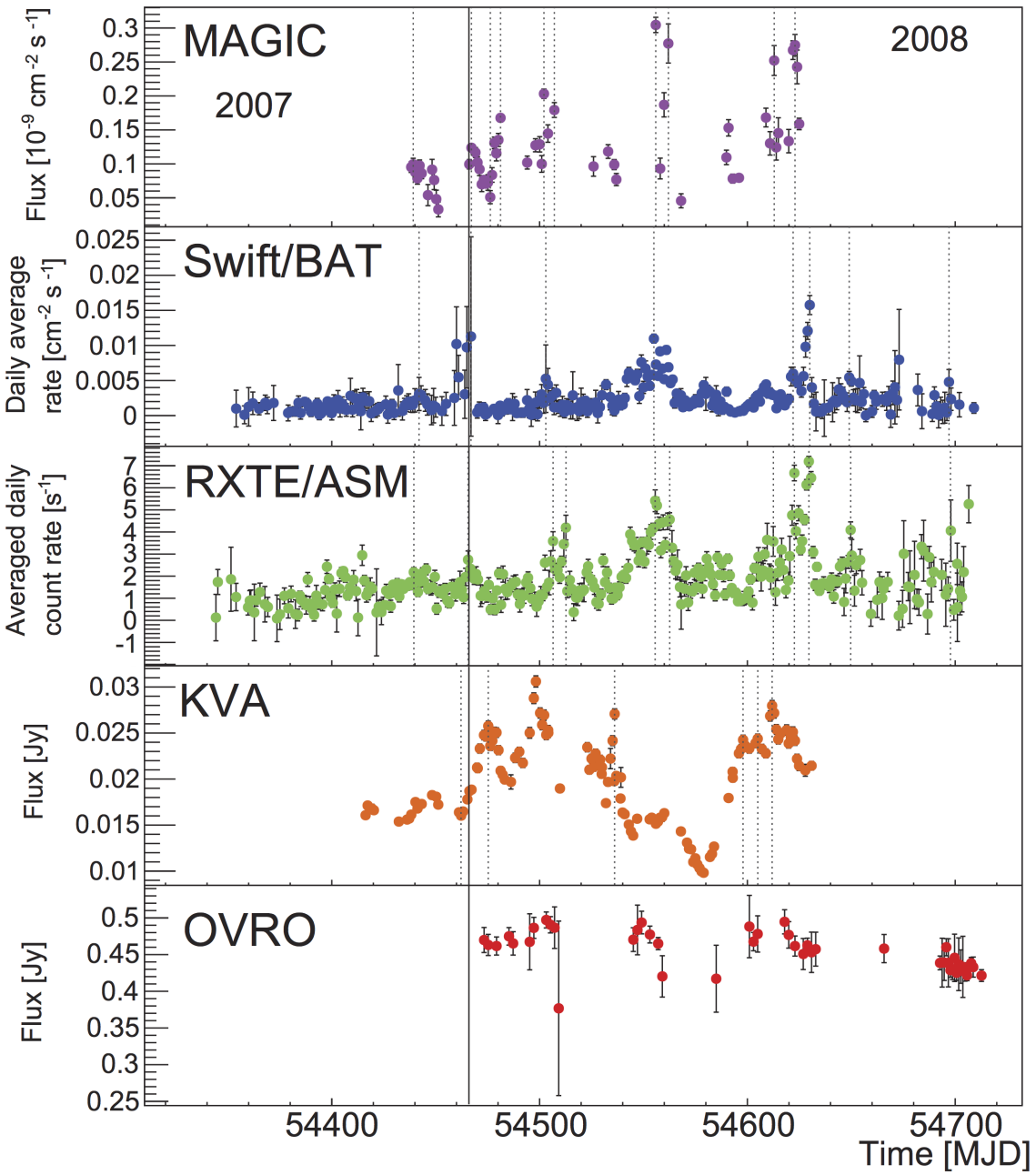

Figure B.2: Mrk 421 light curves of MAGIC, *Swift*/BAT, *RXTE*/ASM, KVA, and OVRO from 09/2007 to 08/2008. The black vertical line represents the division from year 2007 to 2008. The dotted lines represent the flares and minima mentioned in section 7.2.

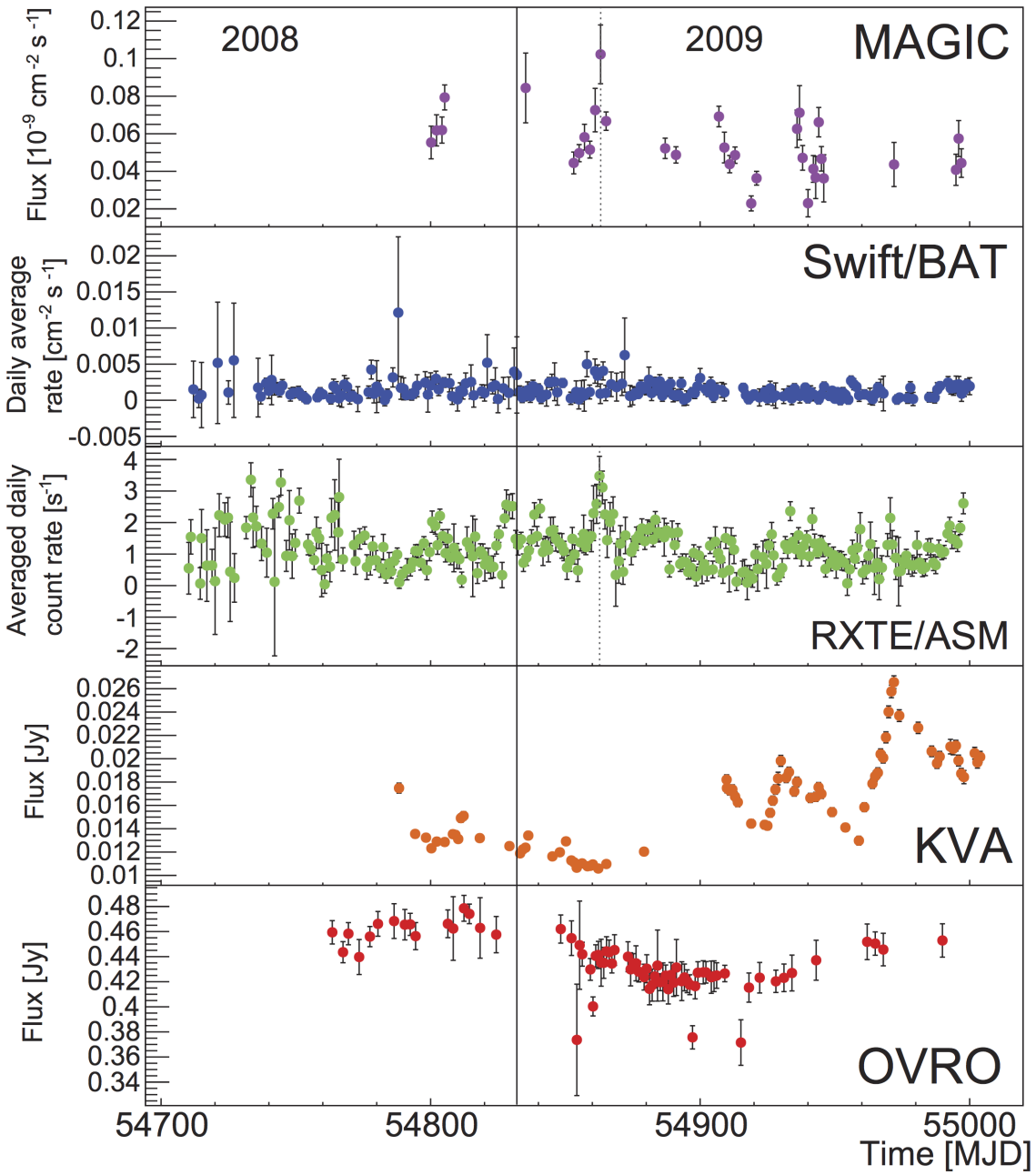

Figure B.3: Light curves of MAGIC, *Swift*/BAT, *RXTE*/ASM, KVA, and OVRO from 09/2008 to 06/2009. The black vertical line represents the division from year 2008 to 2009. The dotted lines represent the flares mentioned in section 7.2.

B.2 Results of variability studies

Table B.1: F_{var} for MAGIC, *Swift*/BAT, *RXTE*/ASM, KVA, and OVRO for the whole time range from 02/2007 to 06/2009. For MAGIC F_{var} was additionally calculated for the three light curves in different energy ranges.

Telescope	F_{var}
MAGIC	0.64 ± 0.01
MAGIC (400 GeV - 600 GeV)	0.50 ± 0.02
MAGIC (600 GeV - 1 TeV)	0.54 ± 0.02
MAGIC (1 TeV - 50 TeV)	0.76 ± 0.02
***Swift*/BAT**	0.46 ± 0.04
***RXTE*/ASM**	0.66 ± 0.01
KVA	0.245 ± 0.002
OVRO	0.032 ± 0.004

Table B.2: F_{var} for MAGIC, *Swift*/BAT, *RXTE*/ASM, KVA, and OVRO for the three time ranges from 02/2007 to 08/2007, from 09/2007 to 08/2008, and from 09/2008 to 06/2009. For MAGIC F_{var} was additionally calculated for the three light curves in different energy ranges.

Telescope	**Time range**	**Time range [MJD]**	F_{var}
MAGIC	03/2007 to 05/2007	54166.9 - 54232.9	0.38 ± 0.07
	12/2007 to 06/2008	54438.2 - 54624.9	0.49 ± 0.01
	11/2008 to 06/2009	54800.2 - 54996.9	0.27 ± 0.03
MAGIC (400 GeV - 600 GeV)	03/2007 to 05/2007	54170.9 - 54232.9	0
	12/2007 to 06/2008	54438.2 - 54624.9	0.35 ± 0.02
	11/2008 to 06/2009	54800.2 - 54996.9	0.18 ± 0.04
MAGIC (600 GeV - 1 TeV)	03/2007 to 05/2007	54166.9 - 54211.9	0.32 ± 0.11
	12/2007 to 06/2008	54438.2 - 54624.9	0.40 ± 0.02
	11/2008 to 06/2009	54800.2 - 54996.9	0.15 ± 0.04
MAGIC (1 TeV - 50 TeV)	03/2007 to 05/2007	54166.9 - 54211.9	0.40 ± 0.12
	12/2007 to 06/2008	54438.2 - 54624.9	0.62 ± 0.02
	11/2008 to 06/2009	54800.2 - 54996.9	0.39 ± 0.04
***Swift*/BAT**	02/2007 to 08/2007	54143 - 54322	0
	09/2007 to 08/2008	54354 - 54709	0.60 ± 0.04
	09/2008 to 06/2009	54712 - 55000	0
***RXTE*/ASM**	02/2007 to 08/2007	54141.4 - 54343.1	0.37 ± 0.05
	09/2007 to 08/2008	54344.3 - 54706.5	0.57 ± 0.01
	09/2008 to 06/2009	54710.3 - 54997.7	0.40 ± 0.02
KVA	02/2007 to 06/2007	54149.2 - 54268.9	0.169 ± 0.004
	11/2007 to 06/2008	54416.3 - 54630.9	0.240 ± 0.002
	11/2008 to 06/2009	54788.3 - 55003.9	0.238 ± 0.003
OVRO	01/2008 to 09/2008	54473.3 - 54712.7	0
	10/2008 to 06/2009	54763.5 - 54989.9	0.037 ± 0.004

B.3 Additional results for cross-correlation

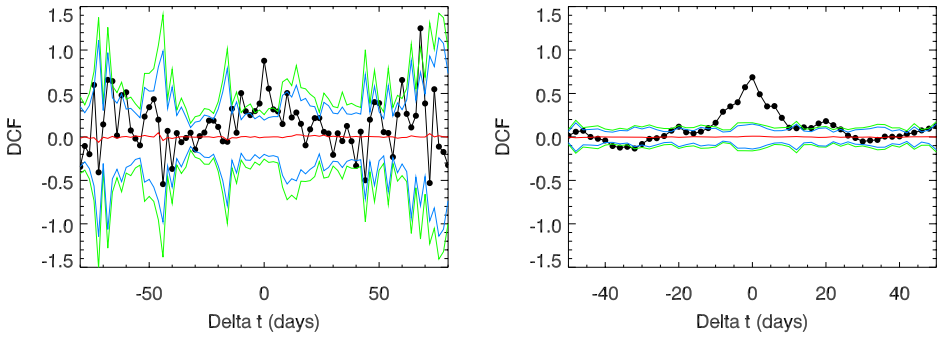

(a) MAGIC and MAGIC, 12/2007 to 06/2008.

(b) *RXTE*/ASM and *Swift*/BAT, 09/2007 to 08/2008.

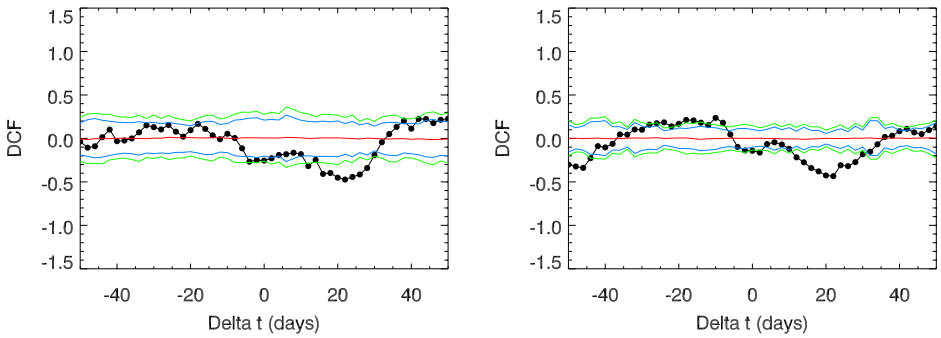

(c) *Swift*/BAT and KVA, 09/2007 to 08/2008.

(d) *RXTE*/ASM and KVA, 09/2007 to 08/2008.

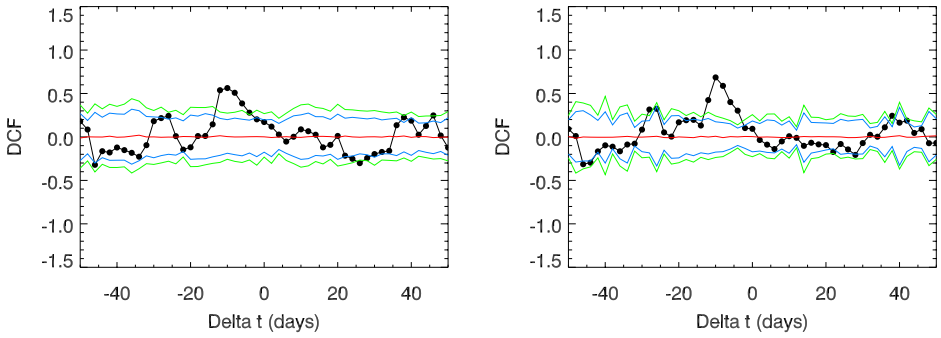

(e) *Swift*/BAT and OVRO, 09/2007 to 08/2008.

(f) *RXTE*/ASM and OVRO, 09/2007 to 08/2008.

Figure B.4: DCF results for different sets of telescopes in the time period from autumn 2007 to summer 2008. For the exact dates and the set of two telescopes see the corresponding caption of each figure. The red line is the median of all 1000 DCFs. The blue and green line represent the 95% and 99% confidence limits.

B.4 Spectral energy distribution

Table B.3: Reference list of instruments for the SED of Mrk 421.

Abbreviation	Instrument
NORTH	Green Bank Northern Sky Survey [Whi92]
DIXON	Ohio State University Radio Observatory (The director of the radio observatory was R. Dixon.) [Dix70]
JVASPOL	Jodrell-VLA (Very Large Array) Astrometric Survey [Jac07]
OVRO	Owens Valley Radio Observatory, data shown in section 7.2
2MASS	Two Micron All Sky Survey [Cut03]
SDSS10	Sloan Digital Sky Survey (10th release) [Ahn14]
USNO	US Naval Observatory [Mon03]
KVA	Kungliga Vetenskapsakademien telescope, data shown in section 7.2
Catalina	Catalina Real-Time Transient Survey [Dra09]
2XMM	XMM (X-ray Multi-Mirror)-*Newton* in pointed mode [Wat09]
XMMSL1	XMM (X-ray Multi-Mirror)-*Newton* in slewing mode [Sax08]
ARIEL	Leicester Sky Survey Instrument on *Ariel V* [War81]
BAT39	*Swift*/BAT after 39 months [Cus10a]
BAT54	*Swift*/BAT after 54 months [Cus10b]
IBISSG4	Fourth IBIS (Imager on Board *INTEGRAL* Spacecraft) Survey Catalog [Bir10]
BAT58	*Swift*/BAT after 58 months [Bau10]
BAT70	*Swift*/BAT after 70 months [Bau13]
AGILE	*Astrorivelatore Gamma ad Imaggini LEggero* satellite [Pit09]
Fermi	Large Area Telescope (LAT) on board the *Fermi* satellite [Nol12]
MAGIC	Major Atmospheric Gamma-Ray Imaging Cherenkov telescopes, this work

Table B.4: Dates and time ranges in MJD for the SED in three different time ranges.

Instrument	2007	2007-2008	2008-2009
OVRO		54473 - 54713	54764 - 54990
KVA	54149 - 54269	54416 - 54631	54788 - 55004
Catalina	54158 - 54273	54417 - 54640	54791 - 54975
2XMM	54229 - 54231	54424 - 54617	54793 - 54976
XMMSL1	54224		
AGILE		54290 - 54648	
Fermi			54683 - 55017
MAGIC	54167 - 54233	54438 - 54625	54800 - 54997

Appendix C
One-zone SSC model for the 2009 SED

In order to get an insight into the emission of radiation in the jet of Mrk 421, data spanning over the whole electromagnetic spectrum have been considered. In section 7.3 the variability of the light curves of different experiments was quantified. A connected variability of X-rays and γ-rays was found. In section 7.4 the correlation of these light curves was examined. It was shown that the γ-ray light curve is directly correlated to the X-ray light curves, but that it is not directly correlated to the optical and radio light curves. In section 7.5 it could be seen that both bumps of the SED behave similarly. All these results hint towards a possible description of the emission process by the SSC emission model.
For the modelling of a SED it is necessary to measure as much as possible of the electromagnetic spectrum during the same emission state. In the active time period from the autumn of 2007 to the summer of 2008 the flux state of Mrk 421 changed frequently. Therefore, it was not possible to get a good sampled SED for these different emission states. Additionally, it would not make sense to model an average SED during this variable time period. The flux emission from the beginning to the summer of 2007 was low and stable. However, the second bump is not fully covered during that time period. Therefore, the time period from the autumn of 2008 to the summer of 2009 is chosen for the SED modelling because firstly, Mrk 421 was in a stable and low emission state, which ensures a stable SED shape, and secondly, the second bump of the SED is covered because *Fermi*-LAT data is available.
The SED to be modelled does not include the radio data point by OVRO because the radio emission is believed not to stem exclusively from the same emission region as the higher energetic radiation. Therefore, it only serves as an upper bound for the modelling. The included data points for the modelling by KVA in the optical waveband, by 2XMM in the X-ray waveband and by *Fermi* and MAGIC in the γ-ray band were already shown in Figure 7.7. The exact dates of these averaged observation results can be found in Table B.4. The data point by Catalina in the optical waveband is not included in the modelling because it is not corrected for the contribution of the host galaxy. The one-zone SSC model used here does not include this contribution. Additionally, average results in the hard X-ray waveband from BAT58 and BAT70 are included. These points were already shown in Figure 7.6.

The SSC emission model is based on the synchrotron emission of an electron population and the subsequent IC scattering of these synchrotron photons on the same electron population. The electron population follows a power law spectrum between γ_{min} and γ_{max}, whereas the electron energy is expressed via $\gamma m_{\mathrm{e}} c^2$. However, a break at γ_{break} in the electron spectrum is assumed because high energetic electrons are suppressed due to the energy loss by synchrotron radiation [Tak11]. The electron energy distribution can be specified as follows:

$$\frac{dN}{d\gamma} = \begin{cases} n_{\mathrm{e}} \cdot \gamma^{-\alpha_1} & \text{for } \gamma_{\mathrm{min}} < \gamma < \gamma_{\mathrm{break}}, \\ n_{\mathrm{e}} \cdot \gamma_{\mathrm{break}}^{\alpha_2-\alpha_1} \cdot e^{\frac{\gamma_{\mathrm{break}}}{\gamma_{\mathrm{max}}}} \cdot \gamma^{-\alpha_2} \cdot e^{-\frac{\gamma}{\gamma_{\mathrm{max}}}} & \text{for } \gamma_{\mathrm{break}} < \gamma. \end{cases} \tag{C.1}$$

Here, n_{e} gives the density of electrons in the emission region and α_1 and α_2 describe the spectral index below and above the break energy γ_{break}. The following additional parameters are needed for the modelling: the radius R of the spherical emission region, the strength of the magnetic field B, and the Doppler factor δ of the emission region. Here, a single zone is assumed as emission region.
The script used here is provided by M. Doert. It uses the SSC model description given in [Tak11]. The code was already successfully applied to the SED of Mrk 501 with data of the year 2009 and the results are to be published in [Ale15c].

For this first rough modelling approach, the parameters γ_{min}, γ_{break}, γ_{max}, α_1, α_2, n_{e}, R, B, and δ are iterated and a resulting model is produced for all combinations. The χ^2 of these models in comparison to the given data points gives a measure for their goodness of fit. In Figure C.1 the five best matching models - according to the smallest resulting χ^2 values, whereas model 1 is the best fitting model - are plotted in comparison to the given data points. It has to be noted that the calculation of the χ^2 includes the error bars of the data points into account. Therefore, the goodness of the fit is dominated by the deviations in the X-ray range because these data points have the smallest error bars. The used model parameters of the five best matching models are summarised in Table C.1.

Table C.1: One-zone SSC model parameters for the 2009 SED of Mrk 421.

Parameter	**Model 1**	**Model 2**	**Model 3**	**Model 4**	**Model 5**
γ_{min}	$1.0 \cdot 10^2$	$1.0 \cdot 10^2$	$1.0 \cdot 10^2$	$1.0 \cdot 10^2$	$1.0 \cdot 10^2$
γ_{break}	$1.3 \cdot 10^5$	$3.5 \cdot 10^4$	$1.0 \cdot 10^4$	$3.5 \cdot 10^4$	$1.3 \cdot 10^5$
γ_{max}	$3.7 \cdot 10^6$	$7.0 \cdot 10^7$	$3.7 \cdot 10^6$	$7.0 \cdot 10^7$	$7.0 \cdot 10^7$
α_1	2.3	2.1	2.3	2.3	2.2
α_2	3.5	3.7	3.5	3.7	3.7
n_{e} [cm^{-3}]	$1.5 \cdot 10^3$	$1.0 \cdot 10^2$	$1.0 \cdot 10^2$	$1.0 \cdot 10^2$	$1.0 \cdot 10^2$
R [cm]	$5.0 \cdot 10^{16}$	$5.0 \cdot 10^{16}$	$1.6 \cdot 10^{17}$	$1.6 \cdot 10^{17}$	$1.6 \cdot 10^{17}$
B [mG]	10.6	47.3	47.3	100	5
δ	50	40	40	20	50

In Figure C.1 it can be seen that all models describe the falling edge of the first bump well. None of the models comes close to the optical point by KVA. All models overestimate the optical flux. The data points of the second SED bump is described best by model 1 and

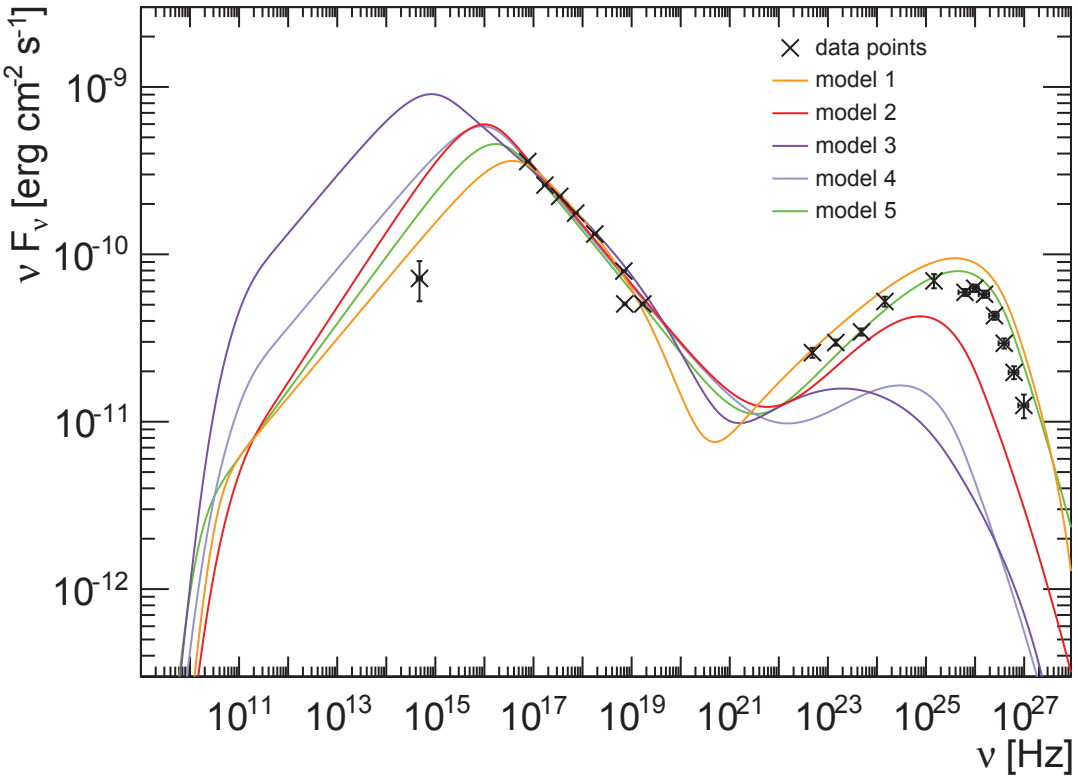

Figure C.1: SED of Mrk 421 in 2009 with five one-zone SSC models with different parameters.

model 5. The other three models clearly underestimate the flux at the higher energies. Model 1 and 5 have a high Doppler factor of $\delta = 50$, a high break energy γ_{break} and a small magnetic field strength B in common. The high Doppler factor is responsible for the apparent brightness at the highest energies. The high break energy causes the peak position of the first SED bump to appear at higher frequencies. This describes the rising edge of the first bump better than the models with lower break energies.

The data set covering the quiet emission state of Mrk 421 from the autumn of 2008 to the summer of 2009 can be roughly described by the one-zone SSC model. However, deviations are seen for the optical data point as well as for the data points in the γ-ray waveband. The given data set was very limited in comparison to the data set e.g. in [Abd11]. In the study by [Abd11] it could also be seen that the given shape of the SED required an electron spectrum with two breaks instead of just one. Due to the limited amount of data points, this was not further investigated here. The resulting values of model 1 and 5 for the radius R, the magnetic field strength B, and the Doppler factor δ of the emission region are comparable to the results found by [Abd11].
It could be shown that the provided script is able to find a model for a one-zone SSC emission scenario for the SED of Mrk 421 during the quiet emission state in 2009. For a given parameter set it determines the goodness of the fit and the best matching model

can be selected. A next step would be a finer grid of the model parameters around the parameters of the best matching model.

List of Figures

2.1 Overview of propagation through the Universe of the messenger particles and their detection. . . . 4
2.2 Hillas plot of different astrophysical sources. . . . 5
2.3 Schematic view of an AGN. . . . 10
2.4 Optical and γ-ray images of Mrk 421. . . . 13
2.5 SED of Mrk 421 between 01/2009 and 06/2009. . . . 14

3.1 MAGIC-I camera images of different events. . . . 17
3.2 Illustration of the principle of the IACT technique. . . . 18
3.3 Photograph of the MAGIC telescopes at night during observations. . . . 20
3.4 Photograph of the FACT telescope at sunset. . . . 23

4.1 Image parameters of a cleaned shower image. . . . 28
4.2 Hadronness values for γ and hadron test sample. . . . 30
4.3 DISP and θ parameters in a cleaned shower image. . . . 31
4.4 ON and OFF regions for the signal detection. . . . 32
4.5 Signal plot of Crab Nebula for 2007 to 2009. . . . 33
4.6 Light curve of the Crab Nebula for 2007 to 2009. . . . 36

5.1 PSF of MAGIC-I from 2007 to 2009 41
5.2 Signal plot of Mrk 421 from April 2007 until February 2009 for a zenith angle below 30°. . . . 45
5.3 Light curve of Mrk 421 between 8th March 2007 and 15th June 2009. . . . 46
5.4 Light curve of Mrk 421 between 8th March and 13th May 2007. . . . 47
5.5 Light curve of Mrk 421 between 4th December 2007 and 8th June 2008. . . . 48
5.6 Light curve of Mrk 421 between 30th November 2008 and 15th June 2009. . . . 50
5.7 Light curve of Mrk 421 between 8th March and 13th May 2007 for the different energy ranges. . . . 51
5.8 Light curve of Mrk 421 between 4th December 2007 and 8th June 2008 for the different energy ranges. . . . 52
5.9 Light curve of Mrk 421 between 30th November 2008 and 15th June 2009 for the different energy ranges. . . . 53
5.10 Ratios of the fluxes in the three different energy ranges. . . . 54
5.11 Short-term light curve of 31st March 2008. . . . 56
5.12 Short-term light curve of 12th March 2008 with flare fits. . . . 58
5.13 Short-term light curve of 31st March 2008 with flare fits. . . . 59
5.14 Effect of the EBL correction on the unfolded spectrum. . . . 63

5.15 Unfolded spectra of the three time periods. 65
5.16 Unfolded spectra of several single nights. 66
5.17 Spectral slope as a function of the integral flux. 67

6.1 Exemplary distribution of periodogram bars Per(p) and Per(p) for each trial period p. 73
6.2 Periodograms for the MAGIC-I light curve from 2007 to 2009. 74
6.3 Periodogram for the modified MAGIC-I light curve from 2007 to 2009. . . . 75
6.4 Light curve of Mrk 421 from 1992 to 2012 measured by several Cherenkov telescopes. 76
6.5 Light curve of Mrk 421 from the end of 2000 to the middle of 2001 measured by the HEGRA CT1 and telescope system. 77
6.6 Periodograms for the Mrk 421 light curve from 1992 to 2012. 78
6.7 Periodograms for the Mrk 421 light curve from 1992 to 2012 without the MAGIC-I data from 2007 to 2008. 79
6.8 Periodograms for the Mrk 421 light curve from 1992 to 2012 without the HEGRA data in 2001. 80
6.9 Excess rate curve of Mrk 421 measured by FACT between January 2013 and January 2015. 81
6.10 Periodograms for the FACT light curve from 2013 to 2015. 82

7.1 Mrk 421 light curves of MAGIC, *Swift*/BAT, *RXTE*/ASM, KVA, and OVRO from February 2007 to June 2009. 88
7.2 Variability for all five instruments for the whole time range. 90
7.3 Variability for all five instruments for the three different observation periods. 91
7.4 DCF results for *Swift*/BAT and MAGIC as well as for *RXTE*/ASM and MAGIC. 95
7.5 DCF results for KVA and MAGIC as well as for OVRO and MAGIC. . . . 97
7.6 SED of Mrk 421. 100
7.7 SED for the three different time periods. 102

A.1 Short-term light curve of 2nd February 2008. 120
A.2 Short-term light curve of 12th March 2008. 120
A.3 Short-term light curve of 5th May 2008. 121

B.1 Mrk 421 light curves of MAGIC, *Swift*/BAT, *RXTE*/ASM, and KVA from 02/2007 to 08/2007. 123
B.2 Mrk 421 light curves of MAGIC, *Swift*/BAT, *RXTE*/ASM, KVA, and OVRO from 09/2007 to 08/2008. 124
B.3 Light curves of MAGIC, *Swift*/BAT, *RXTE*/ASM, KVA, and OVRO from 09/2008 to 08/2009. 125
B.4 DCF results for different sets of telescopes. 128

C.1 SED of Mrk 421 in 2009 with one-zone SSC models. 133

List of Tables

5.1 Mrk 421 good quality data sample. . . . 43
5.2 Crab Nebula data sample. . . . 44
5.3 Short-term light curves of Mrk 421 with constant fit results. . . . 56
5.4 Flare fit results for short-term light curves of Mrk 421. . . . 60
5.5 Fit probability of the correlated fit for the unfolded spectra of the three time periods. . . . 62
5.6 Fit results of the correlated fit of the unfolded spectra for the three time periods. . . . 64

7.1 List of instruments for the SED. . . . 99

A.1 Daily significances of the Mrk 421 data (PSF 13.0 mm, Zd 9° - 30°). . . . 109
A.2 Daily significances of the Mrk 421 data (PSF 13.0 mm, Zd 30° - 45°). . . . 111
A.3 Daily significances of the Mrk 421 data (PSF 14.8 mm, Zd 9° - 30°). . . . 112
A.4 Daily significances of the Mrk 421 data (PSF 14.8 mm, Zd 30° - 45°). . . . 113
A.5 Excluded 50 nights of Mrk 421 data. . . . 113
A.6 List of sources and dates for the selected hadron sample. . . . 114
A.7 Crab Nebula data sample. . . . 115
A.8 Cut values for the significance calculations in *odie*, optimised on data of the Crab Nebula. . . . 115
A.9 Cut values for the significance calculations in *odie*, applied to Mrk 421 data. 115
A.10 Cut values for the calculation of the light curve and spectrum in *fluxlc*, optimised on data of the Crab Nebula. . . . 116
A.11 Light curve results of the Mrk 421 data determined with *fluxlc*. . . . 116
A.12 Constant fit results of the light curves for the whole energy range from 400 GeV to 50 TeV. . . . 119
A.13 Constant fit results of the light curves for the three different energy ranges. 119
A.14 Fit results of the correlated fit of the unfolded spectra of several single nights. 121
A.15 All fit results of the correlated fit of the unfolded spectra for different fit functions. . . . 122

B.1 F_{var} for MAGIC, *Swift*/BAT, *RXTE*/ASM, KVA, and OVRO for the whole time range from 02/2007 to 06/2009. . . . 126
B.2 F_{var} for MAGIC, *Swift*/BAT, *RXTE*/ASM, KVA, and OVRO for the three different time ranges. . . . 127
B.3 Reference list of instruments for the SED. . . . 129
B.4 Time ranges for the SED in three different time ranges. . . . 129

C.1 One-zone SSC model parameters. 132

Bibliography

The numbers after each reference refer back to the pages of citation within this thesis.

[Aar13] Aartsen, M.G., et al. (IceCube Collaboration): *Evidence for High-Energy Extraterrestrial Neutrinos at the IceCube Detector*. Science, 342:1242856, November 2013. 6

[Abd11] Abdo, A.A., et al. (*Fermi*-LAT Collaboration, MAGIC Collaboration): *Fermi Large Area Telescope observations of Markarian 421: The missing piece of its spectral energy distribution*. The Astrophysical Journal, 736:131 (22pp), August 2011. 12, 13, 14, 60, 103, 133

[Abr08] Abraham, J., et al. (Pierre Auger Collaboration): *Observation of the suppression of the flux of cosmic rays above 4×10^{19} eV*. Physical Review Letters, 101:061101, August 2008. 5

[Acc09] Acciari, V.A., et al. (VERITAS Collaboration, MAGIC Collaboration): *Simultaneous multiwavelength observations of Markarian 421 during outburst*. The Astrophysical Journal, 703:169 – 178, September 2009. 103

[Acc11] Acciari, V.A., et al. (VERITAS Collaboration, MAGIC Collaboration): *TeV and multi-wavelength observations of Mrk 421 in 2006 - 2008*. The Astrophysical Journal, 738:25 (19pp), September 2011. 103, 105

[Acc14] Acciari, V.A., et al.: *Observation of Markarian 421 in TeV gamma rays over a 14-year time span*. Astroparticle Physics, 54:1 – 10, July 2014. 69

[Act11] Actis, M., et al. (The CTA Consortium): *Design concepts for the Cherenkov Telescope Array CTA: an advanced facility for ground-based high-energy gamma-ray astronomy*. Experimental Astronomy, 32:193–316, December 2011. 20

[Aha02] Aharonian, F., et al.: *Variations of the TeV energy spectrum at different flux levels of Mkn 421 observed with the HEGRA system of Cherenkov telescopes*. Astronomy and Astrophysics, 393:89 – 99, October 2002. 75

[Aha03] Aharonian, F., et al.: *TeV gamma-ray light curve and energy spectrum of Mkn 421 during its 2001 flare as measured with HEGRA CT1*. Astronomy and Astrophysics, 410:813 – 821, November 2003. 75

[Aha04] Aharonian, F.A.: *Very High Energy Cosmic Gamma Radiation: A crucial window on the Extreme Universe*. World Scientific Publishing, Singapore, 2004. 7, 8, 17, 18

[Ahn14] Ahn, C.P., et al.: *The tenth data release of the Sloan Digital Sky Survey: First spectroscopic data from the SDSS-III Apache Point Observatory Galactic Evolution Experiment.* The Astrophysical Journal Supplement Series, 211:14 (33pp), April 2014. 99, 129

[Ahn15] Ahnen, M.L., et al. (MAGIC Collaboration). *In preparation*, 2015. 85

[Alb07a] Albert, J., et al. (MAGIC Collaboration): *Unfolding of differential energy spectra in the MAGIC experiment.* Nuclear Instruments and Methods in Physics Research A, 583:494–506, December 2007. 36, 37, 61

[Alb07b] Albert, J., et al. (MAGIC Collaboration): *Variable very high energy γ-ray emission from Markarian 501.* The Astrophysical Journal, 669:862–883, November 2007. 57

[Alb08a] Albert, J., et al. (MAGIC Collaboration): *Implementation of the Random Forest method for the Imaging Atmospheric Cherenkov Telescope MAGIC.* Nuclear Instruments and Methods in Physics Research A, 588:424–432, April 2008. 29

[Alb08b] Albert, J., et al. (MAGIC Collaboration): *VHE γ-ray observations of the Crab Nebula and its pulsar with the MAGIC telescope.* The Astrophysical Journal, 674:1037–1055, February 2008. 20, 21, 34, 35, 36, 46, 62, 64

[Ale12a] Aleksić, J., et al. (MAGIC Collaboration): *Mrk 421 active state in 2008: the MAGIC view, simultaneous multi-wavelength observations and SSC model constrained.* Astronomy and Astrophysics, 542:A100, June 2012. 103, 105

[Ale12b] Aleksić, J., et al. (MAGIC Collaboration): *Performance of the MAGIC stereo system obtained with Crab Nebula data.* Astroparticle Physics, 35:435–448, February 2012. 20, 21

[Ale14a] Aleksić, J., et al. (MAGIC Collaboration): *The major upgrade of the MAGIC telescopes, Part I: The hardware improvements and the commissioning of the system.* Accepted for publication in Astroparticle Physics, arXiv: 1409.6073 [astro-ph.IM], September 2014. 19, 20, 21

[Ale14b] Aleksić, J., et al. (MAGIC Collaboration, VERITAS Collaboration): *Unprecedented Study of the Broadband Emission of Mrk 421 during Flaring Activity in March 2010.* Accepted for publication in Astronomy and Astrophysics, arXiv: 1412.3576 [astro-ph.HE], December 2014. 103, 105

[Ale15a] Aleksić, J., et al. (MAGIC Collaboration): *The 2009 multiwavelength campaign on Mrk 421: Variability and correlation studies.* Accepted for publication in Astronomy and Astrophysics, arXiv: 1502.02650 [astro-ph.HE], February 2015. 92

[Ale15b] Aleksić, J., et al. (MAGIC Collaboration, VERITAS Collaboration): *Multiwavelength observations of Mrk501 in 2008.* Astronomy and Astrophysics, 573:A50, January 2015. 89

[Ale15c] Aleksić, J., et al. (MAGIC Collaboration, VERITAS Collaboration, *Fermi*-LAT Collaboration): *Unprecedented temporal evolution of the broad-band emission of the BL Lac Mrk 501 in 2009.* in preparation, 2015. 132

[Ali08] Aliu, E., et al. (MAGIC Collaboration): *Observation of Pulsed γ-Rays Above 25 GeV from the Crab Pulsar with MAGIC.* Science, 322:1221–1224, November 2008. 22

[Ali09] Aliu, E., et al. (MAGIC Collaboration): *Improving the performance of the single-dish Cherenkov telescope MAGIC through the use of signal timing.* Astroparticle Physics, 30:293–305, January 2009. 26, 27

[And13] Anderhub, H., et al. (FACT Collaboration): *Design and operation of FACT - the first G-APD Cherenkov telescope.* Journal of Instrumentation, 8:P06008, June 2013. 19, 22, 23, 80

[Bau10] Baumgartner, W.H., Tueller, J., Markwardt, C., Skinner, G.: *The Swift-BAT 58 Month Survey.* Bulletin of the American Astronomical Society, 41:675, February 2010. 99, 129

[Bau13] Baumgartner, W.H., Tueller, J., Markwardt, C.B., Skinner, G.K., Barthelmy, S., Mushotzky, R.F., Evans, P.A., Gehrels, N.: *The 70 Month Swift-BAT All-Sky Hard X-Ray Survey.* The Astrophysical Journal Supplement Series, 207:19 (12pp), August 2013. 99, 129

[Beh12] Behringer, J., et al. (Particle Data Group): *Review of Particle Physics.* Physical Review D, 86:010001, July 2012. 7, 9, 10, 60

[Bes05] Bessel, M.S.: *Standard photometric systems.* Annual Review of Astronomy and Astrophysics, 43:293 – 336, August 2005. 86

[Bir10] Bird, A.J., et al.: *The Fourth IBIS/ISGRI Soft Gamma-ray Survey Catalog.* The Astrophysical Journal Supplement Series, 186:1 – 9, January 2010. 99, 129

[Bla05] Blazejowski, M., et al. (VERITAS Collaboration): *A multiwavelength view of the TeV blazar Markarian 421: Correlated variability, flaring, and spectral evolution.* The Astrophysical Journal, 630:130 – 141, September 2005. 12, 103

[Blo98] Blobel, V., Lohrmann, E.: *Statistische und numerische Methoden der Datenanalyse.* Verlag Teubner, Stuttgart, Leipzig, 1998. 36

[Blu09] Bluemer, J., Engel, R., Hoerandel, J.R.: *Cosmic Rays from the Knee to the Highest Energies.* arXiv: 0904.0725 [astro-ph.HE], April 2009. 3, 4, 5

[Boe12] Boettcher, M., Harris, D.E., Krawczynski, H.: *Relativistic Jets from Active Galactic Nuclei.* Wiley-VCH Verlag, Weinheim, 2012. 7, 8, 9, 10, 11, 12

[Bol13] Boller, A.S.: *Observations of Markarian 421 in 2010 and 2011 with the MAGIC telescopes.* PhD thesis, ETH Zürich, 2013. 55

[Bre03] Bretz, T., Wagner, R., et al. (MAGIC Collaboration): *The MAGIC Analysis and Reconstruction Software.* Proceedings of 28th International Cosmic Ray Conference (Tsukuba, Japan), August 2003. 25

[Buc96] Buckley, J.H., et al.: *Gamma-ray variability of the BL Lacertae object Markarian 421.* The Astrophysical Journal, 472:L9 – L12, November 1996. 75

[Car08] Carmona, E., Majumdar, P., Moralejo, A., Vitale, V., Sobczynska, D., Haffke, M., Bigongiari, C., Otte, N., Cabras, G., de Maria, M., de Sabata, F. (MAGIC Collaboration): *Monte Carlo Simulation for the MAGIC-II System.* Proceedings of 30th International Cosmic Ray Conference (Merida, Mexico), 3:1373–1376, 2008. 26

[CER11] CERN Courier: *Innovative camera records cosmic rays during full moon.* http://cerncourier.com/cws/article/cern/47816, November 2011. 22

[Cha08] Chatterjee, R., et al.: *Correlated multi-wave band variability in the blazar 3C 279 from 1996 to 2007.* The Astrophysical Journal, 689:79 – 94, December 2008. 92

[Cor13] Cortina, J. and Holder, J. for the MAGIC and VERITAS Collaborations: *MAGIC and VERITAS detect an unprecedented flaring activity from Mrk 421 in very high energy gamma-rays.* The Astronomer's Telegram ATel #4976, April 2013. 81

[Cus10a] Cusumano, G., et al.: *The Palermo Swift-BAT hard X-ray catalogue. II. Results after 39 months of sky survey.* Astronomy and Astrophysics, 510:A48 (20pp), February 2010. 99, 129

[Cus10b] Cusumano, G., et al.: *The Palermo Swift-BAT hard X-ray catalogue. III. Results after 54 months of sky survey.* Astronomy and Astrophysics, 524:A64 (37pp), December 2010. 99, 129

[Cut03] Cutri, R.M., et al.: *2MASS All Sky Catalog of point sources.* http://irsa.ipac.caltech.edu/applications/Gator, June 2003. 99, 129

[Dix70] Dixon, R.S.: *A master list of radio sources.* The Astrophysical Journal Supplement Series, 20:1 – 503, July 1970. 99, 129

[Doe13] Doert, M.: *The talkative AGN next door: Broad-band spectral variability of the TeV blazar Markarian 501.* PhD thesis, Technische Universität Dortmund, February 2013. 37

[Dom05] Domingo-Santamaria, E., Flix. J., Rico, J., Scalzotto, V., Wittek, W. (MAGIC Collaboration): *The DISP analysis method for point-like or extended γ source searches/studies with the MAGIC Telescope.* Proceedings of 29th International Cosmic Ray Conference (Pune, India), 5:363–366, August 2005. 31

[Don09] Donnarumma, I., et al. (AGILE Team, GASP-WESP Team, MAGIC Collaboration, VERITAS Collaboration): *The June 2008 flare of Markarian 421 from optical to TeV energies.* The Astrophysical Journal, 691:L13 – L19, January 2009. 75, 103

[Dor08] Doro, M., et al.: *The reflective surface of the MAGIC telescope.* Nuclear Instruments and Methods in Physics Research A, 595:200–203, September 2008. 21

[Dra09] Drake, A.J., et al.: *First results from the Catalina Real-Time Transient Survey.* The Astrophysical Journal, 696:870 – 884, May 2009. 99, 129

[Dre09] Dreyer, J.: *Neutrinos from Starburst-Galaxies: A source stacking analysis of AMANDA II and IceCube data.* PhD thesis, Technische Universität Dortmund, December 2009. 4

[Ede88] Edelson, R.A., Krolik, J.H.: *The Discrete Correlation Function: A new method for analyzing unevenly sampled variability data.* The Astrophysical Journal, 333:646 – 659, October 1988. 92

[Fal12] Falkenburg, B., Rhode, W.: *From Ultra Rays to Astroparticles - A Historical Introduction to Astroparticle Physics.* Springer Verlag, 2012. 8, 9

[Fer49] Fermi, E.: *On the origin of the Cosmic Radiation.* Physical Review, 75:1169 – 1174, April 1949. 5

[Fom94] Fomin, V.P., Stephanian, A.A., Lamb, R.C., Lewis, D.A., Punch, M., Weekes, T.C.: *New methods of atmospheric Cherenkov imaging for gamma-ray astronomy. I. The False Source Method.* Astroparticle Physics, 2:137–150, May 1994. 22

[Fra08] Franceschini, A., Rodighiero, G., Vaccari, M.: *Extragalactic optical-infrared background radiation, its time evolution and the cosmic photon-photon opacity.* Astronomy and Astrophysics, 487:837–852, September 2008. 8, 62

[Fra15] Frantzen, K.,. PhD thesis, Technische Universität Dortmund, to be published in 2015. 76

[Gai96] Gaidos, J.A., et al.: *Extremely rapid bursts of TeV photons from the active galaxy Markarian 421.* Nature, 383:319–320, September 1996. 11, 13, 55

[Gar13] Garcia, J.R., Dazzi, F., Häfner, D., Herranz, D., Lopez, M., Mariotti, M., Mirzoyan, R., Nakajima, D., Schweizer, T., Teshima, M.: *Status of the new Sum-Trigger system for the MAGIC telescopes.* Proceedings of 33rd International Cosmic Ray Conference (Rio de Janeiro, Brazil), July 2013. 22

[Gau08] Gaug, M., Moralejo, A.: *A handbook of the standard MAGIC analysis chain.* MAGIC internal report, MAGIC-TDAS 08-02, March 2008. 26, 27, 29

[Gie13] Giebels, B. (H.E.S.S. Collaboration): *Status and recent results from H.E.S.S.* Proceedings of 4th Fermi Symposium 2012 (Monterey, CA, USA), March 2013. 19

[Gre66] Greisen, K.: *End to the cosmic ray spectrum?* Physical Review Letters, 16:748 – 750, April 1966. 5

[Gru05] Grupen, C.: *Astroparticle Physics.* Springer Verlag, Berlin, Heidelberg, New York, 2005. 3, 5, 6, 15, 16

[Hal03] Halpern, J.P., Leighly, K.M., Marshall, H.L.: *An Extreme Ultraviolet Explorer Atlas of Seyfert Galaxy Light Curves: Search for Periodicity.* The Astrophysical Journal, 585:665 – 676, March 2003. 72, 77, 80

[Hec98] Heck, D., Knapp, J., Capdevielle, J.N., Schatz, G., Thouw, T.: *CORSIKA: A Monte Carlo Code to Simulate Extensive Air Showers.* Forschungszentrum Karlsruhe, Wissenschaftliche Berichte, FZKA 6019, 1998. 25

[Hes12] Hess, V.F.: *Penetrating Radiation in Seven Ballon Flights.* Physikalische Zeitschrift, 13:1084, 1912. 1

[Hil85] Hillas, A.M.: *Cerenkov light images of EAS produced by primary gamma rays and by nuclei.* Proceedings of 19th International Cosmic Ray Conference (La Jolla, USA), 3:445–448, August 1985. 27

[Jac07] Jackson, N., Battye, R.A., Browne, I.W.A., Joshi, S., Muxlow, T.W.B, Wilkinson, P.N.: *A survey of polarization in the JVAS/CLASS flat-spectrum radio source survey - I. The data and catalogue production.* Monthly Notices of the Royal Astronomical Society, 376:371 – 377, March 2007. 99, 129

[Jel58] Jelley, J.V.: *Čerenkov radiation and its applications.* Pergamon Press, London, New York, Paris, Los Angeles, 1958. 17

[Kat12] Katz, U., Spiering, C.: *High-Energy Neutrino Astrophysics: Status and Perspectives.* Progress in Particle and Nuclear Physics, 67:651 – 704, July 2012. 6, 16

[Ker95] Kerrick, A.D., et al.: *Outburst of TeV photons from Markarian 421.* The Astrophysical Journal, 438:L59 – L62, January 1995. 75

[Kes03] Kestel, M.: *TeV Gamma-Flux and Spectrum of Markarian 421 in 1999/2000 with Hegra CT1 using refined Analysis Methods.* PhD thesis, Technische Universität München, April 2003. 75

[Kon99] Konopelko, A., et al. (HEGRA Collaboartion): *Performance of the stereoscopic system of the HEGRA imaging air Čerenkov telescopes: Monte Carlo simulations and observations.* Astroparticle Physics, 10:275–417, May 1999. 23

[Kra01] Krawczynski, H., et al.: *Simultaneous X-Ray and TeV Gamma-Ray Observation of the TeV Blazar Markarian 421 during 2000 February and May.* The Astrophysical Journal, 559:187 – 195, September 2001. 75

[Kre02] Krennrich, F., et al.: *Discovery of spectral variabillity of Markarian 421 at TeV energies.* The Astrophysical Journal Letters, 575:L9 – L13, August 2002. 13

[Kri13] Krimm, H.A., et al.: *The Swift/BAT hard X-ray transient monitor.* The Astrophysical Journal Supplement Series, 209:14 (33pp), November 2013. 86

[Lev96] Levine, A.L., Bradt, H., Cui, W., Jernigan, J.G., Morgan, E.H., Remillard, R., Shirey, R.E., Smith, D.A.: *First results from the all-sky monitor on the Rossi X-ray Timing Explorer.* The Astrophysical Journal, 469:L33–L36, September 1996. 86, 87

[Li 83] Li , T., Ma, Y.: *Analysis methods for results in gamma-ray astronomy.* The Astrophysical Journal, 272:317–324, September 1983. 34

[Mar72] Markaryan, B.E., Lipovetskii, V.A.: *Galaxies with ultraviolet continuum V.* Astrophysics, 8:89 – 99, April - June 1972. 12

[Maz07] Mazin, D.: *A study of very high energy γ-ray emission from AGNs and constraints on the extragalactic background light.* PhD thesis, Technische Universität München, November 2007. 31, 32

[Mey05] Meyer, M.: *Calibration of the MAGIC telescope using muon rings.* MAGIC internal report, MAGIC-TDAS 05-10, June 2005. 40

[Mon03] Monet, D.G., et al.: *The USNO-B catalog.* The Astronomical Journal, 125:984 – 993, February 2003. 99, 129

[Mor09] Moralejo, A., Gaug, M., Carmona, E., Colin, P., Delgado, C., Lombardi, S., Mazin, D., Scalzotto, V., Sitarek, J., Tescaro, D., et al. (MAGIC Collaboration): *MARS, the MAGIC Analysis and Reconstruction Software.* Proceedings of 31st International Cosmic Ray Conference (Lodz, Poland), July 2009. 25, 26

[Nil99] Nilsson, K., Pursimo, T., Takalo, L.O., Sillanpää, A., Pietilä, H., Heidt, J.: *Two dimensional Photometric Decomposition of the TeV BL Lacertae Objects Markarian 421, Markarian 501, and 1ES 2344+514.* Publications of the Astronomical Society of the Pacific, 111:1223 – 1232, October 1999. 12, 13, 69

[Nis99] Nishikawa, D., et al.: *Periodicity in the TeV gamma rays and X rays from Markarian 501.* Proceedings of 26th International Cosmic Ray Conference (Salt Lake City, USA), August 1999. 69

[Nol12] Nolan, P.L., et al. (*Fermi*-LAT Collaboration): *Fermi Large Area Telescope Second Source Catalog.* The Astrophysical Journal Supplement Series, 199:31 (46pp), April 2012. 99, 102, 129

[Oke74] Oke, J.B., Gunn, J.E.: *The distance of BL Lacertae.* The Astrophysical Journal, 189:L5 – L8, April 1974. 11

[Pao07] Paoletti, R., Cecchi, R., Corti, D., Dazzi, F., Mariotti, M., Pegna, R., Turini, N.: *The Trigger System of the MAGIC Telescope.* IEEE Transactions on Nuclear Science, 54:404–409, April 2007. 18, 21

[Pin99] Piner, B.G., Unwin, S.C., Wehrle, A.E., Edwards, P.G., Fey, A.L., Kingham, K.A.: *VSOP and Ground-based VLBI Imaging of the TeV Blazar Markarian 421 at Multiple Epochs.* The Astrophysical Journal, 525:176 – 190, November 1999. 12

[Pit09] Pittori, C., et al.: *First AGILE catalog of high-confidence gamma-ray sources.* Astronomy and Astrophysics, 506:1563 – 1574, November 2009. 99, 129

[Pou08] Poutanen, J., Zdziarski, A.A., Ibragimov, A.: *Superorbital variability of X-ray and radio emission of Cyg X-1 -II. Dependence of the orbital modulation and spectral hardness on the superorbital phase.* Monthly Notices of the Royal Astronomical Society, 389:1427–1438, September 2008. 89

[Pov09] Povh, B., Rith, K., Scholz, C., Zetsche, F.: *Teilchen und Kerne.* Springer Verlag, Berlin, Heidelberg, 2009. 7

[Pud12] Pudritz, R.E., Hardcastle, M.J., Gabduzda, D.C.: *Magnetic Fields in Astrophysical Jets: From Launch to Termination.* Space Science Reviews, 169:27 – 72, September 2012. 9

[Pun92] Punch, M., et al.: *Detection of TeV photons from the active galaxy Markarian 421.* Nature, 358:477–478, August 1992. 12, 45

[Raj14] Rajotte, J.-F. (VERITAS Collaboration): *Upgrade and performance of the VERITAS telescope array.* Nuclear Instruments and Methods in Physics Research A, 766:61 – 64, December 2014. 19

[Reb06] Rebillot, P.F., et al.: *Multiwavelength Observations of the Blazar Markarian 421 in 2002 December and 2003 January.* The Astrophysical Journal, 641:740 – 751, April 2006. 75

[Ric11] Richards, J.L., et al.: *Blazars in the Fermi era: The OVRO 40 m telescope monitoring program.* The Astrophysical Journal Supplement Series, 194:29(22pp), June 2011. 86, 99

[Rie00] Rieger, F.M., Mannheim, K.: *Implications of a possible 23 day periodicity for binary black hole models in Mkn 501.* Astronomy and Astrophysics, 359:948 – 952, July 2000. 69

[Sai09] Saito, T.Y., Sitarek, J.: *Improvement of the θ^2 analysis by using the Random Forest method in the DISP estimation.* MAGIC internal report, MAGIC-TDAS 09-01, May 2009. 31

[Sar09] Sarty, G.E., et al.: *Periodicities in the high mass X-ray binary system RX J0146.9+6121/LS I+61°235.* Monthly Notices of the Royal Astronomical Society, 392:1242 – 1252, January 2009. 69

[Sat10] Satalecka, K.: *Multimessenger studies of point-sources using the IceCube neutrino telescope and the MAGIC gamma-ray telescope.* PhD thesis, Humboldt-Universität Berlin, May 2010. 30

[Sax08] Saxton, R.D., Read, A.M., Esquej, P., Freyberg, M.J., Altieri, B., Bermejo, D.: *The first XMM-Newton slew survey catalogue: XMMSL1.* Astronomy and Astrophysics, 480:611 – 622, March 2008. 99, 129

[Sch96] Schubnell, M.S., et al.: *Very High Energy Gamma-Ray Emission from the Blazar Markarian 421.* The Astrophysical Journal, 460:644 – 650, April 1996. 75

[Sch08] Schweizer, T., Wagner, R., Lorenz, E.: *A Statistical Study of Sub-Hour Flares of the VHE Gamma-Ray Emission of Markarian 421 During a High Flux State in 2001.* American Institute of Physics Conference Proceeding, 1085, July 2008. 12, 13, 55, 57, 60

[Sch13] Schultz, C.: *Development of New Composite Mirrors for Imaging Cherenkov Telescopes and Observations of the Two Blazar Objects 1ES 0806+524 and 1ES 1011+496 with MAGIC.* PhD thesis, Universita degli Studi di Padova, January 2013. 28

[Sta10] Stanev, T.: *High Energy Cosmic Radiation.* Springer Verlag, Berlin, Heidelberg, New York, 2010. 5, 6

[Ste12] Steinke, B.: *First study of fast variability in Markarian 421 with the MAGIC stereoscopic system.* PhD thesis, Technische Universität München, March 2012. 18

[Str11] Stratta, G., Capalbi, M., Giommi, P., Primavera, R., Cutini, S., Gasparrini, D. (ASDC team): *The ASDC SED Builder Tool description and Tutorial.* arXiv: 1103.0749 [astro-ph.IM], March 2011. 99

[Tak08] Takalo, L.O., Nilsson, K., Lindfors, E., Sillanpää, Berdyugin, A., Pasanen, M.: *Tuorla Blazar Monitoring Program.* American Institue of Physics, 1085:705 – 707, July 2008. 86, 99

[Tak11] Takami, H., Horiuchi, S.: *The production of ultra high energy cosmic rays during the early epochs of radio-loud AGN.* Astroparticle Physics, 34:749 – 754, May 2011. 132

[Tes10] Tescaro, D.: *TeV γ-ray observations of nearby Active Galactic Nuclei with the MAGIC telescope: exploring the high energy region of the multiwavelength picture.* PhD thesis, IFAE at Universitat Autònoma de Barcelona, July 2010. 10

[Tes13] Tescaro, T., López-Oramas, A., Moralejo, A., Mazin, D., Hadasch, D. (MAGIC Collaboration): *The MAGIC telescopes DAQ software and the on-the-fly online analysis client.* Proceedings of 33rd International Cosmic Ray Conference (Rio de Janeiro, Brazil), July 2013. 22

[Thi13a] Thieler, A.M., Backes, M., Fried, R., Rhode, W.: *Periodicity detection in irregularly sampled light curves by robust regression and outlier detection.* Statistical Analysis and Data Mining: The ASA Data Science Journal, 6:73–89, January 2013. 70, 72, 80

[Thi13b] Thieler, A.M., Fried, R., Rathjens, J.: *RobPer: An R Package to Calculate Periodograms for Light Curves Based on Robust Regression.* Technical Report SFB 876, Technische Universität Dortmund, February 2013. 69, 70, 72

[Thi14] Thieler, A.M.: *Robuste Verfahren zur Periodendetektion in ungleichmäßig beobachteten Lichtkurven.* PhD thesis, Technische Universität Dortmund, January 2014. 69, 70, 71, 84

[Tlu10] Tluczykont, M., Bernadini, E., Satalecka, K., Clavero, R., Shayduk, M., Kalekin, O.: *Long-term lightcurves from combined unified very high energy γ-ray data.* Astronomy and Astrophysics, 524:A48, December 2010. 13, 75, 76, 77, 80

[Urr95] Urry, C.M., Padovani, P.: *Unified Schemes for Radio-Loud Active Galactic Nuclei.* Publications of the Astronomical Society of the Pacific, 107:803 – 845, September 1995. 9, 10

[Utt03] Uttley, P., Edelson, R., McHardy, I.M., Peterson, B.M., Markowitz, A.: *Correlated long-term optical and X-ray variations in NGC 5548.* The Astrophysical Journal, 584:L53 – L56, February 2003. 92

[Vau03] Vaughan, S., Edelson, R., Warwick, R.S., Uttley, P.: *On characterizing the variability properties of X-ray light curves from active galaxies.* Monthly Notices of the Royal Astronomical Society, 345:1271–1284, November 2003. 89

[Wag04] Wagner, W.: *Design and Realisation of a new AMANDA Data Acquisition System with Transient Waveform Recorders.* PhD thesis, Universität Dortmund, October 2004. 4

[War81] Warwick, R.S., Marshall, N., Fraser, G.W., Watson, M.G., Lawrence, A., Page, C.G., Pounds, K.A., Ricketts, M.J., Sims, M.R., Smith, A.: *The Ariel V (3A) catalogue of X-ray sources.* Monthly Notices of the Royal Astronomical Society, 197:865 – 891, December 1981. 99, 129

[Wat09] Watson, M.G., et al.: *The XMM-Newton serendipitous survey: V. The Second XMM-Newton serendipitous source catalogue.* Astronomy and Astrophysics, 493:339 – 373, January 2009. 99, 129

[Wee03] Weekes, T.C.: *Very High Energy Gamma-Ray Astronomy.* Institute of Physics Publishing, Bristol, 2003. 7, 8, 9, 10, 11, 12, 15, 16, 17, 18, 19, 29, 30, 44

[Whi92] White, R.L., Becker, R.H.: *A new catalog of 30,239 1.4 GHz sources.* The Astrophysical Journal Supplement Series, 79:331 – 467, April 1992. 99, 129

[Wu 09] Wu , Z., Gu, M., Jiang, D.: *The debeamed luminosity, synchrotron peak frequency and black hole mass of BL Lac objects.* Research in Astronomy and Astrophysics, 9:168 – 178, 2009. 12, 60, 100

[Zat66] Zatsepin, G.T., Kuzmin, V.A.: *Upper limit of the spectrum of cosmic rays.* Physical Review Letters, 4:78 – 80, August 1966. 5

List of Abbreviations

2MASS	Two Micron All Sky Survey
AGILE	*Astrorivelatore Gamma ad Imaggini LEggero*
AGN	Active Galactic Nucleus
AMC	Active Mirror Control
ASDC	Italian Space Agency (ASI) Data Center
ASM	All-Sky Monitor
BAT	Burst Alert Telescope
BH	black hole
BL Lac	BL Lacertae
CAT	Cerenkov Array at Thémis
CMB	cosmic microwave background
CORSIKA	COsmic Ray SImulations for KAscade
CR	cosmic ray
CT	Cherenkov Telescope
CTA	Cherenkov Telescope Array
CU	Crab Unit
DAC	Digital-to-Analog Converter
DCF	Discrete Correlation Function
DM	dark matter
DRS	Domino Ring Sampler
DT	discriminator threshold
EAS	Extensive Air Shower
EBL	extragalactic background light
EC	External Compton (model)
FACT	First G-APD Cherenkov Telescope
FADC	Flash Analog to Digital Converter
FOV	field of view
FSRQ	Flat Spectrum Radio Quasar
G-APD	Geiger-mode Avalanche Photodiode
GRB	gamma-ray burst
GZK	Greisen-Zatsepin-Kuzmin (cut-off)
HBL	high-frequency peaked BL Lac
HE	high energy
HEGRA	High Energy Gamma Ray Astronomy
H.E.S.S.	High Energy Stereoscopic System
IACT	Imaging Atmospheric Cherenkov Telescope
IBIS	Imager on Board *INTEGRAL* Spacecraft

IC	inverse Compton (scattering)
ISM	interstellar medium
JVASPOL	Jodrell-VLA (Very Large Array) Astrometric Survey
KVA	Kungliga Vetenskapsakademien (telescope)
LAT	(*Fermi*) Large Area Telescope
LBL	low-frequency peaked BL Lac
LHC	Large Hadron Collider
M-I, M-II	MAGIC-I, MAGIC-II
MAGIC	Major Atmospheric Gamma-Ray Imaging Cherenkov (telescope(s))
MARS	MAGIC Analysis and Reconstruction Software
MC	Monte Carlo
MJD	Modified Julian Date
MWL	multi-wavelength
NN	next neighbours
NOT	Nordic Optical Telescope
NS	neutron star
NSB	night sky background
ORM	Observatorio Roque de los Muchachos
OVRO	Owens Valley Radio Observatory
phe	photoelectron equivalent
PIC	port d'informació cientifica
PL	power law
PMT	Photomultiplier Tube
PSD	Power Spectral Density
PSF	point spread function
PWN	pulsar wind nebula
QLA	Quick Look Analysis
QSO	quasi-stellar object
RXTE	*Rossi X-Ray Timing Explorer*
SDSS	Sloan Digital Sky Survey
SED	spectral energy distribution
SiPM	Silicon Photomultiplier
SMBH	supermassive black hole
SN	supernova
SNR	supernova remnant
SSC	Synchrotron Self-Compton (model)
USNO	US Naval Observatory
VERITAS	Very Energetic Radiation Imaging Telescope Array System
VHE	very high energy
XMM	X-ray Multi-Mirror
Zd	zenith distance

Acknowledgement/Danksagung

Ich möchte mich herzlich bei Prof. Dr. Dr. Wolfgang Rhode für die Betreuung meiner Doktorarbeit bedanken. Danke auch dafür, dass ich die Möglichkeit hatte mich mit viel Freude an zwei so tollen Projekten wie MAGIC und FACT zu beteiligen.

Ebenfalls bedanken möchte ich mich bei Prof. Dr. Joachim Stolze, der sich bereit erklärt hat der Zweitgutachter dieser Arbeit zu sein.

Mein Dank geht an alle Kollegen von meinem Lehrstuhl, besonders an Marlene Doert, Katharina Frantzen, Julia Thaele und Malwina Uellenbeck.

I want to thank the members of the MAGIC Collaboration for all discussions and advices as well as for great night shifts on La Palma. Mille grazie especially to Marina Manganaro and Diego Tescaro.

I also thank the members of the FACT Collaboration. I am grateful that I was able to be part of this project almost from the beginning, to see how it came to life and successfully works now!

Nicht vergessen werden soll all die Mühe der fleißigen Korrekturleser: Marlene Doert, Daniel Edelhoff, Katharina Frantzen, Thorben Menne, Florian Scheriau, Julia Thaele, Max Wornowizki und natürlich Carla Overkemping und Keith Williams. Herzlichen Dank.

Vielen Dank auch für die finanzielle Unterstützung dieser Arbeit durch den Sonderforschungsbereich SFB 876 (Teilprojekt C3).